Experimental and theoretical investigation of solar molten media methane cracking for hydrogen production

by

Derek Paxman

A thesis submitted in partial fulfillment of the requirements for the degree of

Master of Science

Department of Mechanical Engineering
University of Alberta

Abstract

Canada is the largest H_2 consumer per capita in the world, giving a strong market demand for H_2. H_2 is commercially produced using steam CH_4 reforming, which is energy and CO_2 intensive. Solar molten metal CH_4 cracking is an alternative zero emissions technology. Solar radiation is focused with large curved mirrors onto the molten metal. The molten media provides improved heat transfer, a thermal storage medium against transient solar flux, and a unique method of separating H_2 and C. Blank and molten metal alumina tube reactors are studied from 1023 K to 1323 K. Plug flow, perfectly mixed, and combined perfectly mixed with a bypass (CPMR) reactor models were numerically implemented to simulate the blank reactor and determine the kinetic parameters. The CPMR model incorporated a third parameter that dictates how much flow travels through the bypass. Results for the CPMR model showed $k_0 = 5.43 \times 10^{15}$ 1/s, $E_a = 420.7$ kJ/mol and $\beta = 0.426$. The CPMR model was shown to have $8.3\% \pm 6.8\%$ average error against data found in literature. Sn was selected as the bath material for the molten metal reactor (MMR), and the reaction gas was bubbled through the bath using an injector. 18.9% conversion was obtained at 1273 K, and near zero conversion for lower temperatures. A numerical model of the MMR was implemented using a spherical bubble model coupled with the CPMR model for the blank space above the molten metal. The MMR model showed that the majority of CH_4 conversion occurred in the blank space above the bath. Decreasing bubble size and increasing bath height improved bubble conversion.

Keywords: methane cracking; hydrogen production; direct contact pyrolysis; methane decomposition; liquid metals

To Erin and my children

Acknowledgements

I would like to thank my God for His help. My Heavenly Father has provided inspiration and guidance on this project, and has helped me to manage my time wisely between my many responsibilities as husband, father, student, friend and community roles such as those in the Church of Jesus Christ of Latter-day Saints.

I thank my wife and family for their patience, support, love and strength in this endeavor. My gratitude also goes to my parents.

I also acknowledge and thank my supervising professor Dr. Marc Secanell. His many hours of time and thought have made a major contribution to this work. I appreciate his patience and that he encouraged discussion and defense of my ideas and solutions.

Thank you Robin Lybbert, a great friend all through undergrad and still to this day.

And to my group members, thanks for your help. Lalit, I appreciate your computer skills with openSUSE. Phil and Kailyn, it has been a pleasure to get to know you during this time together and develop a friendship.

A big thanks to Alberta Innovates - Technology Futures for assisting in funding this research, along with the Natural Sciences and Engineering Research Council.

Last, but not least, thank you to Guillermo Ordorica-Garcia, who helped me onto this path. Also Stephanie Trottier, Juan Segura, Allan Chambers and Mehr Nikoo who assisted me at Alberta Innovates - Technology Futures. Your help has been invaluable.

Table of Contents

List of Tables

List of Figures

Nomenclature

Abbreviations

AITF Alberta Innovates - Technology Futures

CPMR Combined perfectly mixed reactor with deadzone or bypass

GC Gas chromatograph

GHSV Gas hourly space velocity, $[hr^{-1}]$

ID Inner diameter

MFC Mass flow controller

MMR Molten metal reactor

OD Outer diameter

PF Plug flow reactor

PFR Plug flow reactor

PMR Perfectly mixed reactor

PT Pressure transducer

S1 Data set containing all experimental data points

S2 Data set containing all but the 1373 K, 30 sccm experimental data points

STP Standard temperature and pressure, 298 K and 1 atm

TC Thermocouple

UHP Ultra high purity

English Letters

$\dot{q_{cond}}$ Conductive heat flux per unit area, $[W/m^2]$

$\dot{q_{conv}}$ Convective heat flux per unit area, $[W/m^2]$

$\dot{Q}$ Heat flux, $[W]$

$\dot{V}$ Volumetric flow rate, $[m^3/s]$

$\overline{u}$ Average flow velocity of gas mixture, $[m/s]$

A Area, $[m^2]$

A_c Cross-sectional area

Bo Bond number, $\rho_{bath} D_{I,in}^2 g/\sigma_{bath}$

c_D Bubble drag coefficient

C_i Concentration of species i, $[mole/m^3]$

c_p Specific heat capacity at constant pressure, $[j/(mole \cdot K)]$

C_T Total concentration, $[mole/m^3]$

D Diameter, $[m]$

D_0 Molecular diffusivity, $[m^2/s]$

D_g Gas diffusion coefficient, $[m^2/s]$

E_a Activation energy, $[J/mol]$

$E_{a,eff}$ Activation energy at which the effective temperature is calculated at, equal to 390 $[kJ/mol]$

f Square of the residual error, res

F_b Buoyancy force, $[N]$

F_d Drag force, $[N]$

F_w Weight, $[N]$

g Gravity, equal to 9.81 $[m/s^2]$

g' Reduced gravity, $[m/s^2]$

Ga Galilei number, $\rho_{bath}^2 D_{I,in}^3 g/\mu_{bath}^2$

H Enthalpy, $[J/kg]$

h Convection heat coefficient, $[W/(m^2 \cdot K)]$

h_f° Enthalpy of formation at STP, -74.85 $[kJ/mol]$

k Reaction rate coefficient, $[1/s]$

k_0 Pre-exponential factor, $[1/s]$

L Length, $[m]$

L_a Length at which the temperature profile begins to linearly decline, $[m]$

L_b Length at which the 1078 K profile drops below 1023 K, $[m]$

L_d Length at which the 1350 K profile drops below 1023 K, $[m]$

L_H Length measured from bottom (closed end) of reactor at which the operating temperature curve drops below 1023 K, $[m]$

L_r Total length of the reactor vessel, $[m]$

L_{bath} Bath height, $[m]$

$L_{H,above}$ Height of the heated blank space above the molten bath, $[m]$

$L_{I,submerged}$ Depth that the injector is submerged in the bath, $[m]$

M Molar mass, $[kg/mole]$

m Mass, $[kg]$

m_{power} Power-law fluid consistency index

Mo Morton number, $\frac{g\mu_{bath}^4}{\rho_{bath}\sigma^3}$

N_i Molar flow rate of species i, $[mole/s]$

n_j Total moles present of species j, $[s]$

n_{power} Power-law behavior index

P Pressure, $[kPa]$

R Universal gas constant, 8.314 $[kJ/(molK)]$

r Reaction rate, $[1/s]$

r_{bubble} Bubble radius, $[m]$

Ra Rayleigh number, equal to $\frac{gc_p\rho^2L^3}{\gamma_g\mu}\frac{\Delta T}{T}$

Re Reynolds number, $\frac{\rho vL}{\mu}$

res Residual error

res_v Residual for the bubble velocity solver

S_t Surface tension force, $[N]$

T Temperature, $[K]$

t Time, $[s]$

t_w Wall thickness, $[m]$

T_0 Operating temperature, $[K]$

T_{eff} Effective temperature, $[K]$

U Scaled gas velocity inside reactor, $[m/s]$

V Volume, $[m^3]$

v Bubble velocity, $[m/s]$

X Conversion

x_i Mole fraction of species i

z Length from bottom (closed end) of reactor, $[m]$

Greek Letters

α Void fraction

β Fraction of total volumetric flow rate that passes through the deadzone

δ Summation of stoichiometric coefficients in reaction equation

ϵ Radiation emissivity, $[W]$

γ Thermal conductivity, $[W/(m \cdot K)]$

λ Reaction order

μ Dynamic viscosity, $[Pa/s]$

ν_i Stoichiometric coefficient for species i

ω Thermal expansion coefficient, $[K^{-1}]$

σ Surface tension of the bath material, $[N/m]$

σ_{SB} Stefan-Boltzmann constant equal to 5.67×10^{-8}, $[W]$

τ Nominal or mean residence time, $[s]$

Θ Ratio of inlet molar conditions to reference species

θ Edge angle of injector nozzle, $[rad]$

θ_0 Reference angle of injector nozzle, $\pi/2$ $[rad]$

Ω Fraction of total volume that comprises the heated zone

ϖ Product of δ and molar fraction of reference species at inlet

Subscripts and Superscripts

0 Operating or inlet conditions

amb At ambient conditions, 298 K and local atmospheric pressure

bath Molten bath

blank Blank reactor or section of reactor that is blank

bubble Spherical gas bubble in the molten bath

d Deadzone

g Gas

H Heated zone

I Injector

i Species index

in	Inner dimension
$init$	Initial estimation
j	Species index
LB	Lower bound
mix	Gas mixture
out	Outer dimension
r	Reactor
STP	At standard temperature and pressure, 298 K and 1 atm
T	Total
UB	Upper bound
w	Wall

Chapter 1

Introduction

1.1 Motivation

Global demand for energy increased from 216.8 EJ to 492.9 EJ, or by 227% from 1970 to 2006 [10]. Various researchers have forcasted that it could rise to as high as 1000 EJ by 2050, or an additional 200% from the 2006 value, though it is likely that large reductions in energy usage via technology and lifestyle changes will limit the figure to a more manageable level [10]. H_2 production is forecasted to rise to approximately 1.3 - 4.6 EJ in 2030 and 14.7 - 43.8 EJ by 2050 [10]. Steam methane reforming is the conventional technology used to produce nearly all H_2 [11]. However, steam methane reforming is CO_2 intensive, producing about 11.9 kg of CO_2 per kg of H_2 [11, 12]. Therefore other methods to produce H_2 that are more greenhouse gas-friendly need to be developed.

Alberta Innovates - Technology Futures (AITF) performed an analysis on leading options for H_2 production. Alberta is a large consumer of H_2 due to the heavy oil refining/oil sands bitumen upgrading and nitrogen fertilizer production industries. Solar H_2 production was identified as a significant opportunity. A comprehensive study of technical and market risks deemed that molten metal methane cracking was a leading option [13]. Molten metal methane cracking was previously studied by one research group at the Argonne National Laboratory, USA by Serban et al. [2].

Molten metal methane cracking has several advantages to other H_2 production processes. If powered by concentrated solar thermal energy, molten metal methane cracking is CO_2 free, and does not require burning of the feedstock to provide the required energy (such as steam methane reforming) [14]. Furthermore, bubbling CH_4 through molten metal provides a higher surface to gas contact ratio which improves

heat transfer. Concentrated solar thermal cracking reactors that are indirectly heated exhibit large re-radiation losses due to the high temperatures that are required [1], whereas the molten metal methane cracking reactor may be able to operate at lower temperatures and reduce these losses. Also, the high heat capacitance of the molten metal will reduce thermal shock damage to the reactor exhibited by other concentrated solar thermal cracking reactors [15]. Finally, the carbon is expected to rise to the molten metal surface. It is believed that conventional methods to remove slag from molten metals can be utilized to harvest the carbon [12]. The carbon can then be either sold as a marketable product for use in tires, inks or pigments, or it can be easily stored in the ground [12].

Experimental analysis of a molten metal methane cracking reactor can be very expensive. Serban et al. [2] studied 0.5 μm Mott spargers as the injector that bubbled CH_4 through the molten metal. A cost estimate has shown that each 0.5 μm Mott sparger is $2500 [16]. Each molten metal experiment also requires the one time use of the Alumina tube reactor vessel, which is $250 each [16]. The pure molten media (Sn) is also expensive. Thus it was found beneficial to reduce costs by developing a numerical model that could predict CH_4 conversion and assist in understanding the key parameters of the molten metal methane cracking reactor concept.

1.2 Literature Review

In this section, the chemistry of CH_4 cracking is first reviewed, including an analysis of multi-reaction mechanisms. Catalytic cracking is then discussed. Following this the experimental and modeling work for non-catalytic cracking or carbon-catalyst cracking is reviewed.

1.2.1 Chemistry of methane cracking

The overall dissociation of CH_4 is given as [17]

$$CH_{4(g)} \rightarrow 2H_{2(g)} + C_{(s)}, \quad h_f^\circ = \text{-}74.85 \quad \text{kJ/kmol} \tag{1.1}$$

where h_f° is the enthalpy of formation of CH_4. Other byproducts such as $C_2H_{6(g)}$, $C_2H_{4(g)}$ and $C_2H_{2(g)}$ as well as polycyclic aromatic hydrocarbons also are recorded byproducts [1, 18–20]. The kinetics are generally defined by the Arrhenius equation as

$$k = k_0 \exp\left(-\frac{Ea}{RT}\right) \tag{1.2}$$

where k_0 is the frequency factor or pre-exponential factor in [1/s], E_a is the activation energy in [kJ/mol], R is the universal gas constant of 8.314 kJ/(mol K), and T is the reaction temperature. The rate of reaction is calculated by

$$-r_{CH_4} = kC^{\lambda}_{CH_4} \tag{1.3}$$

where C_{CH_4} is CH_4 concentration, and λ is the reaction order.

1.2.1.1 Reaction mechanisms

Khan and Crynes [21] provided a review of the non-catalytic CH_4 pyrolysis literature prior to 1970. Shock-tube and nonshock-tube analysis were used to determine reaction mechanisms for various temperature ranges and operating pressures. The author reported overall activation energies in the range of 151 to 422 kJ/mol for nonshock-tube studies and 390-418 kJ/mol for shock-tube studies. It was concluded that the nonshock-tube studies obtained a much larger range of activation energies, but also that they were generally lower than those reported by the shock-tube studies. The author suggested that heterogeneous reactions have less impact in shock-tube studies than in the nonshock studies. It was estimated that the shock-tube studies give much higher gas-to-gas than gas-to-wall collisions than the nonshock-tube studies. However, Eisenberg and Bliss [22] performed some special runs in which two different levels of wall/surface ratio were used. Wall effects were shown to have a minor impact on overall conversion. The special tests were run in a 7 mm OD tubular quartz reactor at an effective temperature of 1458 K with 15% CH_4 in N_2 balance. Other studies have suggested that the lower activation energy for nonshock-tube studies may be because the gas temperature in the nonshock flow tubes are lower than the tube walls at higher feedrates [23]. Since the gas temperature is unknown, the tube wall temperature is used in the kinetics calculations. This problem of measuring the tube wall temperature and not the gas temperature would affect the calculations and result in a lower activation energy.

Only two mechanisms reported by Khan and Crynes [21] gave overall activation energies with pre-exponential factors. These were $k_0 = 1.32 \times 10^{14}$ 1/s for $E_a = 390kJ/mol$, and $k_0 = 1.3 \times 10^{14}$ 1/s for $E_a = 422.6$ kJ/mol. The prior system was for a temperature range of 1656 - 1965 K and the latter was for 1423 - 1573 K. The majority of the papers reviewed accepted that the overall reaction for CH_4 cracking is first-order. Billaud et al. [24] reviewed studies of CH_4 thermal decomposition from 1960 to 1989. Several mechanisms were presented. Chen et al. [25] proposed overall reaction kinetics of $k_0 = 2.8 \times 10^{16}$ 1/s and $E_a = 450.2$ kJ/mol for a temperature

range of 995 - 1103 K. Otherwise, reported kinetic parameters fell within the range of those reported by the review of Khan and Crynes [21]. Also, most papers in Khan and Crynes review assumed first order kinetics.

Methane dissociation in the overall reaction has been described as stepwise dehydrogenation at high temperatures [5, 23].

$$\begin{aligned} 2CH_{4(g)} &\rightarrow C_2H_{6(g)} + H_{2(g)} \rightarrow C_2H_{4(g)} + 2H_{2(g)} \\ &\rightarrow C_2H_{2(g)} + 3H_{2(g)} \rightarrow 2C_{(s)} + 4H_{2(g)} \end{aligned} \tag{1.4}$$

Other more complicated mechanisms have been developed. In 1992, Billaud et al. [20] produced a model comprising 119 elementary reactions that was able to predict gaseous concentrations of various products of CH_4 pyrolysis at 1263 K. The model did not include C formation as it was intended to study the conversion of CH_4 into higher hydrocarbons. Later in 1997, Gueret et al. [3] performed a thermodynamic study on CH_4 pyrolysis with the goal to produce primarily acetylene. An equilibrium curve by the author is given in Figure 1.1. The author used the Gibbs energy minimization method where the species present and number of moles is conserved. Solid carbon is not included in this equilibrium curve, however it does show that H_2 is the primary product of CH_4 dissociation. Temperature is shown to have a large impact on conversion. The study was not conclusive on the question if higher pressure had a significant impact on producing higher order H/C ratio by-products.

In 1995, Olsvik et al. [18] developed a 36 reaction mechanism for methane decomposition for a temperature range of 1473 - 1773 K. The CHEMKIN software package was used to simulate the reaction mechanism in an ideal plug flow reactor (PFR). Only the gas phase was considered. In 2009, Younessi-Sinaki et al. [26] developed a combined 242 reaction with 75 species mechanism to predict methane cracking. The reaction mechanism was developed using various mechanisms for methane pyrolysis and combustion from literature. The reactions containing oxygen were removed. The author assumed a perfectly mixed reactor (PMR). The model was shown to predict well for hydrogen production for temperature ranges of 873-1873 K by comparing to data in literature.

Ozalp et al. [11] studied methane cracking using a 37 gas-phase reaction mechanism to simulate non-catalytic cracking. An eight reaction mechanism from literature was used for catalytic cracking. The gas-phase or homogeneous reaction mechanism included the 36 reaction mechanism and kinetics proposed by Olsvik et al. [18] plus

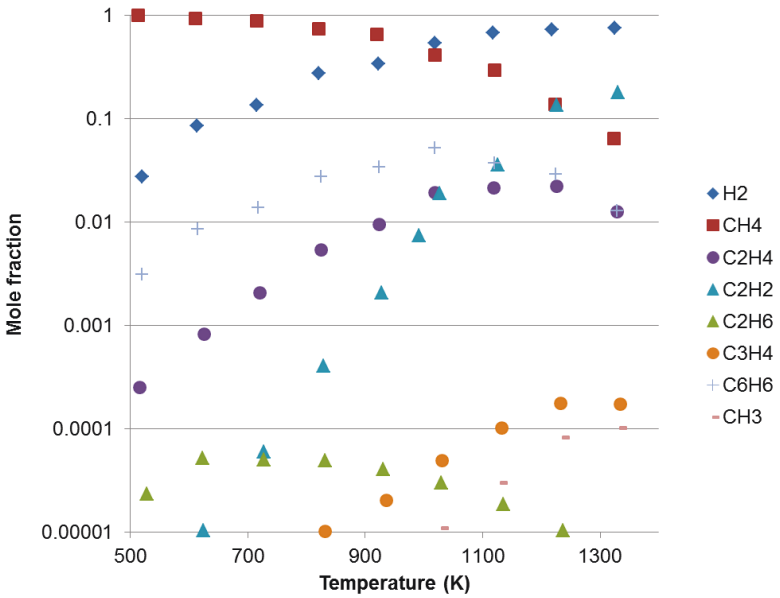

Figure 1.1 – Equilibrium for CH_4 pyrolysis using Gibbs energy minimization method. Data from [3]

another reaction from literature to simulate the formation of C. Thermogravimetric analysis tests were performed to test the activity of solid carbon for CH_4 cracking versus non-catalytic cracking. The author also developed a theoretical model assuming a PFR and using CHEMKIN Pro software with homogeneous and non-homogeneous reaction mechanisms. It was concluded that the non-catalytic mechanism did not predict carbon formation well.

1.2.1.2 Catalytic methane cracking

In 2010 and 2011, Abbas and Daud [27] and Amin et al. [28] performed comprehensive reviews of catalytic CH_4 decomposition, respectively. It was shown that non-catalytic CH_4 cracking at temperatures below 1273 K is very slow, while on the other hand catalytic cracking can occur as low as 773 K [28]. Abbas and Daud [27] presented the catalytic transition metals for CH_4 decomposition in the following order: Co, Ru, Ni, $Rh > Pt$, Re, $Ir > Pd$, Cu, W, Fe, Mo. However it was suggested by some researchers that the addition of alumina as a support can increase the activities of Ni or Fe to the highest [27]. Carbon black and activated carbon have also been studied as catalysts. Sn has not been identified as a catalyst for CH_4 cracking in either review or a current review of literature. The catalyzed CH_4 cracking reaction is generally considered heterogeneous because the hydrocarbons undergo dehydrogenation

at the surface of the catalyst. However, CH_4 that is far away from the catalyst will undergo homogenous reactions. In comparison, homogeneous reactions do not occur on the surface of a material, but heterogeneous reactions do. The surface provides a different pathway for the reaction to occur. Depending on the material of the surface, the pathway could require less energy and thus increase CH_4 conversion.

The primary purpose for using catalysts for methane cracking is to reduce the reaction temperatures to facilitate the growth of amorphous filamentous carbon, which is more desirable to reduce deactivation of the catalyst. Reducing the temperature also improves thermal efficiency. It was concluded by both reviews that deactivation of metal catalysts due to carbon buildup on the catalyst surface is a common issue with catalytic cracking [27, 28]. The primary method to regenerate the metal catalysts is to burn off the C deposition using either CO_2, H_2O or O_2. However, these processes are CO_2 intensive and on the same scale as the commercially accepted steam methane reforming process. Activated carbon catalysts consists of carbon where the porosity depends on the manufacturing process and raw material that was used [27]. The porosity of the activated carbon diminishes quickly over time as the CH_4 cracking reaction proceeds, reducing the effectiveness of the catalyst. Carbon black does not experience the same deactivation due to loss of surface area with pores being filled [27], though over time it will eventually be covered by carbon crystallites. Activated carbon catalysts and carbon black are also expensive [27]. Therefore it is desirable to find a non-catalytic CH_4 cracking solution that is more efficient than the current technologies.

1.2.2 Experimental and modeling methods

Various reactor concepts have been used to study CH_4 dissociation, including shock tube, non-shock or flow tube, and flow reactors with various geometries proposed for solar reactors. Khan and Crynes [21] provides an extensive review of shock and non-shock tube studies prior to 1970. Billaud et al. [24] reviewed experimental and modeling work done between 1960 and 1989, and attempted to find a consensus in the major stages and reaction mechanisms for methane cracking. The author found that the mechanisms were significantly lacking in predicting liquid hydrocarbon and coke products. Abbas and Daud [27] provided a review of more recent non-catalytic and catalytic CH_4 decomposition work done between 2000 and 2009.

Table 1.1 contains a review of experimental and kinetic work performed for CH_4 cracking. Non-catalytic cracking was the focus of this review, even though most researchers have used catalysts. The second focus was made on carbon black or activated carbon catalytic CH_4 cracking. The cracking process produces carbon as a byproduct in either case, which may be autocatalyzing. Steinberg [29] found that fine submicron carbon particles formed by CH_4 cracking can autocatalyze the reaction. The autocatalyzing effect may increase CH_4 conversion by providing a carbon surface for heterogeneous reactions, similar to the carbon black catalyst discussed earlier. However, Muradov et al. [30] found that carbon produced by CH_4 cracking is not sufficiently catalytically active to autocatalyze the reaction.

1.2.2.1 Experimental work

Different energy sources have been used to heat the reactors. These are plasma heating including microwave plasma, solar radiation, and electric furnaces [27, 31, 32]. Several studies reviewed by Abbas and Daud [27] and some studies given in Table 1.1 used an electric furnace or coil to heat the reactor [18, 20, 22, 29]. A large amount of studies use solar radiation furnaces to provide heat to the reactor [1, 15, 33–38]. For proof of concept, however, it is more economical to use an electric furnace. Also, an electric furnace allows more uniform control over the reaction temperature.

Two different heating methods may be used to provide the thermal energy necessary to crack CH_4, namely indirect heating or direct (solar) heating [35]. The indirect method heats the reactor walls via different energy sources, such as electrical energy, plasma or concentrated solar irradiation. The reaction gas is heated by the reactor walls through convection. The directly heated method utilizes direct solar energy and heats the reaction gas directly. Both methods have drawbacks. The directly heated method poses a difficulty of heating the reactant gas since CH_4 is a poor absorber of solar energy in the visible spectrum [35]. The directly heated method also poses a difficult problem of transparent window and breakage due to carbon particle deposition and overheating [1]. On the other hand, the indirect method requires higher temperatures in the walls because of the convective heat transfer limitations of the wall to gas [35]. This can lead to significant re-radiation losses and material selection difficulties [1].

Table 1.1 – Experimental and kinetic studies found in literature

Author	**Year**	**Study type**	**Operating conditions**	**Catalyst**	λ	k_0 **(1/s)**	E_a **(kJ/mol)**
Eisenberg and Bliss [22]	1967	Both	1373-1473 K 101 kPa	none	Not first	-	-
• 7 mm fused quartz tube. Heated by electric resistance coils • Dimensionless PMR assumed. • Five reaction mechanism • Temperature profile measured using thermocouple. Isothermal effective temperature assumed using an integration of the Arrhenius equation over the reactor length. • Study suggests that the overall reaction was not first order within the operating temperature.							
Khan and Crynes [21]	1970	Both	Various	none	n/a	1.30×10^{14}	151-422
• Range of kinetic parameters given in review. • Few overall pre-exponential factors given because review is of proposed reaction mechanisms. • Most papers reviewed assumed first order kinetics.							
Billaud et al. [20]	1992	Both	1263 K 101 kPa	none	n/a	-	-
• 12 mm ID alumina tube. Heated by an electric furnace. • Dimensionless PMR assumed. • Temperature profiling likely an effect because tube extended out of furnace at both ends. Isothermal temperature was assumed. • 119 reaction mechanism.							

Author	Year	Study type	Operating conditions	Catalyst	λ	k_0 (1/s)	E_a (kJ/mol)
Olsvik et al. [18]	1995	Both	1473-1773 K 101 kPa	none	1	1.00×10^{13}	366
• 4 or 9 mm ID alumina tube. • 1D PFR comprised of 30 micromixed reactors assumed. • Temperature profile measured using thermocouple. Isothermal effective temperature assumed using an integration of the Arrhenius equation over the reactor length. • 36 reaction mechanism used, however overall kinetic parameters were calculated.							
Steinberg [29]	1998	Both	973-1173 K 2837-5674 kPa	none	1	5.4×10^{3}	131
• 2.54 cm ID Inconel 617 tube. Total heated tube length is 2.44 m, with 0.91 m cooling zone. Heated by clamshell electric heaters. • Isothermal temperature assumed. • PMR assumed.							
Dahl et al. [39]	2002	Model	1533-2144 K 101 kPa	carbon	4.4	6×10^{11}	208
• Reactor based off of 7.6 mm ID porous graphite tube fluid wall reactor designed by [40]. • Gas and carbon temperatures assumed to vary axially. Wall temperature is assumed to be isothermal. • 1D PFR model assumed. • Heterogeneous reaction mechanisms were ignored.							

Author	**Year**	**Study type**	**Operating conditions**	**Catalyst**	λ	k_0 **(1/s)**	E_a **(kJ/mol)**
Hirsch and Steinfeld [33]	2004	Exp	900-1550 K 101 kPa	carbon	-	-	-

- Vertically orientated 10 cm ID steel-alloy vortex flow reactor. Heated by direct concentrated solar energy.
- Difficulties in keeping the quartz window clean were noted due to buoyancy effects.

Trommer et al. [34]	2004	Both	900-1060 K 101 kPa	carbon	1	1.07×10^6 PFR 7.54×10^6 PMR	147 PFR 162 PMR

- Vertically orientated vortex flow reactor. Heated by direct concentrated solar energy.
- Kinetics found assuming a single isothermal temperature
- 1D PFR and dimensionless PMR models assumed.
- Volume expansion factor used in analysis.

Abanades and Flamant [35]	2006	Both	1563-1813 K 101 kPa	none	1	2×10^8	147

- Vertically orientated 17 mm OD by 61 mm long graphite tube. Heated with a beam-down solar furnace, thus higher temperatures are at the top portion of the tube.
- E_a set to 147 kJ/mol as per Trommer et al. [34] findings.
- Kinetics assumed from Trommer et al. [34].
- 1D PFR model of reaction gas-filled reactor was created. Temperature and CH_4 conversion equations were included. Heterogeneous reactions ignored, but kinetics assumed were for particle seeded reactor. A mean wall temperature was assumed using experimental pyrometry measurements.
- 2D model of an inert gas-filled reactor was created assuming laminar parabolic velocity profile with conduction and radiation. A mean wall temperature was assumed using experimental pyrometry measurements.
- 3D model including CFD, mass and energy transport, and chemical reactions was created. A constant solar heat flux was assumed, allowing varying wall temperatures. Governing equations were not defined.

Author	**Year**	**Study type**	**Operating conditions**	**Catalyst**	λ	k_0 **(1/s)**	E_a **(kJ/mol)**
Abanades and Flamant [36]	2007	Both	1500-2000	none	1	$2.5 - 4.5 \times 10^7$ $5 - 8 \times 10^{10}$ $4.5 - 5.5 \times 10^{13}$	147 250 350

- Reactor same as Abanades and Flamant [35].
- 2D cylindrical model created using Fluent 6.2 for fluid flow, heat transfer, mass transfer and chemical reaction. Ideal incompressible gas assumed.
- Governing equations are not presented, therefore it is unclear if buoyancy was included. A constant solar flux was assumed.
- Gas flow was predicted to be laminar.
- Model showed that significant radial and axial temperature variations exist in reactor.
- Kinetic parameters were determined by setting E_a to low, med and high values found in literature.

Rodat et al. [1]	2009	Both	1500-2300 K 25-40 kPa	none	1	6.60×10^{13}	370

- Reactor is composed of two concentric graphite tubes: 4 mm ID inner tube and 18 mm ID outer tube.
- Reactor is heated by solar energy, and is vertically orientated.
- Dsmoke software used to model non-catalytic reaction mechanism with multiple species.
- Overall kinetics determined by coupling 1D isothermal PFR model with data from Dsmoke software.
- 1D PFR model with Dsmoke software compared to data from experimental reactor.
- Temperature assumed to linearly increase from 300 K to operating temperature in heating zone, maintain an isothermal reaction zone, and then cool linearly to 373 K in cooling zone. Each zone was modeled with separate 1D PFR.

Author	Year	Study type	Operating conditions	Catalyst	λ	k_0 (1/s)	E_a (kJ/mol)
Rodat et al. [37]	2009	Both	1670-1740	none	1	1.47×10^8	205
• Reactor is composed of two concentric graphite tubes: 4 mm ID inner tube and 18 mm ID outer tube. • 1D plug flow model assumed. • Expansion factor included. • 3D thermal simulation was performed using Fluent 6.2. Equations are not presented, but no mention is made of coupling the thermal equations with CFD analysis (and hence no inclusion of buoyancy effects). • The inlet gas and the portion of tubes that are cooled with water are assumed to be at 300 K. A constant solar heat flux is assumed. • The reactor zone inside the cavity was found to be isothermal, with effective cooling in the cooling zones.							
Wyss et al. [15]	2007	Both	1700 - 2135 unknown P	none	7.2 ± 6.9	$5.8 \times 10^8 \pm$ 1.7×10^9	$155.6 \pm$ 123.8
• Vertically orientated 12 mm ID tubular graphite fluid wall reactor. Heated by solar furnace. • PFR model assumed for reactions and energy transfer. • 2D heat transfer and CFD model was solved by Dahl et al. [41] in a previous study. The results were used to estimate the reactor wall temperatures for the PFR model by Wyss et al. [15]. The temperatures ranged from 300 K at the inlet, increased to operating temperature and then cooled to 300 K at the outlet of the tube. • The model by Dahl et al. [41] was coupled with thermal, Navier-Stokes and mass conservation equations. The buoyancy term with gravity g was not included in the Navier-Stokes equation. • The inlet gas and the water-cooled portion of tubes were assumed to be at 300 K. A constant solar heat flux was assumed. The inlet velocity profile was assumed to be plug flow.							

Author	Year	Study type	Operating conditions	Catalyst	λ	k_0 (1/s)	E_a (kJ/mol)
Maag et al. [38]	2010	Both	1670 - 2075 24-77 kPa	carbon	n/a	-	-
• Tubular reactor with inner inlet tube with gas exiting annulus between inner and outer tubes. Reactor is indirectly heated using solar energy concentrated in a graphite cavity. • 1D PFR model assumed for reactions, energy transfer and mass flow. Buoyancy effects are not accounted for. Constant heat flux is assumed in the graphite cavity. Reactor inlet temperature is assumed to be ambient. • 4 reaction mechanism for carbon seeded tubular reactor.							
Homayonifar et al. [42]	2008	Model	880-1644 101 kPa	none	1	6×10^{11}	250
• Simulated 120 mm ID by 2 m long tubular reactor • 2D model including Navier-Stokes, mass conservation, energy conservation and reaction equations using Fluent software. The buoyancy term is included in the Navier-Stokes equation. Gas flow was directed upwards in the tube. • Wall temperature were assumed to be constant, or to increase from mid-level to the end giving a higher temperature at the top of the reactor tube. Thus buoyancy effects would be negligible. • The inlet gas was assumed to be at 880 K. Laminar flow was assumed and verified.							

Author	Year	Study type	Operating conditions	Catalyst	λ	k_0 (1/s)	E_a (kJ/mol)
Patrianakos et al. [19]	2011	Model	1670-1740	carbon	1	1.00×10^{14}	400
• Simulated reactor is composed of two concentric graphite tubes: 4 mm ID inner tube and 18 mm ID outer tube, given by Rodat et al. [1]. • Two-phase 1D PFR model assumed. • The inlet wall temperature was assumed to be at 300 K, ramp linearly up to operating temperature, remain at an isothermal operating temperature, and then ramp linearly down to 373 K over the length of the reactor tube. • k_0 was extracted from literature by setting $E_a = 400$ kJ/mol.							
Ozalp et al. [11]	2013	Both	1500-1823 K 101 kPa	Fluka 05105 (carbon)	n/a	-	-
• 1D Plug flow reactor found in [43] assumed for non-catalytic cracking. • 37 reaction mechanism for non-catalytic cracking was used. • 8 reaction mechanism for catalytic cracking was used. • 3D heat transfer and fluid flow simulated using CFD for catalytic cracking for vortex flow [44] and tornado flow [45] reactors. • Buoyancy effects were included in the study by Ozalp and Jayakrishna [44] using turbulent Navier-Stokes equations, coupled with mass and energy transport. The impact of buoyancy on the mixing of the reactor is not investigated, however. • Buoyancy effects were not mentioned in the study by Ozalp and Kanjirakat [45], though the model assumed the turbulent flow.							

In the above review, reactor materials vary between 304 SS, Inconel 617, graphite, quartz, alumina and heat resistant steel alloy. The majority of the studies use tubular reactors [1, 11, 15, 18–20, 22, 29, 35–38, 42]. Hirsch and Steinfeld [33] and Trommer et al. [34] study a vortex flow reactor, which is vertically orientated and allows the carbon seeded gas to flow from the top of the reactor cavity along a helical path until it exits at the bottom. Krishna and Ozalp [46] analyzed particle deposition inside of an aero-shield cyclone reactor. In the cyclone reactor a tornado flow is used to improve gas residence time and thus CH_4 conversion in the directly irradiated reactor. The cyclone flow also creates a pressure gradient that prevents the carbon particles from depositing on the quartz window.

The above studies were performed in either non-catalytic or catalytic gas flow reactors. Carbon seeding has been used to both catalyze the reaction as well as provide better heat transfer to the gas [33, 34, 38]. Marshall et al. [47] in 2000 investigated the concept of using molten metals to improve direct heat transfer to CH_4 gas. The author showed that flowing CH_4 over a $Pb - Bi$ eutectic molten metal produced 2% conversion to H_2 at 773 K, and 65% at 1173 K. However, the study does not include an analysis of CH_4 cracking of the same reactor void of any molten metal. This experiment would have determined if the conversion amount was due to the molten metal or due to a long residence time.

In 2001, the same research group studied bubbling through Pb between 873-1173 K [48]. The effect of bath height, flow rate and temperature were studied. The author found that bath height did not impact conversion, though the flow rate did. Temperature had a significant impact on conversion. Carbon was found to be segregated in the top of the metal. Thus it was verified that carbon would rise to the surface due to density differences. The authors found that the activation energy was 213 kJ/mol using the partial pressure of H_2 in the product gas stream [48].

In 2003, Serban et al. [2] continued the group's work and created a new experimental apparatus. The reactor vessel was a 1 inch by 14 inch 304 SS vertical tube with one end closed. A 0.5 inch cup which contained the molten metal was inserted in the reactor vessel. The molten media was varied between a 4 inch and 8 inch height. The reactor was heated by a four-zone Thermcraft furnace. The flow rate varied from 2 to 15 ccm, and the temperature from 873 to 1173 K. Four different gas injectors were studied. These were 1/16 inch and 1/4 inch open bore tubes, and 0.5 μm and 2 μm Mott spargers. It was hoped that the spargers would produce smaller bubbles

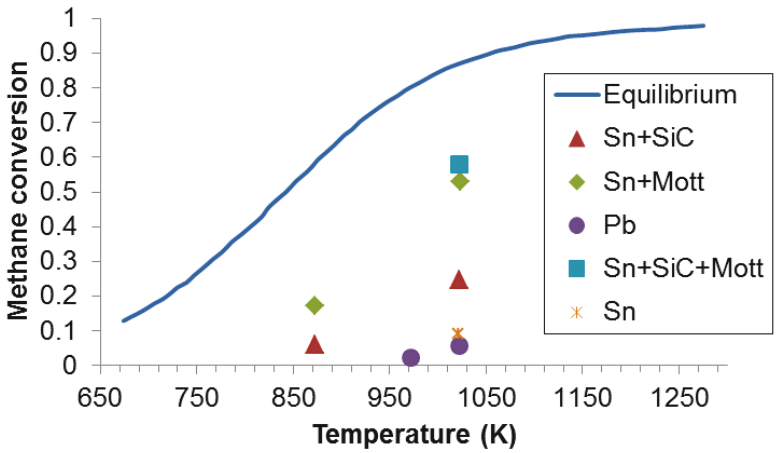

Figure 1.2 – Methane conversion results from Serban et al. [2]'s experimental study.

and hence improve conversion. Both Pb, Sn and Sn-SiC mixture bath materials were studied. The product gases were analyzed using a mass spectrometer and gas chromatograph. A summary of some of the results of work done by Serban et al. [2] is shown in Figure 1.2. The authors found that the Mott spargers had a significant impact on CH_4 conversion. There was no difference in conversion noticed between the use of Pb or Sn as the molten media. The mechanical mixture of Sn-SiC increased the residence time of the gas in the bath and hence conversion. X-ray diffraction (XRD) analysis of carbon formation suggested that the 304 SS reactor wall reacted with the CH_4, C and H_2 environment and formed FeC, thus showing that the reactor material impacted conversion.

In 2012, the Karlsruhe Institute of Technology began studying molten metal CH_4 cracking in conjunction with the Institute for Advanced Sustainability Studies in Potsdam, Germany [49]. The investigations are to be performed at temperatures as high as 1273 K in a quartz tubular reactor.

1.2.2.2 Modeling work

Based on the literature review provided in Section 1.2.1, several multi-step reaction mechanisms have been produced to simulate CH_4 cracking [11, 18, 20–22, 38]. However, the results given in Table 1.1 show that many researchers assume the overall reaction mechanism for CH_4 cracking given in Equation (1.1) [1, 15, 19, 29, 33–37, 42]. Further, implementing these reaction mechanisms is computationally expensive and complicated. In this thesis, the overall reaction was chosen to simplify the problem, and because the primary products of the cracking mechanism are H_2 and C. There-

fore, the studies assuming overall kinetics are reviewed in this section.

Steinberg [29] used an Inconel 617 tubular reactor to study CH_4 conversion. The experiments were performed at high pressures of 2837-5674 kPa, or between 28 to 54 atm, and at temperatures of 973-1173 K. The author found $k_0 = 5.4 \times 10^3$ 1/s, $E_a = 131$ kJ/mol, which is much lower than what is found in literature. Thus it was found that the higher pressures increased the reaction rate. The author suggested that the carbon formed catalyzed the reaction and lowered the activation energy, and that the reactor material increased the rate of methane decomposition. Iron oxide, alumina, graphite, and quartz are materials that increase the rate of reaction, listed in decreasing order of impact.

Dahl et al. [39] studied a carbon seeded tubular aerosol flow reactor. The reactor consisted of a porous graphite wall through which an inert gas diffuses to prevent carbon deposition on the walls of the reactor. The author developed a one dimensional PFR model to determine the kinetic parameters and order of reaction. An energy balance equation that included both solid and gas phase was derived for the model. Heat absorption by radiation to carbon particles was also included. Experimental data for the reactor between 1533-1977 K and at a single flow rate was obtained by the author. The data was used to fit the model and found that $k_0 = 6 \times 10^{11} \pm 8 \times 10^{11}$ 1/s, $E_a = 208 \pm 65$ kJ/mol, and $\lambda = 4.4 \pm 0.52$. The author suggested that the large range of confidence interval in k_0 is due to the random error in the data and recommended more experiment replications. E_a was lower than what was found in literature because of the heterogeneous reactions that occur on the carbon particle surfaces, agreeing with Steinberg [29]

Trommer et al. [34] studied the carbon seeded, vertically orientated and directly heated vortex flow reactor. The reactor was modeled as both a 1D plug flow reactor and a perfectly mixed reactor, stating that these two models would be the limiting cases. The author assumed a two step reaction. The first being adsorption of CH_4 onto the surface of the carbon particles, and the second being decomposition of adsorbed CH_4 into H_2 and C[34]. The author found that, for temperatures greater than 1050 K, CH_4 conversion is higher using the PFR than the PMR. The kinetics for the PFR were reported to be $k_0 = 1.07 \times 10^6$ 1/s, $E_a = 147$ kJ/mol, and for the PMR $k_0 = 7.54 \times 10^6$ 1/s, $E_a = 162$ kJ/mol.

In 2006, Abanades and Flamant [35] developed a vertically orientated, indirectly

heated tubular reactor to study methane cracking at high temperatures. A 1D model was created, based off the Dahl et al. [39] PFR model, and an energy balance including radiative heat transfer to the carbon particles and convective gas transport. $k_0 = 2 \times 10^8$ 1/s was found by setting E_a to 147 kJ/mol, which was reported by Dahl et al. [39], and fitting the experimental results to the PFR model. The study found that the majority of the reactions occurred near the walls where the temperatures are highest.

Abanades and Flamant [36] presented further work on the reactor in Abanades and Flamant [35]. A 2D model was created using Fluent 6.2 software. Fluid flow, heat transfer and chemical reactions were included in the model. Laminar flow was assumed. This assumption was made by calculating the Re number given the average inlet flow velocity based on flow rate. Buoyancy effects were not considered, though very significant temperature profiles existed in the reactor. E_a was set to 147 kJ/mol, 250 kJ/mol and 350 kJ/mol, and the corresponding k_0 were iteratively found to be 2.5-4.5$\times 10^7$ 1/s, 4-8$\times 10^{10}$ 1/s and 4.5-5.5$\times 10^{13}$ 1/s, respectively. The study found again that the reaction occurred mainly on the reactor walls where the temperature was highest, showing that the reaction is heterogeneous.

Rodat et al. [1] analyzed an indirectly heated tubular reactor composed of four sets of two concentric tubes. The gas was injected through the inner tube, and exited the system through the annulus between the two tubes. The author used the Dsmoke software which includes a chemical reaction scheme containing over 240 species and 14000 reactions to predict alkane transformation, and polycyclic aromatic hydrocarbon and soot particle formation. A PFR was fitted to the results from the Dsmoke software to find the overall kinetics, giving $k_0 = 6.6 \times 10^{13}$ 1/s and $E_a = 370$ kJ/mol. Finally, a series of three PFR combined with the Dsmoke software were used to model the experimental reactor and compare it against results. It was found that the model was within 12% mean discrepancy with experimental CH_4 conversion, though usually the model under predicted CH_4 conversion. The authors suggested that it is because Dsmoke software is for homogeneous reactions, and so does not not include the heterogeneous reactions that would occur at the particle or reactor wall surfaces.

Rodat et al. [37] then studied different inner tube configurations to determine which would provide better residence time and reduce carbon deposition. The author assumed a PFR as in [1], and found the kinetic parameters to be $k_0 = 1.47 \times 10^8$ 1/s and $E_a = 205$ kJ/mol. These values are substantially different from their previous

study [1]. It is likely because they are based off of the current experimental data, and not off of the homogeneous reaction Dsmoke software. A 3D analysis was done on the temperature profile inside the reactor using Fluent 6.2 software. It was found that the gas temperature inside the tubes in the heated zone were homogeneous and at the same temperature as the tube walls. This may explain how the PFR model coupled with the Dsmoke homogeneous software was able to predict within 12% of experimental CH_4 conversion results in the previous study [1]. The homogeneous reactions may have been more significant than the heterogeneous reactions because the gas temperatures were the same as the wall. Rodat et al. also found that the gas temperature in the insulated zones after the gas outlet were at higher temperatures than the walls, which led to thermophoretic deposition of carbon on the tubes. Furthermore, the analysis showed that 60% of energy is re-radiated out of the quartz window.

Wyss et al. [15] created a 2D temperature and fluid flow model of a vertically orientated fluid wall reactor using COMSOL. The simulation was performed with inert gases only. The reactor wall temperatures in these simulations were used as inputs into a 1D PFR model. The PFR model incorporated kinetics, radiation absorption of the carbon particles, and convective heat transfers. The model was best fit to the experimental data using the Gauss-Newton method, where the sum of squares of the differences between the experimental and predicted data is minimized. The kinetic parameters were found to be $k_0 = 5.8 \times 10^8 \pm 1.7 \times 10^9$ 1/s, $E_a = 155.6 \pm 125.8$ kJ/mol, and $\lambda = 7.2 \pm 6.9$. The reaction order is much higher than any found in literature. The next highest was calculated by Dahl et al. [39] to be 4.4. Most other literature assume the overall reaction is first order.

Homayonifar et al. [42] studied a tubular reactor to identify operating conditions and methods to reduce carbon deposition inside the reactor. The 2D model included Navier-Stokes, mass conservation, energy conservation and reaction rates. Carbon particle formation and growth is included in the model. The author assumed kinetic parameters within the ranges given in the literature. The values of $k_0 = 6 \times 10^{11}$ 1/s, $E_a = 250$ kJ/mol were used. These values were not previously determined by any other researcher, and as such they may not be a good match for the reaction rate. Homayonifar et al.'s k_0 is one order of magnitude less than what was reported by Abanades and Flamant [36] for $E_a = 250$. In either case, these values would still allow for an analysis on the trends occurring in the reactor. In this study, it was found that thermophoretic and drag forces cause the carbon particles to distance themselves from the wall of the reactor. The thermophoretic forces disappear when

the gas temperature equals the wall temperature. However, the van der Waals and Brownian forces pull the carbon particles to the wall in the slower flowing regions near the wall. The study found that more carbon deposition on the walls occurs when the reactor walls are at a higher temperature than the gas. The study suggests that having a sweeping gas to prevent the reaction gas from touching the reactor wall would decrease deposition.

Patrianakos et al. [19] studied carbon particle formation and growth in the concentric tubular reactor presented by Rodat et al. [1]. The intent of the study was to predict size distribution of carbon formation for the optimization of carbon seeding. The reactor was simplified to a 1D PFR model. Heterogeneous and homogeneous kinetics were included, as well as radiative and convective heat transfer. The author used experimental data from literature to extract the pre-exponential factors for the homogenous and heterogeneous reactions. E_a was assumed to be 400 kJ/mol and 150 kJ/mol for the homogeneous and heterogeneous paths, respectively. The reactions were assumed to be first order. k_0 was then best-fit using the PFR model to the experimental data. The homogeneous and heterogeneous values for k_0 were found to be 1×10^{14} 1/s and 2500 m/s respectively.

To this date, no models for molten metal CH_4 cracking have been published. As such, this thesis will seek to develop a model that furthers the understanding of the physical phenomena that occurs in the reactor.

1.2.3 Thermal buoyancy effects

Many of the researchers in Section 1.2.2.2 assumed a PFR model to characterize the reactor and determine the kinetic parameters. In the PFR models, authors have assumed an effective isothermal temperature [18], isothermal wall temperature [11, 34, 35, 42], variable wall temperatures such as a lower inlet temperature (eg. ambient), ramping up to an isothermal operating temperature, and then ramping down to a cooled outlet temperature [1, 19, 42], or a constant heat flux into the reactor cavity [38]. In the PMR models, authors have assumed an effective isothermal temperature [22] or an isothermal wall temperature [20, 29, 34]. In the 2D models, authors have assumed isothermal wall temperature [35] or a constant solar flux [36]. And finally, for 3D models, authors have assumed a constant solar flux [35, 37, 44, 45, 50]. Those studies that did not include heat transfer equations assumed that the reaction gas was at the same temperature as the wall. In reality, large gas temperature differ-

ences have been found to exist in many of the studies in the above literature review in Section 1.2.2.2. In this thesis it is shown that buoyancy effects can be significant in reactors with large temperature differentials. However, the majority of the studies do not include buoyancy.

Costandy et al. [51] did include buoyancy in a 3D model that studied the effect of reactor geometry on the temperature profile inside the reactor. Turbulent CFD analysis was performed using FLUENT 12.1. Both cylindrical and spherical reactor were studied. It was shown that large temperature differences existed in both reactors.

In 2004, Hirsch and Steinfeld [50] studied the tornado flow reactor using a 3D radiative model that included heat transfer and kinetics. The model did not include CFD, however. In the same year, the authors in Hirsch and Steinfeld [33] report the experimental results of the reactor, and suggested that carbon deposition became a problem during runs where the reactor was mounted vertically due to buoyancy effects. Later in 2013, Ozalp et al. [11] created a 3D heat transfer and turbulent fluid flow simulations of both vortex [44] and tornado flow [45] reactors using computational fluid dynamics (CFD) software. Buoyancy effects were included in the vortex flow reactor, however it is unclear whether buoyancy effects were included in the cyclone reactor. No mention was made of the impact that the buoyancy effects had upon fluid mixing or kinetics in the vortex reactor. The analysis showed temperature differences as large as approximately 800 K in the non-seeded tornado reactor, and approximately 700 K in the vortex flow reactor with 0.2 g/min carbon seeding [45].

Buoyancy effects have been heavily studied in the subject of natural ventilation. Linden [52] gave a comprehensive summary in the study of fluid flow in natural ventilation. Stack driven ventilation is where the temperature differences induce fluid flow inside a building by density differences. Laboratory simulations of this phenomena have been performed at smaller scales using salinity differences in water. Linden suggested that buoyancy forces may be described in terms of reduced gravity, and gave the following definition of reduced gravity

$$g' = g\frac{\Delta\rho}{\rho} = g\frac{\Delta T}{T} \tag{1.5}$$

where $\frac{\Delta T}{T}$ is the fractional change in the fluid where T is in units of K, and g is the acceleration of gravity. The author then gave the equation for the scaling of velocity due to buoyancy effects as

$$U = \sqrt{g'L} \tag{1.6}$$

where L is the vertical length scale overwhich the temperature difference is experienced. The typical experiments using this scaling correspond to a difference of 5 K [52]. However, the method still applies to higher temperature differences such as those caused by building fires. The author discussed ventilation of fires in buildings, and reports that a relatively small fire can reach as high as 1273 K. The density of hot gas at 1273 K is approximately 25% of the density of air at room temperature, yielding non-Boussinesq flows. These buoyant flows are sufficiently large to carry smoke particles, though the process is poorly understood [52]. The methane cracking reactors discussed in the above literature review experience very large temperature differences as well. As an example, a 0.5 m tubular reactor operating at 1500 K with a temperature difference of 500 K would have a scaled velocity of 1.57 m/s. For a temperature difference of 1000 K, the scaled velocity is 3.13 m/s.

Drazin and Reid presented a chapter on thermal instability in fluid flow caused by heating a fluid from a bottom plate [53]. The authors summarized the derivation of Rayleigh's theory. Rayleigh's theory shows that instabilities occur in the Bénard cell when a critical value of what became the Rayleigh number (Ra) is exceeded. Ra for an ideal gas is defined as

$$Ra = \frac{g c_p \rho^2 L^3}{\gamma_g \mu} \frac{\Delta T}{T} \tag{1.7}$$

where $g = 9.81$ m/s is the acceleration of gravity, c_p is the specific heat capacity of the gas, ρ is gas density, γ_g is gas thermal conductivity, μ is dynamic viscosity of the gas, L is the length dimension, and T is temperature. This finding was based on the Boussinesq approximation, which works well for temperatures with a few degrees difference [53]. This essentially means that all other fluid thermodynamic properties such as heat capacity or viscosity can be assumed constant, and density terms in the fluid equations can be ignored except when it is multiplied by g [53]. Thus, for the Boussinesq approximation, the following condition must be met

$$(\rho - \rho_0)/\rho_0 = \omega(T_0 - T) \ll 1 \tag{1.8}$$

where ω is the thermal expansion coefficient, which reduces to $1/T$ for an ideal gas [54]. Drazin and Reid report that $Ra_{critical} = 1708$ for a fluid that is heated from the bottom, with rigid (or no-slip) boundary conditions at the top and bottom surfaces. For free - rigid boundary conditions at the top and bottom surfaces, $Ra_{critical} = 1101$. Instabilities begin to occur above these numbers in the first mode at least [53], and

natural convection currents begin to flow [55]. The convective Bénard cells become turbulent when the Rayleigh number exceeds 3×10^5 [55].

The reactor studied in this thesis exhibited large temperature gradients ranging from $650 \leq \Delta T \leq 1000$ K. A study is performed in 3.1.2 in this thesis that shows that the Ra number calculated for the experimental reactor is above the critical value of $Ra_c = 3 \times 10^5$. Recognizing this, as well as the high scaled velocities of 1.7 m/s to 1.8 m/s in the 0.508 m long reactor, it was assumed that the reactor in this thesis was perfectly mixed.

1.3 Contributions

The novel aspects of this thesis are:

- the development of a method to mathematically model a tubular reactor with a large temperature gradient, recognizing that buoyancy effects due to the high temperature gradient cause enhanced mixing in the reactor
- identification of overall CH_4 cracking reaction kinetics using the above said model coupled with experimental testing of a tubular reactor
- development of the understanding of the physical phenomena of methane cracking in a molten metal reactor and determination of the feasibility of the technology.

1.4 Thesis Outline

The work of this thesis describes the experimental and modeling work done to determine the kinetics of CH_4 cracking, as well as experimental and numerical modeling work of a molten metal reactor. An introduction to CH_4 cracking is given in Chapter 1, highlighting the chemistry of CH_4 cracking, reaction mechanisms, catalytic cracking, experimental and modeling work. Chapter 2 contains the experimental setup, procedure, and discussion of results. Three mathematical reactor models used to determine the kinetics based on the experimental results are given in Chapter 3 for the blank reactor. The following models are derived: a PFR, a PMR, and a combined PMR with a bypass (CPMR). The kinetics from the PMR with a bypass are then used in Chapter 4 where a molten metal reactor is derived and discussed. Chapter 5 contains the conclusions of this work and outlines recommended future work.

Chapter 2

Experimental work

In this chapter the experimental setup, data recording and procedure are described and discussed in Sections 2.1 and 2.2. The reactor temperature profile is characterized in Section 2.3. The experimental design, procedure and post-data processing is presented in Section 2.4. The results are given and discussed in Section 2.6.

2.1 Apparatus description

The experimental apparatus was created to test CH_4 conversion at various temperatures. The reaction gas was composed of N_2 and CH_4. The reaction gas was injected into either a blank reactor to determine the kinetic parameters, or into a molten metal bath to test for the effects of molten metal on the reaction. The product gas composition was read using a micro Gas Chromatograph (GC). Figure 2.1 contains the piping and instrumentation diagram and an overall picture of the apparatus is shown in Figure 2.2. Figure 2.3 shows the tubular reactor installed in the furnace with the furnace door open. The reactor was heated by a three zone cylindrical furnace using a programmable controller (Lindberg/Blue M, Fisher Scientific). The furnace has a 5 inch inner diameter and has a maximum operating temperature of 1373 K.

2.1.1 Reactor assembly

The reactor is composed of (a) the reactor cap, (b) the reactor vessel and (c) an injector. Figure 2.4 shows the reactor-cap assembly. The SS cap was built in-house at AITF. The cap incorporated a centering flange to avoid problems with centering the cap on the reactor tube, and a small surface area Viton o-ring to minimize exposure to the gases in the reactor. The bottom of the cap is shown in Figure 2.5. A wing-nut and bolt assembly with the tube clamp was used to seal the cap over the tube open-

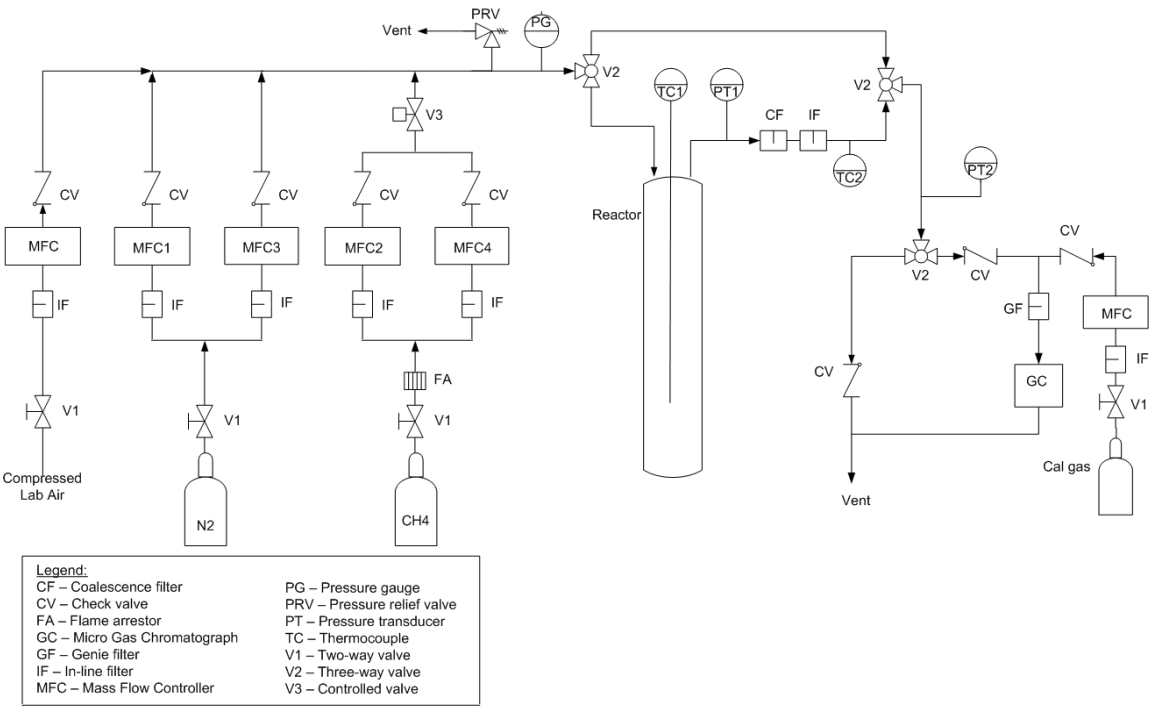

Figure 2.1 – Pressure and Instrumentation Diagram

ing. Swagelok tubing and fittings (Edmonton Valve & Fitting Inc.) were used for all the gas tubing. The 1/16 inch K-type thermocouple (OMEGA Engineering Inc.) was inserted into the reactor through a Swagelok union fitting. The fitting was was bored out by the machine shop to provide a large enough hole for the injector. The seal around the thermocouple was created using Teflon ferrals. The injector passes through a 1/2 inch T-fitting that was large enough to provide an annulus for product gases (annotated in Figure 2.5). A reducer was used at the top of the T-fitting to convert from 1/2 inch tubing to match the size of the injector tube. The reducer was bored through to allow the injector to still pass through, and a Teflon ferral and cap was used to seal the injector tube and the cap assembly from the outside air.

The injectors, used to insert the CH_4/N_2 gas mix into the reactor, are shown in Figure 2.6. The injector may be easily raised or lowered in the reactor while it is at operating temperature by unsealing and resealing the Swagelok nut on the reactor cap. The two types of injectors were a 4-10 μm fused quartz sparger (Technical Glass Products Inc.), and a 6 mm Al_2O_3 tube (McDanel Advanced Ceramic Technologies Inc.).

The reactor vessel was a 50.8 cm long by 5.08 cm OD Al_2O_3 tube with one closed

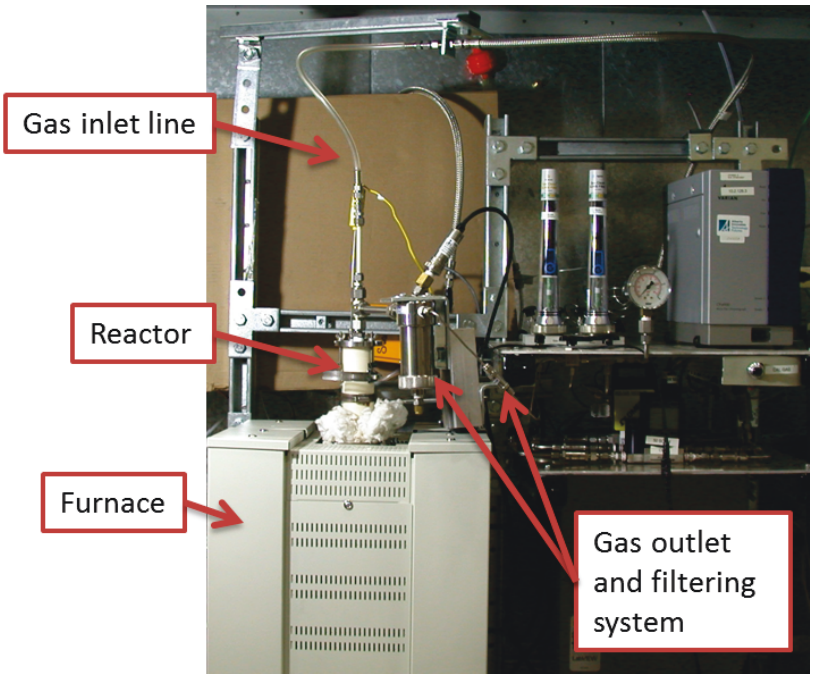

Figure 2.2 – Overall image of experimental apparatus.

end (McDanel Advanced Ceramic Technologies Inc.). The reactor was positioned higher up in the furnace than was originally intended using cinder blocks (Figure 2.3) to reduce the amount of heated gas above the molten metal bath. It was expected that minimizing the heated blank reaxctor volume would distinguish the effect of having a molten bath versus a blank reactor on CH_4 conversion. The reactor bottom was located 21.6 cm below the top insulating cap to accommodate the 20.3 cm bath height. The heating elements extend to approximately 0.6 cm below the bottom of the top insulating cap (Figure 2.7). The hole in the top insulating cap exhibited some wear due to repeated reactor vessel installation and removal. Heat loss from the gap of space between the reactor and the cap was minimized by clamping silicone insulation at the top of the reactor just above the cap. Figure 2.8 shows a side view of the reactor in the furnace. The reactor is supported by a clamp arm off to the side. A fan is set to blow over part of the reactor outside of the furnace and cool it down to protect the Viton O-ring seal in the cap. Viton has a maximum temperature rating of 300℃[56].

2.1.2 Gas supply

The types of reaction gases were 4.0 grade CH_4 (Praxair Canada Inc) and Ultra High Purity (UHP) N_2 (Air Liquide). The GC carrier gases were 4.5 grade He (Praxair

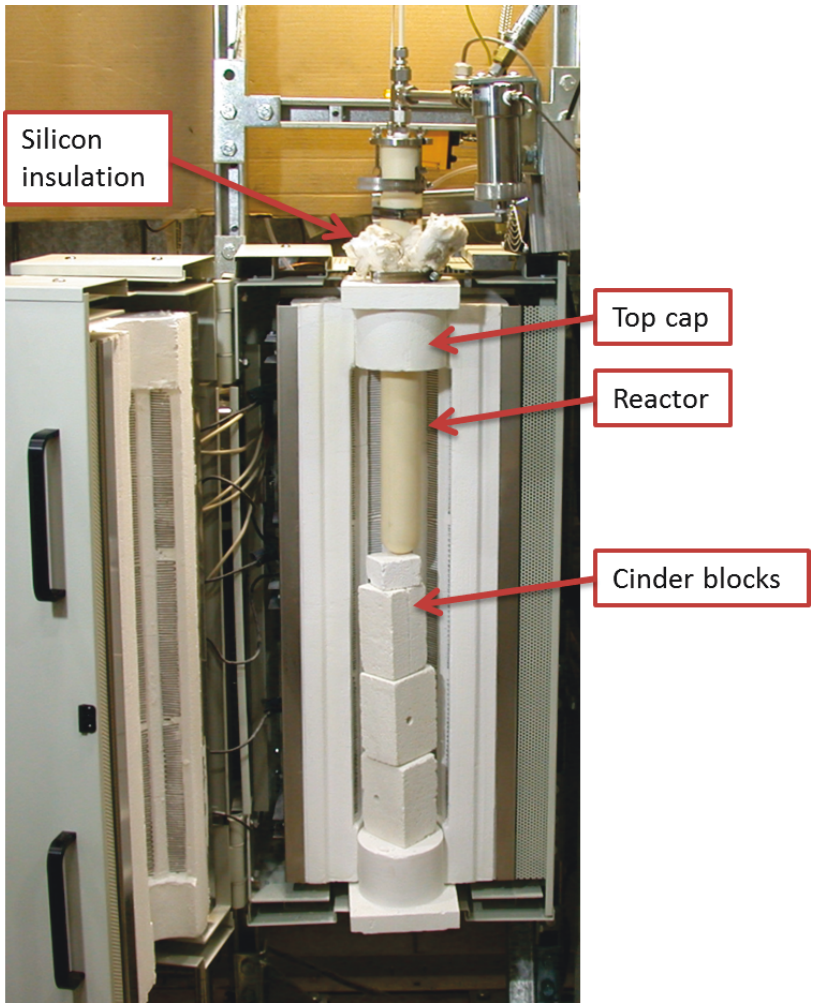

Figure 2.3 – Image showing furnace door open with reactor installed.

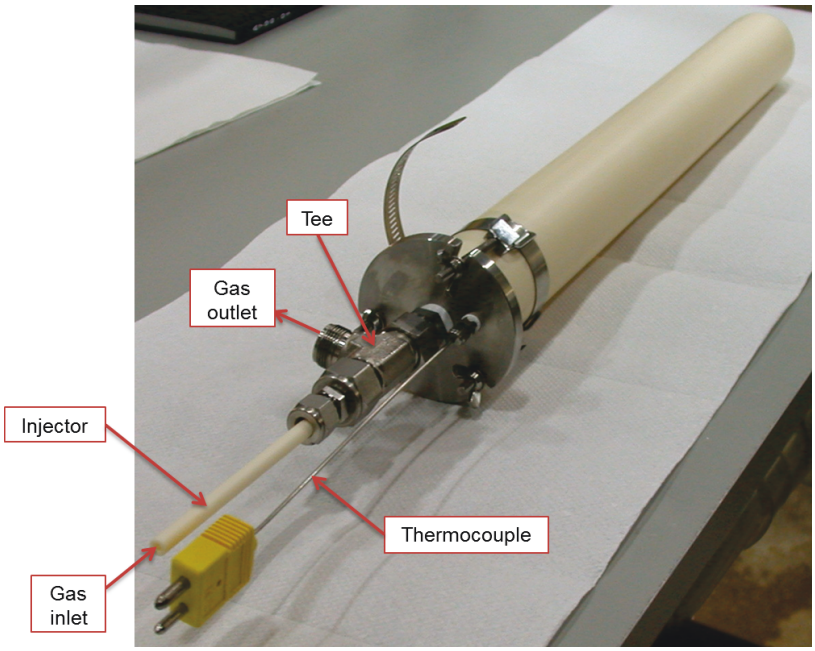

Figure 2.4 – Top view of the sealed reactor vessel tube with alumina injector and thermocouple.

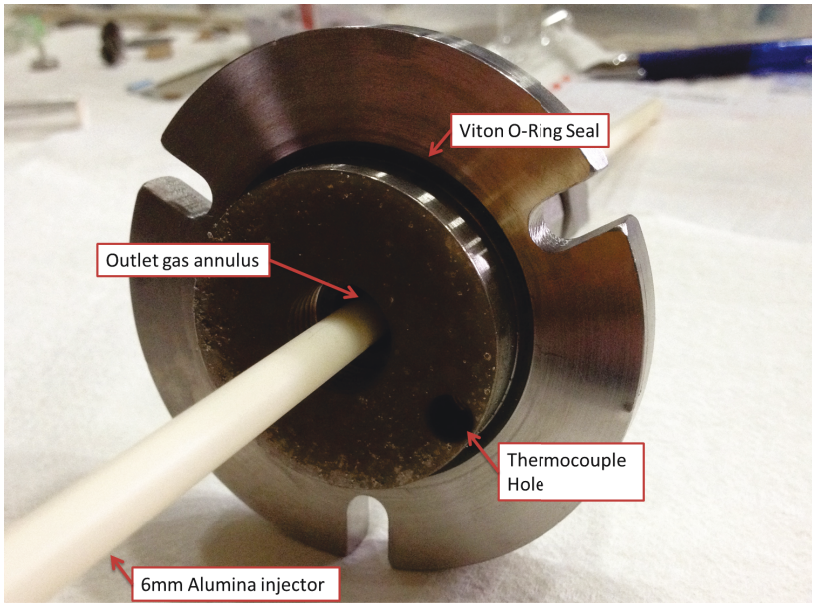

Figure 2.5 – Injector extending from bottom side of cap. O-ring seal is visible around the flange.

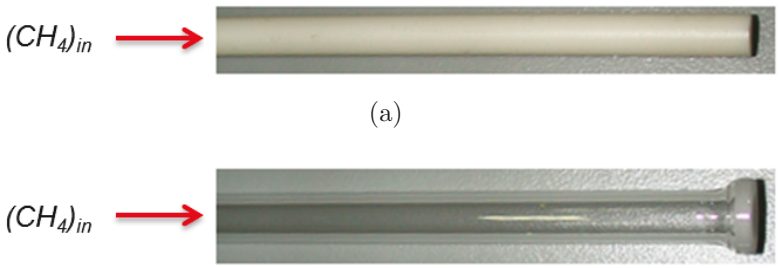

Figure 2.6 – Injectors used during the experiments, (a) 6 mm OD Al_2O_3 tube and (b) 4-10 μm porous quartz sparger.

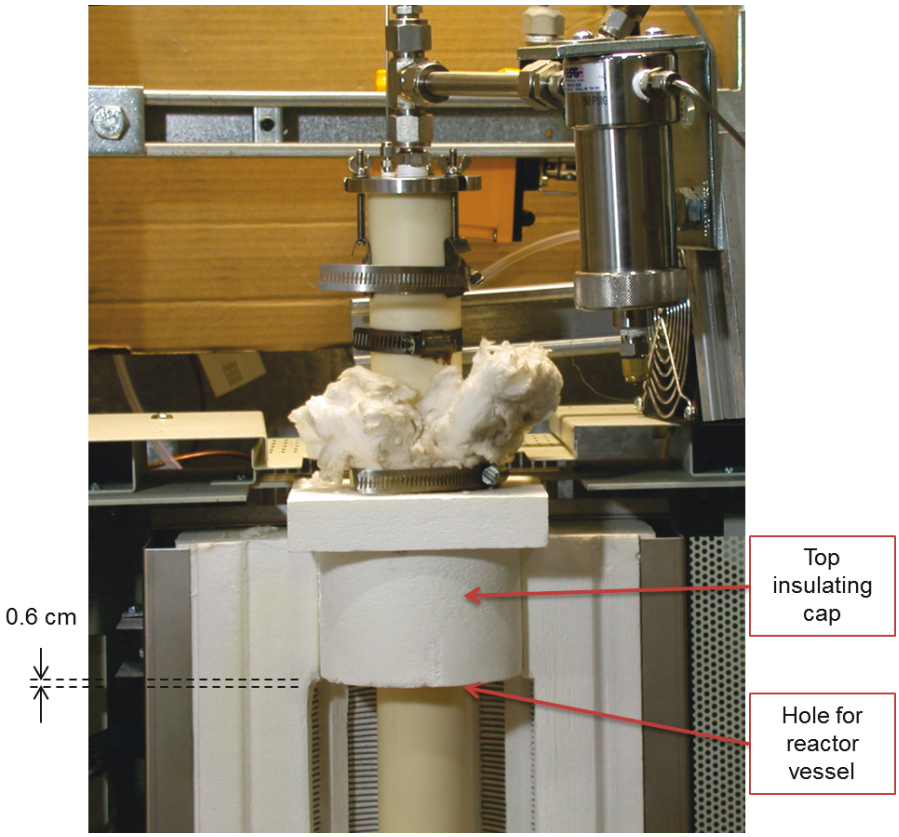

Figure 2.7 – Upper section of the sealed reactor vessel with the furnace door open.

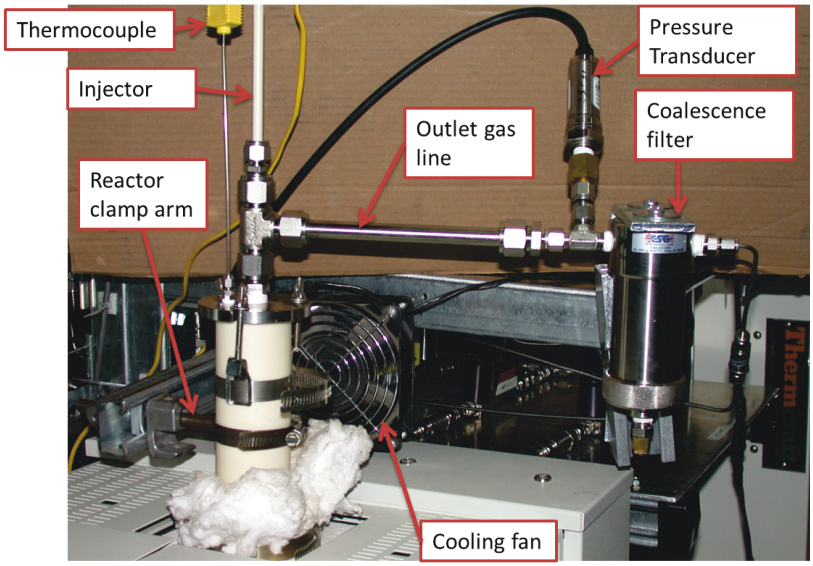

Figure 2.8 – Product and inlet gas tubing and filtration system above the closed furnace.

Canada Inc.) and UHP Ar (Air Liquide). All CH_4 cracking experiments were performed flowing equal flow set points for CH_4 and N_2. Total flow rates ranged between 15.3 sccm to 200 sccm. A flashback arrestor (Air Liquide Canada Inc.) was installed downstream of the cylinder outlet but upstream of the MFCs on the CH_4 line. The pressure regulators (Air Liquide Canada Inc.) were sized according to required pressures. The gases were controlled using mass flow controllers (MFC) (Alicat Scientific Inc). Four different MFCs were installed to allow for high and low flow rate set points for the reactant gas mixture, as shown in the piping and instrumentation diagram in Figure 2.1. The N_2 MFCs had 10 sccm and 200 sccm ranges and the CH_4 MFCs had 50 sccm and 1000 sccm ranges. The MFC with the smallest range possible was selected for each experiment. A fifth MFC with a 1000 sccm range was installed to run compressed building air for pressure testing. The MFCs were controlled using Labview 2012 (National Instruments).

2.1.3 Gas outlet

The product gases exited the reactor through an annulus (see Figure 2.5) and followed the outlet pathway through the stem of the 1/2 inch T-fitting, as shown in Figure 2.9. The product line was reduced to 1/4 inch tubing just prior to entering the first of the three stage filtering system shown in the piping and instrumentation diagram in Figure 2.1. The first stage was a coalescing filter (Model 137, Headline filters supplied

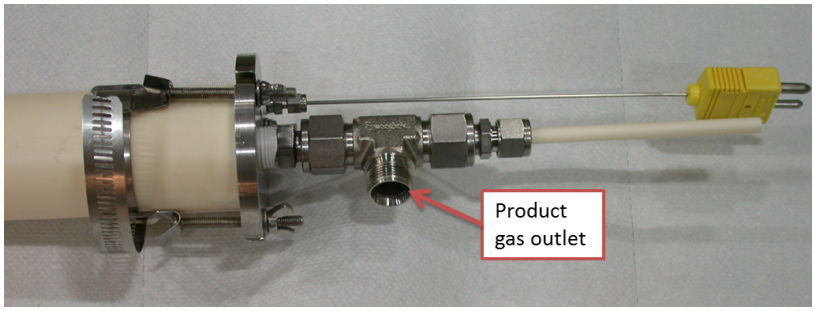

Figure 2.9 – Product gas outlet from T-fitting.

by ESG Filtration Ltd) rated for 95% 10μm particulate removal from the gas stream, located approximately 25 cm downstream from the reactor (shown in Figure 2.8). The gas line was reduced to 1/8 inch OD for the second stage filter, which was a 0.5 μm in-line filter (Swagelok). The final stage was a Genie filter (Model 101, Westech Industrial LTD) which removed the remainder of the particulates and provided clean gas to the GC. The filtered portion of the gas exited the Genie through 1/16 inch tubing, while the rest was vented to the fumehood. The product gas was analyzed in a Varian CP-4900 micro Gas Chromatograph with 10 m 55A and PPU columns.

2.2 Data acquisition and recording

2.2.1 Thermocouples and pressure transducers

The first pressure transducer (OMEGA Engineering Inc.), PT1, in the apparatus has a range of ± 5 psi and is shown in Figure 2.8. This pressure transducer measured the operating pressure in the reactor. PT1 was vertically mounted to help prevent damage due to particulates in the gas flow. The second pressure transducer (OMEGA Engineering Inc.), PT2, was rated for ±2.5 psi. PT2 was located after the first two stages of the filtering system and was used to detect plugging in the filters by watching the pressure differential between PT1 and PT2.

Two Type K thermocouples (OMEGA Engineering Inc.) were incorporated into the data collection system. The first, TC1, was 27 inches long and extended through the cap into the reactor itself (see Figure 2.8). The second thermocouple was located farther downstream and verified that the downstream product gas was at room temperature. A 15 psig analog pressure gauge (Wika Instruments Ltd.) was installed at the inlet of the reactor to warn of injector plugging.

2.2.2 Mass flow controllers and Labview

LabView 2012 (v12.0f3, National Instruments) was used for data acquisition and recording. The LabView program was developed by AITF technician Juan Segura, and communicated to the MFCs using a CDAQ-9174 card (National Instruments). The following data was recorded into Excel 2003 .csv files: MFC outlet gas pressure, temperature, volumetric flow rate at standard temperature and pressure (STP), actual volumetric flow rate at 298 K and local atmospheric pressure, and the set point volume flow rate. The MFCs were calibrated by the manufacturer, Alicat Scientific Inc. The user input set point is for volumetric flow rate at STP. Figure 2.10 shows a photo of three of the mass flow controllers and the LabView page. A sixth MFC (OMEGA Engineering Inc.) was also installed to control the calibration gas flow rates for checking GC calibration prior to each test.

2.2.3 Micro Gas Chromatograph

The GC was calibrated for CH_4, H_2, N_2, C_2H_2, C_2H_4, C_2H_6, and CO_2 using gas standards obtained from Air Liquide Canada Inc. Calibration for O_2 was completed using two data points. One, as a rough estimate, used compressed building air and assumed that the air O_2 concentration was 20.9%. The second point was more reliable at 0.494% because it was in a gas standard. The purpose of calibration for O_2 was to assist in detecting any abnormalities of O_2 in the system for safety considerations, and so precise calibration was not necessary. Calibration checks or curve shifting for CH_4, H_2, N_2, and C_2H_6 were performed prior to each experiment. Due to limited calibration gas availability, checks for C_2H_2 and C_2H_4 were not performed. If any abnormalities were noticed, such as discrepancies over 1% or a shift in the retention times, then the GC was reconditioned using a burn-out method. EZChrom software (v3.2.1, Varian Inc.) was used to control the GC, collect data, integrate the curves, and record the data to .csv files. The GC method was programmed with a run time of 60 seconds, and a sampling frequency of 50 seconds. A screen shot of the software GUI and a photo of the GC with carrier gas column filters are given in Figure 2.11.

The H_2 calibration curve was slightly non-linear below 30% concentration. Therefore, two different calibration ranges were used. The first was for 0-24.8% using a quadratic best fit line. The second was for the 24.8-99.999% range using a linear

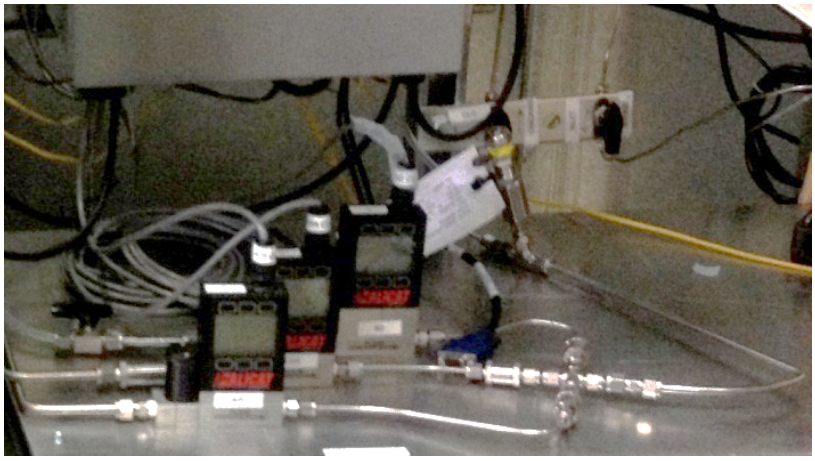

(a)

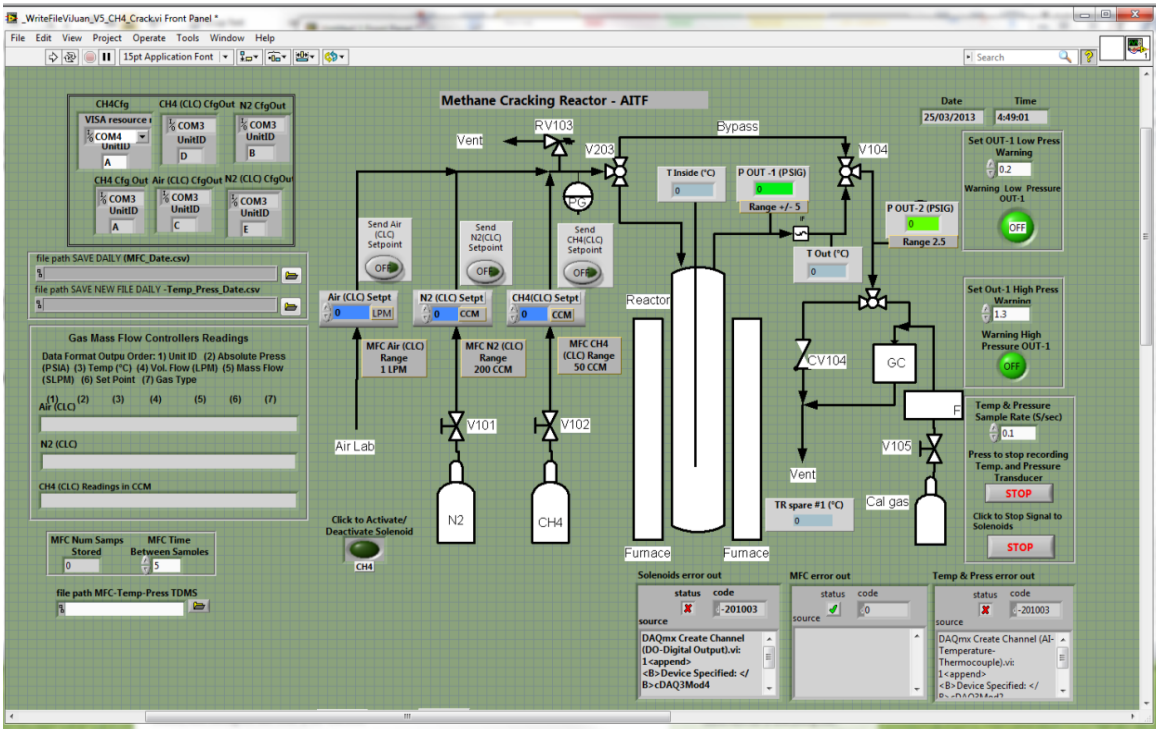

(b)

Figure 2.10 – Gas control and data collection, including (a) Mass flow controllers and (b) Labview screen shot

Table 2.1 – Setpoints used during and actual measured operating temperatures

Temperature level	Test 1 (K)	Test 2 (K)
Low	1034	1029
Mid	1184	1182
High	1337	1334

best fit. The proper range was selected depending on the amount of percent concentration of H_2 expected in the product gas stream. If the expected H_2 amount was unknown, the larger range was used. The data was post-processed with the low range calibration if H_2 concentration was below 24.8%. Nitrogen calibration extended from 0-99.997% concentration and was best fit with a quadratic line. CH_4 was calibrated with a cubic fit from 0-99.997%. The other by-product gases of C_2H_2, C_2H_4, C_2H_6 were calibrated with ranges of 0-2.03%, 0-1.98%, and 0-9.99%, respectively. Each calibration was set to pass through zero. The calibration curves are given in Figures 2.12 and 2.13, where the x-axis represents the area under the GC detection curve. The GC detection curve, measured in [mV], contains the resulting peaks detected by the GC over time as various gases elute from the column.

2.3 Experimentally measured temperature profile

It was necessary to obtain the temperature profile of the reactor because of the known sensitivity of CH_4 cracking on temperature [27]. Two tests were performed on the cracking reactor to verify the reactor temperature profile. The two tests had approximately 6 months in between. A diagram showing the experimental setup is given in Figure 2.14. The thermocouple was raised and lowered inside the reactor with temperature measurements being made approximately every 1-2 cm. Enough time was provided at each step to ensure that the temperature in the thermocouple had stabilized. The thermocouple was linked to a multimeter device (Model HHM16, OMEGA Engineering Inc.). The furnace setpoints used at the low, mid and high temperature ranges are given in Table 2.1.

The setpoints varied a small amount between Test 1 and Test 2 due to misplacing the notes containing the setpoints for the first profile testing, and then finding them after the second experiment was finished. However, the differences were considered negligible in the final results. The reactor in the first test was placed so that the base

(a)

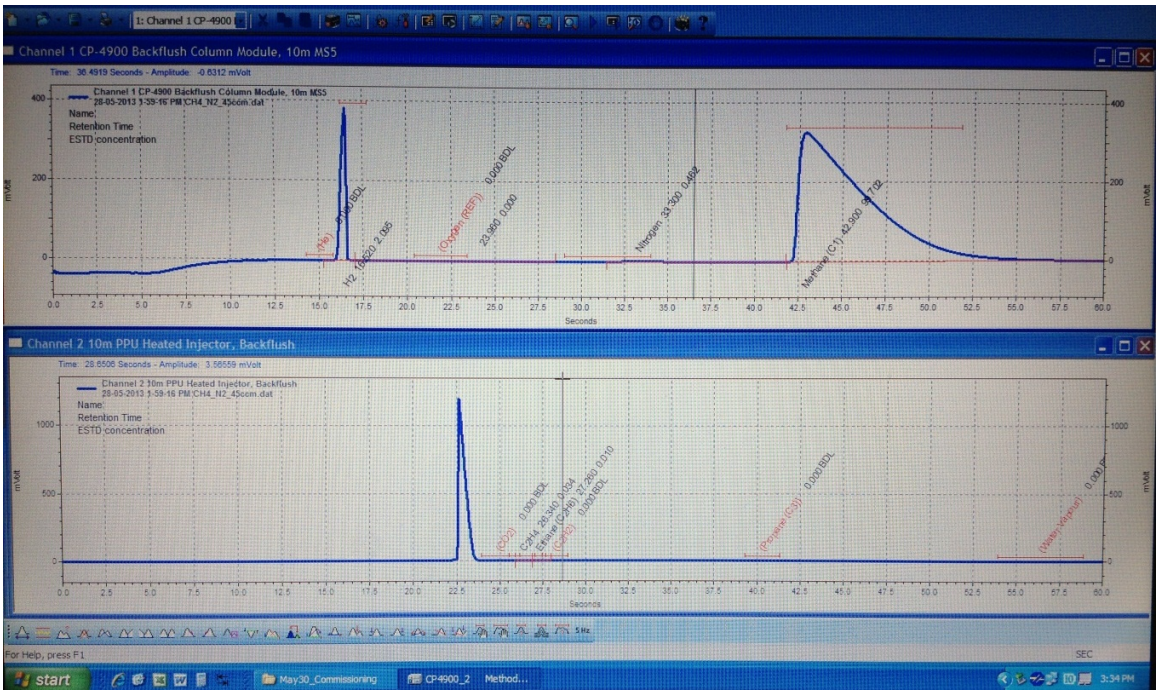

(b)

Figure 2.11 – Gas concentration measurement, including (a) Micro Gas Chromatograph and (b) GC software EZChrom screen shot

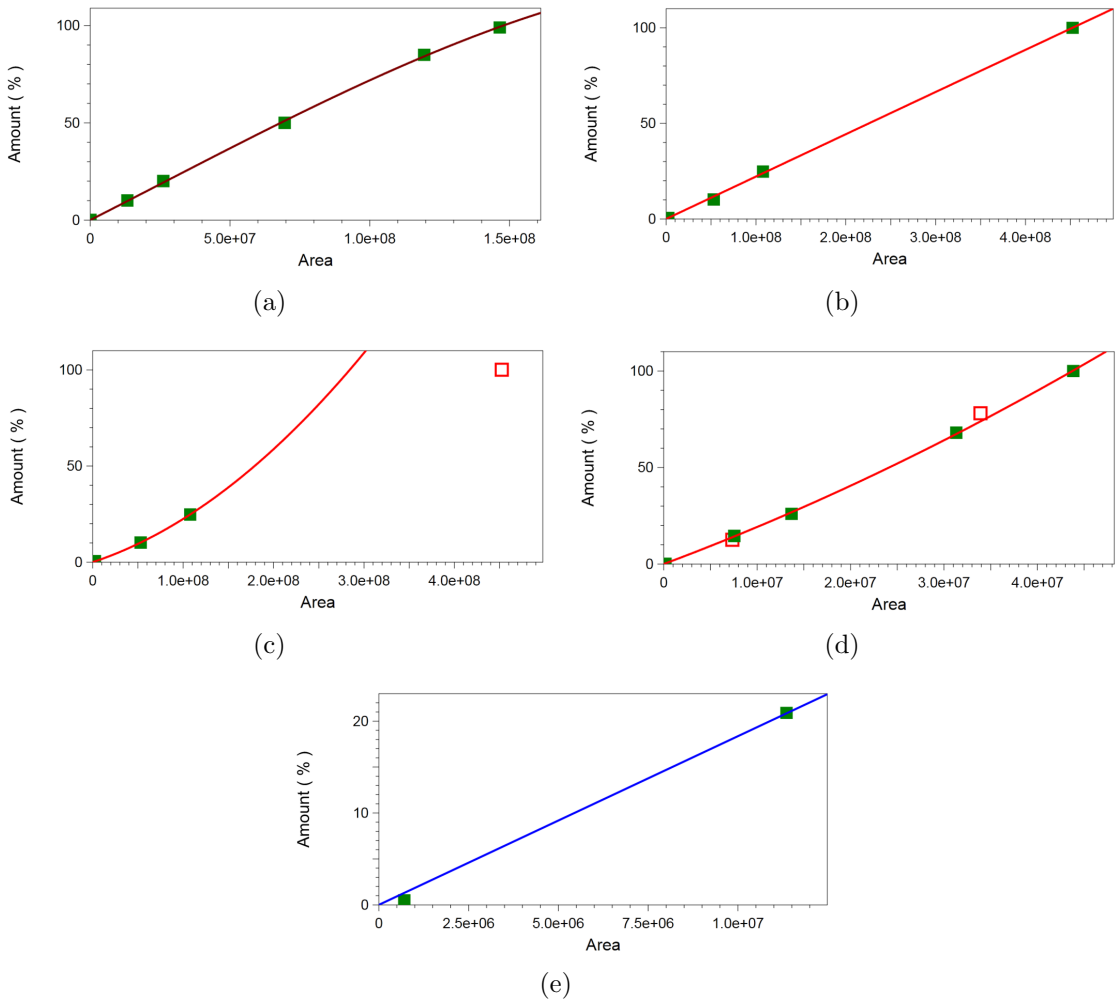

Figure 2.12 – GC calibration curves for (a) CH_4 (b) H_2 full range (c) H_2 low range, (d) N_2, and (e) O_2. The open symbols represent data points that were ignored. In (c) the data point with the open symbol was ignored to provide a low H_2 range, and in (d) the data point with the open symbol was ignored because it was from the atmosphere and not a calibration gas.

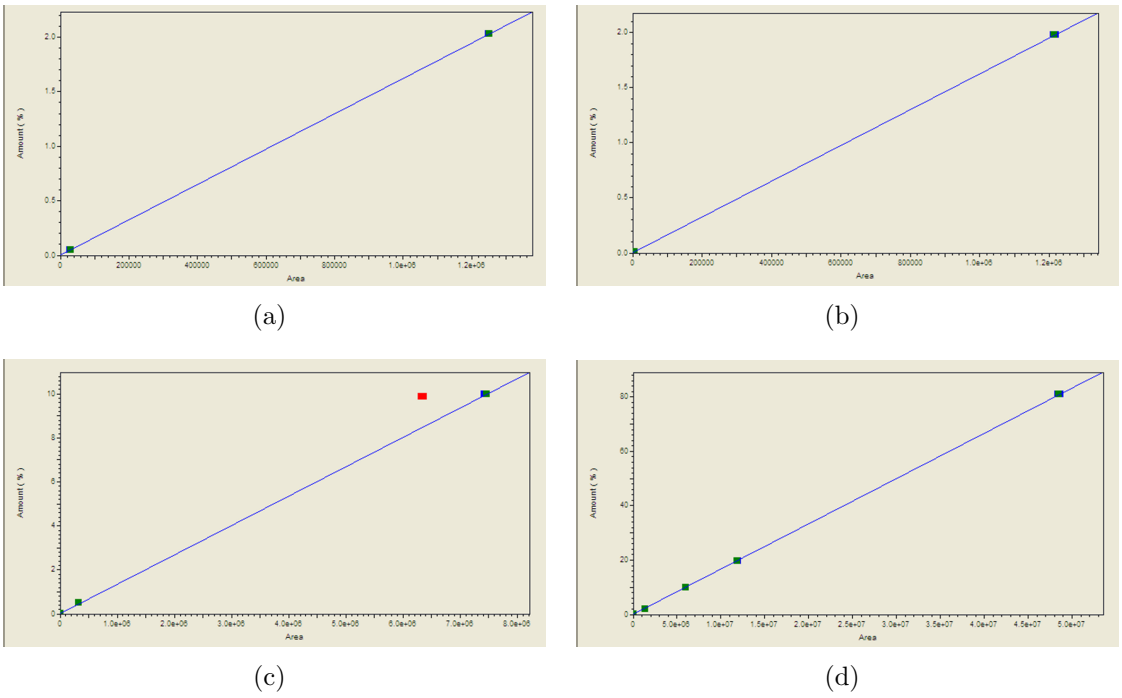

(a) (b) (c) (d)

Figure 2.13 – GC calibration curves for (a) C_2H_2 (b) C_2H_4 full range (c) C_2H_6 low range, and (d) CO_2

extended approximately 21.6 cm under the bottom of the top insulating cap. In the second test, the reactor was approximately 24.1 cm under the bottom insulating cap. This variance in location was due to a change in experimental procedures that occurred during the extensive period of time between profiling tests. The depth change was integrated into the system by removing a 1 inch cinderblock from the stack. The first profiling test took place during the commissioning of the reactor, while the latter test occurred after all the cracking experiments were completed. Thus the depth change was taken into account by shifting the data for the first test by 1 inch or 2.54 cm. It was assumed that the temperature at the increased depths would be constant with operating temperatures. The results of the tests are shown in Figure 2.15. The locations of interest shown in Figure 2.15 are tabulated in Table 2.2.

The resulting profiles were very similar, with little variance. At the bottom of the top insulating cap, the temperature dropped between approximately 123 K to 134 K from the operating temperature. The profile appears fairly linear from that point on, which is consistent with the tube being insulated and above the heating elements. The temperature drop is caused largely by the cooling fan positioned on the top of the furnace.

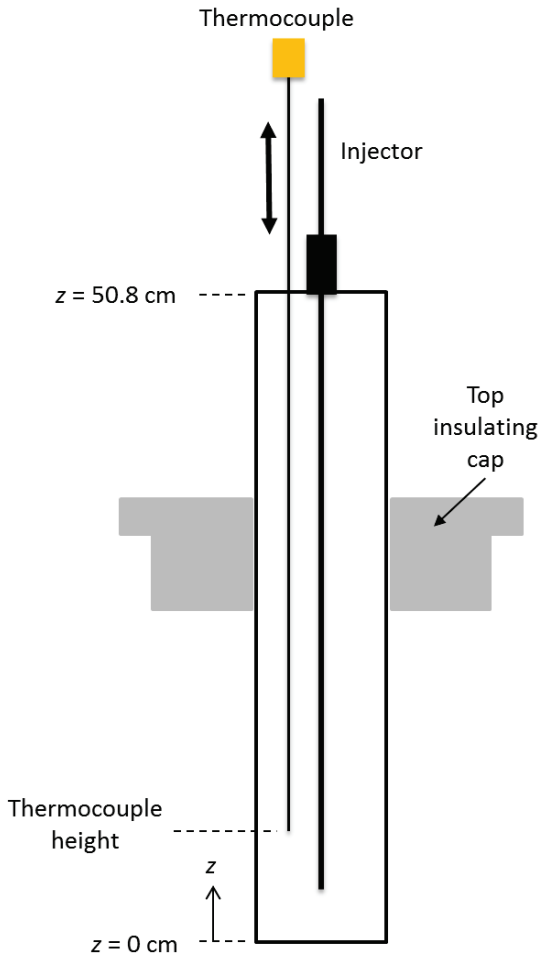

Figure 2.14 – Graphical representation of the reactor temperature profile tests.

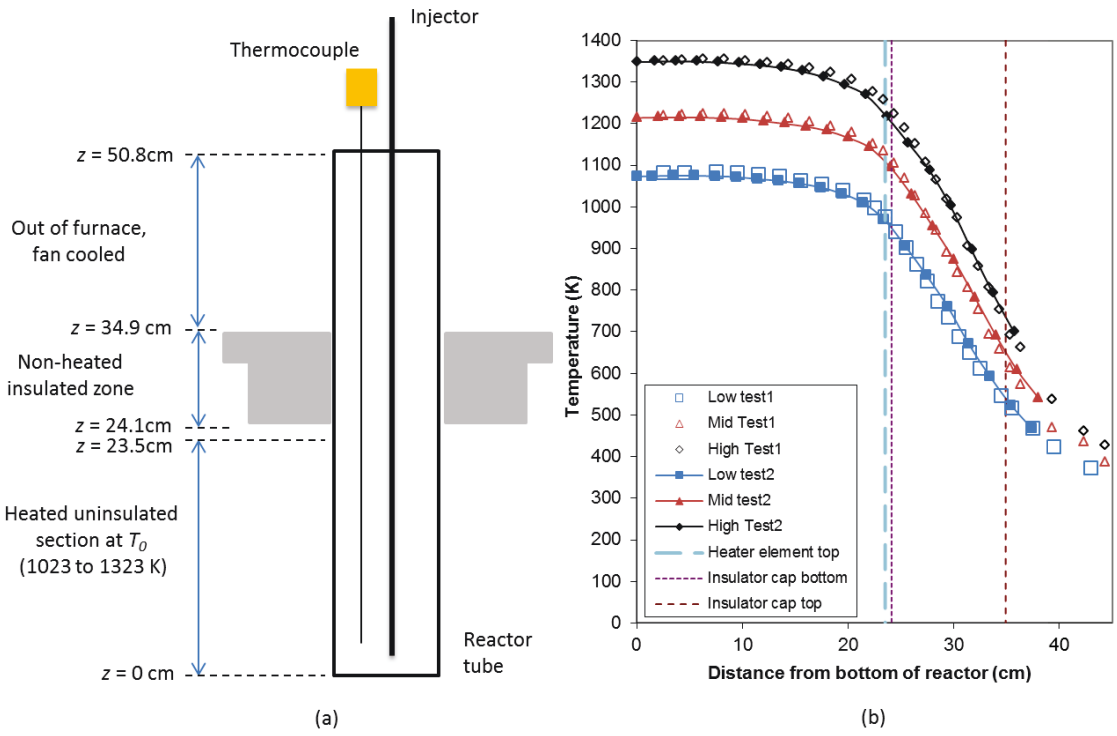

Figure 2.15 – Temperature profile tests results, with (a) graphical representation of reactor with locations of interest and (b) experimentally determined temperature plot showing temperature profile in the reactor.

Table 2.2 – Tabulated data from temperature profile test at various locations

Distance from bottom (cm)	High (K)	Mid (K)	Low (K)
34.9	728	640	536
24.1	1217	1094	944
23.5	1234	1111	961
1.0	1350	1218	1078

2.4 Experiment design

The number of levels for each factor considered for the kinetic parameters k_o and E_a experiments and subsequent molten metal reactor effectiveness experiments are shown in Table 2.3. The factors bath material and injector are qualitative, while temperature and flow rate are quantitative. The effects of temperature were expected to potentially be non-linear due to the non-linearity of the equilibrium curve in Figure 2.16. Therefore the experiments were designed to have at least five levels for temperature. The other factors had one or two levels for the blank and molten metal reactor experiments, respectively. The blank and molten metal reactor experiments had 5 and 2 levels for total flow rate, respectively. The molten metal experiments exhibited low conversions at the usual flow rates used in the blank reactor experiments, therefore lower range flow rates were studied. Tables 2.4 and 2.5 identify the level magnitudes for experiments that were performed. The results from the blank reactor tests were used for both determining the kinetics and for analyzing the effects of factors on reactor performance.

The 4-10 μm sparger was made of fused quartz (Technical Glass Products Inc.), and has an annealing temperature of 1215℃ [57]. However, due to safety concerns by AITF, the maximum permitted temperature was 900℃. The 6.3 mm Al_2O_3 injector tube was operated up to 1100℃, or at the recommended maximum temperature for long periods of time (i.e. a few hours) without damaging the furnace.

Serban et al. [2] tested both Sn and Pb for the molten bath material. They both exhibit low temperature melting points. The author found that the difference in CH_4 conversion between the two metals was negligible, and proceeded to complete the rest of the experiments with Sn because it is less toxic [2]. To allow better comparison

Table 2.3 – Number of levels in a) experiments used to determine the kinetic parameters, and b) experiments analyzing the effectiveness of the molten metal reactor

	Number of levels			
	Temperature	**Bath material**	**Injector**	**Flow rate**
Kinetic Experiments	6	1	1	5
Molten metal Experiments	5	2	2	2

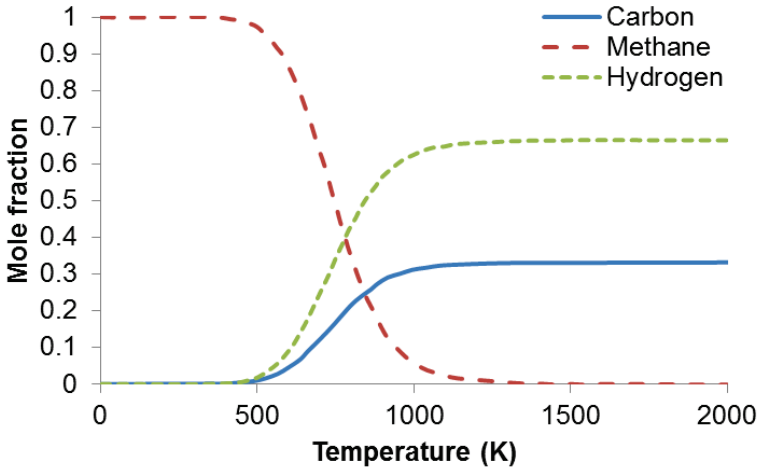

Figure 2.16 – Equilibrium curve for methane cracking, data from [4]

Table 2.4 – Experimental plan for determining kinetic parameters E_a and k_o. Tests were performed in a blank reactor with the 6 mm Al_2O_3 tube injector.

Experiment no.	Temperature (K)	Bath material[1]	Injector type[2]	Flow rate (ccm)	Replicas
1	1073	1	1	33	0
2	1073	1	1	67	0
3	1073	1	1	113	0
4	1123	1	1	33	0
5	1123	1	1	67	0
6	1123	1	1	113	0
7	1123	1	1	154	0
8	1173	1	1	154	0
9	1173	1	1	224	0
10	1223	1	1	33	0
11	1223	1	1	67	0
12	1223	1	1	113	0
13	1223	1	1	154	0
14	1223	1	1	224	1
15	1273	1	1	33	0
16	1273	1	1	67	0
17	1273	1	1	113	0
18	1273	1	1	154	1
19	1273	1	1	224	0
20	1323	1	1	33	0
21	1323	1	1	67	0
22	1323	1	1	113	0
23	1323	1	1	154	0
24	1323	1	1	224	0
25	1373	1	1	33	0

[1] 1 = blank reactor, 2 = 20.3 cm molten tin bed
[2] 1 = 6 mm Al_2O_3 tube injector, 2 = 4-10μm quartz sparger

Table 2.5 – Molten tin experimental plan.

Experiment no.	Temperature (K)	Bath material[1]	Injector type[2]	Flow rate (sccm)	Replicas
1	1023	2	1	17	0
2	1023	2	2	17	1
3	1123	2	1	17	0
4	1123	2	1	156	0
5	1123	2	2	17	1
6	1148	2	2	17	1
7	1173	2	2	17	1
8	1273	2	1	17	0
9	1273	2	1	156	0

[1] 1= blank reactor, 2= 20.3 cm molten tin bed
[2] 1= 6 mm Al_2O_3 tube injector, 2= 4-10 μm quartz sparger

with the study performed by Serban et al. [2]., 99.97% pure Sn was selected for the molten bath in this thesis.

2.4.1 Experimental procedure

The general procedure for each experiment was as follows. The reactor vessel, cap, injector and thermocouple were assembled and installed into the furnace. The silicone insulation was clamped to the top of the tube just above the top insulating cap. At room temperature, the system was pressurized to 5 psi by turning on the air MFC and closing the three way valve at the gas outlet. The system was leak tested using Snoop (Swagelok). The cooling fan above the furnace was turned on. The furnace controller was programmed to ramp up to the desired temperatures. A cool down sequence was also included. The apparatus was purged using N_2 while the furnace ramped up from room temperature. The reactor gas outlet was set to vent to the fumehood, and the GC calibration was checked using two of the gas calibration gas mixtures that were available. A minimum of five samples per gas was run at 100 sccm. Once the furnace was at operating temperature, the reactor assembly was pressurized again under N_2 conditions by closing the three-way valve at the outlet. The system was checked for leaks for a final time. After passing the leak test, the reactor outlet was switched again to the GC. The calibration gas flow was set to 0 sccm, thus finishing all preparations for the experiment.

The reactant gas flow was set to the desired setpoints, with a 50-50% split for N_2 and CH_4. The GC was set to continuously sample the outlet gas for the entire duration of the experiment. The reactor outlet gas was allowed to stabilize for a minimum of 20 to 30 minutes. After stabilization, reactor was purged with N_2. If further tests were desired at a different temperature or flow rate, the furnace was ramped up or down to the new setpoint temperature, and the desired reactant gas flow setpoint was initialized again. When the experiments were completed, the furnace cool down was initiated and the GC was shut down.

2.4.2 Post processing

Post processing of the experimental data is described in this section. The GC output the percent concentrations of the reactant gas CH_4 and N_2, and the product gases H_2, C_2H_2, C_2H_4, C_2H_6. The total percent concentration of the calibration should culminate to 100%. However the GC only measures the percent concentration based on the area under the curve of the signal it receives as the gas elutes from the column. The GC data output did not usually add up to exactly 100%. It was found during experiments that the total composition usually amounted to approximately 98% to 99%. Equation (2.1) was used to normalize the data to 100%.

$$x_i = \frac{x_{i,act}}{\sum_j x_{j,a}} \tag{2.1}$$

where x_i is the normalized GC percent composition of species i, and $x_{i,act}$ is the actual GC percent composition of species i.

2.4.2.1 Methane conversion equation

The general definition for calculating conversion for CH_4 is given by

$$X_{CH_4} = \frac{N_{CH_4,0} - N_{CH_4}}{N_{CH_4,0}} \tag{2.2}$$

where $N_{CH_4,0}$ is the inlet molar flow rate of CH_4 in [mol/s] and N_{CH_4} is the outlet molar flow rate of CH_4 in [mol/s]. The outlet molar flow rate takes into account that some solid carbon is left behind in the reactor vessel or filtering system prior to the point of measurement of the outlet CH_4 mole fraction. In this case, the inlet and outlet points of measurement are assumed to be at ambient pressure and temperature. The inlet molar flow rate can be described as

$$N_{CH_4,0} = x_{CH_4,0} \frac{\dot{m}_0}{M_{mix,0}} \tag{2.3}$$

where $x_{CH_4,0}$ is the inlet mole fraction of CH_4, $\dot{m}_0$ is the inlet mass flow rate, and $M_{mix,0}$ is the molar mass of the gas mixture at the inlet. $\dot{m}_0$ is defined as

$$\dot{m}_0 = \dot{V}_0 \rho_0 \tag{2.4}$$

where $\dot{V}_0$ is the inlet total volumetric flow rate, and ρ_0 is the inlet gas density. Using the ideal gas law, ρ_0 is given as

$$\rho_0 = \frac{P_0 M_{mix,0}}{RT_0} \tag{2.5}$$

where P_0, T_0 and $M_{mix,0}$ are the pressure, temperature, and molar mass of the gas mixture at the inlet point of measurement. Substituting this in, the inlet mass flow rate becomes

$$\dot{m}_0 = \dot{V}_0 \frac{P_0 M_{mix,0}}{RT_0} \tag{2.6}$$

Substituting Equation (2.6) into Equation (2.3) and simplifying, the inlet molar flow rate becomes

$$N_{CH_4,0} = x_{CH_4,0} \frac{\dot{V}_0 P_0}{RT_0} \tag{2.7}$$

Assuming an ideal gas, $x_{CH_4,0}$ is calculated by the following

$$x_{CH_4,0} = \frac{\dot{V}_{CH_4,0}}{\dot{V}_0} \tag{2.8}$$

where $\dot{V}_{CH_4,0}$ is the inlet volumetric flow rate of CH_4 in [m^3/s].

The outlet molar flow rate can be defined as

$$N_{CH_4} = x_{CH_4} C_T \overline{u} A_c \tag{2.9}$$

where x_{CH_4} is the outlet mole fraction of CH_4, C_T is the total concentration at the outlet in [mol/m^3], , and $\overline{u}$ is the outlet flow velocity of the gas mixture. A_c is the cross-sectional area of the tubing at the outlet point of measurement in the apparatus, i.e. at the GC. Substituting Equations (2.3) and (2.9) into Equation (2.2) therefore gives

$$X_{CH_4} = \frac{x_{CH_4,0} \frac{\dot{V}_0 P_0}{RT_0} - x_{CH_4} C_T \overline{u} A_c}{x_{CH_4,0} \frac{\dot{V}_0 P_0}{RT_0}} = 1 - \frac{x_{CH_4} C_T \overline{u} A_c RT_0}{x_{CH_4,0} \dot{V}_0 P_0} \tag{2.10}$$

$C_T \overline{u}$ is found using the following analysis. The general conversion equation for CH_4 cracking can be described as follows. Recognizing that some CH_4 goes unreacted and is in the product stream, and the solid carbon remains inside the reactor vessel

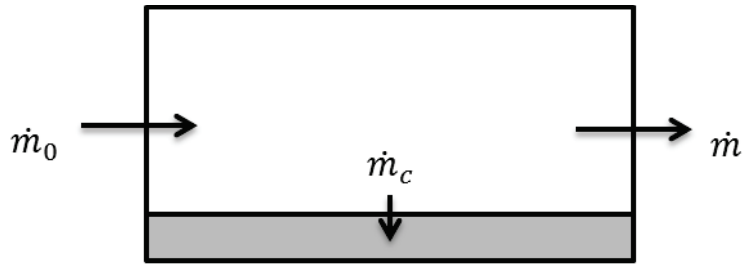

Figure 2.17 – Mass flow balance of the reactor and filter assembly.

and filtering system, a representative figure showing the inlet and outlet mass flow rates of the reactor and filtering systems is given in Figure 2.17. $\dot{m}_C$ represents the mass flow of carbon deposition, $\dot{m}$ is the outlet mass flow, and $\dot{m}_0$ is the inlet gas mass flow. The conversion inside the reactor is

$$CH_{4(g)} + N_{2(g)} \rightarrow aC_{(s)} + bCH_{4(g)} + cH_{2(g)} + N_{2(g)}$$

where a, b and c are stoichiometric coefficients. Higher order hydrocarbons of the form C_xH_y are neglected in this calculation due to limitations on data gathering. The stoichiometric coefficients are calculated as follows. For the H balance,

$$\begin{aligned} 4 &= 4b + 2c \\ 2 &= 2b + c \\ c &= 2 - 2b \end{aligned} \tag{2.11}$$

and for the C balance,

$$\begin{aligned} 1 &= b + a \\ a &= 1 - b \end{aligned} \tag{2.12}$$

The mole fraction of H_2 and CH_4 are measured at the outlet using the GC. The stoichiometric coefficient b can be determined using x_{CH_4} as follows. In the gas phase, the mole fraction of CH_4 at the outlet can be described as

$$x_{CH_4} = \frac{b}{b + c + 1} = \frac{b}{b + 2 - 2b + 1} = \frac{b}{3 - b} \tag{2.13}$$

solving for b gives

$$\begin{aligned} 3x_{CH_4} - bx_{CH_4} &= b \\ b &= \frac{3x_{CH_4}}{1 + x_{CH_4}} \end{aligned} \tag{2.14}$$

c and a can then be determined from b. As a check, c and b can then be used to predict the outlet mole fraction of H_2 as follows

$$x_{H_2} = \frac{c}{b+c+1} = \frac{2-2b}{3-b} \tag{2.15}$$

where b is from Equation (2.14).

The mass flow rate at the outlet, $\dot{m}$ is calculated as

$$\begin{aligned} \dot{m} &= \rho \overline{u} A_c \\ &= (C_T M_{mix}) \overline{u} A_c \\ &= C_T \overline{u} M_{mix} A_c \end{aligned} \tag{2.16}$$

where ρ is the gas mixture density at the outlet in [kg/m^3]. Rearranging,

$$C_T \overline{u} = \frac{\dot{m}}{A_c M_{mix}} \tag{2.17}$$

An expression for $\dot{m}$ can be given as

$$\begin{aligned} \dot{m} &= b N_{CH_4,0} M_{CH_4} + c N_{CH_4,0} M_{H_2} + 1 \times N_{CH_4,0} M_{N_2} \\ &= (b M_{CH_4} + c M_{H_2} + M_{N_2}) N_{CH_4,0} \end{aligned} \tag{2.18}$$

where b and c are stoichiometric coefficients, M_i is the molar mass of species i at the outlet, and $N_{CH_4,0}$ is the inlet molar flow rate of CH_4, given in Equation (2.3). Substituting Equation (2.3) into Equation (2.18),

$$\dot{m} = \frac{(b M_{CH_4} + c M_{H_2} + M_{N_2})\, x_{CH_4,0} \dot{V}_0 P_0}{R T_0} \tag{2.19}$$

Substituting Equation (2.19) into Equation (2.17) gives

$$C_T \overline{u} = \frac{(b M_{CH_4} + c M_{H_2} + M_{N_2})\, x_{CH_4,0} \dot{V}_0 P_0}{A_c M_{mix} R T_0} \tag{2.20}$$

The final equation for CH_4 conversion is then found by substituting Equation (2.20) into Equation (2.10), giving

$$\begin{aligned} X_{CH_4} &= 1 - \frac{\left[\frac{(b M_{CH_4} + c M_{H_2} + M_{N_2}) x_{CH_4,0} \dot{V}_0 P_0}{A_c M_{mix} R T_0} \right] x_{CH_4} A_c R T_0}{x_{CH_4,0} \dot{V}_0 P_0} \\ &= 1 - \frac{(b M_{CH_4} + c M_{H_2} + M_{N_2})\, x_{CH_4}}{M_{mix}} \end{aligned} \tag{2.21}$$

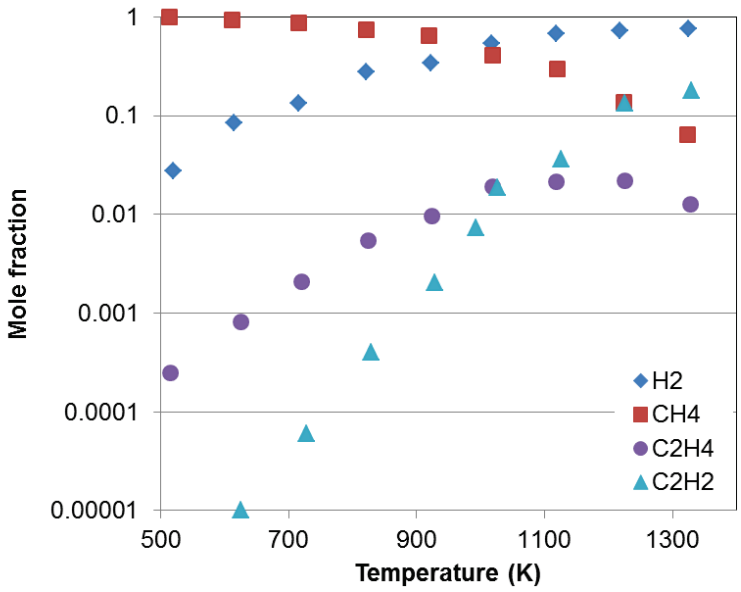

Figure 2.18 – Mole fractions of various hydrocarbons at equilibrium for the combustion of CH_4. Data from [5].

Thus methane conversion was calculated from experimental data using Equation (2.21). The GC experimental data at the reactor outlet gave lower CH_4 mole fractions than what was injected into the reactor even at low temperatures at which no reaction could possibly occur. This suggested that a bias existed for X_{CH_4}. The bias also differed depending on the flow rate that was used. Thus the bias amount was estimated for each flow rate using data at which no H_2 was in the product stream (i.e. when no reaction occurred). In summary, the final CH_4 conversion was corrected at each flow rate by subtracting the respective bias. The assumption that the lack of H_2 in the product stream signified that no conversion occurred was verified using Figure 2.18 [5]. The second largest component is C_2H_4, and it is one to two orders of magnitude smaller than H_2. Therefore it is likely that if the GC was not detecting H_2, then all other gaseous products would also be zero.

2.5 Sources of error

The sources of error are discussed in this section, and are listed as follows.

1. The pressure in the reactor tended to slowly build up during tests due to gradual plugging of the filters. Le Chatelier's principle suggests that the methane cracking reaction would be slowed due to the stoichiometry of the CH_4 cracking reaction, where two moles of $H_{2(g)}$ were produced for every one mole of $CH_{4(g)}$

consumed [58]. Tests were performed until the reactor pressure reached 5 psi due to plugging. At this point, the experiments were shut down.

2. There were less than ideal number of replicas performed. Only two replicas were performed out of the twenty seven total blank reactor experiments. The molten metal experiments had 4 replicas for a total of 9 experiments, which was much more favourable.

3. The replicas that were performed were not 'true' replicas because, due to cost limitations, the reactor assembly was not fully disassembled and reassembled with a new reactor, injector and cap for each experiment.

4. Tolerances for size of reactors and injectors are small but error in volume may be as high as 18%. This was obtained by calculating the maximum and minimum volumes given the measurement tolerances and taking the ratio. The dimensions and tolerances for the reactor and tube injectors are:

    - Al_2O_3 reactors: 508.00 ± 1.6 mm long by 50.8 ± 2.03 mm OD and 44.45 ±1.78 mm ID
    - Al_2O_3 tube injector: 711.20 ± 1.6 mm long by 6.35 ± 0.33 mm OD and 3.18 ±0.15 mm ID.

5. The GC has error in the volumetric fraction measurements it makes. The calibration standards were run as samples throughout the experimental stage to check the calibration and drift of the GC curves. It was found using approximately 20 of these trials that CH_4 ranged from 1.2 - 2.2% error, H_2 from 1.5 - 2.1% error, and N_2 from 0.8 - 2.0% error.

6. The pressure transducers have 0.08% best straight line error. They were also repeatedly exposed to pressures above their limits during pressure buildups due to plugging of the filters. The error on their measurements may not be as specified by the manufacturer due to this damage. Also, PT1 was located approximately 25 cm downstream of the reactor but was before the filters, and likely had some error due to particulate buildup. However, these errors were considered negligible because the pressure transducers were used only to signal if plugging was occurring in the filters or injector.

7. N_2 and CH_4 were UHP and 4.0 grade, respectively. Hence there were negligible errors due to gas concentrations.

8. O_2 was measured by the GC during some experiments, however because the O_2 calibration was very rough, the amount of O_2 measured was unreliable. Abnormalities in O_2 concentrations may have been because of unidentifiable leaks. This and the poor calibration of O_2 may have affected the percent concentration values of the other gas components. Baseline for oxygen was approximately 0.4 to 0.9%, but it did reach up to 1.3%.

9. The temperature readings in LabView and a hand held device for the thermocouple inside the reactor did not give the same values, having differences as large as 10 K at operating temperatures above 1023 K. This constitutes a possible 0.1% error in temperature reading, which was considered negligible.

10. Thermocouple radiation error was considered negligible (see Section 2.5.1).

11. Mass flow controller error (see Section 2.5.2).

2.5.1 Thermocouple radiation error

The thermocouple temperature reading may be higher than the actual gas temperature due to radiation effects from the reactor walls, which in turn may be hotter than the gas temperature outside of the reactor due to radiation from the heating elements. The gas temperature in the furnace heating zone was measured by the built in furnace thermocouples, which were located approximately 1/4 inch outside of the furnace walls. The furnace thermocouples received negligible amounts of radiation from the heating elements because the thermocouples and radiation elements are not in view of each other. Generally the furnace thermocouple temperature readings were 19 to 39℃ lower than the type K thermocouple that is extended into the reactor. The magnitude of this possible error was determined by analyzing a simple one dimensional system, as shown in Figure 2.19

The analysis was performed at the lower section of the reactor that exhibited an isothermal operating temperature, shown in Section 2.3. Three equations were evaluated to verify that the temperatures of the reactor wall, injector, and gas inside the reactor were the same, and hence conclude that the thermocouple temperature must be the same as the gas temperature. The first equation consisted of balancing the two convective heat loss terms from the reactor wall with the radiation heat transfer from the reactor wall to the injector. The second equation balanced the convective heat transfer that occurred from the reactor and the injector walls to the

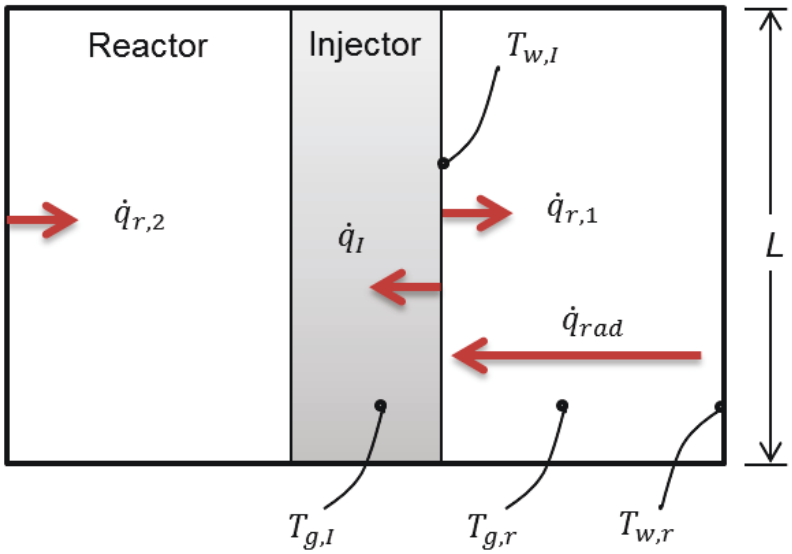

Figure 2.19 – Heat transfer diagram of the reactor and injector with isothermal walls.

reactor gas. The final equation was a heat balance for the injector gas. The following assumptions were made:

1. Radiation between the reactor and injector walls, convection between the gas in the reactor and the exterior injector wall, and convection between the gas in the injector and the interior injector wall are the main heat transfer modes heating the injector wall.

2. Heat transfer via conduction is negligible.

3. The emissivity of alumina is 0.45. This is conservative for the range of 0.65 to 0.45 for a temperature range of 800 K to 1400 K, as given by Cengel [55].

4. The gas is ideal and isothermal.

5. The convection coefficient, h, is assumed to be 30 W/(m^2·K). The convection coefficient for laminar flow is 5-30 W/(m^2·K), and 30 to 200 W/(m^2·K) for turbulent flow [59].

6. The temperature in the alumina is isothermal vertically and through the thickness of the reactor and injector walls due to: a) high thermal conductivity, $\gamma_{1073K} = 8.2$ W/(m^2·K) [60], b) thin injector and reactor wall thicknesses, $t_{w,I}$ and $t_{w,r}$ are 0.003 m and 0.006 m, respectively, and c) isothermal heating in the lower section of the furnace. This assumption was validated by comparing heat

convection vs conduction through the reactor wall over the same temperature differential, $T_{high} - T_{low}$:

$$\dot{q}_{conv} = h(T_{high} - T_{low}) = 30 \times (1323 - 1200) = 3.7 \times 10^3 \quad \text{W/m}^2$$
$$\dot{q}_{cond} = \gamma \frac{(T_{high} - T_{low})}{t_{w,r}} = 8.2 \times \frac{(1323 - 1200)}{0.006} = 1.7 \times 10^5 \quad \text{W/m}^2$$

which shows two orders of magnitude difference between convection and conduction.

Radiation heat transfer between the reactor wall and the injector is estimated using the following equation for infinitely long concentric cylinders [55].

$$\dot{Q}_{radiation} = A_{I,out} \frac{\sigma_{SB}(T_{w,I}^4 - T_{w,r}^4)}{\frac{1}{\epsilon_I} + \frac{1-\epsilon_r}{\epsilon_r}(\frac{0.5 \times D_{I,out}}{0.5 \times D_{r,in}})} \tag{2.22}$$

where σ_{SB} is the Stefan-Boltzmann constant, equal to 5.67E-8 W/(m^2·K^4), $T_{w,r}$ is the reactor wall temperature in [K], ϵ_r and ϵ_I are respectively the emissivities of the reactor and injector, and $D_{r,in}$ and $D_{I,out}$ are the inner and outer radii of the reactor and injector in [m], respectively. The equation for convection inside the injector is

$$\dot{Q}_I = A_{I,in} h (T_{w,I} - T_{g,I}) \tag{2.23}$$

where $T_{w,I}$ is the wall temperature of the injector in [K], and $T_{g,I}$ is the temperature of the N_2-CH_4 gas mixture inside the injector in [K]. The equation for convection inside the reactor from the injector wall is

$$\dot{Q}_{r,1} = A_{I,out} h (T_{w,I} - T_{g,r}) \tag{2.24}$$

where $T_{g,r}$ is the temperature of the N_2-CH_4 gas mixture inside the reactor in [K]. The equation for convection inside the reactor from the reactor wall is

$$\dot{Q}_{r,2} = A_{r,in} h (T_{w,r} - T_{g,r}) \tag{2.25}$$

where $T_{w,r}$ is the wall temperature of the reactor in [K]. The energy entering the injector via the gas flow was found by

$$\dot{m}_{I,0} H_{I,0} = \frac{1}{M_{mix}} c_{p,amb} \dot{V} \rho_{amb} T_{amb} \tag{2.26}$$

where the M_{mix} is the molar mass of the gas mixture in [kg/mole], $c_{p,atm}$ is the specific heat capacity at constant pressure of the inlet gas in [J/(mol·K)], $\dot{V}$ is the volumetric flow rate of the gas mixture in [m^3/s], ρ_{amb} is the inlet gas density in

[kg/m^3], and T_{amb} is the inlet gas temperature in [K]. To be conservative in this analysis, T_{amb} was set to be at ambient or 298 K. The energy exiting the injector via the gas flow was found by

$$\dot{m}_I H_I = \frac{1}{M_{mix}} c_{p,g,I} \dot{V} \rho_{g,I} T_{g,I} \tag{2.27}$$

where $c_{p,g,I}$ is the specific heat capacity at constant pressure of the injector outlet gas in [J/(mol·K)], $\rho_{g,I}$ is the injector outlet gas density in [kg/m^3], and $T_{g,I}$ is the injector outlet gas temperature in [K].

The energy exiting the reactor via the gas flow was found by

$$\dot{m}_r H_r = \frac{1}{M_{mix}} c_{p,g,r} \dot{V} \rho_{g,r} T_{g,r} \tag{2.28}$$

where $c_{p,g,r}$ is the specific heat capacity at constant pressure of the reactor outlet gas in [J/(mol·K)], and $\rho_{g,r}$ is the reactor outlet gas density in [kg/m^3]. The three unknown temperatures $T_{g,I}$, $T_{g,r}$ and $T_{w,I}$ were found by solving the following three equations simultaneously.

$$0 = \dot{Q}_{radiation} - \dot{Q}_I - \dot{Q}_{r,1} \tag{2.29}$$

$$0 = \dot{Q}_{r,1} + \dot{Q}_{r,2} + \dot{m}_I H_I - \dot{m}_r H_r \tag{2.30}$$

$$0 = \dot{m}_{I,0} H_{I,0} - \dot{m}_I H_I + \dot{Q}_I \tag{2.31}$$

Equation (2.29) is a heat balance at the injector wall, Equation (2.30) is a heat balance for the gas in the reactor, and Equation (2.31) is a heat balance for the injector gas. The built in function `solve()` in Matlab 2012a was used to find the steady state temperatures. The results are shown in Figures 2.20. The temperature percent differences between the reactor wall and the injector wall, and between the reactor wall and the reactor gas were respectively calculated as

$$T_{w,r-w,I} = \frac{T_{w,r} - T_{w,I}}{T_{w,r}} \times 100 \tag{2.32}$$

$$T_{w,r-g,r} = \frac{T_{w,r} - T_{g,r}}{T_{w,r}} \times 100 \tag{2.33}$$

The final result of the above analysis shows that the the difference in temperatures between the gas in the injector and the reactor wall was 47 K, giving the largest temperature difference. However, the gas spends the majority of its residence time in the reactor, and the thermocouple is measuring the temperature in the reactor. Considering this, the temperature of the injector wall was less than 0.98% of the

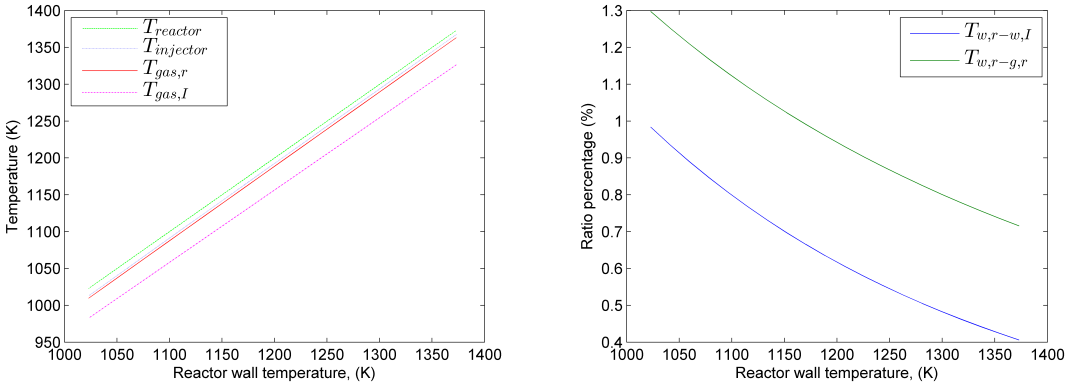

(a) (b)

Figure 2.20 – Results of radiation analysis in a) steady state temperatures and b) percent differences between reactor gas and injector wall vs reactor wall.

reactor wall temperature. The difference between the reactor wall and the reactor gas temperatures was less than 1.3%. These correspond to a 10 K difference in temperatures between the injector and reactor walls, and a 13 K difference between the reactor wall and the gas in the reactor. From this it was determined that the thermocouple inside the reactor was measuring within reasonable limits the actual gas temperature inside the reactor. Thus, this temperature is very close to the same as the injector wall and the reactor wall. This analysis also verifies the assumption that radiation absorption of the methane gas is negligible, since the temperature differential is very small.

2.5.2 Mass flow controller error

One source of error in this study was caused by potential miss-calibration of the MFCs by the manufacturer, Alicat Scientific Inc. A series of tests using a bubble flow meter were performed to check this. Figure 2.21 shows a graphical representation of the test set up. The MFC with the smallest range possible was used for each setpoint. For example, if the flow rates were set to 50-50ccm N_2-CH_4, then MFC-3 and MFC-2 were used for the gases, respectively.

The MFCs are rated for ± (0.8% of reading + 0.2% of full scale). The bubble flow meter is a glass column with a gas inlet at the bottom and a gas outlet at the top (see Figure 2.22). The bottom of the glass column has a bulb attached with soap in it. The soap is used to produce soap bubbles in the column. When the gas is flowing, the bubbles rise up in the column. A stopwatch was used to measure the time for the

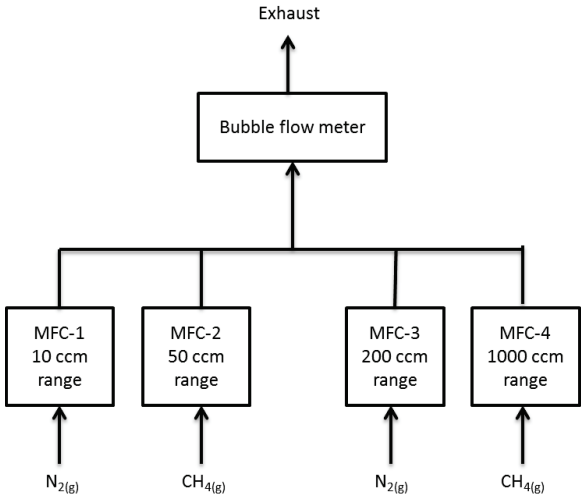

Figure 2.21 – Graphical representation the mass flow controller (MFC) output variance from the setpoint.

bubble to pass markings on the graduated column. The flow was then calculated by taking the volumetric area over which the bubble passed up the column and dividing it by the time recorded. If desired, the flowrate can be standardized to reference conditions for both test systems, usually standard temperature and pressure (STP). This is done by making a correction of temperatures and pressures by using the ideal gas law as given in Equation (2.34)

$$\dot{V}_{STP} = \dot{V}_{amb}(\frac{T_{STP}}{T_{amb}})(\frac{P_{amb}}{P_{STP}}) \tag{2.34}$$

where $\dot{V}$ is the flow rate in [m^3/s], T is temperature in [K], and P is pressure in [Pa]. The subscripts $_{amb}$ and $_{STP}$ mean ambient pressure and temperature or standard temperature and pressure, respectively. The bubble flow meter tests did not incorporate this temperature and pressure correction because the purpose of the test was to check for the composition mole fractions of the inlet gas. The setpoints for N_2 and CH_4 were always set equal to each other, so a 50% - 50% composition was expected. Otherwise, data taken from both the inlet and the outlet of the reactor were at room temperature and atmospheric pressure, so no correction was necessary.

Eight to ten measurements were taken for each flow rate, with standard deviations of 0.1 sccm to 1 sccm for the low flow rates, and 0.5 sccm to 2.0 sccm for the higher flow rates, with the exception of 200 sccm setpoints where the standard deviations were 8.3 sccm for the N_2 MFC-4 and 4.9 sccm for the CH_4 MFC-3. The tabulated results for the bubble flow meter tests are shown in Table 2.6.

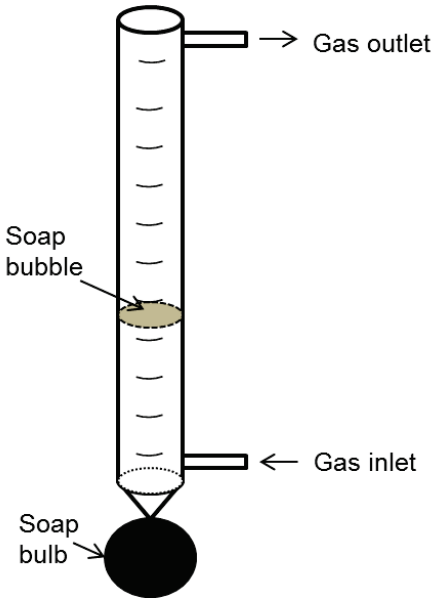

Figure 2.22 – Graphical representation the mass flow controller (MFC) output variance from the setpoint.

Table 2.6 – Bubble flow meter test results with expected calibration error (i.e. 0.8% of Reading + 0.2% of Full Scale)

Setpoint (sccm)	**MFC-1 (10 sccm N_2)**	**Calibration error (ccm)**	**MFC-2 (50 sccm CH_4)**	**Calibration error (ccm)**
100	-	-	-	-
70	-	-	-	-
50	-	-	56.30	0.50
30	-	-	33.82	0.34
15	-	-	16.42	0.22
10	11.50	0.10	11.22	0.18
7.63	8.48	0.08	8.53	0.16

Setpoint (sccm)	**MFC-3 (200 sccm N_2)**	**Calibration error (ccm)**	**MFC-4 (1000 sccm CH_4)**	**Calibration error (ccm)**
100	113.73	1.20	110.21	2.80
70	78.57	0.96	74.96	2.56
50	56.51	0.96	-	-
30	33.34	0.80	-	-
15	16.61	0.64	-	-
10	-	-	-	-
7.63	-	-	-	-

The flow rate measured using the bubble flow meter consistently were higher than the desired setpoint plus expected calibration error in all cases. Thus most cases showed flow rates above the calibration limits provided by Alicat Scientific Inc., the manufacturer of the MFCs. These results were not because the bubble flow meter results were at ambient conditions and the MFC setpoints are at STP. If the bubble flow meter results were changed from an ambient reading to STP, the flow rate would actually decrease. Edmonton ambient pressure is normally 92.9 kPa as recorded by Environment Canada during the years of 1971-2000 in the Station Data [61], and the building temperature is usually 22℃. Entering this into Equation (2.34), the equation becomes:

$$\dot{V}_{STP} = (\frac{298}{293})(\frac{92900}{101325})\dot{V}_{amb} = 0.93\dot{V}_{amb} \tag{2.35}$$

which suggests that the ambient volumetric flow rates will be 7% lower than the setpoints, which are measured at STP. The MFCs output to Labview of the actual volumetric flow rate data at ambient conditions confirmed this calculation. The percent composition or mole fraction using the inlet flow rate settings are calculated for N_2 and CH_4 using Equation (2.36)

$$x_{j,0} = \frac{\dot{V}_{j,0}}{\dot{V}_{T,0}} \tag{2.36}$$

where $\dot{V}_{j,0}$ is the inlet volumetric flow rate of species j, and $\dot{V}_{T,0}$ is the total volumetric flow rate in [m^3/s]. The bubble flow meter results were used in the calculations, and the results are shown in Figure 2.23. GC data points at 100 sccm and 10 sccm were compared to the bubble flow meter test results.

The percent composition of N_2 and CH_4 from the GC data agreed with the trends suggested by the bubble flow meter results for the 100 sccm setpoint. However the offset ratio from the GC was much larger than the 7.63 sccm setpoint MFC offset. This suggests that the GC discrepancy is more sensitive to calibration than MFC flow setpoints, because the trend between the GC datapoints at 100 sccm and 7.63 sccm show similar concentrations of CH_4 and N_2. For example, at 100 sccm, N_2 concentration is 51.2%, and at 7.63 sccm, N_2 concentration is at 51.8%, which are essentially the same. Conversely, for CH_4, the concentrations for these respective points are 48.8% and 48.2%. Thus the offset of the GC data from a 50-50% concentration ratio is essentially the same at both setpoints. However, the MFC data readings show that the percent composition should be closer to an even 50-50% concentration ratio at the lower setpoints. The N_2 mole fraction was above 0.5 in both GC measurements. The majority of the bubble flow meter results were above 0.5 for N_2, though the difference

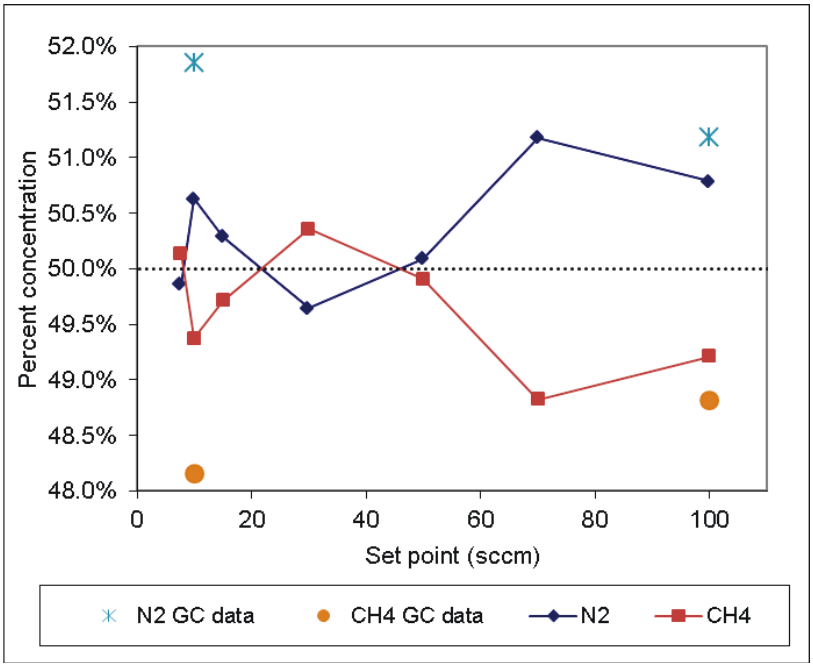

Figure 2.23 – Discrepancies in percent ratios of N_2 or CH_4 of the total flow rate as read by the bubble flow meter tests and GC data.

is largest at the 70 sccm and 100 sccm setpoints.

In summary, there were significant discrepancies between the bubble flow meter and the MFCs results. The GC data also suggested that there is a bias in the gas composition at the inlet. Because of the described discrepancy, the corresponding data from the bubble flow meter results were used as inlet parameters for this study rather than the setpoints themselves. These values are not at standard temperature and pressure because they were measured at ambient conditions.

2.6 Results and Discussion

Gas concentrations at steady state were measured for several experiments at steady state using the micro GC. Methane conversion was calculated for each experiment using Equation (2.21), assuming the idealized cracking reaction

$$CH_{4(g)} \xrightarrow{k} C_{(s)} + 2H_{2(g)} \qquad h_f^{\circ} = \text{-74.4 kJ/mol} \tag{2.37}$$

where $k = k_0 \exp\left(-\frac{Ea}{RT}\right)$. Deviation from this ideal reaction is discussed qualitatively in Section 2.6.1. Methane conversion and gas concentrations are also presented and discussed in this chapter. The blank reactor results are given in Section 2.6.2.

The molten metal reactor results are given in Section 2.6.3. All the data presented in this section is at steady state.

2.6.1 Carbon and hydrocarbon products

A gas chromatography-mass spectrometry analysis was performed by AITF on the hydrocarbon buildup on the inline filter shown in Figure 2.24(a). The powder was determined to contain polycyclic aromatic hydrocarbons, or polycyclic aromatic hydrocarbons, including naphthalene ($C_{10}H_8$), phenanthrene ($C_{14}H_{10}$), fluoranthene ($C_{16}H_{10}$) and pyrene ($C_{16}H_{10}$) and their isomers. The chromatogram is shown in Figure 2.24(b). Examples of carbon buildup on the injectors are shown in Figure 2.25. It was found that at the carbon build up on the injector was more flaky at temperatures equal to or lower than 1173 K. Carbon powder was formed at higher temperatures. Growths of carbon filaments were also noted on the reactor and injector walls.

Scanning electron microscopy was performed on various samples. Representative results are shown in Figure 2.26. It was found that at the lower temperatures, the carbon spheres ranged from 100 nm to 2 μm for the 1223 K sample. The carbon amalgamated together at the higher temperature of 1373 K. X-ray diffraction was performed on the flake and powder samples as well. It was found that the samples were composed of over 99% carbon [13].

2.6.2 Blank reactor

The results for the blank reactor experiments are discussed in two parts. The first is the gas concentrations as determined by the GC. The second is the calculated methane conversion. The data for CH_4 conversion was later used in Chapter 3 for determining the kinetic parameters.

2.6.2.1 Outlet gas concentrations

The concentration profiles at the outlet of the reactor with respect to operating temperature for each flow rate are presented in Figure 2.27. More hydrogen was produced at higher temperatures. Temperature has a large impact on steady state concentrations. Gaseous products of C_2H_2, C_2H_4 and C_2H_6 were negligible in all experimental cases, which agrees with equilibrium studies performed by Holmen et al. [5] on combustion of CH_4.

(a)

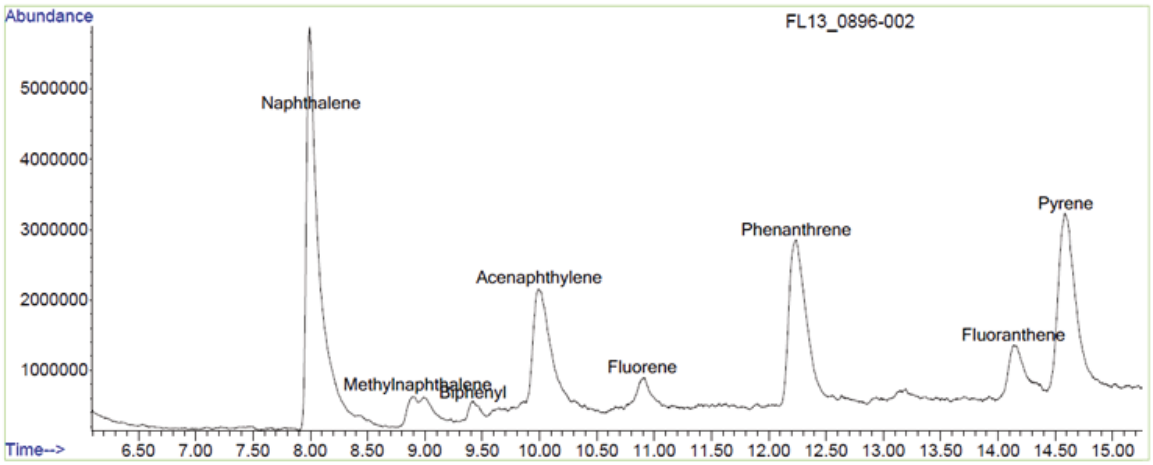

(b)

Figure 2.24 – Higher order hydrocarbon results for (a) buildup trapped in an inline filter, shown in (b) a gas chromatogram plot

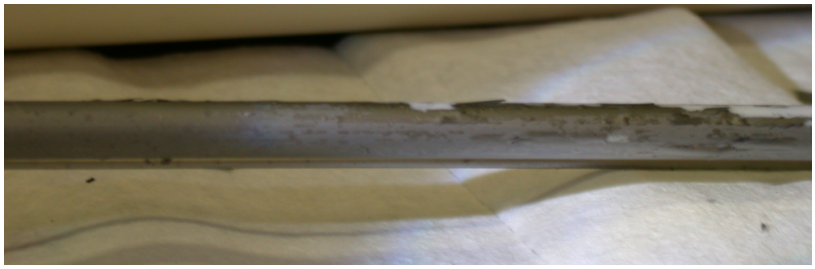

(a)

(b)

Figure 2.25 – Photos of (a) carbon flake buildup on a tube injector and (b) powder buildup on a tube injector

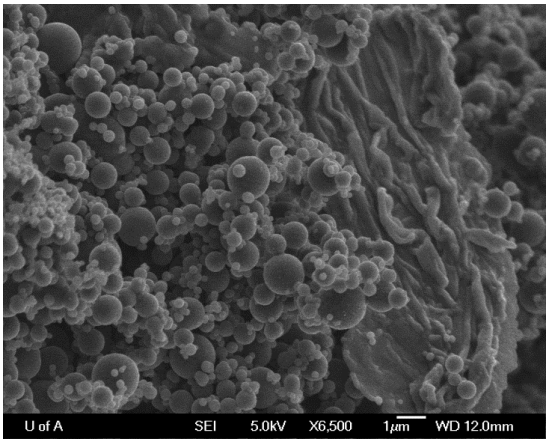

(a)

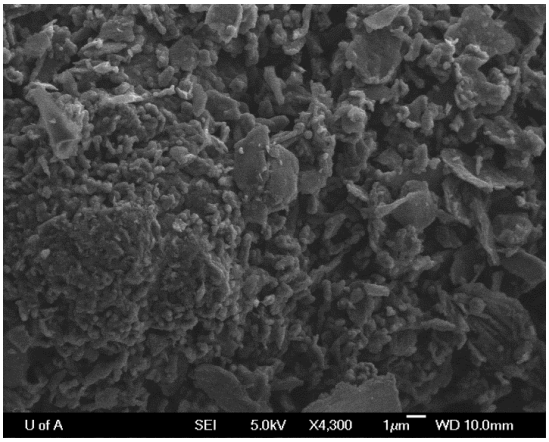

(b)

Figure 2.26 – SEM analysis for samples obtained from experiments at operating temperatures of (a) 1223 K and (b) 1373 K

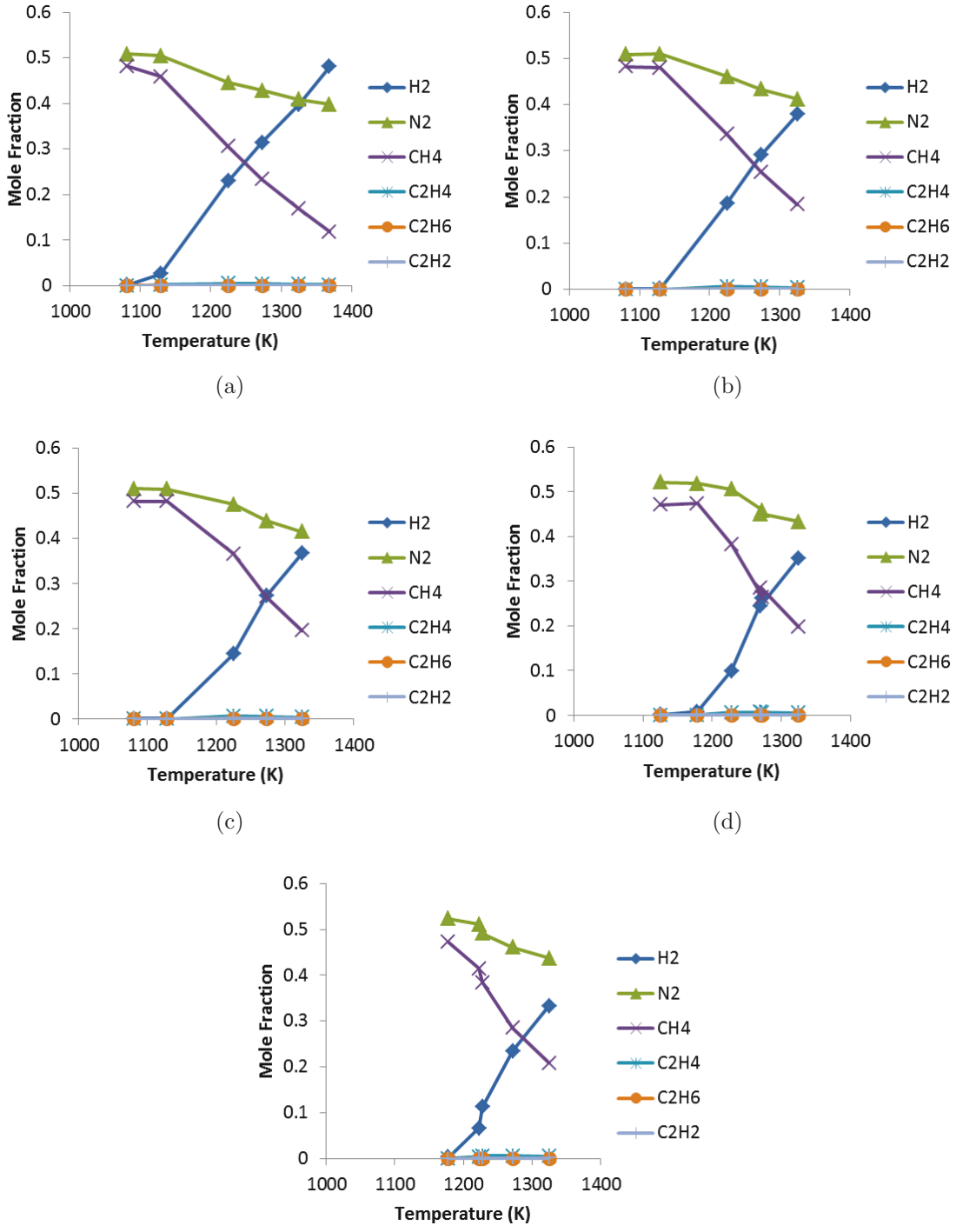

Figure 2.27 – Blank reactor outlet gas mole fractions for (a) 33 ccm, (b) 67 ccm, (c) 113 ccm, (d) 154 ccm, and (e) 224 ccm.

Comparisons of concentration profiles as they change with temperature or flow rate are shown in Figure 2.28. The plots on the left hand side show that temperature has a large impact on steady state concentrations. The plots on the right hand side suggest that flow rate has a small impact on steady state concentrations.

2.6.2.2 Replicas and repeatability

There were only two replicas for the blank reactor experiments. These were at 1273 K and 154 ccm, and at 1223 K and 224 ccm. The average values for CH_4, H_2 and N_2 concentrations and CH_4 conversion with the percent difference were calculated and are shown in Tables 2.7 and 2.8. The percentage difference in conversion amounts were calculated for each replica using

$$\text{Difference} = \frac{|X_{CH_4,1} - X_{CH_4,2}|}{X_{CH_4,1}} \times 100\% \tag{2.38}$$

where the subscripts 1 and 2 denote the respective replica. The percent difference for $T_0 = 1273$ K was 14.1%, and for the $T_0 = 1223$ K was 39.2%. The difference at $T_0 = 1223$ K is probably much larger because the the lower temperature yielded a relatively smaller conversion amount. At $T_0 = 1223$ K, the average conversion was 11.7% instead of the 33.1% obtained at 1273 K. Therefore differences in x_{CH_4} and x_{H_2} would have a much larger impact on the total conversion.

Also, these replicas were not true replicas, because they were performed at slightly different operating temperatures. The lower temperature tests were actually measured at 1223 K and 1228 K, respectively for replicas 1 and 2. The data at 1228 K showed higher CH_4 conversion of 13.6% rather than 9.8%. This may be due to a high sensitivity to temperature shown in the above analysis of blank reactor results in this section, though 5 K is a small difference. The replicas performed at the higher temperature had actual operating temperatures measured at 1272 K and 1270 K. The respective conversion for these temperatures were 35.6 % and 30.6%, which again suggests higher conversion for higher temperature, though 2 K is an even smaller temperature difference. It is probably that another unknown factor played a role in the difference of conversions. More replicas are required to develop a reliable analysis on repeatability and to ascertain whether temperature really was the major factor in differences of conversion.

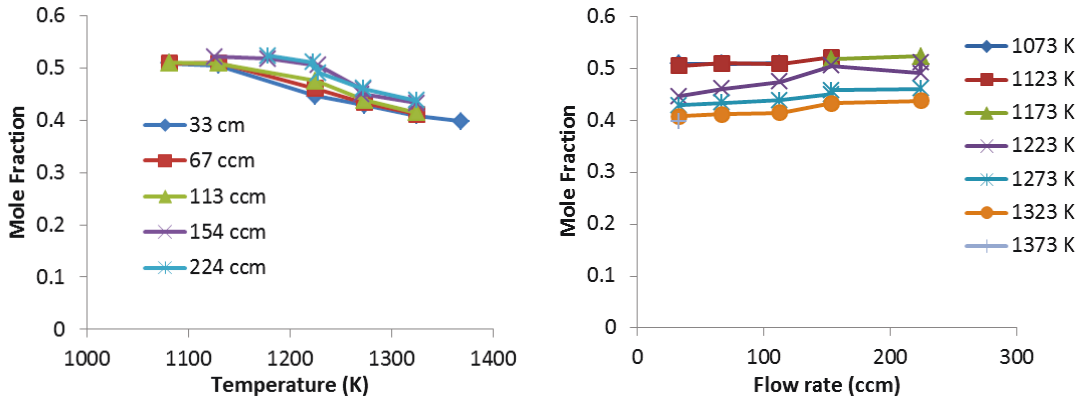

(a)

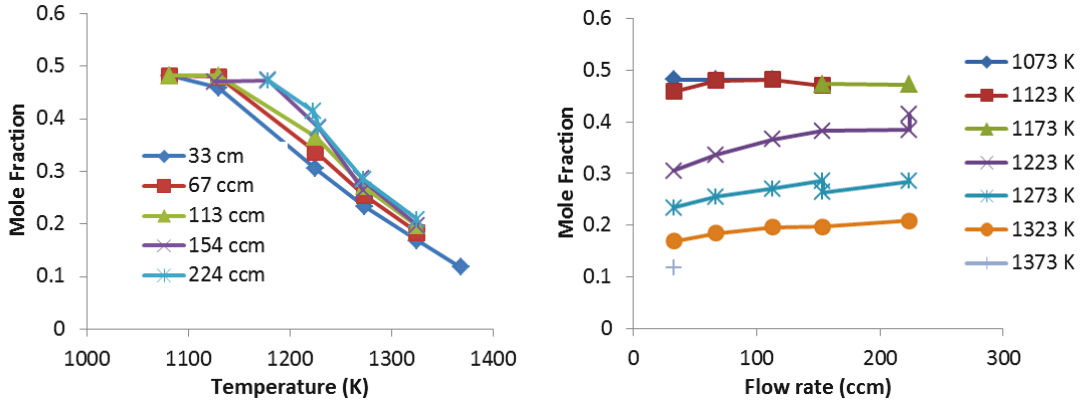

(b)

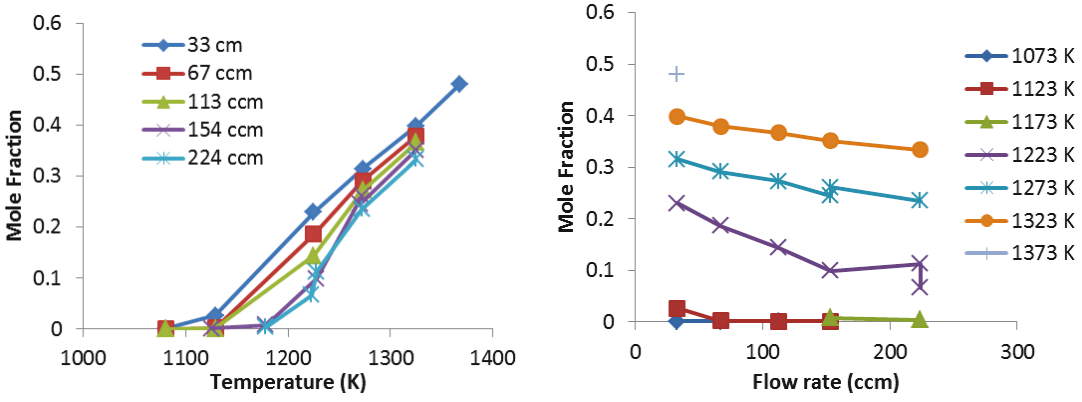

(c)

Figure 2.28 – Blank reactor outlet mole fractions for (a) N_2, (b) CH_4, and (c) H_2

Table 2.7 – Replica data for 1273 K and 154 ccm.

1273 K	x_{CH_4}	x_{H_2}	x_{N_2}	X_{CH_4}
Replica 1	0.264	0.261	0.458	0.356
Replica 2	0.286	0.244	0.450	0.306
Average	0.27	0.25	0.454	0.331
Difference (%)	8.33	6.24	1.77	14.1

Table 2.8 – Replica data for 1223 K and 224 ccm.

1223 K	x_{CH_4}	x_{H_2}	x_{N_2}	X_{CH_4}
Replica 1	0.414	0.066	0.511	0.098
Replica 2	0.384	0.113	0.491	0.136
Average	0.40	0.09	0.501	0.117
Difference (%)	7.24	69.9	3.91	39.2

2.6.2.3 Methane conversion

The results for CH_4 conversion for the blank reactor are shown in Figure 2.29. The profiles follow a similar pattern to the CH_4 concentration plot. Temperature had a large effect, with higher temperatures producing more conversion. Conversions as high as 64.8% for an operating temperature of 1373 K were observed.

Flow rate appeared to have little effect, even though lower flow rates consistently obtained higher conversions. In most cases, conversions were nearly leveled out at flow rates above 154 ccm. Zero conversion was calculated for experiments with operating temperatures below 1123 K and total flow rates above 33 ccm.

2.6.3 Molten metal reactor

The results for molten metal CH_4 cracking are discussed in this section. Each experiment was performed with a 20.3 cm bed of Sn. It was quickly found during molten metal experiments that zero conversion was obtained for all flow rates used in the blank reactor experiments. The flow rate was reduced to obtain results that showed conversion. The gas hourly space velocity (GHSV) using the heated section of the reactor to determine the blank reactor volume was used to compare molten metal cracking results with the blank reactor results. The GHSV for the blank and

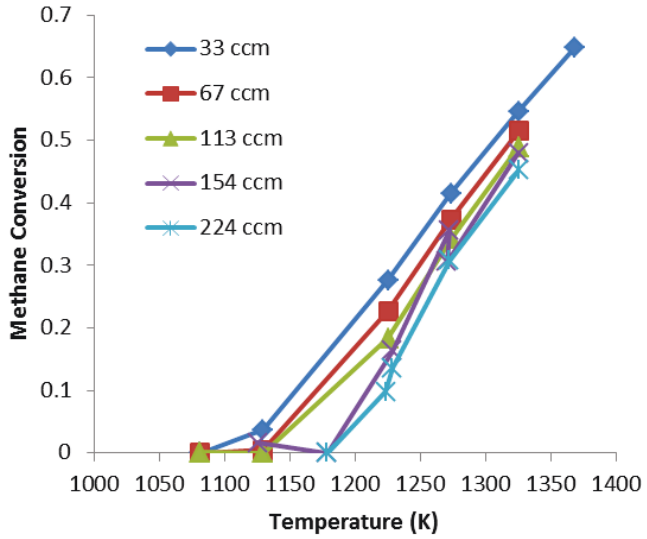

(a)

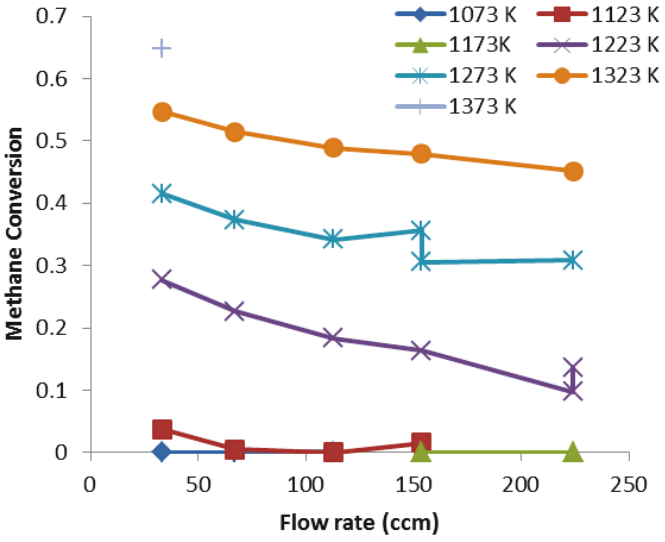

(b)

Figure 2.29 – CH_4 conversion in a blank reactor showing (a) temperature effects and (b) flow rate effects

molten metal reactors were calculated as follows. The volume of the molten bath in the reactor is defined as

$$V_{bath} = m_{bath}/\rho_{bath} \tag{2.39}$$

where m_{bath} is the mass of the molten media put into the reactor in [kg], and ρ_{bath} is the density of the molten bath at operating temperature in [kg/m^3]. The total blank volume of the reactor is

$$V_{r,blank} = \frac{1}{4}\pi D_{r,in}^2(L_H - \frac{D_{r,in}}{2}) + \frac{1}{12}\pi D_{r,in}^3 \tag{2.40}$$

where $D_{r,in}$ is the inner diameter of the reactor vessel in [m] and L_H is the heated length of the reactor, or the location at which the gas temperature drops below 1023 K, in [m]. The first term in Equation (2.40) is the cylindrical volume of the reactor minus the half-sphere closed end. The second term in Equation (2.40) is the volume of the half-sphere closed end. The empty volume of the molten metal reactor was calculated by

$$V_{r,bath} = V_{r,blank} - V_{bath} \tag{2.41}$$

The GHSV is defined as

$$\text{GHSV} = \frac{\dot{V}_{T,0}}{V} \tag{2.42}$$

where $V_{T,0}$ is the total volumetric flow rate in [m^3/hr], V is the volume of the respective GHSV, given by Equations (2.40) or (2.41).

The experiments were originally planned to range from 1023 K to 1373 K. As such, the GHSV corresponding to the mid-range temperature of 1273 K was chosen to calculate the reduced flow rate for molten metal experiments. The length at which the temperature dropped below 1023 K was $L_H = 26.6$ cm, using the blank reactor temperature profile data measured in Section 2.3. No experimental temperature profile data was available for the space above the molten metal. The portion of the blank reactor below 20.4 cm was approximately isothermal, and the bath height was calculated to be 20.3 cm. Therefore it was assumed that the blank reactor temperature profile measured in Section 2.3 was still applicable to the molten metal reactor. It was found that a total flow rate setpoint of 17 ccm for the molten metal experiments would match the GHSV of the blank reactor experiments at 67 ccm using a reactor volume with $L = L_H$. Thus with the original tests at 154 ccm, this provided two different flow rate levels at which the molten metal experiments were tested at for the tube injector. The corresponding GHSVs to these flow rates were calculated to be 24.75 hr^{-1} and 21.07 hr^{-1} for the blank and molten metal reactors at 154 ccm, and

9.07 hr^{-1} for the blank and molten metal reactors at 17 ccm. The quartz injector experiments were later performed at 17 ccm only.

2.6.3.1 Outlet gas concentrations

The gas concentrations at the reactor outlet are given in Figure 2.30. A very slight increase in H_2 concentration occurred as the temperature increased. However, the only experiment that obtained notable H_2 concentration was at 1273 K for the tube injector, shown in Figure 2.30(b). Otherwise the mole fraction of H_2 and other gaseous components remained below 0.01.

2.6.3.2 Methane conversion

The methane conversion results are shown in Figure 2.31. From the above GHSV analysis, the 67 ccm blank and the 17 ccm molten metal reactors should have been similar. However, it was found that these reactors had conversions of 37.3% and 18.9% at 1273 K, respectively. The quartz injector molten metal reactor obtained 1.1% conversion with 17 ccm total flow rate at 1173 K.

Comparison of CH_4 conversion with Serban et al. [2] is shown in Figure 2.32. All data points in Figure 2.32 were performed in Sn with the exception of the 'Serban 2 ccm, tube + Pb data'. It is difficult to compare the results directly because Serban et al.'s experimental apparatus is not fully described in the paper. For example, the actual heated volume in the authors reactor is not given, nor is the height of the 1.27 cm cup that contained the molten metal in the reactor vessel. Serban et al.'s reactor vessel was 35.56 cm long by 2.54 cm OD. Also, Serbian et al.s results are for a 10.2 cm bath. The results from the molten metal experiments contained in this thesis would have been higher due to the additional approximate 26.4 cm of heated blank volume if a 10.2 cm bath height was used instead 20.3 cm. Regardless, the GHSVs studied in this thesis for the reactor at the low flow rates are lower than those reported by Serban et al. The GHSVs in Serban et al. [2] were 18 and 133 hr^{-1} for flow rates of 2 sccm and 15 sccm, respectively. The GHSVs in this thesis were 9.07 hr^{-1} for 17 ccm. The GHSV is 1.94 hr^{-1} if the entire reactor length is used and not just the heated length, L_H.

From the above analysis, it is reasonable to assume that the experimental setup in this thesis provided longer overall residence times, including bubble residence time and blank reactor residence time, than that in Serban et al.'s. Therefore the conver-

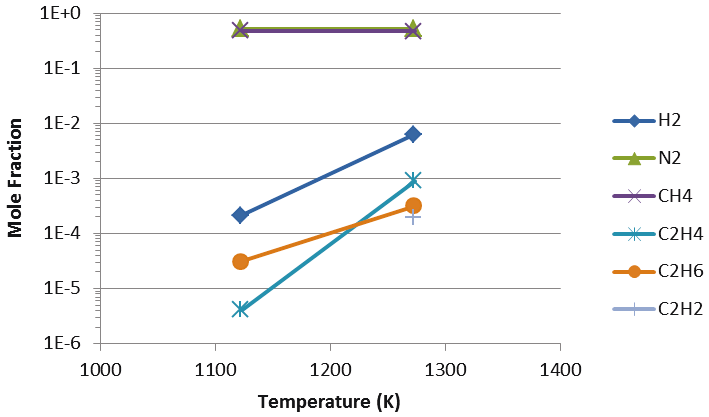

(a)

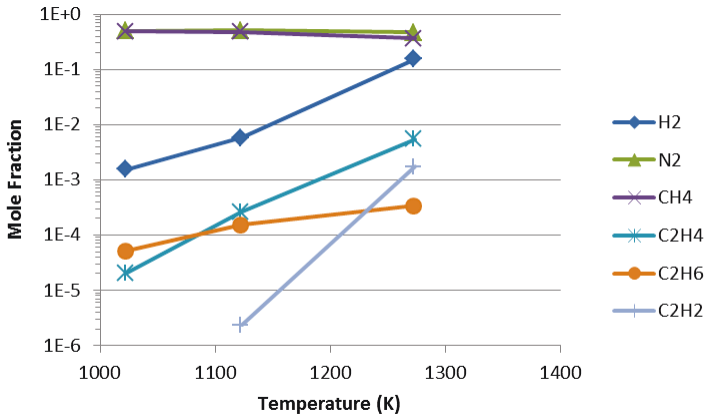

(b)

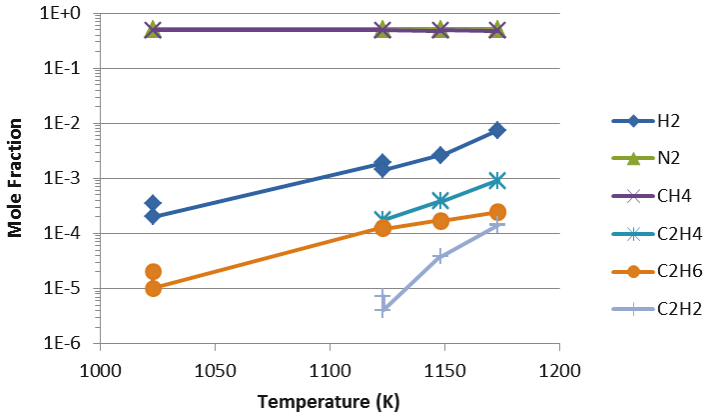

(c)

Figure 2.30 – Molten metal reactor outlet mole fractions for (a) 6 mm tube injector at 154 ccm, (b) 6 mm tube injector at 17 ccm, and (c) 4-10 μm quartz injector at 17 ccm

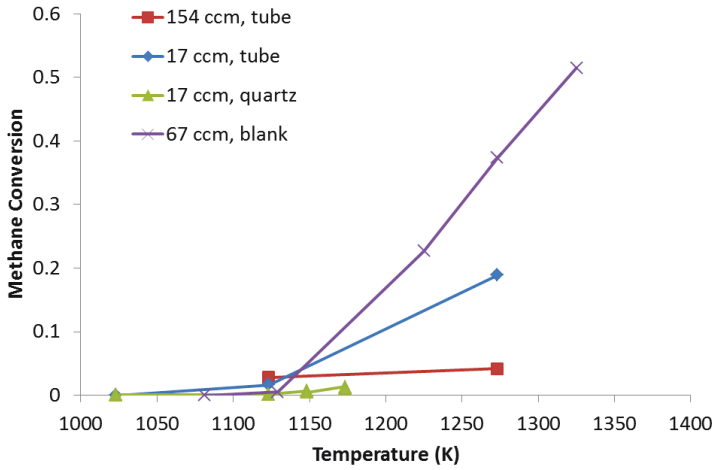

Figure 2.31 – CH_4 conversion in a molten metal reactor compared to the 67 ccm blank reactor results.

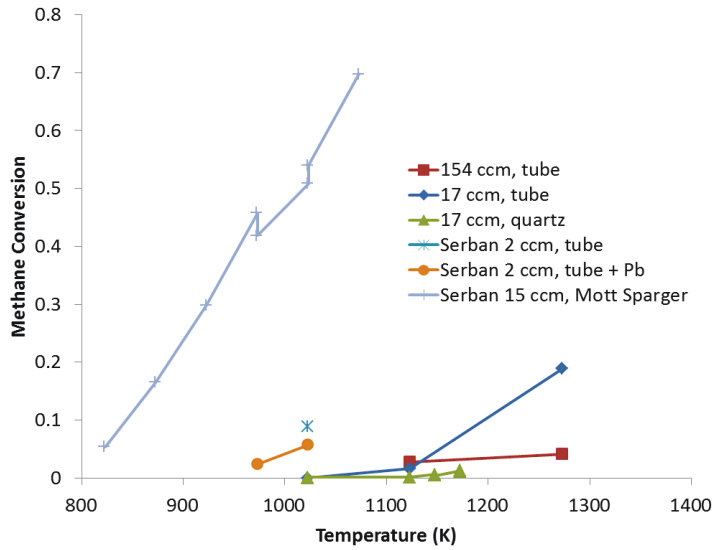

Figure 2.32 – Comparison of CH_4 conversion to Serban et al. [2] results.

sions obtained in this study should also be larger. However, the results are grossly opposite. As can be seen in Figure 2.32, all of Serban et al.'s results are larger than those measured in the current experiments.

The reactor used by Serban et al. was made of 304 SS. X-ray diffraction analysis showed that iron carbide existed in the sample scraped from the reactor wall [2]. It may be that the SS reactor catalyzed the reaction that occurred in Serban et al.'s apparatus. One theory is that the 1.27 cm molten metal cup with the 0.64 cm injector tube attached to the Mott sparger provided an ideal setting in which very small bubbles were formed and attached to the surface of the reactor. Furthermore, the limited space in the cup with the injector in place would enhance interaction between the bubbles and the cup surface. The interaction would increase catalytic effect of the 304 SS walls on CH_4 conversion. The open bore 0.64 cm injector would still facilitate some bubble attachment to the reactor wall, but not as much due to the larger bubble size. This may explain the huge effect of the injector type on CH_4 conversion.

In the setup described in Section 2.1 in this thesis, the reactor vessel is made of Al_2O_3, which would not facilitate a chemical reaction with CH_4. Furthermore, the inner diameter of the reactor vessel is 4.4 cm, which is 3.5 times larger than the outer diameter of the cup in Serban et al.'s study. The larger diameter would decrease the likelihood of bubble interaction with the walls, as having bubbles attach would increase the residence time of the bubbles as well.

The purpose of this study was to investigate the feasibility of the molten metal CH_4 cracking reactor with the majority of the reaction occuring in the molten metal. Therefore it was attempted to minimalize the amount of conversion that would happen in the blank space above, without allowing the molten Sn to freeze on the reactor walls if it splashed too high in the cold zone. In order to upscale the resulting conversions from this study to larger reactors, the molten metal reactor is studied numerically in Chapter 4. The amount of conversion occuring in the bath compared to overall conversion is estimated, and key parameters such as bubble size, bath height, and temperature are analyzed.

2.6.3.3 Replicas and repeatability

The quartz injector with molten metal experiments were performed with one replicate. Both sets of experiments showed negligible difference in results. No replicas were performed for the tube injector molten metal experiments.

Chapter 3

Kinetics

Three models of ideal reactors are presented in this section. These are the perfectly mixed reactor (PMR), the perfectly mixed reactor combined with a bypass to simulate a bypass (CPMR), and the plug flow reactor (PFR). The PMR and CPMR models are zero-dimensional, while the PFR model is 1D. However, the PFR model is derived such that CH_4 conversion at the outlet of the reactor is numerically solved. First, the general assumptions are provided, as well as model-specific assumptions. The governing equations are then derived, and the methodology for determining the kinetic parameters is presented. The derivations for the PMR and PFR are based from Fogler [62]. Finally, the resulting kinetic parameters of the CH_4 cracking reaction are given with a discussion on the results.

3.1 Assumptions

General assumptions

The general assumptions applicable to all three ideal models are as follows.

- Methane conversion follows the idealized reaction

$$CH_{4(g)} \xrightarrow{k} C_{(s)} + 2H_{2(g)} \quad h_f^\circ = -74400 \text{ J/mol} \tag{3.1}$$

  where all methane converted turns into H_2 and C. The heat of reaction at 298 K and 1 atm is given by [55], and was obtained from the enthalpy of formation for CH_4 directly because C and H_2 are at their reference states. Other byproducts are assumed to be negligible.

- The reaction rate is first order and follows the Arrhenius equation,

$$k = k_0 \exp\left(-\frac{Ea}{RT}\right)$$

- The reaction that occurs in the injector is negligible (see Section 3.1.0.4 for verification).
- The reaction and product gases are ideal.
- The reaction gas properties are as given in Appendix A.
- The reaction gases at the inlet are perfectly mixed.
- The reactors operate at steady state.
- The pressure drops due to, for example, friction, viscous effects, entry effects or pipe losses are negligible.
- The system is isobaric and at atmospheric pressure.
- The temperature in the reactor is isothermal. An effective temperature is used to compensate for the non-uniform temperature profile (discussed further in Section 3.1.1).
- The gas and wall temperatures are equal, and radiation effects are negligible (see Section 2.5.1).

PMR assumptions

The assumptions relating only to the PMR are as follows

- The gas is perfectly mixed all through the reactor.
- The reaction rate occurs uniformly throughout the reactor.

CPMR assumptions

The assumptions relating only to the PMR are as follows

- The same assumptions as those for the PMR above, with the exception that a portion of the gas escapes the reactor without reacting due to the high buoyancy effects (described further in Section 3.2.2).

PFR assumptions

The assumptions relating only to the PFR are as follows

- No back mixing occurs.
- The concentration and reaction rates vary axially only.

3.1.0.4 Verification for neglecting injector reaction effects

The nominal holding time or mean residence time for a reactor is given by

$$\tau = \frac{V}{\dot{V}_0} \tag{3.2}$$

where V is the volume and $\dot{V}_0$ is the inlet volume flow rate in [m^3/s]. Thus τ becomes for the injector and reactor, respectively

$$\tau_I = \frac{V_I}{\dot{V}_0} \tag{3.3}$$

$$\tau_r = \frac{V_r}{\dot{V}_0} \tag{3.4}$$

Dividing Equation (3.3) by Equation (3.4) and simplifying, the ratio of nominal holding times between the injector and reactor is

$$\frac{\tau_I}{\tau_r} = \frac{V_I}{V_r} \tag{3.5}$$

The volume of space in the injector and for the reactor tubes are defined respectively as

$$V_I = \frac{\pi}{4} D_{I,in}^2 L \tag{3.6}$$

$$V_r = \frac{\pi}{4}(D_{r,in}^2 - D_{I,out}^2)L \tag{3.7}$$

where $D_{I,in}$ and $D_{r,in}$ are the inner diameters of the injector and reactor in [m], $D_{I,out}$ is the outer diameter of the injector tube in [m], and L is the heated length of the reactor, also in [m]. The area of the reactor is found by subtracting the cross-sectional area of the injector from the reactor area. Substituting Equations (3.6) and (3.7) into Equation (3.5) and then simplifying, the following final relation for the ratio of nominal holding times is

$$\frac{\tau_I}{\tau_r} = \frac{D_{I,in}^2}{D_{r,in}^2 - D_{I,out}^2} \tag{3.8}$$

The inner and outer diameters of the injector are 0.00318 m and 0.00635 m, respectively. The inner diameter of the reactor is 0.04445 m. Substituting this in gives

$$\begin{aligned} \frac{\tau_I}{\tau_r} &= \frac{(0.00318)^2}{(0.04445)^2 - (0.00635)^2} \\ &= 0.00522 \end{aligned}$$

In summary, the ratio of nominal holding times between the injector and the reactor is approximately 0.5%. Therefore the phenomena happening in the injector was considered negligible.

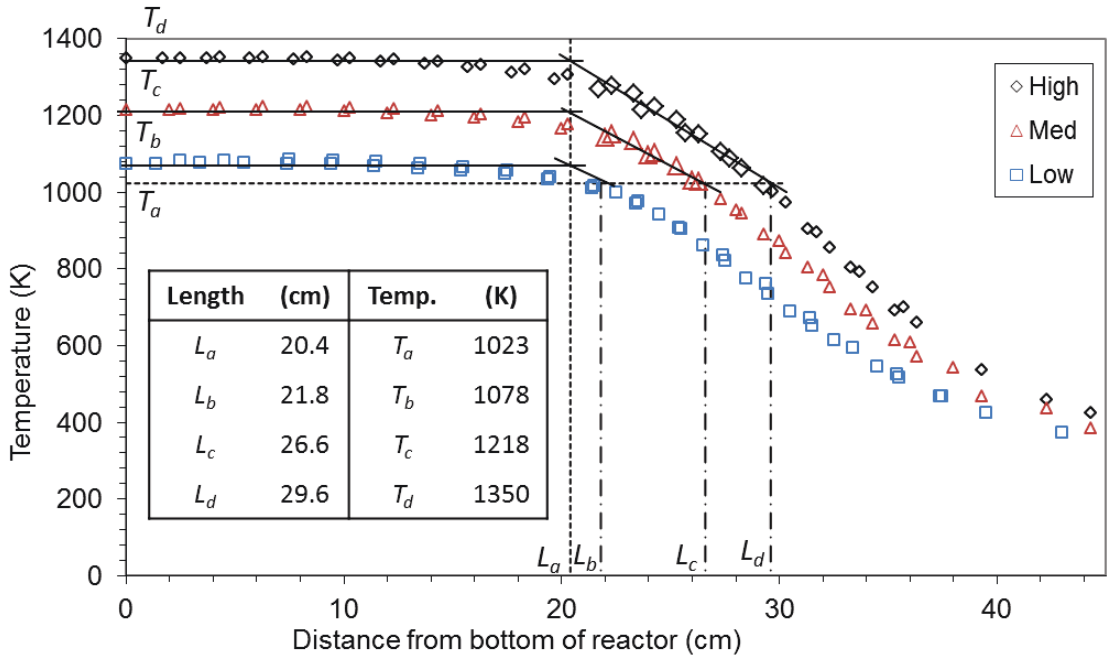

Figure 3.1 – Graphical method of determining equation for averaging the temperature over the length of the reactor.

3.1.1 Effective temperature calculation

The constant temperature assumption in this study required that an effective temperature be used. A similar approach to Olsvik et al. [18] and Eisenberg and Bliss [22] was used. No noticeable reaction occurred below $T_a = 1023$ K, and so the section of reactor below this temperature was not included in the averaging. Figure 3.1 shows the actual temperature profiles for various temperature setpoints and locations. The temperature profile was previously determined in Section 2.3.

Lengths L_a, L_b, L_c, and L_d, correspond to the location at which the linear portion of the temperature change is assumed to begin, and where the linear portions end for the high, medium and low temperatures, respectively. Temperature T_a represents the boundary temperature below which no reaction is assumed to occur. T_b, T_c, T_d represent the low, medium and high isothermal temperatures for the experimentally measured profiles, respectively. The corresponding lengths and temperatures are labeled and defined in Figure 3.1. Two key assumptions for the assumed temperature profiles are that 1) all linear temperature profiles between L_a and L_d have the same slope, and 2) all lengths at which each operating temperature curve drops to 1023 K can be linearly interpolated between L_a and L_d. Essentially, it is assumed that the operating temperatures are horizontal, or isothermal, prior to L_a, and linearly

decreasing after L_a until the temperature drops below 1023 K.

The length at which the temperature curve drops below 1023 K, or the heated length L_H, is found using the following

$$L_H(T_0) = (T_0 - T_b)\frac{\partial L}{\partial T} + L_b \tag{3.9}$$

where $\frac{\partial L}{\partial T}$ is the slope of the temperature profile that descends from the isothermal temperature to the lower boundary temperature, T_a. $\frac{\partial L}{\partial T}$ can be approximated linearly as $\frac{(L_d - L_b)}{(T_d - T_b)}$, which gives

$$L_H(T_0) = (T_0 - T_b)\frac{(L_d - L_b)}{(T_d - T_b)} + L_b \tag{3.10}$$

where T_0 is the setpoint operating temperature of the reactor. The equation for the operating temperature curve is given as

$$T(z) = \begin{cases} T_0 & \text{if } z < L_a \\ T_0 + \left(\dfrac{T_a - T_0}{L_H - L_a}\right)(z - L_a) & \text{if } z \geq L_a \end{cases} \tag{3.11}$$

where z is the distance measured from the bottom closed end of the reactor, located deepest inside the furnace. Finally, the effective temperature is found by

$$k_0 \exp\left(\frac{E_{a,eff}}{RT_{eff}}\right) L_H = \int_0^{L_H} k_0 \exp\left(\frac{E_a}{RT}\right) dz \tag{3.12}$$

or, taking k_0 out of the integral and canceling,

$$\exp\left(\frac{E_{a,eff}}{RT_{eff}}\right) L_H = \int_0^{L_H} \exp\left(\frac{E_a}{RT}\right) dz \tag{3.13}$$

The activation energy, $E_{a,eff}$ was set to 390 kJ/mol to reflect values for homogeneous CH_4 cracking found in literature [1, 18, 19, 21]. T_{eff} was solved for numerically using MATLAB built-in functions. `quadl()` solved the integral on the RHS. `fsolve()` was used then solve for T_{eff}. The results for the effective temperature corrections are in Figure 3.2. The largest difference between T_{eff} and T_0 was 13 K for the highest experimental operating temperature of 1350 K. The difference becomes 18 K if the operating temperature is extrapolated to 1400 K.

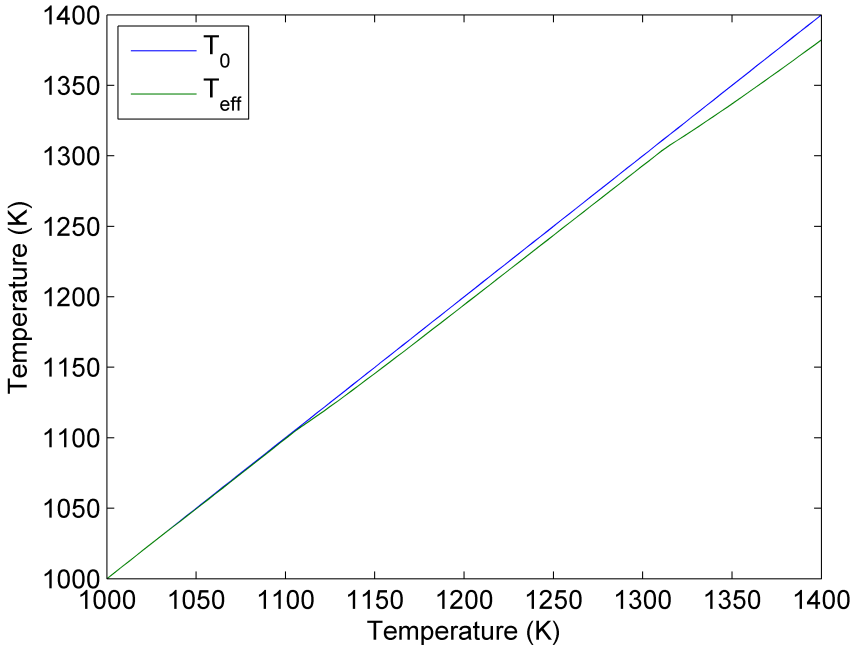

Figure 3.2 – Difference between effective temperature and operating temperature in the blank reactor

3.1.2 Temperature driven buoyancy mixing effects

In this section the assumption that the reactor can be assumed to be perfectly mixed due to thermal buoyancy effects is verified using the Rayleigh number, Ra. The critical value at which natural convection becomes turbulent for an enclosure is $Ra_c \simeq 3 \times 10^5$ as given by Cengel [55], or $Ra_c \simeq 5 \times 10^4$ by Incropera et al. [63]. The temperature profiles and dimensions used in this section are shown in Figure 3.1 in Section 3.1.1. The Ra number for an ideal gas is given by

$$Ra(L) = \frac{g c_p \rho^2 L^3}{\gamma_g \mu} \frac{(T_{hot} - T_{cold})}{T} = \frac{g c_p \rho^2 L^3}{\gamma_g \mu} \frac{\Delta T}{T} \tag{3.14}$$

where L is the characteristic length, T_{hot} is the hot temperature, and T_{cold} is the cold temperature. The gas properties are determined at a mean temperature of $T = (T(z) - T_{cold})/2$. It is shown below that flow velocity due to temperature differences is scaled by

$$U = \sqrt{g \frac{\Delta T}{T} L} \tag{3.15}$$

Thus the Ra number is proportional to the square of the scaled velocity. Separating terms, Ra can also be described as

$$Ra(L) = \frac{c_p \rho^2 L^2}{\gamma_g \mu} g \frac{\Delta T}{T} L = \frac{c_p \rho^2 L^2}{\gamma_g \mu} U^2 \tag{3.16}$$

The Peclet number, Pe, and Reynolds number, Re, are described as [64]

$$Pe = \frac{\rho U L}{\alpha_{thermal}} = \frac{\rho U L c_p}{\gamma} \tag{3.17}$$

$$Re = \frac{\rho U L}{\mu} \tag{3.18}$$

where $\alpha_{thermal}$ is the thermal diffusivity of the material. Substituting in Equations (3.17) and (3.18) into Equation (3.16), the Ra can be reduced to

$$Ra(L) = RePe \tag{3.19}$$

In summary, the capability of the Ra to predict turbulent mixing is because it is proportional to Re. For the reactor studied in this thesis, Ra becomes

$$Ra(z) = \frac{g c_p \rho^2 (L_r - z)^3}{\gamma \mu} \frac{(T(z) - T_{cold})}{T} \tag{3.20}$$

where $g = 9.81$ m/s^2 is the acceleration of gravity, c_p is the specific heat capacity of the gas, ρ is gas density, γ is gas thermal conductivity, μ is dynamic viscosity of the gas, and z is the location from which the $Ra(z)$ number is being determined, as measured from the bottom (hottest) portion of the reactor to the uppermost or cold portion of the reactor. Also, the critical length is $L = L_r - z$, where L_r is the length of the reactor. z ranges from 0 to L_a, which represents the isothermal operating temperature zone. $L_a = 0.204$ m, previously defined in Section 3.1.1, is the point at which the isothermal operating temperature begins to linearly decline. $T(z)$ is the corresponding profile temperature at z, and was experimentally determined in Section 2.3. T_{cold} is the temperature at the cold section of the reactor. The geometry definitions for calculating the Ra are shown in Figure 3.3.

The experimental determination of the temperature profile did not include a temperature at the reactor cap assembly. T_{cold} is assumed to be 373 K. As seen in Figure 3.1, the temperature dropped to at least 373 K in the $T_0 = 1078$ and 1218 K temperature profiles. For $T_0 = 1350$ K, the assumption of $T_{cold} = 373$ K was considered plausible if (1) the 304 SS cap has a large thermal conductivity, thereby providing high conductive heat transfer, and (2) the convective heat transfer from the gas inside the reactor to the cap is sufficiently large.

The thermal conductivity of 304 SS is 14.9 W/(m·K) at 300 K [55]. In comparison, the thermal conductivity of H_2 is two orders of magnitude less, at approximately

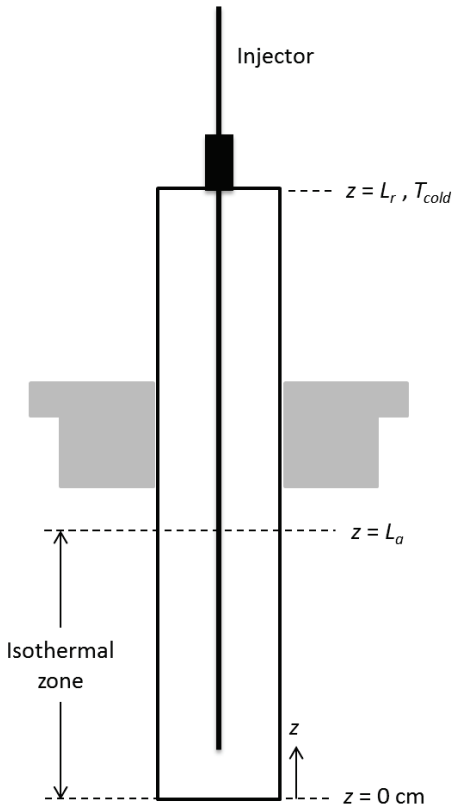

Figure 3.3 – Geometry and method of calculating Ra for the reactor

0.18 W/(m·K) at 300 K [55]. H_2 is the most conductive of the gases considered in the reactor. Second, it is also shown below that Ra_c is surpassed, and as such the gas flow inside the reactor is most likely turbulent and has a high convective heat transfer from the gas to the cap. Therefore, it was assumed that the gas inside the reactor at the reactor cap was at the same temperature as the surface of the cap outside the reactor.

The assumption is further justified by the following two observations: (1) the snoop soap did not boil when checking for leaks at the reactor cap, and (2) the cap was at a low enough temperature that it could be touched by hand without burning.

The results for Ra are presented in Figure 3.4. $T(z)$ and T_{cold} for 1350 K and 1078 K are shown on the right-hand side in Figures 3.4(a) and 3.4(b), respectively. The resulting Ra values are shown on the left-hand sides in Figures 3.4(a) and 3.4(b). Minimum values of $Ra = 1.54 \times 10^7$ and $Ra = 2.38 \times 10^7$ were obtained for $T_0 = 1350$ K and $T_0 = 1078$ K, respectively. Therefore, $Ra_c = 3 \times 10^5$ [55] was exceeded in both cases and it was verified that turbulent mixing was most likely occurring inside the reactor.

It was shown above that turbulent mixing is occurring inside the reactor. The next step is to determine the extent of the mixing occurring inside the reactor. Linden suggested that buoyancy forces are described in terms of reduced gravity, and gave the following for defining the reduced gravity [52]

$$g' = g\frac{\Delta\rho}{\rho} = g\frac{\Delta T}{T} \tag{3.21}$$

where g is the acceleration of gravity, and $\frac{\Delta T}{T}$ is the fractional change in the fluid where T is in units of K. The source of this equation can be derived using Newton's second law accounting for the buoyancy force due to temperature differences in a control volume and its weight. Viscous or drag effects were assumed to be negligible in this derivation. Then,

$$dF_b - dF_w = \frac{d\overline{u}}{dt}dm \tag{3.22}$$

where $\overline{u}$ is the average velocity of the gas in the control volume, and $dm = \rho_{hot}dV$ is the mass of the control volume. ρ is the density of the control volume measured at a reference temperature of $T = (T_{hot} + T_{cold})/2$, and dV is the volume of the control volume. dF_B and dF_W are the buoyancy and weight forces, given as

$$dF_b \;=\; \rho_{cold}gdV \tag{3.23}$$

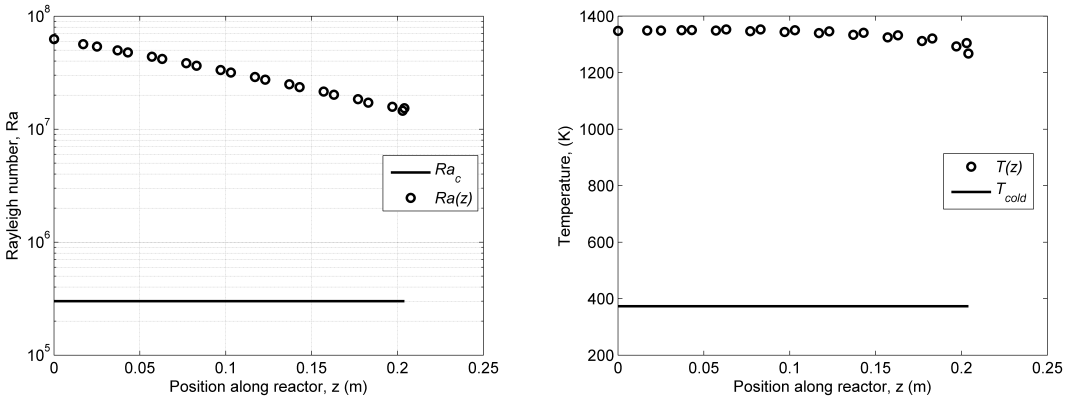

(a)

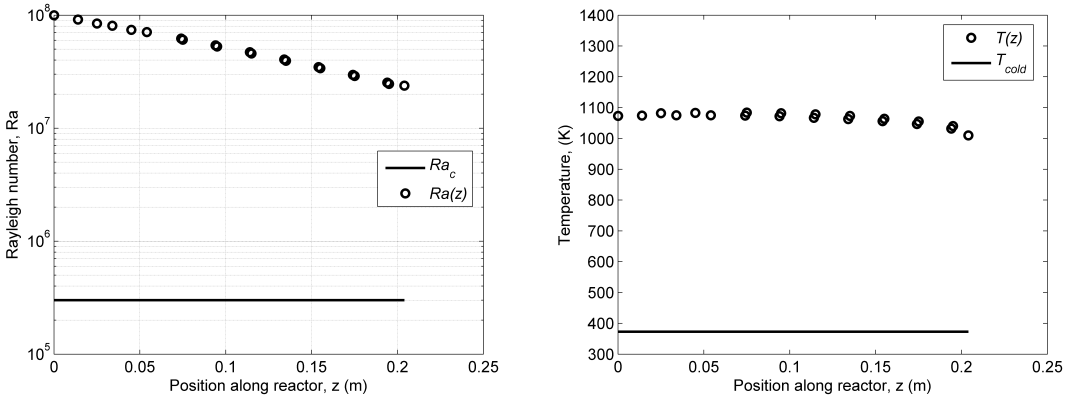

(b)

Figure 3.4 – Results for the *Ra* analysis of the reactor using experimental temperature profile data for operating temperatures of (a) 1350 K and (b) 1078 K.

$$dF_w = \rho_{hot} g dV \tag{3.24}$$

where ρ_{cold} is the density of the cold gas,ρ_{hot} is the density of the hot gas, and g is the acceleration of gravity, Substituting in Equations (3.23) and (3.24), and canceling dV,

$$\rho_{cold} g - \rho_{hot} g = \rho \frac{d\overline{u}}{dt} \tag{3.25}$$

Simplifying,

$$\frac{d\overline{u}}{dt} = g' = g\frac{\Delta\rho}{\rho} \tag{3.26}$$

$\frac{\Delta\rho}{\rho}$ can be assumed to be [53, 54]

$$\frac{\Delta\rho}{\rho} = -\omega\Delta T \tag{3.27}$$

where ω is the thermal expansion coefficient. ω is defined as

$$\omega = -\frac{1}{\rho}\left(\frac{\partial\rho}{\partial T}\right)_P \tag{3.28}$$

which reduces to $1/T$ for an ideal gas [54]. Thus,

$$\frac{\Delta\rho}{\rho} = \frac{\Delta T}{T} \tag{3.29}$$

and

$$g' = g\frac{\Delta\rho}{\rho} = g\frac{\Delta T}{T} \tag{3.30}$$

which is the same as (3.21). The reduced gravity term, g', can be used to determine the scale of the velocities inside the reactor. Linden [52] stated that velocity scales as follows for reduced gravity-driven flows

$$U = \sqrt{g'L} \tag{3.31}$$

where L is the characteristic vertical length scale over which the temperature difference is experienced, measured from the top (open end) of the reactor. The cold temperature at the capped end of the reactor, $z = L_r$, is assumed to be at least 373 K using the same arguments earlier in this section. The characteristic length scale is assumed to be

$$L = L_r - L_a = 0.508 \text{ m} - 0.204 \text{ m} = 0.304 \text{ m} \tag{3.32}$$

L_a is the length at which the temperature of the reactor begins to linearly decrease from the isothermal temperature zone, as explained previously in this section.

Table 3.1 – Tabulated velocity scaling for various operating temperatures

Operating Temperature (K)	g' **(m/s²)**	U **(m/s)**	$\overline{u}$ **(m/s)**
1078	6.4	1.70	0.0079
1218	6.8	1.78	0.0090
1350	7.1	1.84	0.0099

It was also necessary to calculate the average velocity of the gas flow in the reactor to determine if the forced gas flow would be significant compared to the scaled velocities of the buoyant flows. The average velocity of the flow due to forced flow from the gas injected into the reactor is given by

$$\overline{u} = \frac{\dot{V}}{A_c} \tag{3.33}$$

where A_c is the cross-sectional area of the annular spaces in the reactors. The gas flow rate, $\dot{V}$, was corrected to volumetric flow at operating temperature and pressure. The results are given in Table 3.1.

Buoyancy forces yield scaled gas velocities of 1.7 m/s to 1.8 m/s. The average velocities are three or two orders of magnitude less at 0.0079 m/s to 0.0099 m/s. Therefore the effects due to buoyancy are very significant. The length of the reactor is 0.508 m, and the mean residence time in the entire blank reactor is approximately $V_{reactor}/\dot{V} = 67$ s. The high residence time coupled with the relatively large scaled velocity to the reactor length therefore allow the reactor to be perfectly mixed. Based on this finding, in conjunction with the finding that turbulent mixing was indeed occurring in the reactor due to the Ra exceeding the critical value, it was assumed that the reactor was perfectly mixed. However, in this thesis the PFR model was still derived for comparison of results.

It was found in the literature review in Section 1 that high temperature differences exist in most high temperature CH_4 cracking reactors. However, very little work dealing with incorporating buoyancy effects into high temperature CH_4 cracking models is reported in the literature. Only two authors included buoyancy effects in a 3D reactor model, Ozalp and Jayakrishna [44] in 2010 and Costandy et al. [51] in 2012. The impact of the buoyancy terms on fluid flow or mixing however was not discussed in either paper. The lack of buoyancy effects in most literature models may be due to the studies in literature being performed at higher flow rates with smaller

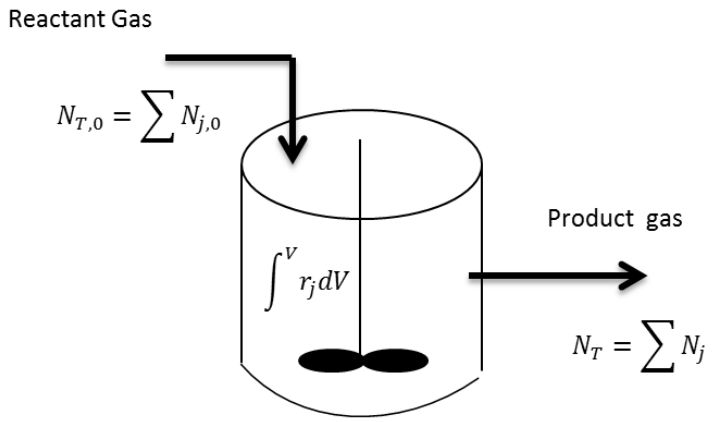

Figure 3.5 – Graphical representation of a perfectly mixed reactor

cross-sectional areas, thus increasing the effect of forced convection over natural convection. Hirsch and Steinfeld [33] studied a reactor that utilized a vortex flow to create a cyclone effect. The cyclone or tornado effect was designed to reduce carbon deposition on the quartz window by means of creating a pressure gradient that would pull the carbon particles away from the window and down into the reactor. The authors do not analyze the effects of buoyancy, however they do mention that carbon deposition became a problem due to buoyancy effects during runs where the reactor was mounted vertically.

3.2 Mathematical modeling of ideal reactors

3.2.1 Perfectly mixed reactor

The general chemical equation used for this derivation is

$$aA \rightarrow bB + cC \tag{3.34}$$

with the stoichiometric coefficients a, b, and c normalized by a as follows

$$\nu_A a+ \rightarrow \nu_b B + \nu_c C \tag{3.35}$$

where

$$\nu_a = -1, \quad \nu_b = \frac{b}{a} \quad \text{and} \qquad \nu_c = \frac{c}{a}$$

It is assumed that the forward reaction only occurs, and that the reverse reaction rate kinetic parameters $E_{a,r}$ and $k_{0,r}$ are insignificant. Furthermore, the forward kinetic rate parameters E_a and k_0 are fitted to the experimental data, and so reflect

the amount of conversion that is expected in the reactor. The general mole balance equation in the gas phase is given by [64]

$$\frac{\partial C_j}{\partial t} + \nabla \cdot (\vec{v} C_j) = r_j \tag{3.36}$$

where $\hat{C}_j$ is the concentration of species j, in [mol/m^3], $\vec{v}$ is the velocity of the gas, and r_j is the reaction rate in units of [mol/(m^3 s)]. The reaction rate r_{CH_4} is given as

$$r_{CH_4} = -kC_{CH_4} = -k_0 C_{CH_4} \exp\left(\frac{E_a}{RT}\right) \tag{3.37}$$

where k_0 is the preexponential factor in units of [1/s], E_a is the activation energy in [J/mol], R is the ideal gas constant of 8.314 J/(mol K), and T is the reactor temperature in [K]. The equation is then integrated over a control volume, which gives

$$\int \frac{\partial C_j}{\partial t} dV + \int \nabla \cdot (\vec{v} C_j) dV = \int r_j dV \tag{3.38}$$

The first term on the left hand side of Equation (3.38) can be further simplified by recognizing that $\frac{\partial C_j}{\partial t}$ is not a function of the control volume

$$\int \frac{\partial C_j}{\partial t} dV = \frac{\partial C_j}{\partial t} \int dV = \frac{\partial C_j}{\partial t} V = \frac{\partial n_j}{\partial t} \tag{3.39}$$

where V is reactor volume in [m^3], n_j is the total number of moles present in the reactor of species j. The second term on the left hand side of Equation (3.38) can be simplified recognizing that $(\vec{v} C_j) = \vec{\hat{N}}_j$,

$$\int \nabla \cdot (\vec{v} C_j) dV = \int \nabla \cdot \vec{\hat{N}}_j dV \tag{3.40}$$

where $\vec{\hat{N}}_j$ is three dimensional vector of molar flux of species j at any time t in units of [mol/(m^2 s)]. Using the Divergence Theorem [65], the equation becomes

$$\int \nabla \cdot \vec{\hat{N}}_j dV = \int \vec{\hat{N}}_j \cdot \hat{n} dS \tag{3.41}$$

where $\hat{n}$ is the normal vector pointing outwards from the surface S of the control volume. Recognizing that that the gases enter and exit through two surfaces only with directly opposing $\hat{n}$ vectors, the following equation is reached

$$\int \vec{\hat{N}}_j \cdot \hat{n} dS = N_j, 0 - N_j \tag{3.42}$$

where $N_{j,0}$ is inlet molar flow rate of species j in units of [mol/s]. In summary, the following final equation is obtained for one dimensional flow through a reactor.

$$N_{j,0} - N_j + \int r_j dV = \frac{dn_j}{dt} \tag{3.43}$$

Steady state is assumed, so $\frac{dn_j}{dt} = 0$. The reactor is perfectly mixed, so there are no spacial variations in the reaction term. Thus Equation (3.43) becomes

$$N_{j,0} - N_j + r_j V = 0 \tag{3.44}$$

and rearranging,

$$V = -\frac{N_{j,0} - N_j}{r_j} \tag{3.45}$$

Conversion of species j, X_j, is determined by

$$X_j = \frac{N_{j,0} - N_j}{N_{j,0}} \tag{3.46}$$

Substituting Equation (3.46) into (3.44), the general mixed reactor design equation for j becomes

$$V = -\frac{N_{j,0} - N_{j,0}(1 - X_j)}{r_j} = -\frac{N_{j,0} X_j}{r_j} \tag{3.47}$$

The design equation for a perfectly mixed methane cracking reactor, where $j = CH_4$, is

$$X = -\frac{r_{CH_4} V}{N_{CH_4,0}} \tag{3.48}$$

where X_{CH_4} is set to X for brevity. Then,

$$X = -k\frac{C_{CH_4} V}{N_{CH_4,0}} \tag{3.49}$$

In order to obtain the CH_4 conversion, an expression is needed for C_{CH_4}. The reaction given in (3.1) produces two moles of H_2 for every mole of CH_4 consumed. Thus it is considered as a varying volume flow system because the gas expands due to stoichiometry as the reaction proceeds. Other factors that lead to varying volume flow systems are changes in pressure and temperature. Using a ratio of ideal gas laws for the inlet and at steady state concentrations, as well as stoichiometry, a relationship is derived for steady state CH_4 concentration. At the inlet, the total concentration for an ideal gas is defined as

$$C_{T,0} = \frac{N_{T,0}}{\dot{V}_0} = \frac{P_0}{RT_0} \tag{3.50}$$

where the subscript $C_{T,0}$ is the total concentration at the inlet [mol/m^3], $N_{T,0}$ is the inlet molar flow rate in [mole/s], $\dot{V}_0$ is the inlet total volumetric flow rate in [m^3/s], P_0 is the inlet pressure in [Pa], and T_0 is the inlet temperature in [K]. At the outlet, the total steady state concentration for an ideal gas is

$$C_T = \frac{N_T}{\dot{V}} = \frac{P}{RT} \tag{3.51}$$

where N_T is the steady state molar flow rate in [mole/s], $\dot{V}$ is the steady state total volumetric flow rate in [m^3/s], P is the steady state pressure in [Pa], and T is the steady state temperature in [K]. Dividing Equation (3.51) with Equation (3.50) and rearranging gives

$$\dot{V} = \dot{V}_0 \frac{N_T}{N_{T,0}} \left(\frac{P_0}{P}\right) \left(\frac{T}{T_0}\right) \tag{3.52}$$

Next a relationship between the total flow rate at the inlet and at steady state outlet conditions needs to be derived. Recognizing that $\nu_j = \frac{N_{j,0}}{N_{A,0}}$, Equation (3.46) can be rearranged to give

$$N_j = N_{j,0} + \nu_j N_{A_0} X \tag{3.53}$$

$N_{j,0}$ can be described in terms of species $N_{A,0}$ as follows

$$N_{j,0} \;=\; \Theta_j N_{A,0} \tag{3.54}$$

with

$$\Theta_j = \frac{n_{j,0}}{n_{A,0}} = \frac{C_{j,0}}{C_{A,0}} = \frac{x_{j,0}}{x_{A,0}} \tag{3.55}$$

where $x_{j,0}$ is the inlet mole fraction for species j, and $x_{A,0}$ is the inlet mole fraction for species A. Θ_j is a ratio of inlet molar conditions for species j. Substituting Equations (3.54) and (3.55) into Equation (3.53) and simplifying gives

$$N_j = N_{A,0}(\Theta_j + \nu_j X) \tag{3.56}$$

The total molar flow rate in the reactor is therefore given by summing all the molar flow rates together

$$N_T = \sum N_j = \sum N_{A,0}(\Theta_j + \nu_j X) \tag{3.57}$$

Now, the first term in Equation (3.57)

$$\sum N_{A_0}\Theta_j \;=\; N_{A_0}(\frac{x_A}{x_A} + \frac{x_B}{x_A} + \frac{x_C}{x_A})$$

$$= \frac{N_{A_0}}{x_A} = N_{T,0} \tag{3.58}$$

and the second term in Equation (3.57) becomes

$$\sum N_{A,0}\nu_j X = (\frac{c}{a} + \frac{b}{a} - 1)N_{A,0}X = \delta \cdot N_{A,0}X \tag{3.59}$$

by letting $\delta = \frac{c}{a} + \frac{b}{a} - 1$. Substituting Equations (3.58) and (3.59) into Equation (3.57) gives

$$N_T = N_{T,0} + \delta \cdot N_{A,0}X \tag{3.60}$$

Equation (3.60) can now be substituted into Equation (3.52), giving

$$\begin{aligned} \dot{V} &= \dot{V}_0 \frac{(N_{T,0} + \delta \cdot N_{A,0}X)}{N_{T,0}} \left(\frac{P_0}{P}\right)\left(\frac{T}{T_0}\right) \\ &= \dot{V}_0(1 + \delta \cdot \frac{N_{A,0}}{N_{T,0}}X) \left(\frac{P_0}{P}\right)\left(\frac{T}{T_0}\right) \\ &= \dot{V}_0(1 + \delta \cdot x_{A,0}X) \left(\frac{P_0}{P}\right)\left(\frac{T}{T_0}\right) \end{aligned} \tag{3.61}$$

Defining ϖ as

$$\varpi = \delta \cdot x_{A,0} = \left(\frac{c}{a} + \frac{b}{a} - 1\right) x_{A,0} \tag{3.62}$$

and substituting Equation (3.62) into Equation (3.61), gives

$$\dot{V} = \dot{V}_0 \left(1 + \varpi X\right) \left(\frac{P_0}{P}\right)\left(\frac{T}{T_0}\right) \tag{3.63}$$

Now remembering that

$$C_j = \frac{N_j}{\dot{V}} \tag{3.64}$$

and substituting in Equation (3.63) for total volumetric flow rate $\dot{V}$ and Equation (3.56) for N_j, the molar flow rate of species j, the following equation for concentration as a function of volumetric flow expansion for the reactor is derived

$$C_j = \frac{N_{A,0}(\Theta_j + \nu_j X)}{\dot{V}_0(1 + \varpi X)(\frac{P_0}{P})(\frac{T}{T_0})} = \frac{N_{A,0}}{\dot{V}_0} \frac{(\Theta_j + \nu_j X)}{(1 + \varpi X)} \left(\frac{P}{P_0}\right)\left(\frac{T_0}{T}\right) \tag{3.65}$$

which simplifies to the following by applying Equation (3.64) again to the inlet ratio of $N_{A,0}/\dot{V}_0$

$$C_j = C_{A,0} \frac{(\Theta_j + \nu_j X)}{(1 + \varpi X)} \left(\frac{P}{P_0}\right)\left(\frac{T_0}{T}\right) \tag{3.66}$$

Now, for the CH_4 cracking reaction given in Equation (3.1), the stoichiometry coefficient $\nu_{CH_4} = -1$, and $\Theta_{CH_4} = \frac{n_{CH_4,0}}{n_{CH_4,0}} = 1$ using Equation (3.55). ϖ is found recognizing that only CH_4 and H_2 are in the gas phase, and solid C is ignored. Using Equation (3.62), ϖ becomes

$$\varpi = \left(\frac{2}{1} + \frac{0}{1} - 1\right) x_{CH_4,0} = x_{CH_4,0} \tag{3.67}$$

Therefore, CH_4 concentration with variable volume flow is

$$C_{CH_4} = C_{CH4,0} \frac{(1-X)}{(1 + x_{CH_4,0} X)} \left(\frac{P}{P_0}\right) \left(\frac{T_0}{T}\right) \tag{3.68}$$

Putting Equation (3.68) into the general design Equation (3.49) and rearranging gives the design equation for a variable volume flow system

$$\begin{aligned} X &= -k \frac{C_{CH_4} V}{N_{CH_4,0}} \\ X &= -k C_{CH4,0} \frac{(1-X)}{(1 + x_{CH_4,0} X)} \left(\frac{P}{P_0}\right) \left(\frac{T_0}{T}\right) \frac{V}{N_{CH_4,0}} \end{aligned} \tag{3.69}$$

Further simplification by using Equation (3.64) gives

$$X = -k \frac{(1-X)}{(1 + x_{CH_4,0} X)} \left(\frac{P}{P_0}\right) \left(\frac{T_0}{T}\right) \frac{V}{\dot{V}_0} \tag{3.70}$$

Equation (3.70) can be transformed into a quadratic polynomial form by the following steps

$$k \frac{V}{\dot{V}_0} (1 - X) = X (1 + x_{CH_4,0} X) \left(\frac{P_0}{P}\right) \left(\frac{T}{T_0}\right) \tag{3.71}$$

For further simplification, τ is the nominal holding time, given by

$$\tau = \frac{V}{\dot{V}_0} \tag{3.72}$$

Applying Equation (3.72) and expanding,

$$\begin{aligned} k\tau - k\tau X &= \left(\frac{P_0}{P}\right) \left(\frac{T}{T_0}\right) X + x_{CH_4,0} \left(\frac{P_0}{P}\right) \left(\frac{T}{T_0}\right) X^2 \\ 0 &= -k\tau + k\tau X + \left(\frac{P_0}{P}\right) \left(\frac{T}{T_0}\right) X + x_{CH_4,0} \left(\frac{P_0}{P}\right) \left(\frac{T}{T_0}\right) X^2 \\ 0 &= x_{CH_4,0} \left(\frac{P_0}{P}\right) \left(\frac{T}{T_0}\right) X^2 + \left\{ k\tau + \left(\frac{P_0}{P}\right) \left(\frac{T}{T_0}\right) \right\} X - k\tau \end{aligned} \tag{3.73}$$

If the reactor is isothermal and isobaric, the design equation becomes

$$0 = x_{CH_4,0} X^2 + (k\tau + 1) X - k\tau \tag{3.74}$$

Therefore,

$$X = \frac{-(k\tau + 1) \pm \sqrt{(k\tau + 1)^2 + 4k\tau x_{CH_4,0}}}{2x_{CH_4,0}} \tag{3.75}$$

Noting that X must always be positive, Equation (3.75) becomes

$$X = \frac{-(k\tau + 1) + \sqrt{(k\tau + 1)^2 + 4k\tau x_{CH_4,0}}}{2x_{CH_4,0}} \tag{3.76}$$

which is the final analytical equation for a steady state, isothermal, isobaric and perfectly mixed reactor with variable volume flow due to stoichiometry. The gas is assumed to be ideal. The flow is called overflowing because volume V is set constant. After X_{CH_4} is calculated, the mole fractions of all the species is determined through the following equations. The total molar flow rates for CH_4 and H_2 are calculated as

$$N_{CH_4} = N_{CH_4,0}(\Theta_{CH_4} + \nu_{CH_4} X) = N_{CH_4,0}(1 - X) \tag{3.77}$$

$$N_{H_2} = N_{CH_4,0}(\frac{x_{H_2,0}}{x_{CH_4,0}} + 2X) \tag{3.78}$$

And the molar flow rate for the non-reactant N_2 is

$$N_{N_2} = N_{N_2,0} \tag{3.79}$$

The total molar flow rate is

$$N_T = N_{CH_4} + N_{H_2} + N_{N_2} \tag{3.80}$$

The mole fractions for CH_4, H_2 and N_2 are calculated as

$$x_{CH_4} = N_{CH_4}/N_T \tag{3.81}$$

$$x_{H_2} = N_{H_2}/N_T \tag{3.82}$$

$$x_{N_2} = N_{N_2,0}/N_T \tag{3.83}$$

3.2.2 Perfectly mixed reactor with bypass

Figure 3.6 is a diagram of the blank experimental reactor. As can be seen, the reactor has been broken down into two main sections. One of these sections is a heated zone, and the top section is a dead or non-heated zone. The location at which the temperature drops below 1023 K is called L_H. The length L_H is dependent on the operating temperature of the reactor.

Based on the observations in Section 3.1.2, it is reasonable to assume that the gas that was injected oscillates between the heated and cold zones in the reactor,

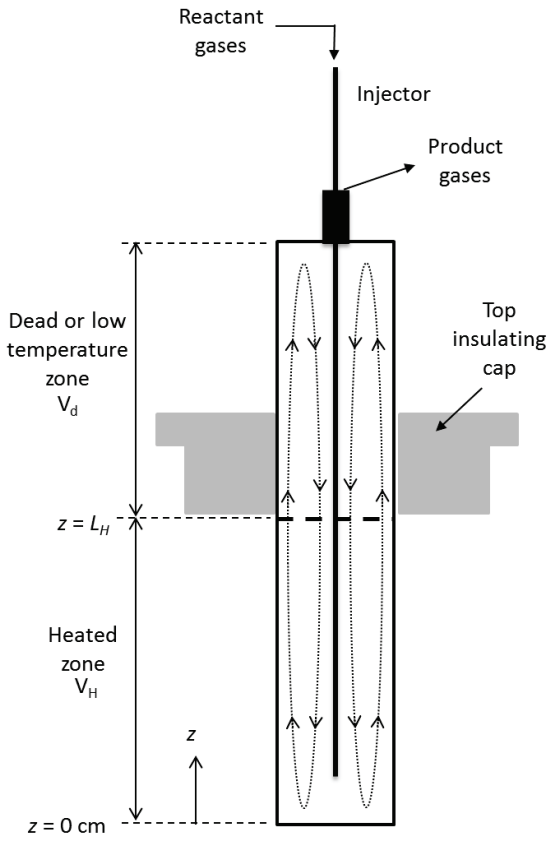

Figure 3.6 – Graphical representation of the perfectly mixed reactor with a bypass in the top section where no reaction occurs due to low temperatures.

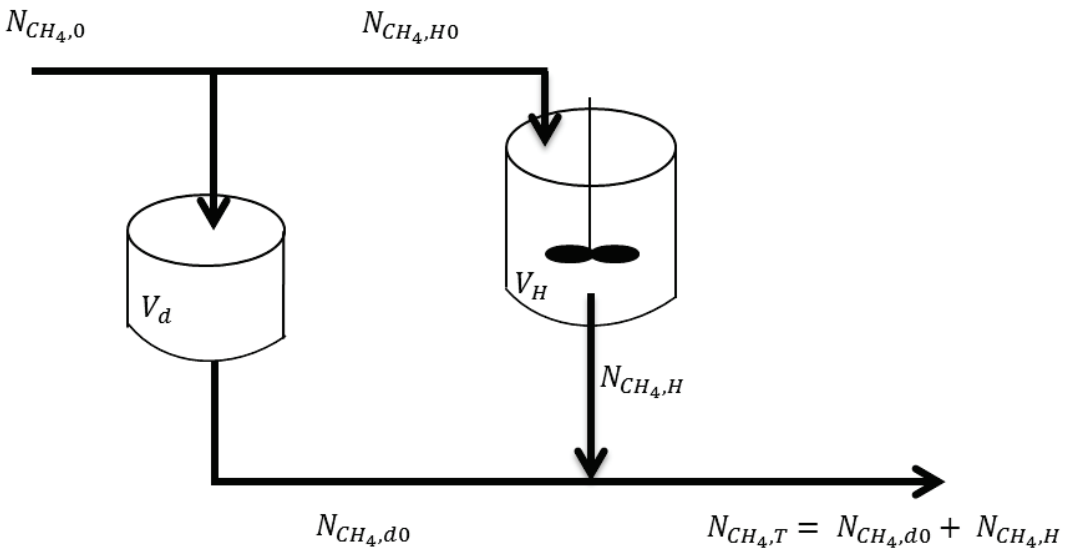

Figure 3.7 – Equivalent graphical representation of the perfectly mixed reactor with a bypass equation derivation purposes.

with the amount of time in the cold zone dependent on the volume of the cold zone compared to the overall reactor volume. At $T_0 = 1078$ K, for instance, the heated length of the reactor is approximately 0.21 m (using Equation (3.10)). Therefore the buoyancy effects would cause the gas to spend the majority of its residence time in the low temperature zone of the reactor, where no reaction occurs. At $T_0 = 1350$ K, the heated length is 0.30 m, so the gas would spend the majority its time in the heated zone. Figure 3.6 shows visually the low temperature zone in the reactor. This analysis therefore led to a mathematical model where a perfectly mixed reactor is put in conjunction with a bypass, as shown in Figure 3.7. The gas that flowed through the bypass route received negligible conversion due to spending the majority of the time in the unheated zone before it exited the reactor.

In this derivation, it is assumed that the separation of the total volumetric flow rate entering the reactor is defined by a constant β. The total inlet volumetric flow rate was separated into the low temperature and high temperature volumetric flow rates, $\dot{V}_{d0}$, and $\dot{V}_{H0}$ respectively. The low temperature volumetric flow rate represents the amount of the inlet flow that spends the majority of time in the non-reactive or deadspace zone of the reactor vessel. The high temperature volumetric flow rate represents the amount of the inlet flow that spends the majority of time in the high

temperature or reactive zone. These are defined as

$$\dot{V}_{H0} = (1-\beta)\dot{V}_0 \tag{3.84}$$

$$\dot{V}_{d0} = \beta\dot{V}_0 \tag{3.85}$$

where $\dot{V}_0$ is the total inlet volumetric flow rate in [m^3/s]. The low temperature and high temperature volumes are separated using a constant Ω

$$V_H = \Omega V \tag{3.86}$$

$$V_d = (1-\Omega)V \tag{3.87}$$

A mole balance is performed at the junction after the perfectly mixed reactor as follows

$$N_{CH_4,T} = N_{CH_4,d0} + N_{CH_4,H} \tag{3.88}$$

where $N_{CH_4,T}$ is the total molar flow rate at the outlet of the reactor in [mol/s]. $N_{CH_4,d0}$ is the molar flow rate of the reaction gas that goes through the bypass, and $N_{CH_4,H}$ is the molar flow rate of the gas that is exiting the heated reaction zone, i.e. the perfectly mixed reactor. $N_{CH_4,d0}$ is defined as

$$N_{CH_4,d0} = \dot{V}_{d0}C_{CH_4,0} \tag{3.89}$$

where $\dot{V}_{d0}$ is the inlet gas volumetric flow rate in [m^3/s] that is diverted through the bypass, and $C_{CH_4,0}$ is the inlet concentration of CH_4 in [mol/m^3]. $C_{CH_4,0}$ is calculated using the ideal gas law, as follows

$$C_{CH_4,0} = x_{CH_4,0}\frac{P_0}{RT_0} \tag{3.90}$$

where $x_{CH_4,0}$ is the inlet molar fraction of methane, P_0 is the inlet gas pressure in [Pa], R is the universal gas constant in [J/mol·K] and T_0 is the inlet gas temperature in [K]. $N_{CH_4,H}$ is derived from Equation (3.46) as

$$N_{CH_4,H} = N_{CH_4,H0}(1-X_H) \tag{3.91}$$

where $N_{CH_4,H0}$ is the molar flow rate that enters the heated section of the mixed reactor in [mol/s], and X_H is CH_4 conversion that occurs in the heated portion of the reactor. The amount of methane converted in the heated section of the perfectly mixed reactor is found by using the design equation derived in Equation (3.70) and solving it using the quadratic equation given in Equation (3.76) and the nominal holding time τ in Equation (3.72).

$N_{CH_4,H0}$ is derived similarly to $N_{CH_4,d0}$ using Equation (3.84), and is given as

$$N_{CH_4,H0} = \dot{V}_{H0} C_{CH_4,0} \tag{3.92}$$

In summary, the final equation for the molar flow rate exiting the heated portion of the reactor is given as follows by substituting in Equations (3.76) and (3.92) into Equation (3.91),

$$N_{CH_4,H} = \dot{V}_{H0} C_{CH_4,0} \left(1 - \frac{-(k\tau+1) + \sqrt{(k\tau+1)^2 + 4k\tau x_{CH_4,0}}}{2x_{CH_4,0}} \right) \tag{3.93}$$

Thus the total molar flow rate at the outlet of the entire perfectly mixed reactor is given by Equation (3.88) . Total CH_4 conversion for the entire reactor is found by

$$X_T = \frac{N_{CH_4,0} - N_{CH_4,T}}{N_{CH_4,0}} \tag{3.94}$$

where $N_{CH_4,0}$ is the total inlet molar flow rate that enters the entire reactor in [mol/s], given by

$$N_{CH_4,0} \quad = \quad \dot{V}_0 C_{CH_4,0} \tag{3.95}$$

Substituting in Equations(3.88),(3.89), (3.93), and (3.95),

$$X_T = \frac{\dot{V}_0 C_{CH_4,0} - \dot{V}_{d0} C_{CH_4,0} - \dot{V}_{H0} C_{CH_4,0} \left(1 - \frac{-(k\tau+1) + \sqrt{(k\tau+1)^2 + 4k\tau x_{CH_4,0}}}{2x_{CH_4,0}} \right)}{\dot{V}_0 C_{CH_4,0}} \tag{3.96}$$

Dividing by $C_{CH_4,0}$, and substituting in Equations (3.85) and (3.84),

$$X_T = \frac{\dot{V}_0 - \beta\dot{V}_0 - (1-\beta)\dot{V}_0 \left(1 - \frac{-(k\tau+1) + \sqrt{(k\tau+1)^2 + 4k\tau x_{CH_4,0}}}{2x_{CH_4,0}} \right)}{\dot{V}_0} \tag{3.97}$$

Dividing by $\dot{V}_0$, the equation is simplified to

$$X_T = 1 - \beta - (1-\beta) \left(1 - \frac{-(k\tau+1) + \sqrt{(k\tau+1)^2 + 4k\tau x_{CH_4,0}}}{2x_{CH_4,0}} \right) \tag{3.98}$$

which is the final equation to find total CH_4 conversion.

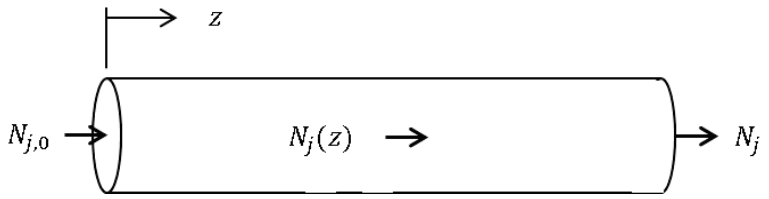

Figure 3.8 – Graphical representation of a plug flow reactor

3.2.3 Plug flow reactor

A diagram representing a plug flow model is presented in Figure 3.8. The general transient equation for a flow system was given in Equation (3.36), and is given below again for reference,

$$\frac{\partial C_j}{\partial t} + \nabla \cdot (\vec{v} C_j) = r_j \tag{3.99}$$

It is assumed that the reactor is at steady state, so

$$\frac{\partial C_j}{\partial t} = 0 \tag{3.100}$$

Substituting in Equation (3.39), and recognizing again that $(\vec{v} C_j) = \vec{\hat{N}}_j$, the following is obtained

$$\nabla \cdot \vec{\hat{N}}_j = r_j \tag{3.101}$$

Now, $\vec{\hat{N}}_j$ is in units of [mol/(m^2 s)]. Multiplying by the cross-sectional area of the reactor then gives

$$\vec{\hat{N}}_j = \frac{\vec{N}_j}{A_c} \tag{3.102}$$

The PFR model is one dimensional, therefore $\vec{N}_j = N_{j,z} = N_j$. Substituting in Equation (3.102) into Equation (3.101), the following is obtained

$$\frac{dN_j}{dz} = r_j A_c 1.59 \tag{3.103}$$

Equation (3.103) is the general design equation for a steady state plug flow reactor. Rearranging Equation (3.46) to derive N_j, and substituting into Equation (3.103), then gives

$$\frac{d}{dz}[N_{j,0}(1 - X_j)] = r_j A_c \tag{3.104}$$

or

$$N_{j,0} \frac{dX_j}{dz} = -r_j A_c \tag{3.105}$$

For CH_4 cracking where $j = CH_4$

$$N_{CH_4,0}\frac{dX}{dz} = -r_{CH_4}A_c \tag{3.106}$$

where $X_{CH_4} = X$ for brevity. The integral form is given as

$$\int_0^X \frac{N_{CH_4,0}}{-r_{CH_4}}dX = \int_0^L A_c dz \tag{3.107}$$

noting that r_{CH_4} is a function of conversion X as defined in Equations (3.37) and (3.68) and given below again as

$$r_{CH_4} = -kC_{CH_4}$$

and

$$C_{CH_4} = C_{CH4,0}\frac{(1-X)}{(1+x_{CH_4,0}X)}\left(\frac{P}{P_0}\right)\left(\frac{T_0}{T}\right)$$

the final integral form is

$$\begin{aligned} V &= N_{CH_4,0}\int_0^X \frac{1}{-r_{CH_4}}dX \\ &= N_{CH_4,0}\int_0^X \frac{1}{kC_{CH4,0}}\frac{(1+x_{CH_4,0}X)}{(1-X)}\left(\frac{P_0}{P}\right)\left(\frac{T}{T_0}\right)dX \end{aligned} \tag{3.108}$$

Assuming an isothermal and isobaric reactor, gives

$$V = \frac{N_{CH_4,0}}{kC_{CH_4,0}}\int_0^X \frac{(1+x_{CH_4,0}X)}{(1-X)}dX \tag{3.109}$$

The integration table in Fogler [62], gives

$$\int_0^x \frac{1+ax}{1-x} = -(1+a)\ln(1-x) - ax \tag{3.110}$$

Using Equation (3.110), the following design equation for an isothermal plug flow reactor is found

$$V = \frac{N_{CH_4,0}}{kC_{CH_4,0}}\left[-(1+x_{CH_4,0})\ln(1-X) - x_{CH_4,0}X\right] \tag{3.111}$$

Equation (3.64) related $C_{CH_4,0}$ and $N_{CH_4,0}$ to $\dot{V}$ by

$$C_j = \frac{N_j}{\dot{V}}$$

and the nominal holding time τ was given by Equation (3.72) as

$$\tau = \frac{V}{\dot{V}_0}$$

Thus after substituting in Equations (3.64) and (3.72) into Equation (3.111), the following final equation was found for an ideal isothermal and isobaric plugflow reactor.

$$(1 + x_{CH_4,0}) \ln(1 - X) + x_{CH_4,0} X + \tau k = 0 \tag{3.112}$$

This equation was solved in MATLAB using the `fminbnd()` function and bounding X between 0 and 1.

3.3 Parameter estimation

3.3.1 Parameter ranges

The range limits for the kinetic parameter fitting were based on the literature review performed in Chapter 1. Steinberg [12] found values as low as $k_0 = 5.4 \times 10^3$ 1/s and $E_a = 131$ kJ/mol and Chen et al. [25] calculated values as high as $k_0 = 2.8 \times 10^{16}$ 1/s and $E_a = 450.2$ kJ/mol. Thus the PMR, CPMR and PFR ranges for k_0 and E_a were

$$k_0 \in (1 \times 10^3, 1 \times 10^{19})$$

$$E_a \in (1.2 \times 10^5, 5 \times 10^5)$$

The CPMR incorporated a third parameter, β, that defined the separation of the total volumetric flow rate entering the reactor. The range for β was therefore

$$\beta \in (0, 1)$$

3.3.2 Parameter estimation procedure

3.3.2.1 Genetic Algorithm

The genetic algorithm provided by MATLAB was used to optimize the kinetic parameters E_a and k_0, and the reactor constant β. The number of variables varies from between two for the PFR and PMR, and three for the CPMR. The `ga()` solver minimized the square of the residual given by

$$f = \sum_{i=1}^{N} (X_{model} - X_{exp})^2 \tag{3.113}$$

were N is the total number of experimental samples taken, X_{model} is CH_4 conversion predicted by the model at a certain operating temperature and flow rate, and X_{exp} is the corresponding experimental data point for the same operating temperature and flow rate. The residual is calculated by

$$res = \sqrt{f} \tag{3.114}$$

The genetic algorithm works by first creating a random initial population either within upper and lower boundaries or default boundary values [66]. This is the initial generation. The next generation is created using the prior generation, and are made up of crossovers from two elite parents from the previous generation, or mutations from a single parent [66]. The elite parents are the ones with the best score or scaled residual from the previous generation. The mutations allow for random selection to check for local or global minima. The algorithm stops once the stopping criteria is reached. The stopping criteria implemented is given later in Table 3.2 in Section 3.4. The criteria `TolFun` measures the maximum average relative change of the best fitness function or residual equation that should be obtained before a solution is reached.

3.3.3 Sequence of computing operations

A flow chart showing the sequence of events used in the MATLAB code to solve for a solution is given in Figure 3.9. The type of model is first chosen, whether it be PFR, PMR or CPMR and the corresponding function handle is assigned to the solver. The dimensions and operating parameters of the reactor are initialized. The inlet conditions were set to match experimental conditions as discussed in Section 2.5.2. It was found in Section 2.5.2 that the bubble flow meter and setpoint values of the MFCs differed substantially, and so the flow rates from the bubble flow meter were used (given in Table 2.6). The inlet mole fractions for the models corresponded to those shown in Figure 2.23. The experimental results given in Chapter 2 are incorporated into the model. Initial scaling variables for $k_{0,init}$ $E_{a,init}$ and β_{init} are set. The upper and lower bounds (UB and LB) for k_0 and E_a are scaled using

$$LB = [k_{0,LB} \quad E_{a,LB}] = \left[\frac{1 \times 10^3}{k_{0,init}} \quad \frac{1.2 \times 10^5}{E_{a,init}}\right] \tag{3.115}$$

$$UB = [k_{0,UB} \quad E_{a,UB}] = \left[\frac{1 \times 10^{17}}{k_{0,init}} \quad \frac{5 \times 10^5}{E_{a,init}}\right] \tag{3.116}$$

where the ranges were previously determined in Section 3.3.1. The genetic algorithm solver (`ga()`) is then run to determine new optimized values for k_0 E_a and β. The

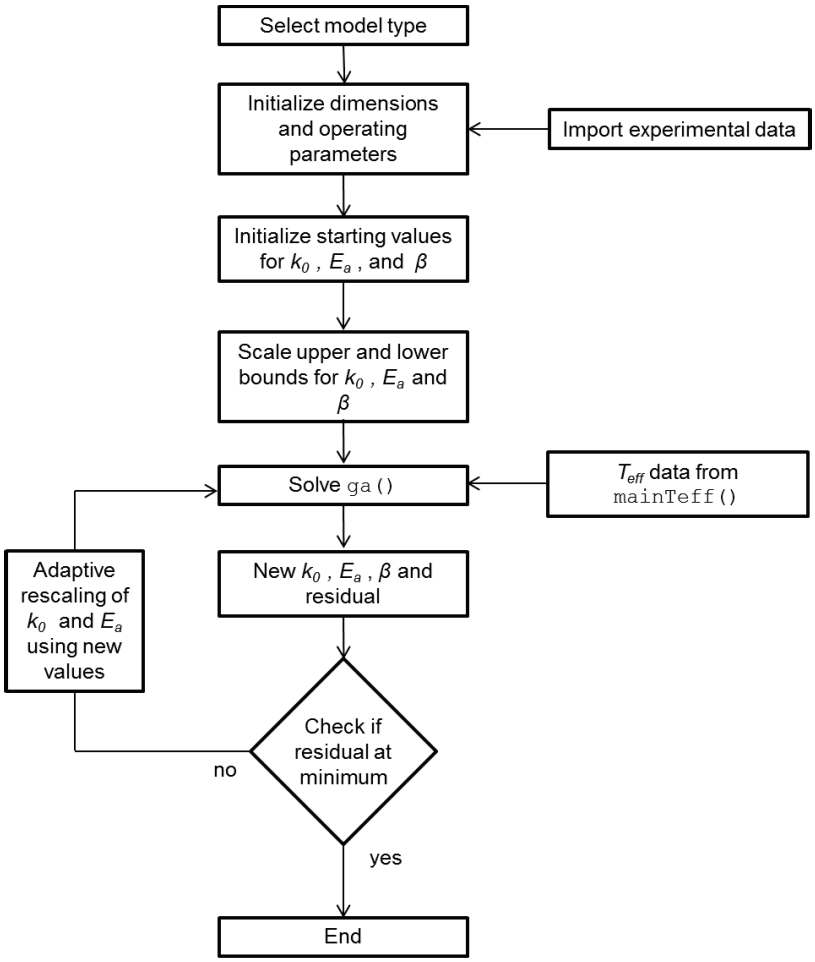

Figure 3.9 – Flow chart of numeric operations for solving for kinetic parameters.

magnitudes, however, of k_0 can range from 1×10^3 to 1×10^{19}. Therefore it was necessary to use an adaptive re-scaling process to ensure the algorithm does not stall with a local minima [67]. Subsequent runs were therefore performed using the new parameter values obtained from the previous solution to re-scale the upper and lower boundaries using Equations (3.115) and (3.116). A minimum of 10 runs were made to ensure that the residual given by Equation (3.113), which is outputted by `ga()`, was at the lowest value possible.

3.4 Model input parameters

The `ga()` algorithm options that were set are given in Table 3.2. The dimensions that were input into the model are given in Table 3.3. The initial values for scaling the kinetic parameters E_a and k_0, the value of $E_{a,eff}$ for calculating the effective temperature (defined in Section 3.1.1), and reactor operating pressure are given in

Table 3.2 – Input option parameters for `ga()` algorithm

Criteria	**Default setting**	**CPMR and PMR settings**	**PFR settings**
Population size	$nvar \times 100$	1×10^5	1×10^4
Generations	$nvar \times 100$	1×10^5	1×10^5
Mutation function	`adaptive feasible`	`adaptive feasible`	`adaptive feasible`
Vectorized	off	on	off
Time limit	infinite	50 hrs	50 hrs
Stall generations	`TolFun`	`TolFun`	`TolFun`
Stall time limit	infinite	infinite	infinite
Function tolerance (`TolFun`)	1×10^{-6}	1×10^{-14}	1×10^{-14}

Table 3.3 – Input dimension parameters

Dimension	**(m)**
L_b	0.218
L_c	0.292
L_a	0.204
$D_{I,out}$	6.35×10^{-3}
$D_{r,in}$	44.45×10^{-3}
L_{bath}	0

Table 3.4.

3.5 Results and discussion

3.5.1 Kinetics using CPMR model

The CPMR numerical model was used to best fit the kinetic parameters using experimental data from Chapter 2. The effect of the single 1373 K data point on the fitting of the kinetic parameters was first analyzed. Two data sets, S1 and S2 were constructed from the data. In S1, all the data points were included. In S2, the 1373 K, 33 ccm data point was excluded. The resulting kinetic parameters are given in Table 3.5. k_0 and E_a using dataset S1 were within their expected ranges as per what

Table 3.4 – Input kinetic parameters and operating pressure

Parameter	Value
$E_{a,eff}$	390 kJ/mol
Ea_{init}	390 kJ/mol
$k_{0,init}$	3.2×10^{14} 1/s
P_0	101.325 kPa

Table 3.5 – Comparison of overall kinetic parameters for PMR, PFR, and CPMR models

Model	Dataset	k_0 (1/s)	E_a (kJ/mol)	β	res
CPMR	S1	5.43×10^{15}	420.7	0.426	0.150
CPMR	S2	8.46×10^{17}	471.1	0.475	0.107

was found in the literature (see Section 3.3.1). However, the kinetics for dataset S2 were above the expected ranges. $k_{0,S2}$ was two orders of magnitude larger than the largest found in literature, which was 2.8×10^{16} 1/s. $E_{a,S2}$ was 20.9 kJ/mol larger than the highest value in literature, which was 450.2 kJ/mol. On the other hand, the value for β increased dramatically from 0.426 to 0.475 from dataset S1 to dataset S2, respectively. The residual, res is calculated using Equation (3.113). res_{S1} is also larger than res_{S2}, but the difference was exacerbated by the fact that S1 had an extra data point. The S1 residual reduces to 0.125 if the 1373 K, 33 ccm data point is ignored in the calculation. This value is still larger than $res_{S2} = 0.107$, but it is a relatively significant reduction from $res_{S1} = 0.150$ where all data points are considered.

The kinetic rate constants for the CPMR kinetic parameters were calculated using the Arrhenius equation (Equation (1.2)). Both sets of parameters were included. The curves for the PMR, PFR and CPMR were extended to 1973 K to allow for comparison to the data found in literature because most studies have been performed at higher temperatures. The results are shown in Figure 3.10. Both curves fell within the expected literature range. The curve $k_{CPMR,S2}$ is more steep than those in literature, while the $k_{CPMR,S1}$ curve is closer to the expected profile. The above analysis suggests that more experimental data should be obtained for higher temperatures, specifically for $T_0 = 1373$ K. This would have allowed the model to more accurately predict higher temperature conversion by decreasing β and changing k_0 and E_a to fit accordingly. At this point in time, β limits the total possible amount of CH_4 conversion that can occur. The kinetics determined using dataset S1 were used for the remainder of this

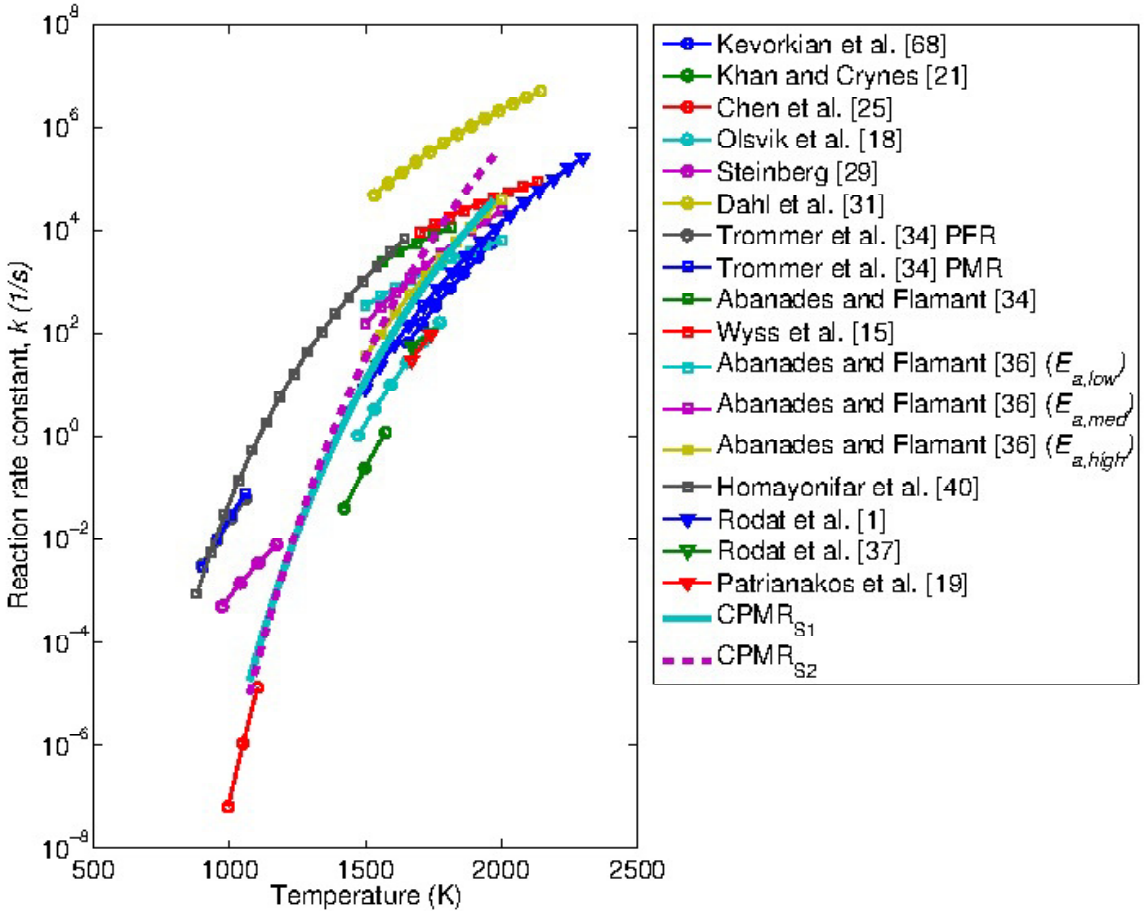

Figure 3.10 – Comparison of the rate constant k using the Arrhenius equation for data sets S1 and S2 using the CPMR numerical model. The CPMR curves have been extrapolated from 1373 K to 1973 K for comparison to literature at higher temperatures.

thesis for the following reasons. First, the kinetics using dataset S1 falls within the expected ranges, and secondly the kinetic rate constant curve $k_{CPMR,S1}$ is similar to literature values. It is recommended however that further experiments be performed to improve reliability of the fitted parameters at higher temperatures.

The CPMR model was used to determine overall kinetic parameters as well as different β values for each flow rate. In the latter case, a new β for the CPMR model was calculated for each flow rate by holding k_0 and E_a constant at their respective overall best fit values and fitting β. The results are shown graphically in Figures 3.11(a) for the overall kinetics and 3.11(b) for a varying β. The numerical results for a varying β are given in Table 3.6. β decreased with increasing flow rate, with the exception of the fitting for 33 ccm data. Dataset S1, which included all experimental

Table 3.6 – CPMR overall and per flow rate kinetic results

Flow rate	k_0 **(1/s)**	E_a **(kJ/mol)**	β	res
33 ccm	5.43×10^{15}	420.7	0.418	0.0.113
67 ccm	5.43×10^{15}	420.7	0.458	0.0326
113 ccm	5.43×10^{15}	420.7	0.443	0.0350
154 ccm	5.43×10^{15}	420.7	0.406	0.0558
224 ccm	5.43×10^{15}	420.7	0.395	0.0530
Overall	5.43×10^{15}	420.7	0.426	0.150

datapoints, was used in each fitting. Unlike the other flow rates, the 33 ccm set included a datapoint at 1373 K. Therefore the 33 ccm β was reduced to allow a better fitting to the extra data point at $X_{CH_4,exp} = 64.8\%$. However, it can be seen that the overall best fit values for E_a and k_0 did not allow the curve to rise high enough to predict the extra data point with accuracy. Instead a 11.6% discrepancy is found between predicted and experimental conversions for 1373 K and 33 ccm, using the 33 ccm best fit β. It should also be noted that the extra data point increased the residual error for the 33 ccm curve. If this data point was removed, the error drops from 0.113 to 0.0840, which is still higher than the other residuals but is relatively closer.

In summary, the CPMR model does predict well for the 993 K to 1323 K region. The model incorporates an ideal perfectly mixed reactor with a bypass, but it is likely that the bypass used in the CPMR is not truly a bypass. The reaction gas does react somewhat as it rises to the low temperature zone, or mixes into the heated section in the reactor again, before it escapes through the outlet. Disregarding this, however, the CPMR model is computationally inexpensive and provided a means to determine realistic kinetic parameters.

3.5.2 Comparison of CPMR, PFR and PMR overall kinetics

The overall kinetic parameters E_a, k_0, and β were determined using the PFR, PMR and CPMR models using all the experimental data points, i.e. dataset S1. The resulting kinetic parameters are presented in Table 3.7. The residual, res is calculated using Equation (3.113).

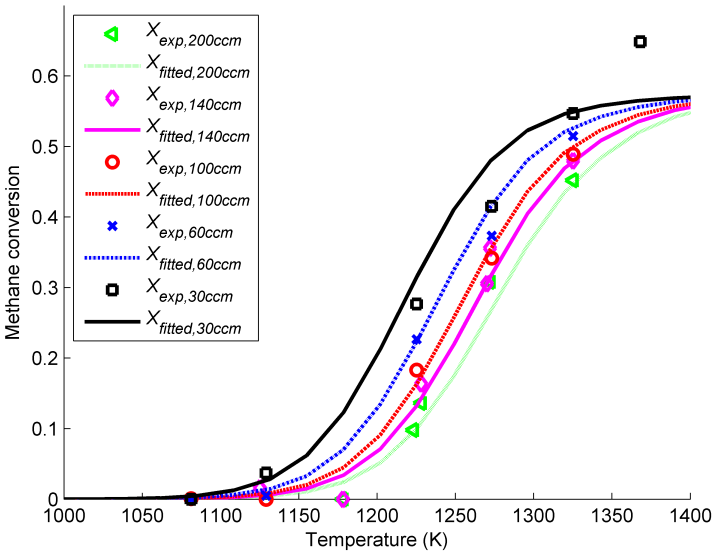

(a)

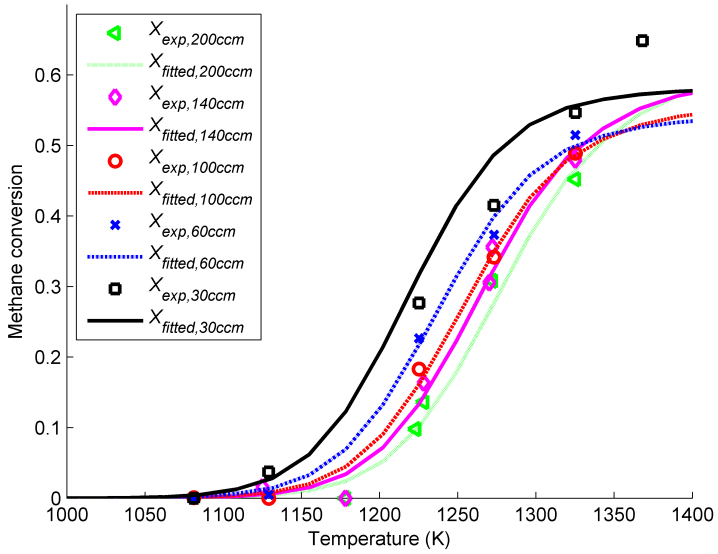

(b)

Figure 3.11 – Results of CPMR model with (a) overall kinetics and (b) setting E_a and k_0 to the overall kinetic values and varying β for each flow rate

Table 3.7 – Comparison of overall kinetic parameters for PMR, PFR, and CPMR models

Model	k_0 **(1/s)**	E_a **(kJ/mol)**	β	res
PMR	3.18×10^7	231.7	-	0.422
PFR	1.20×10^5	177.8	-	0.595
CPMR	5.43×10^{15}	420.7	0.426	0.150

As can be seen, there are major differences in the kinetic parameters that were determined for the three models. The PMR and PFR models exhibited $k_0 = 3.18 \times 10^7$ 1/s, $E_a = 231.7$ kJ/mol and 1.2×10^5 1/s, $E_a = 177.8$ kJ/mol, respectively. On the other hand, the CPMR model produced $k_0 = 5.43 \times 10^{15}$, $E_a = 420.7$ kJ/mol and $\beta = 0.426$. Thus the pre-exponential factor has two orders of magnitude difference between the PMR and PFR, eight orders of magnitude difference between the PMR and CPMR, and ten orders of magnitude difference between the PFR and CPMR. In all cases the overall kinetics fell within the upper and lower boundaries discussed in Section 3.3.1. However, E_a for the PFR and PMR is at the low end of the values found in literature. Various authors in literature have suggested that lower activation energies reflect heterogeneous reaction pathways, due to catalytic or surface effects, entering into the kinetics to lower the activation energy [1, 5, 18, 19, 21]. There were no catalysts in the experimental reactors in this thesis, however, so the activation energy should be higher. This shows that if numerical models are used to fit kinetic parameters, then the numerical model needs to be truly representative of the reactor. This is done by making assumptions that truly reflect the physical phenomena occurring inside the reactor, including mass transport and fluid flow. Unfortunately this is difficult, however, because the phenomena occuring inside the reactor at high temperatures are difficult to observe. Otherwise the kinetic parameters will be intrinsic to the model assumptions and not representative of what is actually occurring inside the reactor.

The predicted conversions for each model are given graphically for 33, 113 and 224 ccm total flow rates in Figure 3.12. It can be seen that the CPMR reactor fits the data much more closely than either the PMR or the PFR for 1073 K to 1323 K. The PMR and PFR models have significant residuals of $res = 0.422$ and $res = 0.595$, respectively. The CPMR model is more accurate with $res = 0.150$. The CPMR reactor is limited in total conversion due to the parameter β. β is a ratio of the total flow rate that enters the perfectly mixed reactor. The rest of the flow enters the bypass or low

temperature section where no reaction takes place. More experimental data should be obtained at higher temperatures to expand and validate the prediction range of the CPMR by potentially changing the parameter β so that higher conversions can be reached.

The Arrhenius equation (Equation (1.2)) was applied to the kinetic results for all three models as well as those kinetic parameters found in literature (see Section 1.2). The curves for the PMR, PFR and CPMR were extended to 1973 K as before. The results are presented in Figure 3.13. As can be seen, the curves for the PMR and PFR do not follow the trends found in literature. The reaction rate constant does not increase as significantly at higher temperatures. The reaction rate constant however is higher than that of the CPMR at lower temperatures, but is still lower than that found in literature, with the exception of Chen et al. [25].

The curve for the CPMR is fairly close to that of Chen et al. [25] between 995 K to 1103 K. At higher temperatures, the CPMR curve is in the mid range of the reaction rate of those in literature, but matches reasonably closely with Abanades and Flamant [36], Rodat et al. [1], Steinberg [29], and Kevorkian et al. [68]. It was assumed that the homogeneous reactions would dominate in the reactor studied in this thesis. The only studies that used carbon seeding in Figure 3.13 were Trommer et al. [34], Dahl et al. [39] and Patrianakos et al. [19]. The reaction rate constant curves from Dahl et al. and Trommer et al. are higher than most in literature, however the curve presented by Patrianakos et al. is in the low range of all the curves. The prior two researchers determined their respective kinetic parameters assuming a single phase 1D plug flow reactor models, however Patrianakos et al. incorporated a two-phase 1D plug flow model where heterogeneous reactions were considered. Patrianakos et al. [19] set the activation energy to 400 kJ/mol and found k_0 by fitting the model to data in literature. Thus the kinetic parameters presented by Patrianakos et al. should reflect the homogeneous reaction pathway. In conclusion, the rate constant curve using the CPMR kinetics is within the expected range of literature which either assumed homogeneous reactions, or did not use catalysts or carbon seeding.

3.5.3 Comparison to literature data

The kinetic results from the CPMR model were compared to the study by Rodat et al. [1]. The author performed 17 experiments using a reactor comprised of four

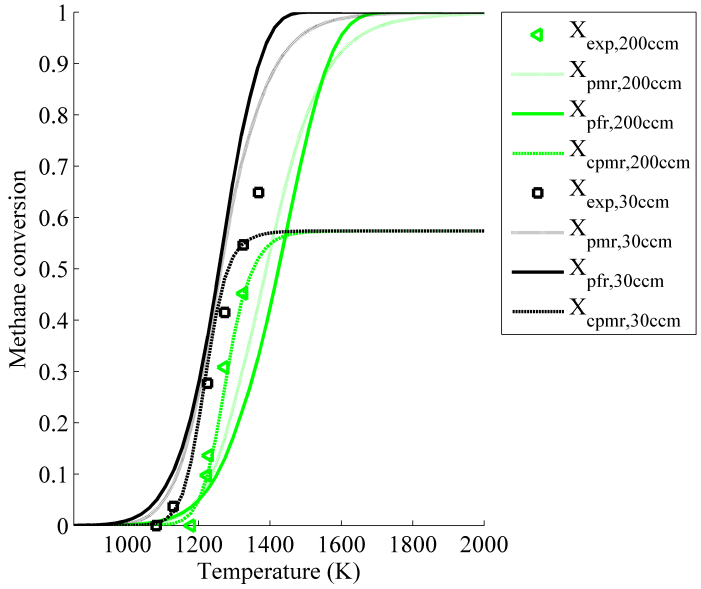

(a)

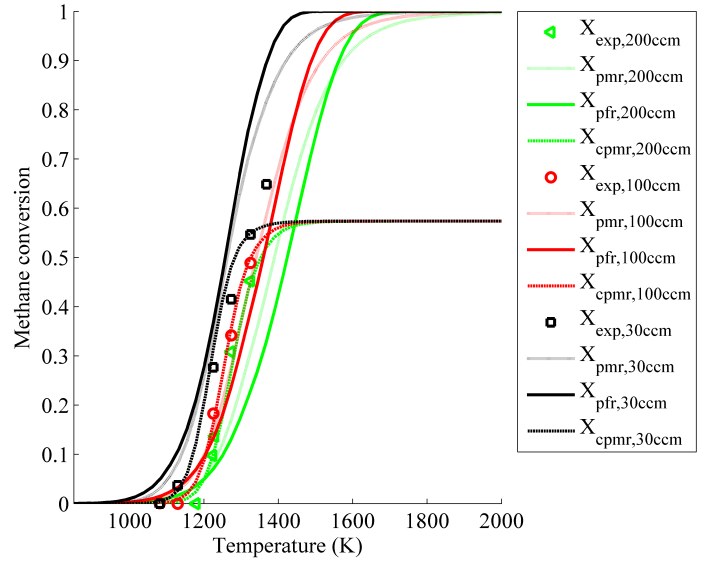

(b)

Figure 3.12 – Comparison of the PMR, PFR and CPMR models with their respective best fit kinetics. Plots with (a) two flow rates and (b) three flow rates are presented.

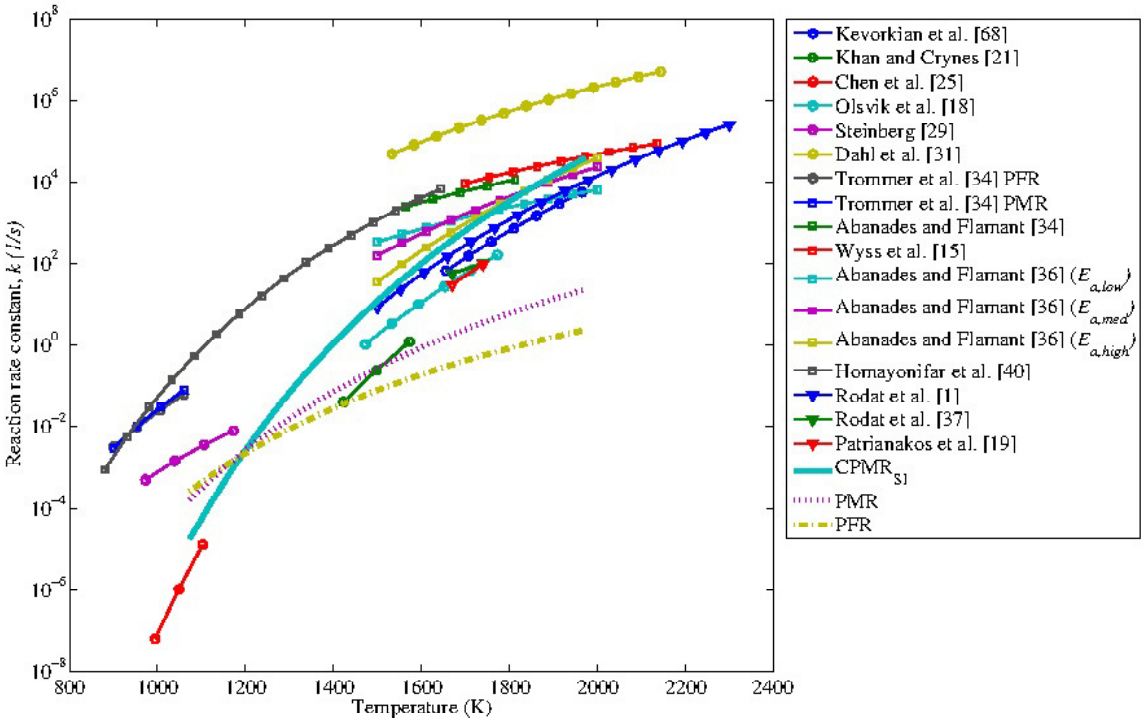

Figure 3.13 – Comparison of the rate constant k using the Arrhenius equation for the PMR, PFR and CPMR. The curves have been extrapolated from 1373 K to 1973 K for comparison to literature at higher temperatures.

tube assemblies made of two concentric tubes each. A diagram of a tube assembly is shown in Figure 3.14. The inner tube was 4 mm ID and 12 mm OD. The outer tube was 18 mm ID. The isothermal zone was approximately 0.161 m long, and the cooling and heating zones about 0.203 m. The reactor was heated using a 1 MW solar furnace, powered by 63 heliostats that reflected solar radiation onto a parabolic concentrator. The parabolic concentrator then focused the concentrated radiation into the graphite cavity that contained the isothermal zones of the reactor tubes. The experiments were performed at reduced pressures using a vacuum pump. The reaction conditions varied with $1670 \leq T \leq 1770$ K, $25 \leq P \leq 40$ kPa, $10 \leq \dot{V}_{total} \leq 30$ L/min, $0.1 \leq x_{CH_4,0} \leq 0.33$, and $0.012 \leq \tau \leq 0.035$ s. A summary of the experimental conditions and results from Rodat et al. [1] are given in Table 3.8. Equation (2.21) was used to calculate X_{CH_4}.

It was found previously that β reduced with increasing flow rate. Therefore it was expected that the value for β would greatly reduce if the flow rates in the reactor studied by Rodat et al. were high enough. The experiments by Rodat et al. were performed at much higher flow rates with smaller cross-sectional areas than the reactor

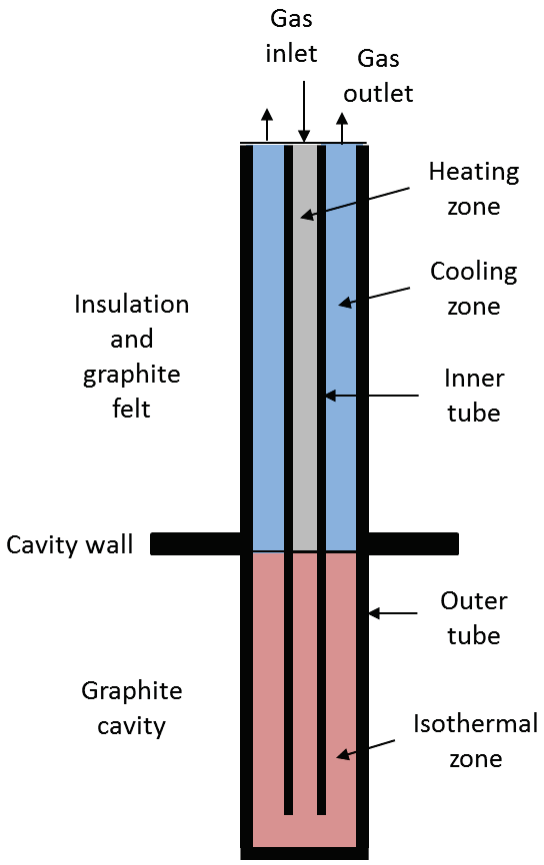

Figure 3.14 – Graphical representation of reactor studied by Rodat et al. [1]

Table 3.8 – Experimental conditions and results from Rodat et al. [1]

Run no.	$\dot{V}_{Ar}$ (m^3/s)	$\dot{V}_{N_2}$ (m^3/s)	P (kPa)	T_0 (K)	τ (s)	X_{CH_4}
1	10.8	1.2	40	1770	0.032	0.98
2	16	4	38	1770	0.018	0.94
3	16	4	35	1770	0.017	0.97
4	20	4	35	1770	0.014	0.95
5	16	4	32	1700	0.018	0.87
6	16	6	35	1710	0.017	0.90
7	16	6	25	1710	0.012	0.77
8	10.8	1.2	30	1670	0.027	0.78
9	16	8	30	1670	0.013	0.60
10	18	2	30	1670	0.018	0.64
11	16	4	30	1670	0.018	0.69
12	14	6	30	1670	0.018	0.76
13	18	2	30	1740	0.018	0.83
14	16	4	30	1740	0.018	0.86
15	14	6	30	1740	0.018	0.86
16	24	6	30	1740	0.012	0.70
17	8	2	30	1740	0.035	0.98

studied in this thesis. The average and scaled velocities were calculated for both reactors in question. The equation for average velocity is given as

$$\overline{u} = \frac{\dot{V}}{A_c} \tag{3.117}$$

where A_c is the cross-sectional area of the annular spaces in the reactors. The volume flow rate, $\dot{V}$, was corrected for pressure and temperature using Equation (3.63). CH_4 conversion was neglected by setting $X = 0$, giving

$$\dot{V} = \dot{V}_{MFC}(\frac{P_{ref}}{P_0})(\frac{T_0}{T_{ref}}) \tag{3.118}$$

where T_{ref} and P_{ref} are the reference temperature and pressure at which the MFCs setpoints measure from. V_{MFC} is the MFC setpoint in [m^3/s]. The scaled velocities for high temperature differentials, U, were calculated using Equation (3.31).

At 1673 K and 10000 ccm, the average and scaled velocities for the Rodat et al. reactor were $\overline{u} = 4.8$ m/s and $U = 1.7$ m/s. At 1350 K and 224 ccm, the velocities for the thesis reactor were calculated to be $\overline{u} = 0.01$ m/s and $U = 1.7$ m/s. The velocities for the Rodat et al. reactor were the same magnitude of order, but there

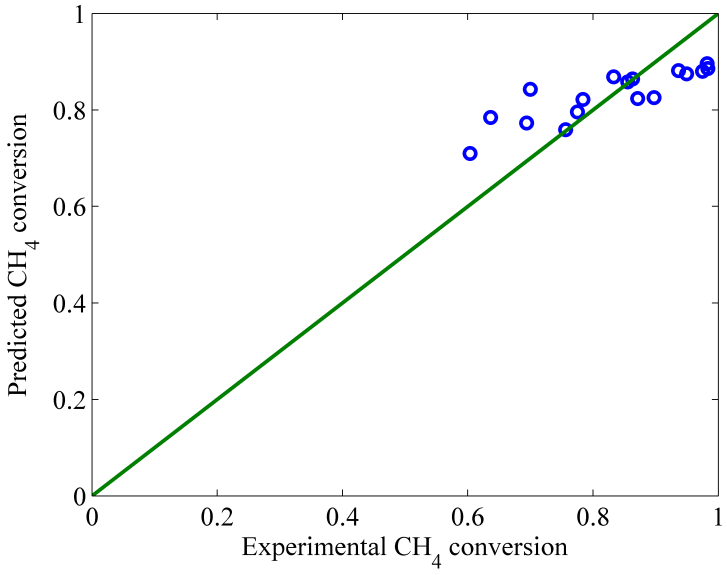

Figure 3.15 – Comparison of CPMR numerical results to data given by Rodat et al. [1] for $\beta = 0.089$

were two orders of magnitude difference between the thesis reactor velocities. The variation in the average velocities between the reactors is due to the difference between cross-sectional areas and inlet flow rates. Thus the Rodat et al. reactor may not experience the same level of mixing due to buoyancy effects as the thesis reactor, and as such the β parameter most likely has a much smaller effect.

The resulting numerical predictions using the CPMR model were plotted against the experimental values from Rodat et al. The results are shown in Figure 3.15. β was optimized to 0.089 for a best fit to the experimental results. The average error between the numerical and experimental results was 8.3% with a standard deviation of 6.8%. Thus it was found that the CPMR numerical model fit the results from Rodat et al. [1] reasonably well.

The CPMR model reduces to the PMR model when β goes to zero. It was shown earlier that the Rodat et al. [1] experiments were performed at higher volumetric flow rates, and the scaled velocities due to buoyancy effects and the average velocities were on the same order of magnitude. This suggests that a PFR may also be appropriate to model the reactor by Rodat et al. [1] because buoyancy forces may be outweighed with forced flow. Three different sets of kinetic parameters k_0 and E_a were considered for the PFR. These are given in Table 3.9. The results are shown in Figure 3.16.

Table 3.9 – Kinetic parameters used to compare the PFR with the experimental data by Rodat et al. [1].

Model	k_0 **(1/s)**	E_a **(kJ/mol)**	**Source**
Case 1	1.20×10^5	177.8	PFR kinetics
Case 2	5.43×10^{15}	420.7	CPMR kinetics
Case 3	1.47×10^8	205	Rodat et al. [37]

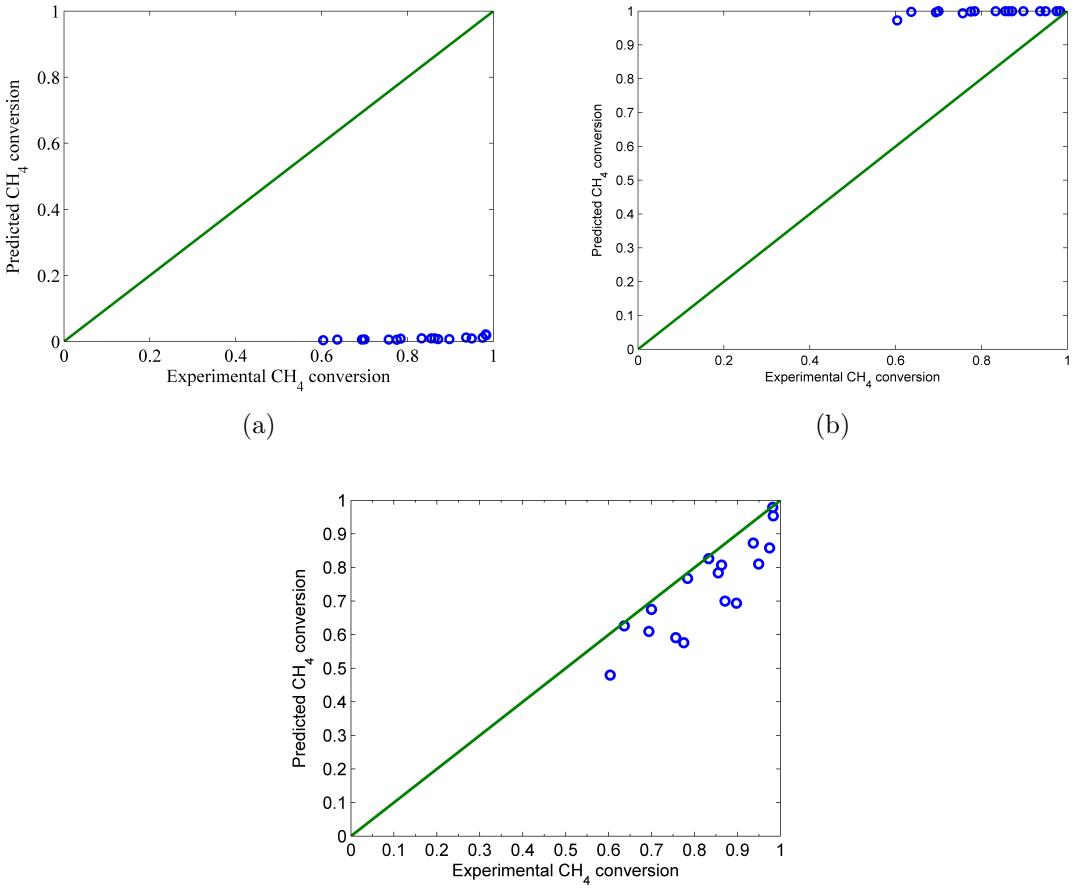

Figure 3.16 – Comparison of PFR numerical results to the data given by Rodat et al. [1] for (a) Case 1, (b) Case 2, and (c) Case 3.

In Case 1 the PFR predicts near zero conversion for all datapoints. Case 2 predicts near 100% conversion for all datapoints. Case 3 predicts within 10.7% average error with a standard deviation of 8.7%. The kinetics from Case 3 were taken from Rodat et al. [37], wherein Rodat et al. used a PFR model to determine the kinetic parameters for the reactor. The author used two PFR in series, with one of them being in the isothermal zone and the other in the cooling zone. It is shown graphically in Rodat et al. [1], however, that the CH_4 conversion occurs in the isothermal zone.

Thus the CPMR model has a slightly smaller average error than the PFR in predicting the results by Rodat et al. [1]. All three models are beneficial for the analysis of experimental reactors studied in literature. The PFR is appropriate for high flow and low cross-sectional area tubular reactors, where buoyant forces are outweighed by the forced flow. The CPMR is optimal for low flow with larger cross-sectional areas where buoyant forces play a major role. The CPMR can be reduced to a PMR by setting β to zero, if needed. The scaled and average velocities are of the same order of magnitude in the case of the reactor studied by Rodat et al. [1], and as such the buoyant and forced convective terms may both be non-negligible. Therefore the CPMR and PFR models would both be appropriate. The reactor studied in this thesis was dominated by buoyant forces, leaving the CPMR model more appropriate for the blank reactor.

3.5.4 Sensitivity plots

The sensitivity of predicted X_{CH_4} to the kinetic parameters k_0, E_a and β were also analyzed for the CPMR, PMR and PFR. The parameters ranged between 50% to 150% of their respective best fit values. The numerical results for E_a are given in Figure 3.17. The maximum difference between conversions for $1.5 \times E_a$ and $0.5 \times E_a$ was essentially 100% for the PFR, PMR and CPMR numeric models respectively. Thus all models have high sensitivity to E_a. The trends showed that less CH_4 conversion is obtained with higher activation energies, as expected.

The numerical results for k_0 are shown in Figure 3.18. As can be seen, the variation of k_0 had a smaller effect on predicted conversion for all three models than E_a. The variation between the maximum and minimum k_0 for the PFR model reached 34.5% at 1276 K. The PMR and CPMR models showed maximum variations of 24.5% at 1276 K and 13.6% at 1237 K, respectively. The PFR model showed it was slightly more sensitive to a change in k_0 than the PMR or CPMR models. The CPMR model

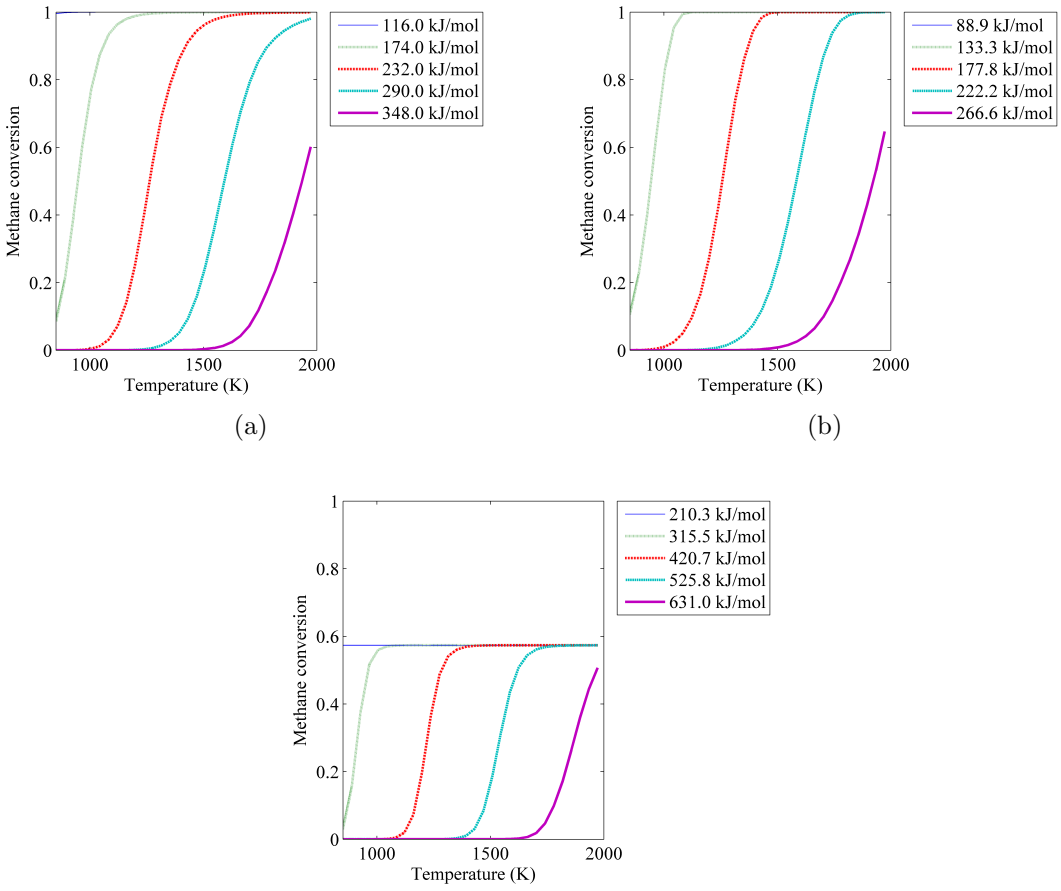

Figure 3.17 – Sensitivity analysis of E_a using corresponding kinetics and model at $\dot{V} = 33$ ccm for the (a) PMR (b) PFR, and (c) CPMR.

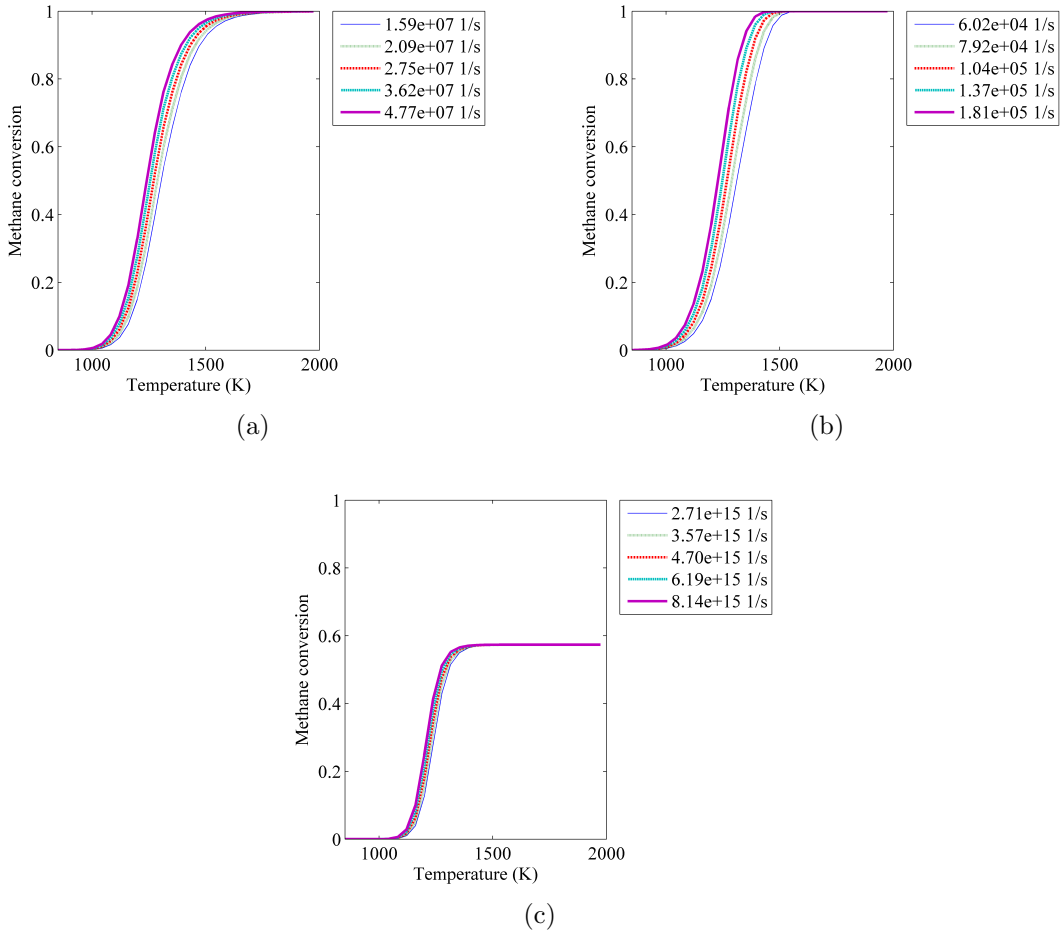

Figure 3.18 – Sensitivity analysis of k_0 at $\dot{V} = 33$ ccm using the (a) PMR model (b) PFR model, and (c) the CPMR model.

showed the smallest sensitivity to k_0, and this is most likely because the β value limits the maximum conversion in the reactor. In all three cases, higher values for k_0 predicted higher conversions.

Finally, the numerical sensitivity analysis for β is shown in Figure 3.19. A maximum difference of 42.6% CH_4 conversion was predicted between $1.5 \times \beta$ and $0.5 \times \beta$. The slope between zero conversion and maximum conversion grew with increasing β. As expected, it was found that with increasing β the maximum capability of the reactor for CH_4 conversion was increased. Therefore designing a reactor that would minimize β would be optimal.

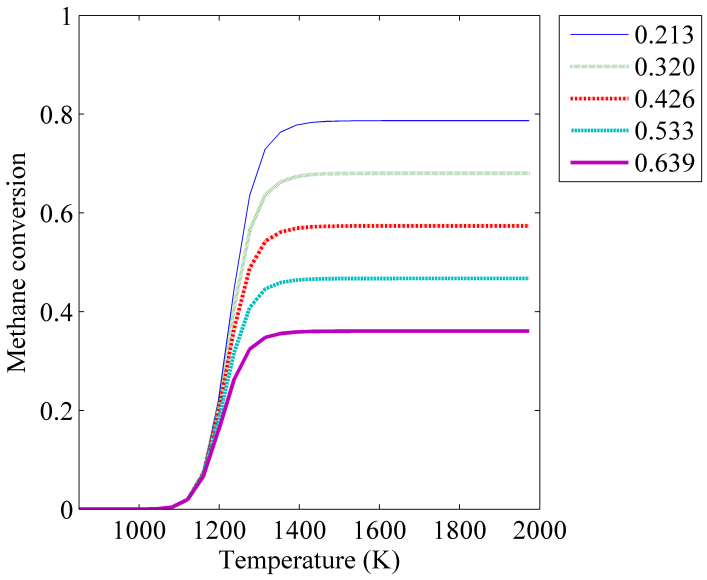

Figure 3.19 – Sensitivity analysis of β using the CPMR model at $\dot{V} = 33$ ccm.

Chapter 4

Molten metal reactor model

In this chapter the numerical model for the molten metal CH_4 cracking reactor is presented and discussed. First, the general assumptions are listed. Then, the general governing equations and boundary conditions for the bubble model are derived. Next, the application of the CPMR numerical model to the gas space above the molten bath is described. Finally, the results of the model are presented and discussed. Figure 4.1 gives a graphical representation of the reactor.

4.1 Assumptions

The following assumptions are used to develop the mathematical model,

- The molten media is a Newtonian fluid.
- The molten media is isothermal at operating temperature due to its high conductivity. A comparison of thermal conductivities shows that at 1373 K, $\gamma_{Sn} =$ 50.3132 W/(m×K) and $\gamma_{H_2} = 0.7094$ W/(m×K). H_2 is the most conductive out of N_2, CH_4, and H_2. Therefore the thermal conductivity for Sn is two orders of magnitude higher than H_2 and will allow for an isothermal bath temperature.
- Diffusion is studied using Fick's first law of diffusion.
- Diffusion coefficient is assumed to be for a CH_4-N_2 gas mixture.
- Nitrogen is assumed to be the solvent because 50% of the mixture is initially N_2 and it does not react.
- The gas does not dissolve into the molten metal.
- The enthalpy of reaction for the general CH_4 cracking equation, h_f, was defined by fitting data given by Holmen et al. [5].

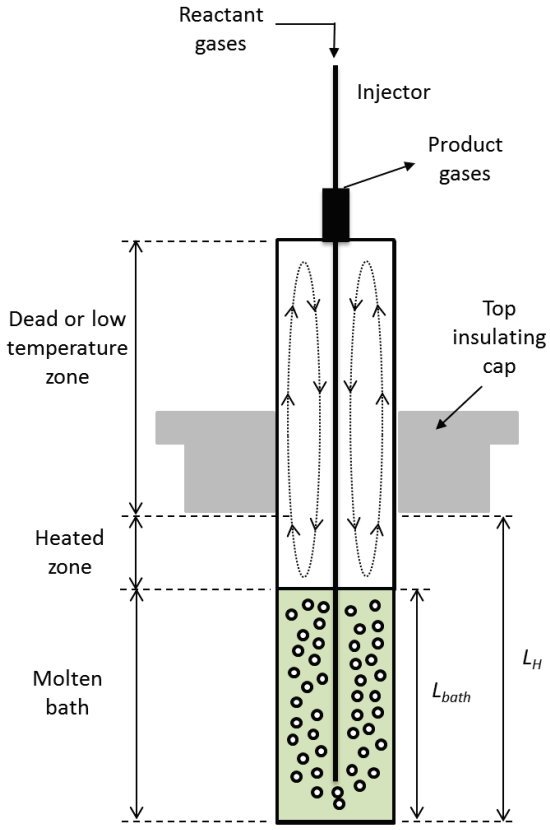

Figure 4.1 – Graphical representation of the molten metal reactor

- The bubble forms and detaches from the injector very quickly such that it is at operating temperature but unreacted at the point of detachment.
- Kinetic model parameters from the CPMR model using the blank reactor results, namely $k_0 = 5.43 \times 10^{15}$ 1/s and $E_a = 420.7$ kJ/mol are applicable (see Chapter 3).
- The volumetric flow rate factor $\beta = 0.426$ as found in Chapter 3 is used.
- The void fraction α is defined as $\tau_{bubble}\dot{V}/V_{bath}$, where τ_{bubble} is the bubble residence time, V_{bath} is the volume of the bath and $\dot{V}$ is the inlet gas volumetric flow rate corrected for temperature and pressure (see Section 4.2.1.6).
- The bubble is assumed to be spherical and have a constant diameter. In future works, the following considerations would have to be included if bubble diameter and shape were allowed to vary:
  - Bubble size change with each step in time due to bubble conversion because two moles of H_2 are produced for every mole of CH_4 consumed,
  - Bubble size change due to change of hydrostatic pressure as the bubble rises,
  - Variations in surface tension as gas composition and temperature changes,
  - Bath and gas pressures, surface tensiona dn bubble curvature are realated via the Lapace equation, defined as $\Delta P_L = \sigma\left(1/R_{bubble,1} + 1/R_{bubble,2}\right)$ [69], where σ is surface tension, and $R_{bubble,1}$ and $R_{bubble,2}$ describe the three dimensional bubble surface curvature.
  - Dynamic fluctuations of bubble shape and path as the bubble rises.

4.2 Mathematical model of molten metal reactor

4.2.1 Bubble model

In this section the phenomena occurring inside the bubble as well as bubble velocity and rise time is analyzed. The governing equations for the mass transport and heat transfer that occur inside the bubble are described. The formulations for predicting bubble size are then presented. Finally, the methodology for determining bubble velocity and rise time is discussed.

4.2.1.1 Mass conservation and transport

The general equation for methane cracking was given in Equation (1.1), and is listed below for reference,

$$CH_{4(g)} \rightarrow 2H_{2(g)} + C_{(s)} \tag{4.1}$$

Assuming a spherical bubble, mass conservation and Fick's law of diffusion, the governing reaction equations are

$$\frac{\partial C_{CH_4}}{\partial t} = \frac{1}{r^2}\frac{\partial}{\partial r}\left(r^2 D_g \frac{\partial C_{CH_4}}{\partial r}\right) - k_o C_{CH_4} \exp\left(-\frac{E_a}{RT}\right) \tag{4.2}$$

$$\frac{\partial C_{H_2}}{\partial t} = \frac{1}{r^2}\frac{\partial}{\partial r}\left(r^2 D_g \frac{\partial C_{H_2}}{\partial r}\right) + 2k_o C_{CH_4} \exp\left(-\frac{E_a}{RT}\right) \tag{4.3}$$

$$\frac{\partial C_T}{\partial t} = -k_o C_{CH_4} \exp\left(-\frac{E_a}{RT}\right) + 2k_o C_{CH_4} \exp\left(-\frac{E_a}{RT}\right) \tag{4.4}$$

where C_{CH_4} is methane concentration, C_{H_2} is hydrogen concentration, C_T is total concentration, D_g is the diffusion coefficient, k_o is the pre-exponential factor, E_a is the activation energy, and R is the ideal gas constant. The N_2 concentration is then obtained as $C_{N_2} = C_T - C_{CH_4} - C_{H_2}$. The associated boundary conditions at the bubble center are

$$N_{r_{bubble},CH_4} = 0 \quad \text{at} \quad r_{bubble} = 0 \tag{4.5}$$

$$N_{r_{bubble},H_2} = 0 \quad \text{at} \quad r_{bubble} = 0 \tag{4.6}$$

where $N_{r,i} = -D_g \frac{\partial C_i}{\partial r_{bubble}}$ is the molar flux for gas species $i = CH_4$ or H_2. Simplifying, the boundary conditions at $r_{bubble} = 0$,

$$\frac{\partial C_{CH_4}}{\partial r} = 0 \quad \text{at} \quad r_{bubble} = 0 \tag{4.7}$$

$$\frac{\partial C_{H_2}}{\partial r} = 0 \quad \text{at} \quad r_{bubble} = 0 \tag{4.8}$$

Similarly, assuming negligible dissolution of gases into the molten metal, the boundary conditions at the bubble surface are

$$\frac{\partial C_{CH_4}}{\partial r} = 0 \quad \text{at} \quad r_{bubble} = \frac{D_{bubble}}{2} \tag{4.9}$$

$$\frac{\partial C_{H_2}}{\partial r} = 0 \quad \text{at} \quad r_{bubble} = \frac{D_{bubble}}{2} \tag{4.10}$$

The initial conditions are

$$C_{CH_4,0} = x_{0,CH_4}\frac{P_{bath,0}}{RT_0} \quad \text{at} \quad t = 0 \tag{4.11}$$

$$C_{H_2,0} = x_{0,H_2}\frac{P_{bath,0}}{RT_0} \quad \text{at} \quad t = 0 \tag{4.12}$$

$$C_{T,0} = \frac{P_{bath,0}}{RT_0} \quad \text{at} \quad t = 0 \tag{4.13}$$

where $P_{bath,0}$ is the gas pressure at the injector outlet. The Laplace pressure is ignored and liquid and gas pressures are assumed in equilibrium. $P_{bath,0}$ is given as

$$P_{bath,0} = \frac{P_0 + \rho_{bath} g L_{I,submerged}}{RT_0} \tag{4.14}$$

where P_0 is the operating pressure, ρ_{bath} is the molten media density at operating temperature, g is the acceleration of gravity, $L_{I,submerged}$ is the starting depth of the bubble in the bath from the free surface, and T_0 is the operating temperature.

4.2.1.2 Heat transfer

The heat transfer governing equation is [59].

$$\rho_{bubble} c_p \frac{\partial T}{\partial t} = \frac{1}{r^2}\frac{\partial}{\partial r}\left(r^2 \gamma_{bubble} \frac{\partial T}{\partial r}\right) - h_f k_o \exp\left(-\frac{Ea}{RT}\right) C_{CH_4} \tag{4.15}$$

where ρ_{bubble}, c_p , and γ_{bubble} is the density, specific heat capacity, and thermal conductivity of the gas bubble, respectively. h_f is the heat of formation of CH_4 and is a function of temperature [5]. The associated boundary conditions are given as

$$\frac{\partial T}{\partial r} = 0 \quad \text{at} \quad r = 0 \tag{4.16}$$

$$\gamma_{bath} \frac{\partial T}{\partial r} = h(T_0 - T_s) \quad \text{at} \quad r = R \tag{4.17}$$

where γ_{bath} is the thermal conductivity of the molten bath, T_0 is the operating temperature of the molten media, T_s is the temperature of the gas at the bubble surface. The convection coefficient, h, was assumed to be 20 W/(m^2 K). In literature, the range for natural convection in a gas in literature is 5 to 30 $W/(m^2K)$ [59]. The property values for Sn, CH_4, N_2, and H_2 are given in Appendix A.

In Section 2.5.1 it was shown that at steady state the injector gas would be a maximum of 47 K less than the the reactor wall temperature, when the reactor wall was at operating temperature. Therefore the initial condition for the temperature was set to

$$T_{bubble} = T_0 - 47 \text{ K} \quad \text{at} \quad t = 0 \tag{4.18}$$

Table 4.1 – Input option parameters for `pdepe()` solver

Criteria	Default setting	Current setting
$RelTol$	1×10^{-3}	1×10^{-8}
$AbsTol$	1×10^{-6}	1×10^{-10}
$tspan$	-	$[0\ \tau_{bubble}]$
$tspan_{count}$	-	100
$rspan$	-	$[0\ D_{bubble}]$
$rspan_{count}$	-	25

4.2.1.3 Numerical solution

Equations (4.2), (4.3), (4.4), and (4.15) with boundary conditions (4.7) - (4.10), (4.16) (4.17) and initial conditions (4.11) - (4.13), (4.18) were solved using the transient partial differential equation (PDE) solver `pdepe()` in MATLAB.

The `pdepe()` MATLAB solver is made to solve 1D parabolic-elliptic PDE problems. Initial conditions and boundary conditions are inputed. The solver discretizes the PDE's into ordinary differential equations in space to determine approximate solutions [66]. The solver uses MATLAB's ode15s to perform time integration [66]. The mesh that the solver uses is user inputed. The time span inputed by the user only defines at what time steps the `pdepe()` solver outputs information. Otherwise the solver determines the time steps dynamically [66]. The convergence criteria, timespan and xmesh inputs are given in Table 4.1. $tspan$ is the range of time overwhich the solver operates, and $tspan_{count}$ is the number of data points in the time span. $rspan$ is the bubble radius over which the solver creates the mesh, and $rspan_{count}$ is the number of nodes in the mesh.

4.2.1.4 Bubble formation and size

A review on bubble formation was made by Kulkarni and Joshi [70]. Several formulations have been proposed to predict bubble formation for tubular injectors orientated upwards. However, in this thesis the injector is pointing downwards, and few studies have been performed for this orientation [9]. Many different liquid mediums have been studied, including methanol, ethanol, propanol, isopropanol, glycerol, potassium chloride [71], as well as glucose and molten copper [9, 70–72]. Bubble formation in molten $NaOH$ using a downwards pointing nozzle has been studied by Tsuge et al. [9] using distilled water. Distilled water has similar fluid physical properties to molten salt, including the Morton number, Mo, at 773 K [73]. The Morton number

is a dimensionless value that groups the effects of liquids, in terms of their physical properties, on bubble shape and motion. Mo is given as

$$Mo = \frac{g\mu_{bath}^4}{\rho_{bath}\sigma^3} \tag{4.19}$$

where μ_{bath}, ρ_{bath} and σ are the dynamic viscosity, density and surface tension of the molten media, respectively.

Thus far a formulation to predict bubble size in molten Sn has not been found in known literature. All known formulations do not apply to the reactor studied in this thesis because factors such as Mo, injector direction, injector dimension, and temperature fall out of range. Two correlations have been taken to give an approximation for the order of magnitude of bubble size. After which a sensitivity analysis is performed to determine the effect of bubble size on molten metal CH_4 cracking. Recommendations are then made for bubble sizes to obtain desired CH_4 conversion. The models are as follows.

Tate's Law

Park et al. [8] used what is referred to as Tate's law to predict bubble sizes [74]. Tate's law was derived by equating the surface tension and buoyant forces in order to find the bubble volume. The assumptions were

- No vicious effects
- The injector / capillary tip is directed upwards in the liquid
- The angle of the bubble surface to the injector wall at the point of intersection is 180°, thus allowing the direction of the surface tension to be parallel to the tube wall.
- Bubble is spherical
- Bubble is attached at orifice OD
- Low flow rate. A study done on an air-water system by Blanchard and Syzek in 1977 suggests that bubble frequency formation should be less than 30 bubbles per minute [75]. The bubbles tend to deform at frequencies higher than this. The study by Blanchard and Sysek used Tate's law for low flow-rate applications and ranged orifice sizes between 0.1-1000 μm.
- Orifice diameter is small (less than 3 mm) [75]

- No bubble coalescence
- Bubble density is constant.

Buoyancy force, F_b, bubble weight, F_w, and surface tension force S_t are given as

$$F_b = \frac{\pi D_{bubble}^3}{6}\rho_{bath}g \tag{4.20}$$

$$F_w = \frac{\pi D_{bubble}^3}{6}\rho_{bubble}g \tag{4.21}$$

$$S_t = \pi D_{I,in}\sigma \tag{4.22}$$

where D_{bubble} is bubble diameter, ρ_{bath} is the density of the molten bath, ρ_{bubble} is the density of the bubble, g is gravity, $D_{I,in}$ is the inner tube diameter, and σ is bubble surface tension. A balance of force in the vertical direction gives

$$F_b - F_w - S_t = 0 \tag{4.23}$$

Substituting Equations (4.20), (4.21) and (4.22) into (4.23) and simplifying gives the following equation for bubble diameter, noting that $V_{bubble} = 1/6\pi D_{bubble}^3$.

$$D_{bubble} = \left(\frac{6D_{I,in}\sigma}{g\Delta\rho}\right)^{1/3} \tag{4.24}$$

The assumption of a vertically-directed injector gives rise to significant errors in results. Blanchard and Syzek [75] showed that 15 μm capillary tips directed 10 degrees from the vertical line give actual bubble diameters 8% smaller than the theory. Capillary tips with radii of approximately 4 μm directed 25-30 degrees from the vertical line gave bubble diameters 18% smaller than predicted. Blanchard and Syzek [75] suggested that prior studies have shown as much as $\pm$30% error for actual bubble sizes compared to theoretical predictions. These deviations are caused by variations on tip geometry. Injectors pointing downwards tend to produce larger bubbles with smaller growth rates [70] than injectors pointing upwards [70]. In the methane cracking apparatus, the tube and 7 μm porous injector are directed downwards into the molten media. Therefore larger errors from theory are possible for our case.

The assumption that 30 bubbles per minute are being formed is also most likely not being met in the molten metal reactor studied in this thesis. This would most likely lead to bubble deformation and coalescence. Finally, the assumption that the direction of surface tension force of the bubble connecting to the injector tube is parallel to the tube wall is probably incorrect. These failings in meeting assumptions lead to error in bubble size determination, such that Equation (4.24) provides an

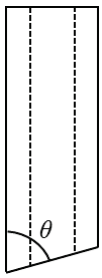

Figure 4.2 – Injector tip angle

approximation of bubble size.

Formulation by Tsuge et al.

The model suggested by Tsuge et al. [9] gives a correlation that covers operating conditions of $54 \leq \dot{V} \leq 630$ ccm and $3 \leq D_I, out \leq 8.8$ mm, and a $Mo \sim 1 \times 10^{-11}$. Tsuge et al. [9] found the following empirical correlation for bubble volume

$$\frac{V_{bubble}}{D_{I,in}^3} = 7.32\left(\frac{D_{I,out}}{D_{I,in}}\right)^{0.63}\left(\frac{\theta}{\theta_0}\right)^{0.40}\left(\frac{\dot{V}^2}{D_{I,out}^5 g}\right)^{0.29} Bo^{-0.17} Ga^{-0.032} \tag{4.25}$$

where V_{bubble} is bubble volume, $D_{I,in}$ is the inner orifice or injector tube diameter, $D_{I,out}$ is the outer diameter of the orifice or injector tube, θ is the edge angle of the nozzle, $\theta_0 = \pi/2$ is reference edge angle of the nozzle, $Bo = \rho_{bath} D_{I,in}^2 g/\sigma_{bath}$ is the Bond number, and $Ga = \rho_{bath}^2 D_{I,in}^3 g/\mu_{bath}^2$ is the Galilei number. The model assumed single bubble formation. The injector angle θ is shown in Figure 4.2. In this thesis, the edge angle of the nozzle does not change from the reference angle of $\pi/2$. Therefore the correlation becomes

$$\frac{V_{bubble}}{D_{I,in}^3} = 7.32\left(\frac{D_{I,out}}{D_{I,in}}\right)^{0.63}\left(\frac{\dot{V}^2}{D_{I,out}^5 g}\right)^{0.29} Bo^{-0.17} Ga^{-0.032} \tag{4.26}$$

The bubble diameter for a spherical bubble is then calculated by

$$D_{bubble} = \left(\frac{6}{\pi} V_{bubble}\right)^{1/3} \tag{4.27}$$

The formulation was found to have approximately 35% error using over 700 experimental data points.

4.2.1.5 Bubble velocity and rise time

Empirical, semi-empirical and theoretical approaches have been made for determining bubble rise velocity. A comprehensive review of these methods is given by Kulka-

rni and Joshi [70]. Semi-empirical methods to calculate bubble velocity use a force balance and estimate the drag coefficient based off of experimental data. The semi-empirical method was chosen for this thesis because the theory is well developed for low Re regimes [70]. Recognizing that $A = \frac{1}{4}\pi D_{bubble}^2$ is the frontal area of a spherical bubble, the drag force is given by

$$\begin{aligned} F_d &= \frac{1}{2} c_D \rho_{bath} v^2 A \\ &= \frac{\pi}{8} c_D \rho_{bath} v^2 D_{bubble}^2 \end{aligned} \tag{4.28}$$

where ρ_{bath} is the density of the molten bath, v is bubble velocity and c_D is the drag force coefficient. The latter variable depends on the value of Re. The following assumptions were made for calculating the terminal velocity of the bubble:

- The system is at steady state
- There is no interaction between bubbles (no bubble coalescence [76])
- All bubbles are spherical
- Properties in the molten metal are uniform.
- The molten metal is Newtonian

The free body diagram of the bubble is given in Figure 4.3. The buoyancy force is calculated as

$$F_b = \frac{\pi D_{bubble}^3}{6} \rho_{bath} g \tag{4.29}$$

The weight of the bubble is given by

$$F_w = \frac{\pi D_{bubble}^3}{6} \rho_{bubble} g \tag{4.30}$$

where ρ_{bubble} is the density of the bubble, and g is gravity. A balance of forces in the vertical direction gives

$$m_{bubble} \frac{dv}{dt} = F_b - F_d - F_w \tag{4.31}$$

Substituting in Equations (4.28), (4.29), and (4.30) and simplifying

$$\begin{aligned} m_{bubble} \frac{dv}{dt} &= \frac{\pi D_{bubble}^3}{6} \rho_{bath} g - \frac{\pi}{8} c_D \rho_{bath} v^2 D_{bubble}^2 - \frac{\pi D_{bubble}^3}{6} \rho_{bubble} g \\ \frac{dv}{dt} &= \frac{\pi}{m_{bubble}} \left[\frac{D_{bubble}^3}{6} g(\rho_{bath} - \rho_{bubble}) - \frac{1}{8} c_D \rho_{bath} v^2 D_{bubble}^2 \right] \end{aligned} \tag{4.32}$$

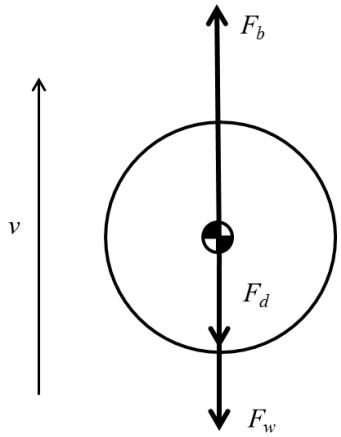

Figure 4.3 – Free body diagram of a bubble

If it is assumed that the bubble reaches terminal velocity very quickly, then $\frac{dv}{dt} = 0$. The equation then simplifies to

$$\begin{aligned} v^2 &= \frac{4gD_{bubble}(\rho_{bath} - \rho_{bubble})}{3c_D\rho_{bath}} \\ v &= \left[\frac{4gD_{bubble}(\rho_{bath} - \rho_{bubble})}{3c_D\rho_{bath}}\right]^{1/2} \end{aligned} \tag{4.33}$$

And in the case of negligible transient effects in bubble rise velocity, the bubble residence time was estimated using

$$\tau_{bubble} = \frac{L_{bath}}{v} \tag{4.34}$$

where L_{bath} is the height of the molten metal bath. The assumption that the transient effects of bubble rise time is negligible is verified later in Section 4.2.2, following the derivation of the bubble drag coefficient.

4.2.1.6 Bubble drag coefficient

Several formulations for c_D were included in the review by Kulkarni and Joshi [70]. The studies were performed in a variety of liquids, including water, 2-propanol, ethyl ether, pyridine, nitrobenzen, aniline, acetone, n-butanol, methanol, benzene, toluene, ethyl acetate, cotton seed oil, glacial acetic acid, mercury, molten silver, and different concentrations of glycerin in water [70]. Newtonian and non-Newtonian liquids have been considered. Most tests in literature use tap water [77]. Bubble rise in Newtonian liquids is dependent on bubble size, pressure, temperature and extent of contamination. Thus bubble rise is dependent on gravity, buoyancy and drag forces

only. Contaminants have a large effect on bubble rise characteristics and reduce bubble terminal velocity [70].

Ford and Loth [78] report that bubbles less than 1 mm in diameter tend to be spherical and act as rigid particles. Bubble velocity increases with bubble diameter in this region. At a large enough diameter, significant bubble deformation into ellipsoidal shapes causes the bubbles to move in helical or sinusoidal trajectories. Thus at this point the terminal velocity is adversely affected by increasing bubble size. Kulkarni and Joshi [70] summarized three distinct regions which determine bubble shape. The first is at low Re and is viscosity dominated. Rigid spherical bubbles are maintained and velocity increases with increasing bubble diameter. The second region is surface tension dominated and bubbles leave their spherical state. The terminal velocity is no longer directly related to bubble diameter in this region. In the final region the bubble velocity is inertia dominated. The bubble deforms into a spherical capped or bullet shape. Velocity increases with the equivalent diameter in this regime. No mention is made of the bubble following a helical path however, and so perhaps the vertical terminal velocity is adversely affected.

Rodrigue [6] derived an equation that is applicable to all Newtonian viscous and non-viscous fluids for any bubble volume. The author compiled a database of 2207 points from literature. Gas bubbles composed of air, CO_2, N_2, N_2, He, CH_4, $N_2O\backslash N_2$, and $N_2O\backslash H_2$ were included. Water, glycerin\water, ethyl alcohol, mercury, and molten silver were included for the median through which the gases were bubbled. The resulting formulation was

$$c_D = \frac{16}{Re} \frac{\left(1 + 0.02\left(\left[\frac{3}{4}c_D Re^2 Mo\right]^{8/9}\right)^{10/11}\right)^{10/11}}{\left(1 + 1.31 \times 10^{-5} Mo^{11/20}\left(\left[\frac{3}{4}c_D Re^2 Mo\right]^{8/9}\right)^{73/33}\right)^{21/176}} \tag{4.35}$$

Rodrigue [6] found that Equation (4.35) fit over 13 orders of magnitude difference in Mo. The formulation was found to have an average of 10% deviation from experimental data for a range of 18 decades of Mo. Equation (4.35) was solved for various Re against data to verify proper implementation, as shown in Figure 4.4.

The majority of studies were for single bubbles. Studies applicable to bubble swarms are very sparse [7, 70, 79]. Two articles of note for bubble swarms were considered applicable to this thesis. Kendoush [79] attempted to find an analytical

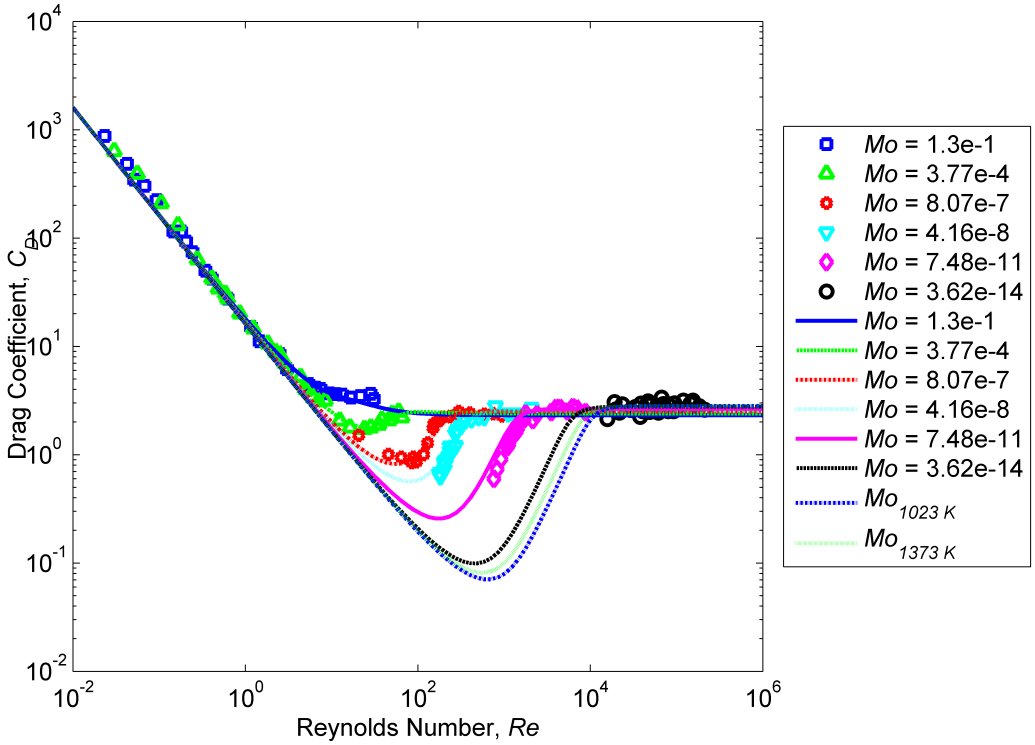

Figure 4.4 – Verification of proper implementation of Equation (4.35) against data in Rodrigue [6]

solution that assumed a steady state flow of spherical bubbles in a swarm. It was found that the drag coefficient could be defined by the following relation

$$c_D = \frac{48}{Re(1-\alpha)^2} \tag{4.36}$$

where α is the void fraction. Assuming the transient effects of bubble velocity are negligible, the void fraction is calculated by

$$\alpha = \tau_{bubble}\frac{\dot{V}}{V_{bath}} \tag{4.37}$$

where $V_{bath} = A_c L_{bath}$ is the volume of the bath. $\dot{V}$ is the inlet gas volumetric flow rate and is corrected by temperature and pressure using Equation (3.63). For simplicity, X_{CH_4} in the bubble is neglected in this calculation, giving

$$\dot{V} = \dot{V}_{ref}\left(\frac{P_{ref}}{P_0}\right)\left(\frac{T_0}{T_{ref}}\right) \tag{4.38}$$

where T_{ref} and P_{ref} are the reference temperature and pressure at which the inlet volumetric flow rate, V_{ref}, is measured. Kendoush [79] showed that Equation (4.36) was in accordance with experimental data and other analytical expressions found in literature. The author suggests that the applicable range for Equation (4.36) is $1 \leq Re \leq 100$, and that $0 \leq \alpha \leq 0.3$ in practicality, though for maximum packing α can reach 0.779.

Kishore et al. [7] performed an analysis on bubble swarms in power-law media, which is a type of non-Newtonian fluid. A non-Newtonian fluid is where "the shear stress is not linearly proportional to the shear strain rate"[80]. Thus the fluids can be shear thinning, meaning they become less viscous as the fluid is in motion, or shear thickening, where they become more viscous as the fluid moves. The study was created for a range of $0.6 \leq n_{power} \leq 1.6$, $1 \leq Re \leq 200$ and $1 \leq Sc \leq 1000$. The Schmidt number, Sc, is given by

$$Sc = \frac{m_{power}}{\rho_{bath} D_0}\left(\frac{v}{D_{bubble}}\right)^{n_{power}-1} \tag{4.39}$$

where D_0 is the molecular diffusivity in [m^2/s], m_{power} is the power-law fluid consistency index and n_{power} is the power-law behavior index. The following relationship was found for overall drag coefficient [7],

$$c_D = \left(\frac{2^{2n_{power}+2}}{Re}\right)\left(\frac{1}{1-\alpha^{1/(n_{power}+2)}}\right)\times$$

$$\left[1.03 + 0.009Re^{0.9}(1-\alpha)^{0.3} - 0.108Re^{(n_{power}-1)/n_{power}}(1-\alpha)^3\right] + \left(\frac{0.79}{0.3 + 0.11Re^{0.89}((1-\alpha)^{-(15n_{power}-7)}}\right) \tag{4.40}$$

Setting $n_{power} = 1$ for a Newtonian fluid, the equation becomes

$$c_D = \left(\frac{16}{Re}\right)\left(\frac{1}{1-\alpha^{1/3}}\right)\left(1.03 + 0.009Re^{0.9}(1-\alpha)^{0.3} - 0.108(1-\alpha)^3\right) + \left(\frac{0.79}{0.3 + 0.11Re^{0.89}((1-\alpha)^{-8}}\right) \tag{4.41}$$

Kishore et al. [7] reports that the maximum error of Equation (4.40) is 29.83%.

The results of Rodrigue [6], Kendoush [79] and Kishore et al. [7] are shown in Figure 4.5. In Figure 4.5(a), the drag coefficient for a single spherical bubble for three different formulations are compared against the experimentally determined drag coefficient for a solid smooth sphere. It was found that the results calculated using the formulations by Rodrigue [6] and Kishore et al. [7] for $\alpha = 0$ agree fairly well. The results by Kendoush are higher by up to one order of magnitude. The curve by Rodrigue extends past $Re = 100$ and predicts a higher drag coefficient than that of a solid sphere. The curves from Kishore et al. and Kendoush match more closely at a void fraction of 0.3 in Figure 4.5(b). In Figure 4.5(c) it is clear that the drag coefficient is reduced as the void fraction is decreased.

In this thesis, a mixture of the formulations by Kishore et al. and Rodrigue is used to approximate the drag coefficient in this thesis. However a sudden drop in the drag coefficient from the Kishore et al. curve to the Rodrigue curve would occur at $\alpha = 0.3$ and $Re = 200$ if the range of $1 \leq Re \leq 200$ was used for the Kishore et al. curve. Therefore it was assumed that the curve approximated by Kishore et al. could be extrapolated to the point at which it intersects the curve predicted by Rodrigue. An example at 1373 K is shown in Figure 4.6.

Kishore et al.'s formulation allows for a range of void fractions. This is favorable because various flow rates are used in this thesis. Rodrigue showed that the drag coefficient for a single bubble at higher Re is larger than what has been experimentally determined for a solid smooth sphere (see Figure 4.5). This phenomena is most likely due to bubble deformation which increases drag. Due to the lack of bubble swarm formulations in literature at higher Re numbers, the curve presented for a single bubble by Rodrigue [6] was used for higher Re. The drag coefficients by Kishore et al. for

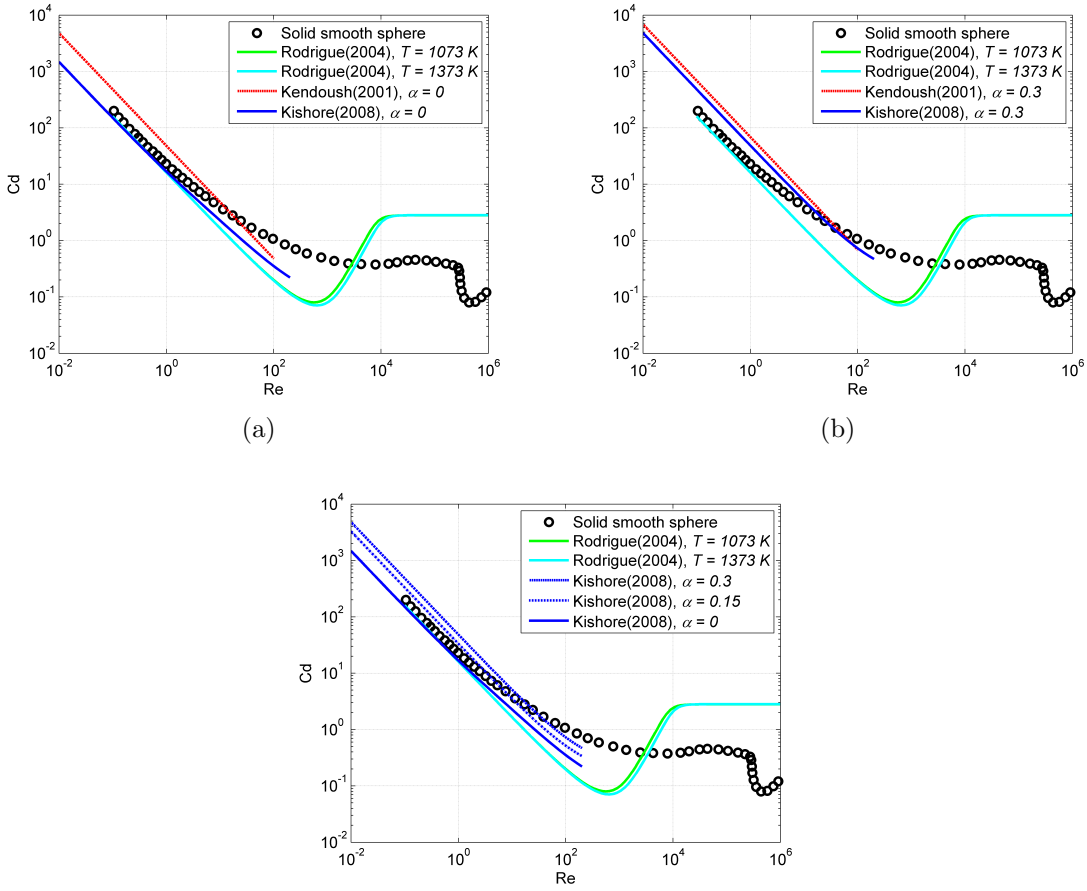

Figure 4.5 – Comparison of the drag coefficient curves from literature, where (a) considers single bubble flow (b) compares single bubble flow with $\alpha = 0.3$, and (c) comparison of different α for Kishore et al. [7].

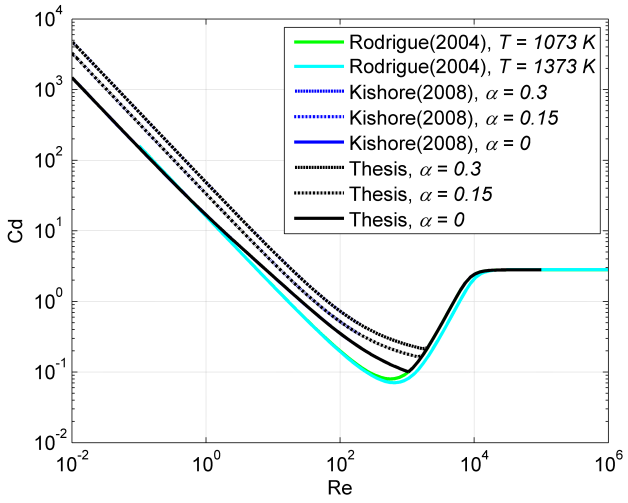

Figure 4.6 – Assumed drag coefficient curve at $T_0 = 1373$ K

bubble swarms were higher than what was reported by Rodrigue for a single spherical bubble. If this pattern continues at higher Re, then the drag for a bubble swarm will be larger again than what is calculated using Equation (4.35). This should result in a more conservative calculation in CH_4 conversion at higher Re because the model will predict lower-than-actual residence times. Finally, Kendoush [79] suggested that in practicality α would not exceed 0.3. Therefore α was bounded to $0 \leq \alpha \leq 0.3$.

4.2.2 Transient bubble velocity effects

Transient bubble velocity was determined assuming that

$$\frac{dv}{dt} = \frac{v_{i+1} - v_i}{\Delta t} \tag{4.42}$$

where v_{i+1} is bubble velocity at $t = t_{i+1}$, and $\Delta t = t_{i+1} - t_i$. Therefore, Equation (4.32) becomes

$$\frac{v_{i+1} - v_i}{\Delta t} = \frac{\pi}{m_{bubble}} \left[\frac{D_{bubble}^3}{6} g(\rho_{bath} - \rho_{bubble}) - \frac{1}{8} \rho_{bath} D_{bubble}^2 c_{D,i} v_i^2 \right] \tag{4.43}$$

where $c_{D,i}$ and v_i are the drag coefficient and velocity at time t_i. Rearranging,

$$v_{i+1} = \frac{\pi}{m_{bubble}} \left[\frac{D_{bubble}^3}{6} g(\rho_{bath} - \rho_{bubble}) - \frac{1}{8} \rho_{bath} D_{bubble}^2 c_{D,i} v_i^2 \right] \Delta t + v_i \tag{4.44}$$

The initial conditions were set to $t_0 = 0$ s and $v_0 = 0$ m/s. The problem was solved using MATLAB R2012a, with various bubble diameters of $1 \times 10^{-2} m$, 1×10^{-3}

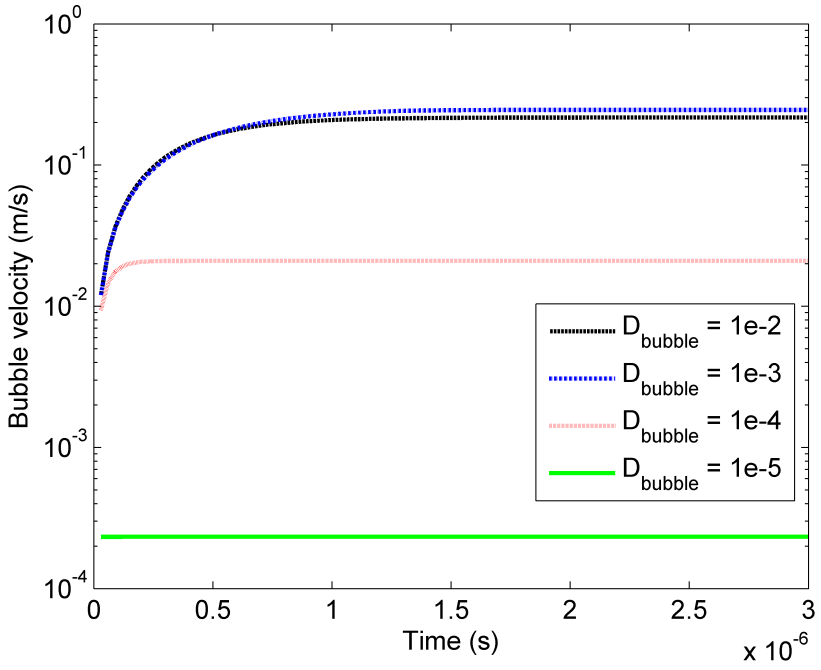

Figure 4.7 – Transient bubble velocity for various bubble diameters at $T_0 = 1173$ K and $\alpha = 0.3$.

m, 1×10^{-4} m, and 1×10^{-5} m. The time differential Δt was set to 1×10^{-10} s, and with a time span of $t_{range} \in [0 \quad 0.3 \times 10^{-5}]$. The operating temperature was set to $T_0 = 1173$ K, and the void fraction to $\alpha = 0.3$.

The results are shown in Figure 4.7. As can be seen, the bubble reaches terminal velocity within approximately 1×10^{-6} s for the larger bubble sizes, and even faster for the smaller bubble sizes. The problem was also solved using a time differential Δt of 1×10^{-12} s, and the same results were produced. Given that a typical bubble residence time is on the order of 1 to 10 seconds, it was verified that the transient effects of bubble rise time are negligible, and the terminal velocity equation given by (4.33) was used in the molten metal methane cracking model.

4.2.3 Reactor space above molten media

The space above the molten media was modeled using the CPMR numerical model derived in Section 3.2.2. It is expected that the value for β would be different than what was found during Chapter 3. This is because the ratio between the low temperature or bypass against the heated zone is much larger in the molten CH_4 cracking reactor than in the blank reactor due to the molten tin taking up space. Therefore

the high buoyancy forces experienced in this section would reduce the residence time of the reactant gas in the high temperature zone. However, because no experimental data exists to determine this β, the value from the CPMR model in Chapter 3 was used.

The CPMR model was implemented using the end results of the bubble model as the bubble exits the molten media. Thus x_{CH_4} at the inlet of the CPMR model was set to be equal to the value of x_{CH_4} at the bubble model outlet. The same experimentally measured temperature profiles in Section 2.3 were assumed to be applicable because no experimental data was available. It was assumed that the gas from the bubble reaches the temperature profile temperature very quickly after the bubble exits the molten metal. This assumption was verified in Section 2.5.1, where in the blank reactor the gas inside the reactor after the injector was within 13 K of the reactor wall temperature at steady state. The effective temperature was calculated using the same approach defined in Section 3.1.1. The actual heated length of the CPMR section above the molten media was calculated using

$$L_{H,above} = L_H - L_{bath} \tag{4.45}$$

where L_H was the total heated length of the reactor, and L_{bath} is the height of the molten bath. L_H was determined still using the equation (3.10).

4.2.4 Solution procedure

A flow chart showing the methodology for solving the molten metal CH_4 cracking model is shown in Figure 4.8. The input variables are first initialized, including reaction parameters, reactor dimensions, and operating conditions. These parameters are given in Table 4.2. The bubble size is then determined using either the formulation by Tate [8] or by Tsuge et al. [9]. An initial guess for bubble velocity is made using Equation (4.33) assuming an initial drag coefficient of 1. τ_{bubble} and α are calculated using Equations (4.34) and (4.37). Following this, `fsolve()` is used to solve for v using the following Equation for the residual:

$$res_v = v_{old} - v_{new} \tag{4.46}$$

where v_{old} is the previous value for velocity, and v_{new} is the newly calculated value for velocity. The function must find a match between Re, c_D and v, because $Re = Re(v)$, $v = v(c_D)$ and $c_D = c_D(Re)$. The tolerance for obtaining res_v from the

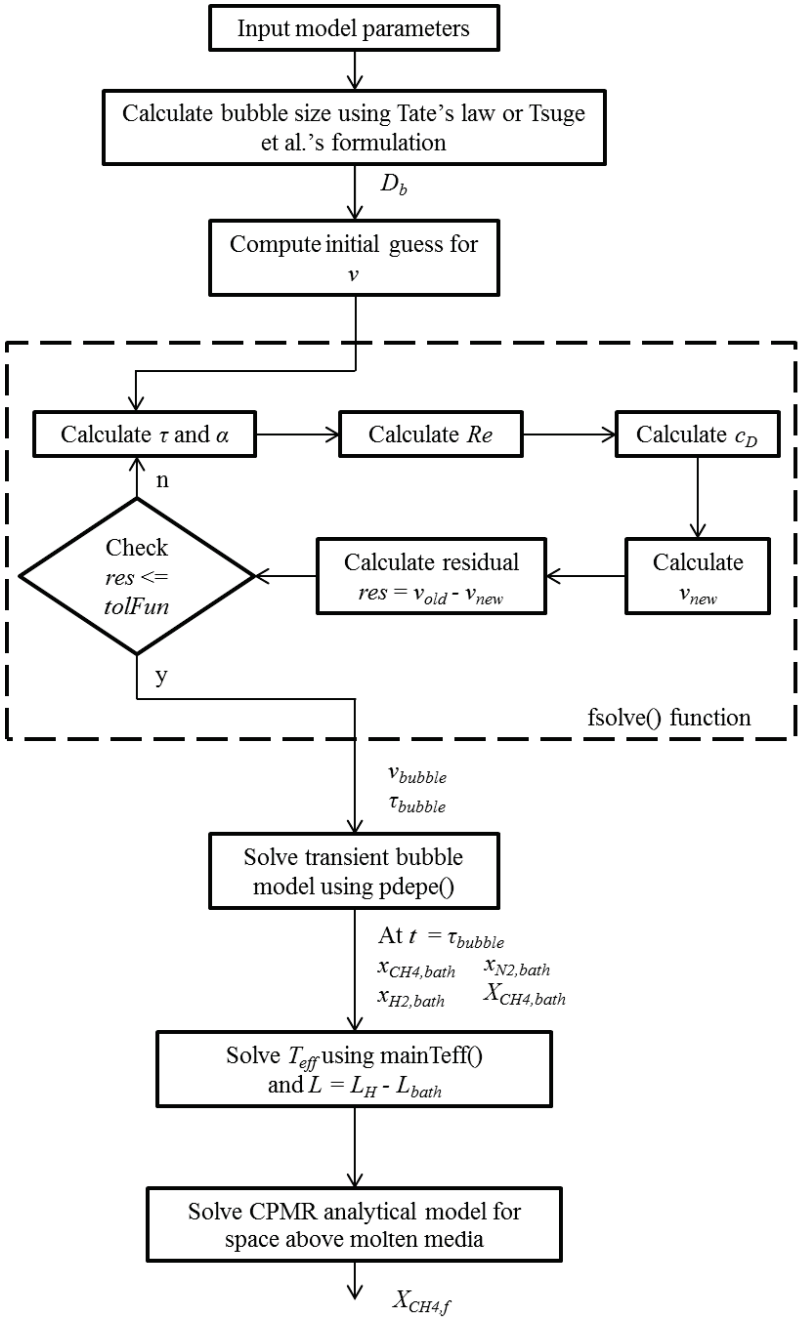

Figure 4.8 – Flow chart for sequence of events in solving the molten metal reactor model

Table 4.2 – Input parameters for the molten metal reactor model

Parameter	Default setting
k_0	5.43×10^{15} 1/s
E_a	420.7 kJ/mol
β	0.426
P_0	101325 kPa
L_r	0.508 m
L_{bath}	0.203 m
$D_{r,in}$	0.04455 m
L_b	0.218 m
L_d	0.292 m
L_a	0.204 m

`fsolve()` function was set to $TolFun = 1 \times 10^{-10}$, with the minimum tolerance to change between steps to $TolX = 1 \times 10^{-8}$. The PCG iteration termination tolerance was set to 1×10^{-6}, from the default of 0.1.

Once bubble velocity and residence time are determined, the spherical bubble model is solved using `pdepe()` in MATLAB. The function `mainTeff()`, discussed in Section 3.1.1, is then executed over the length reactor above the molten metal to obtain an effective temperature for the CPMR model. Following this, the values for CH_4 conversion and gas mole fractions at the time that the bubble exits the molten media, or $t = \tau_{bubble}$, were inputed into the CPMR model. Finally, total CH_4 conversion was obtained using the following

$$X_f = 1 - (1 - X_{CPMR})(1 - X_{bubble}) \tag{4.47}$$

where X_{CPMR} and X_{bubble} are the CH_4 conversion that occurred in the heat blank space above the molten metal and in the bubble before exiting the bath, respectively.

4.3 Results and discussion

4.3.1 Bubble model

In this section the bubble model parameters are varied to ensure that the model performs as expected. The bubble size for the quartz sparger and 6.35 mm tube injectors are estimated, as well as other injector orifice diameters. The effects of volumetric flow rate on bubble rise parameters c_D, τ_{bubble}, α, and v are analyzed next. The variance of bubble diameter with changing flow rate is also studied. Following

Table 4.3 – Orifice diameters for various injectors

Case	$D_{I,in}$ [m]	$D_{I,out}$ [m]
1	8.8×10^{-3}	11.0×10^{-3}
2	3.18×10^{-3}	6.35×10^{-3}
3	1.0×10^{-4}	$n_f \times 1.0 \times 10^{-4}$
4	1.0×10^{-5}	$n_f \times 1.0 \times 10^{-5}$
5	7.0×10^{-6}	$n_f \times 7.0 \times 10^{-6}$
6	5.0×10^{-7}	$n_f \times 5.0 \times 10^{-7}$

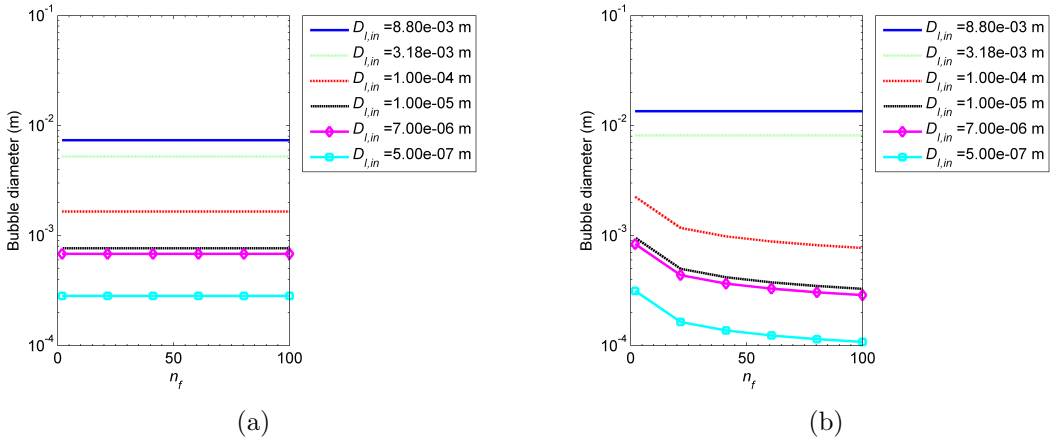

Figure 4.9 – Calculating bubble diameter using (a) Tate's law [8], and (b) the formulation by Tsuge et al. [9]

this, the effects of changing bubble diameter on c_D, τ_{bubble}, α, and v is determined. Finally, the uniformity of mass transport and heat transfer with respect to bubble radius is characterized.

4.3.1.1 Bubble size estimation

Tate's law [8] and the formulation by Tsuge et al. [9] were used to calculate bubble diameters for various inner orifice or injector tube diameters, $D_{I,in}$. The dimensions for Cases 1 through 6 are given in Table 4.3. $D_{I,in}$ was known only for Cases 1 and 2. $D_{I,out}$ was estimated for the porous Cases 3 through 6 by multiplying $D_{I,in}$ with a factor n_f. The bubble diameters were then calculated over $2 \leq n_f \leq 100$. Tsuge et al. [9] studied the Case 1 tube injector for bubbles in molten $NaOH$. The tube injector in Case 2 is studied in this thesis. Case 5 represents the quartz injector that was used in this thesis. The results are shown in Figure 4.9.

As expected, Tate's law does not show any effect resulting from the factor n_f. However, the formulation by Tsuge et al. [9] shows variations of 1.5×10^{-3}, 6.3×10^{-4}, 5.5×10^{-4}, and 2.1×10^{-4} for Cases 3 through 6. The formulation by Tsuge et al. was created for ranges of $54 \leq \dot{V} \leq 630$ ccm and $3 \leq D_{I,out} \leq 8.8$ mm, and a $Mo \sim 1 \times 10^{-11}$. In this thesis, Mo is on the order of 1×10^{-14}, and $D_{I,out}$ is below 3 mm for the quartz sparger. The quartz sparger has a pore size of 4 to 10 μm, as specified by the manufacturer, but the dimension $D_{I,out}$ is an unknown. Either formulation predicts the same order of magnitude for the bubble size, however. Therefore it was decided that Tate's law would be used to determine an order of magnitude to approximate the bubble diameter for the quartz sparger. The formulation by Tsuge et al. was used for injectors where which $D_{I,out}$ is known. Using this assumption, the 6.35 mm injector was estimated to produce bubbles on the order of $D_{bubble} = 8 \times 10^{-3}$ m, and the quartz injector on the order of $D_{bubble} = 700$ μm.

4.3.1.2 Effect of volumetric flow rate on bubble rise

The effect of the total flow rate on bubble diameter, residence time, void fraction, drag coefficient, and bubble velocity was studied for the 6.35 mm tube injector and the quartz sparger. The total flow rate was varied between 5 ccm and 200 ccm. Each run was also performed with temperatures of 1073 K and 1373 K. The quartz sparger was assumed to have a 7 μm average pore size. The formulation by Tsuge et al. [9], given in Equation (4.27), was used to estimate bubble diameter for the 6.35 mm tube injector. Tate's law, given in Equation (4.24), was used to estimate bubble diameter for the quartz injector.

The results for the 6.35 mm tube injector are given in Figure 4.10. The flow rate has an impact on all five parameters. The void fraction increased with larger flow rate, though the magnitude of the void fraction was still relatively small. The drag coefficient increased rapidly within the first 50 ccm, and then it leveled off to approximately 2.8. Bubble diameter increased from approximately 6 mm to 12 mm over the range of the flow rate. Bubble residence time decreased from approximately 1.1 s to 0.87 s. Bubble velocity increased from approximately 0.185 to 0.235 m/s. The bubble velocity profile mirrored the bubble residence time curve. In summary, lower flow rates produced larger residence times, which would lead to higher CH_4 conversion. It was also found at flow rates above 23.7 ccm, temperature had an adverse effect on bubble residence time, but increasing temperature increased bubble diameter. This effect is most likely due to the reduced viscosity, density and decreased surface tension at higher temperatures. However, at flow rates below 23.7 ccm, a switch in the

temperature effects on bubble residence time and velocity curves is noticed. This may be because bath density takes a relatively larger role in the terminal velocity calculations at at lower flow rates when the bubble diameter and drag coefficient are predicted to be lower.

The results for the quartz sparger are given in Figure 4.11. As can be seen, the flow rate did not have any affect on the bubble drag coefficient, diameter, residence time or velocity. The void fraction did show a linear increase, though it had no effect on the drag coefficient. The lack of effect of flow rate is probably due to the fact that Tate's law, given in Equation (4.24) is independent of flow rate and is suited for low flow systems where less than 30 bubbles are formed in a minute [75]. Temperature had an effect on all the parameters. The same trends for the tubular injector were found for the void fraction and drag coefficient of the quartz injector. In these cases, higher temperatures produced higher void fractions and higher drag coefficients. On the other hand, Tate's law predicted smaller bubble diameters and velocity, but higher residence time for higher temperatures. The formulation by Tsuge et al. [9] for 6.35 mm injector tube predicted the opposite trend for higher flow rates for these three parameters. However, this may be because predicted bubble size and drag coefficient are already sufficiently small enough so that the bath density plays a larger role in the velocity calculation.

The quartz sparger and 6.35 mm tube injectors both predict similar residence times. The quartz sparger gives 0.785 to 0.805 s, and the tube injector gives 0.85 s to 1.12 s, depending on temperature.

4.3.1.3 Effect of bubble diameter on bubble rise

The effect of bubble diameter was analyzed for two cases. The first of which the total volume flow rate was set to $\dot{V} = 17$ ccm, and $x_{CH_4,0} = 0.5$, $x_{N_2,0} = 0.5$, which is what eleven of the thirteen experimental runs were performed at. The second case was at a total volume flow rate of $\dot{V} = 200$ ccm, while keeping $x_{CH_4,0} = 0.5$, $x_{N_2,0} = 0.5$. In both cases bubble diameter was varied between $5e \times 10^{-5}$ m and 5×10^{-2} m.

The results for the first case are shown in Figure 4.12. At bubble diameters lower than 3×10^{-4} m, an increase in the void fraction was noticed. The drag coefficient and hence bubble residence time also increased substantially. The drag coefficient increased in part due to increased void fraction. It is expected that increasing the void fraction would affect bubble drag due to larger bubble-bubble hydrodynamic

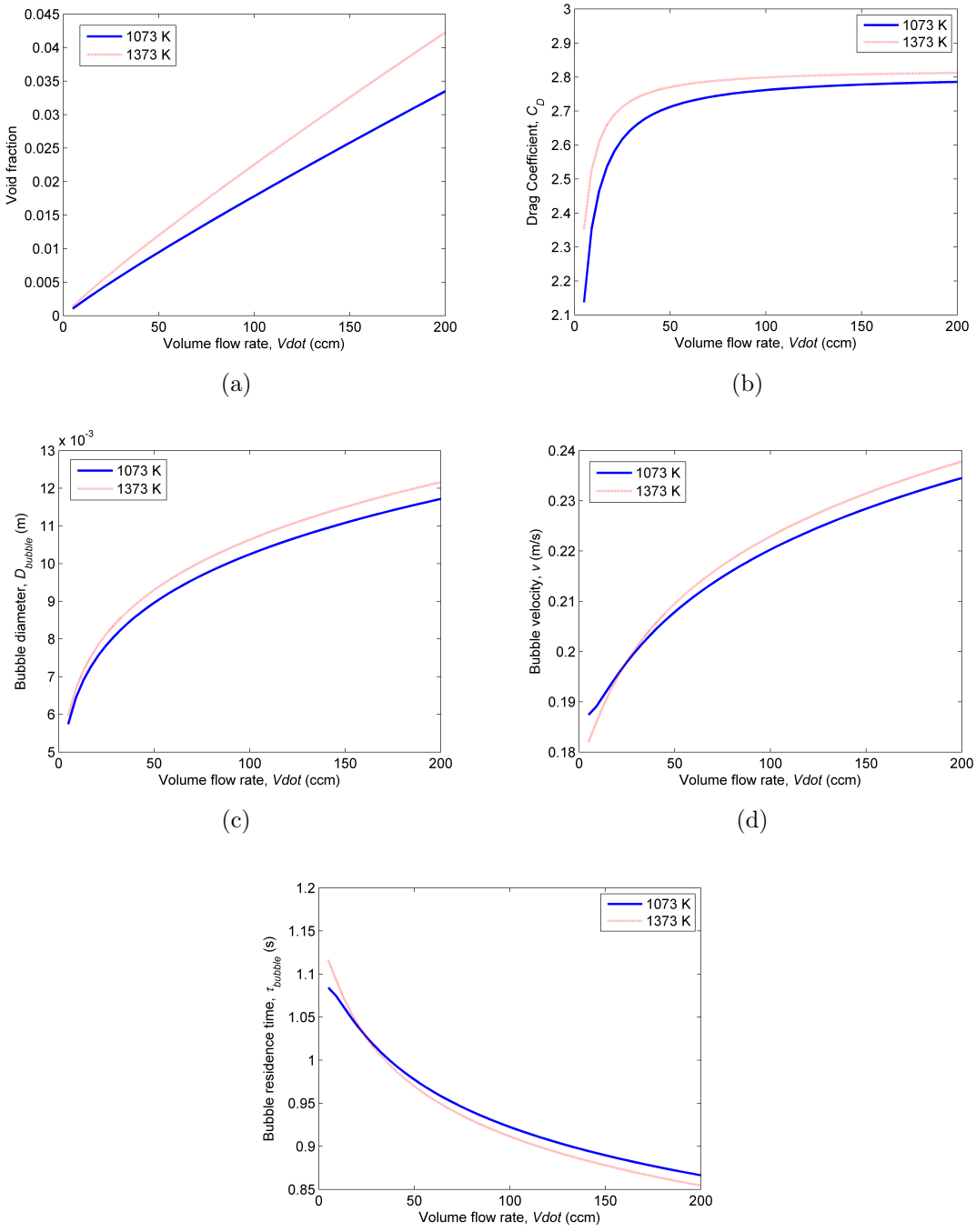

Figure 4.10 – Characterization of the flow for the 6.35 mm injector tube, assuming the bubble formulation by Tsuge et al. [9].

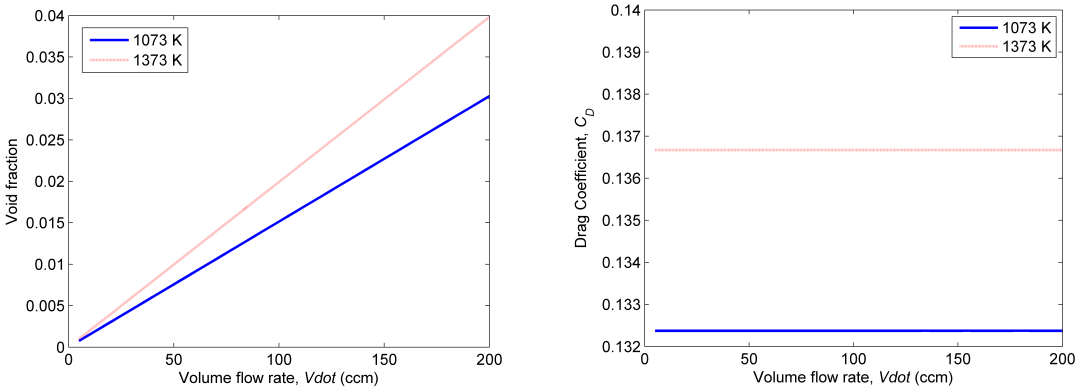

(a)

(b)

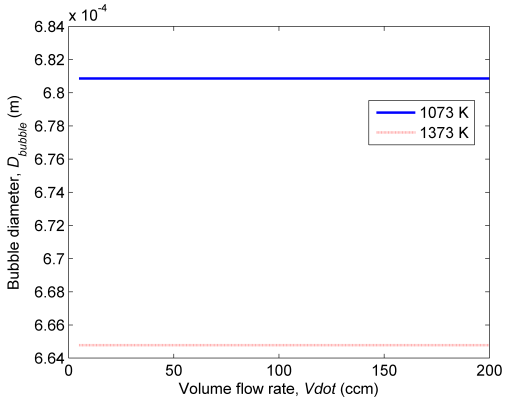

(c)

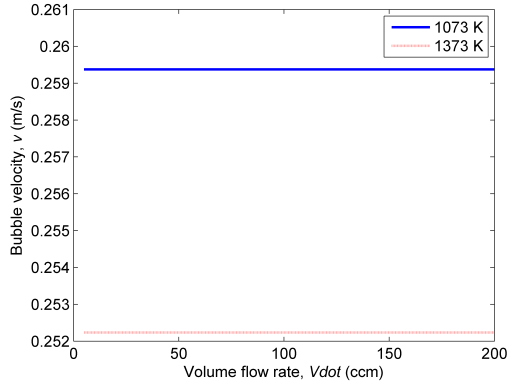

(d)

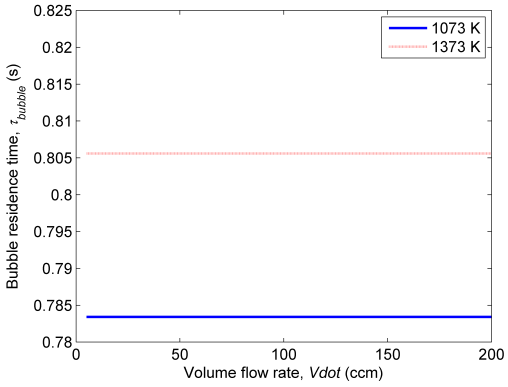

(e)

Figure 4.11 – Characterizing the flow for the 7 μm quartz sparger, assuming Tate's law for the bubble formulation [8].

interactions [7]. The drag coefficient is simply the sum of the pressure and friction drag coefficients [7], and both of these increase with increased void fraction [7]. Bubble 'wake' or fluid disturbance as the bubble rises has been noted by Kendoush [79]. Delnoij et al. [77] identified bubble collision, which causes either bubble coalescence, separation, or bubbles bouncing off each other. Coalescence occurs if there is enough force of motion to push the molten Sn out from between both bubbles. The effect of the increasing void fraction on drag coefficient is apparent in the drag coefficient curve for $D_{bubble} \leq 5 \times 10^{-4}$ m. There was no effect of void fraction changes for $D_{Bubble} \geq 5 \times 10^{-4}$ m. At this bubble diameter Re surpasses 1×10^{3}. At this point the drag coefficient is predicted using the curve by Rodrigue [6], given in Equation (4.35), where the void fraction is not considered. The effect of temperature is not as substantial as bubble diameter, though for $D_{bubble} \leq 5 \times 10^{-4}$ m, higher temperatures decrease the drag coefficient, increase bubble velocity and decrease bubble residence time.

The results for the second case are shown in Figure 4.13. The higher flow rate gives a higher void fraction than the first case. The void fraction shows more variation for $D_{bubble} \in [1 \times 10^{-4}\ 5 \times 10^{-2}]$ m. However, the Re for $D_{bubble} \in [6 \times 10^{-4}\ 1 \times 10^{-1}]$ m was large enough so the drag coefficient was calculated by the formulation by Rodrigue [6] in Equation (4.35). The formulation by Rodrigue does not depend on α. Therefore the change in void fraction must be solely due to the temperature difference at higher flow rates. This deviation in α is on the order of 0.05, which is very small and does not have a large impact on the end solution anyway. Similar to the first case, the trends for velocity and residence time curves are direct opposites of each other. It should be noted that the bubble residence times for the second case are higher than what was predicted in the first case. In the first and second case, maximum values of approximately 20 s and 40 s were obtained at $D_{bubble} = 1 \times 10^{-4}$ and 1030 K.

4.3.1.4 Bubble radial effects

The transient bubble model was studied to determine the effect of bubble diameter on the radial profile of CH_4 conversion and heat transfer mechanisms. The four cases that were considered are shown in Table 4.4. The largest expected bubble size was on the order of 1×10^{-3} m for $\dot{V} = 200$ ccm, based on the numerical results in Figure 4.10(c) for the 6.35 mm tube injector. Larger injectors would only decrease the bubble residence time and as such would be impractical. τ_{bubble} was set to 5 seconds because radial effects are most likely noticed in the short term. $\dot{V}$ was set to 30 ccm, and bath

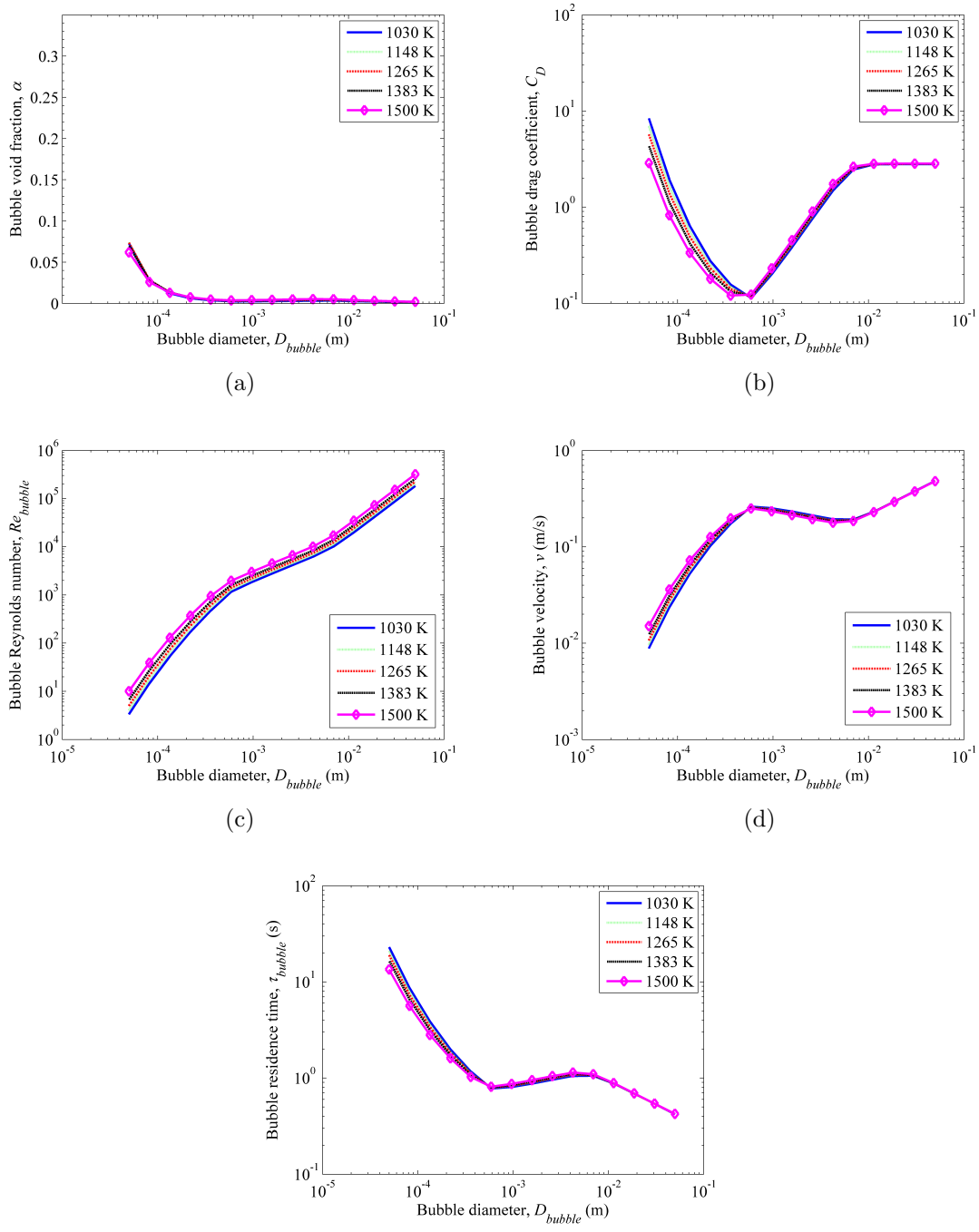

Figure 4.12 – Effect of bubble diameter on bubble rise parameters, $\dot{V} = 17$ ccm.

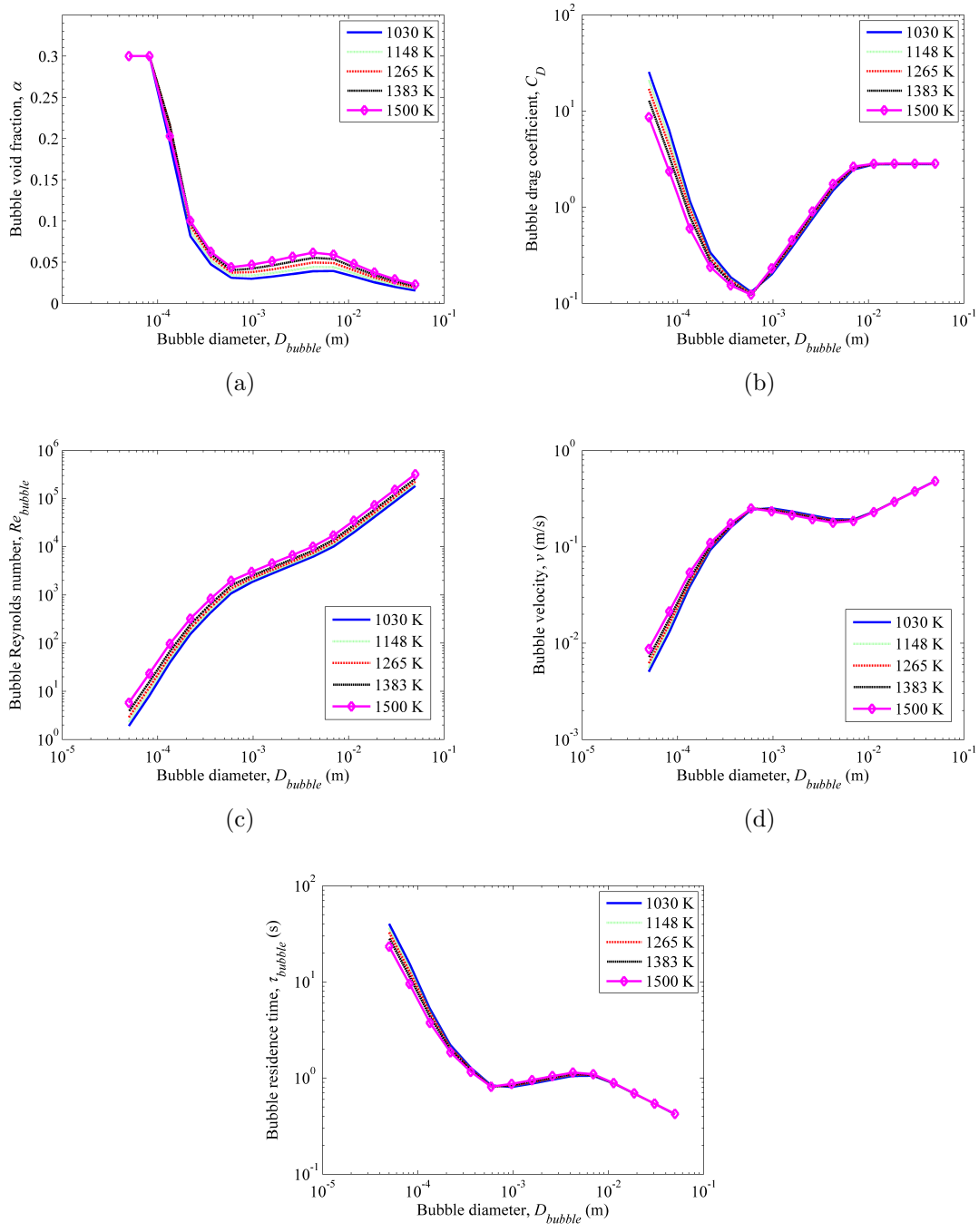

Figure 4.13 – Effect of bubble diameter on bubble rise parameters, $\dot{V} = 200$ ccm.

Table 4.4 – Input parameters for testing effect of D_{bubble} on reaction and heat transfer mechanisms.

Case	D_{bubble} **(m)**	T_0 **(K)**
1	4×10^{-2}	1023
2	4×10^{-2}	1373
3	1.0×10^{-4}	1023
4	1.0×10^{-4}	1373

height was set to 20.3 mm. The results are shown in Figure 4.14. It can be seen that some profiling occurs in the temperature plots of Cases 1 and 2, but the deviations were less than 2.5 K, which was considered negligible. Cases 3 and 4 did not show any profiling. Concentration profiles were also uniform in all four cases. Therefore it was assumed that the bubble was isothermal and the reaction mechanism performed uniformly such that the bubble was well mixed.

4.3.1.5 Summary

To this point the results from the bubble model were as expected with no anomalies observed. The bubble diameters for the quartz sparger and 6.35 mm tube injector were within reasonable limits. The effects of bubble diameter and volumetric flow rate on bubble rise parameters were studied and were found to follow expected trends. It was verified that the bubbles could be assumed to be isothermal with uniform concentrations.

The following sections study the final molten metal CH_4 cracking model, which was completed by combining the CPMR model with the bubble model. The bubble model predicted $X_{CH_4,bubble}$, or the amount of CH_4 conversion at the point of the bubble exiting from the bath. The CPMR model covered the heated blank space above the molten bath and predicted $X_{CH_4,f}$, which is the total CH_4 conversion that occurred inside the reactor.

4.3.2 Numerical results and experimental validation

The numerical molten metal CH_4 cracking model was compared with the results presented in Section 2.6.3. The experimental runs can be categorized into three different cases based on total volumetric flow rate and injector type. The cases are listed in Table 4.5.

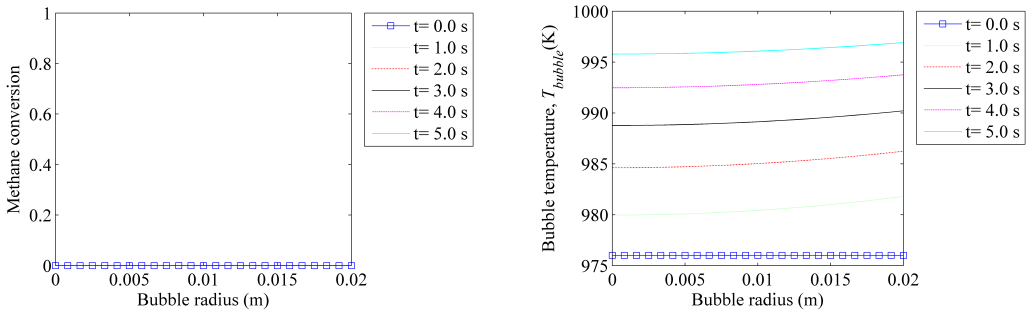

(a)

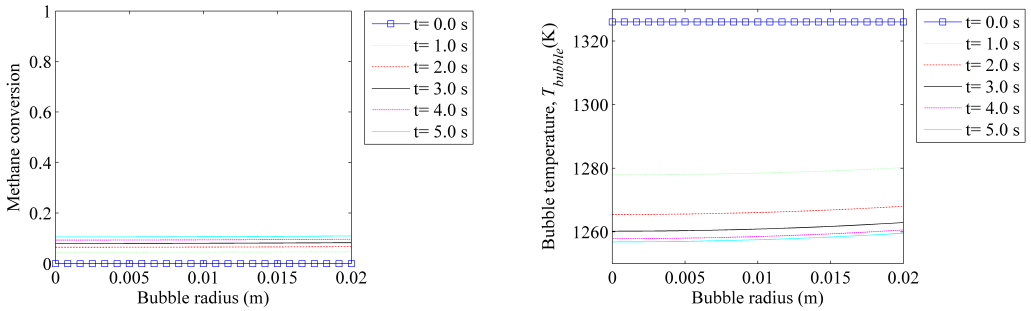

(b)

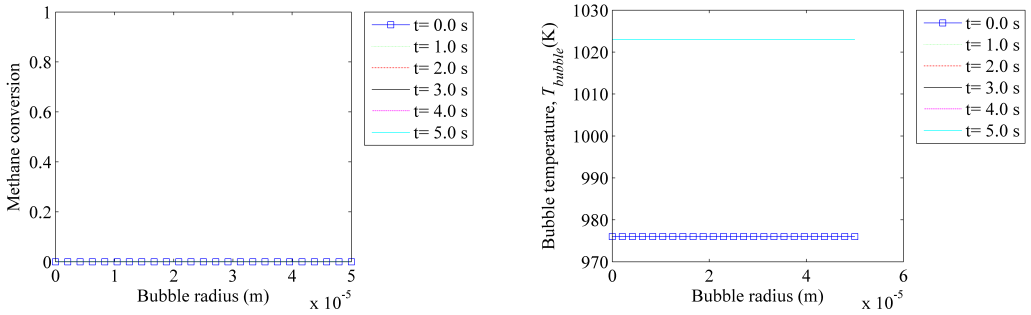

(c)

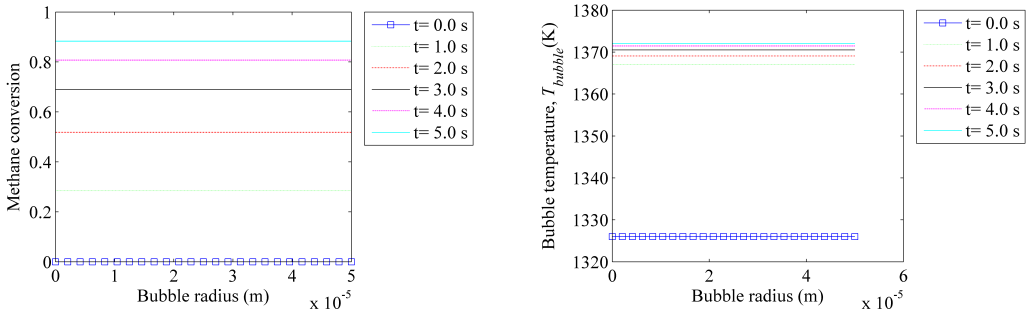

(d)

Figure 4.14 – Bubble conversion and temperature numerical results for (a) Case 1, (b) Case 2, (c) Case 3 and (d) Case 4.

Table 4.5 – Three main cases that were tested experimentally.

Case	Injector	Flow rate (ccm)
1	6.35 mm tube	17
2	6.35 mm tube	152
3	quartz sparger	17

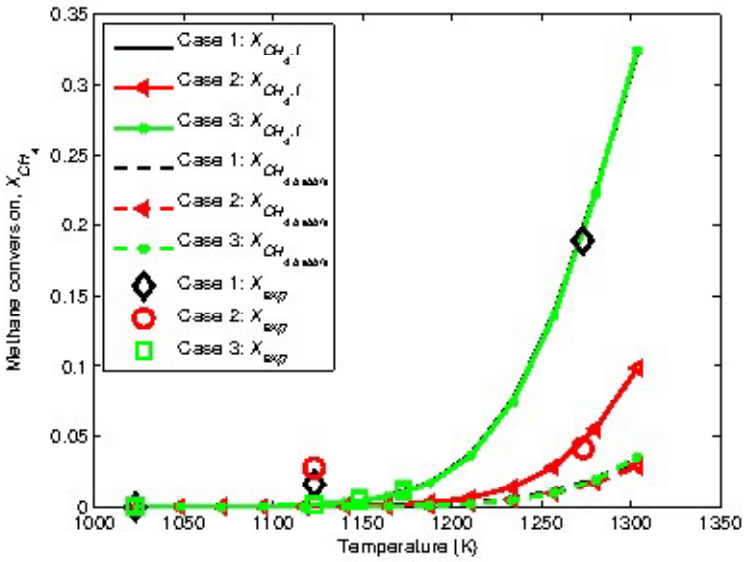

Figure 4.15 – Comparison of numerical model to experimental results for the molten metal CH_4 cracking reactor. $\beta = 0.426$.

The results are shown in Figure 4.15. The numerical results were close to the experimental results. The only data point that had greater than $X_{CH_4} = 0.042$ conversion was in the Case 1 dataset. The experimental and numerical values for these corresponding conditions at 1273 K were 0.189 and 0.195, which gives 3% error. The numerical model predicted similar results between Cases 1 and 3, which suggests that the bubble residence time in the molten bath between these two models were very similar. This is consistent with the findings in Section 4.3.1.2 where residence time was calculated for different volumetric flow rates. It is also consistent with Section 4.3.1.4, where it is shown that the bubble is very nearly uniform in temperature and CH_4 conversion, and so the expected difference in bubble size is not able to significantly affect CH_4 conversion.

It can be seen in Figure 4.15 that the primary amount of CH_4 conversion occurred

in the blank heated space above the molten metal. This is because the reaction gas spends the majority its time in this space. The residence time of the gas in the blank space is estimated using

$$\tau_{above} = \frac{V_{H,above}}{\dot{V}_0}$$

where the volume of space above the molten metal, $V_{H,above}$, is described as

$$V_{H,above} = \frac{\pi}{4}(D_{r,in}^2 - D_{I,out}^2)L_{H,above}$$

where $L_{H,above}$ is the length of heated space above the molten metal, given by Equation (3.7). $D_{r,in}$ is the inner diameter of the reactor vessel. The heated length at 1273 K is estimated to be 0.274 m using Equation (3.10) and assuming the injector has an outer diameter of 6.35 mm. Thus $L_{H,above} = 0.071$ m for a bath height of 0.203 m. The corresponding residence time of the heated blank space above the molten metal is then approximately 380 s. This is assuming that the gas spends all the time in the blank space, when in reality a portion of the flow rate is actually mixed into the rest of the reactor due to the large temperature differentials. The above results were computed assuming $\beta = 0.426$ from the CPMR best-fit results in Chapter 3. This would correspond to a gas residence time of 195 s in the heated blank space. If the actual β value for the molten metal reactor is estimated using the length scales of the heated blank space and the total blank space, the β would equal

$$\beta = 1 - \frac{0.071}{(0.508 - 0.203)} = 0.77$$

where the total reactor length is 0.508 m. In this case the gas residence time would spend approximately 89 s in the heated blank space above the bath. It should be noted, however, that the temperature profile in the space above the molten tin decreases from operating temperature to 1023 K. This requires the calculation of an effective temperature (see Section 4.2.3). Figure 4.16 shows a plot of the equivalent effective temperature for the space above the molten metal at different operating temperatures. At 1273 K, the effective temperature is approximately 1207 K. The residence time of the bubble in the molten metal for Case 3 at 1273 K is on the order of 1 s. Given the above analysis, it would be expected that the majority of CH_4 conversion would occur in the blank space above the reactor, though the effective temperature would reduce the amount of conversion that took place. It is apparent from Figure 4.15, however, that the amount of residence time in the space above the molten metal was sufficient enough to provide the majority of CH_4 conversion.

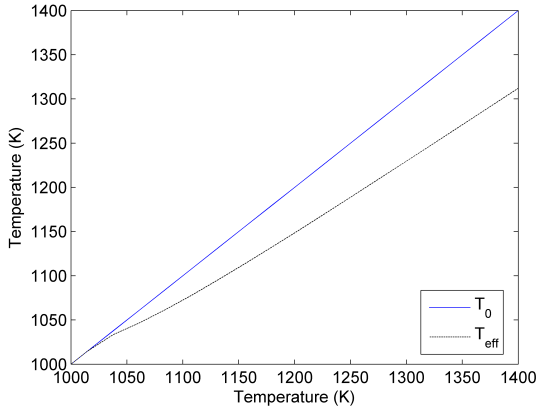

Figure 4.16 – Effective temperature compared to operating temperature for the heated blank space above the reactor.

A comparison against experimental data for $\beta = 0.77$ is shown in Figure 4.17. The error for the Case 1, 1273 datapoint increased to 29%. However, the same trends observed with $\beta = 0.462$ are observed where the majority of CH_4 conversion occurs in the blank space above the reactor.

4.3.3 Comparison to literature

The numerical molten metal CH_4 cracking model was compared to the results reported by Serban et al. [2]. The reactor was similar to the one studied in this thesis, however the molten bath was contained in a 0.5 inch cup inside the 1 inch OD by 14 inch long reactor vessel to ensure the reactor vessel could be re-used. A thermocouple was inserted in the space between the reactor vessel and cup to measure operating temperature. The reactor was heated using a Thermcraft four zone furnace with a temperature controller. The reaction gas was composed of either 100% CH_4 or natural gas. The gas was bubbled through the molten metal by inserting the injector pointing downwards into the molten bath.

There was not enough information reported by Serban et al. [2] to successfully model the entire reactor. The height of the cup containing the molten metal was not specified. The temperature profile inside the reactor was not reported. Furthermore, the author did not record the location of the molten metal inside the furnace, or how much blank space was heated above the reactor. Nor was it reported how the reactor was cooled at the top, if at all. Because of this missing information, the following comparison to Serban et al.'s work is only to determine how much conversion would have occurred inside the bath for each molten metal experiment.

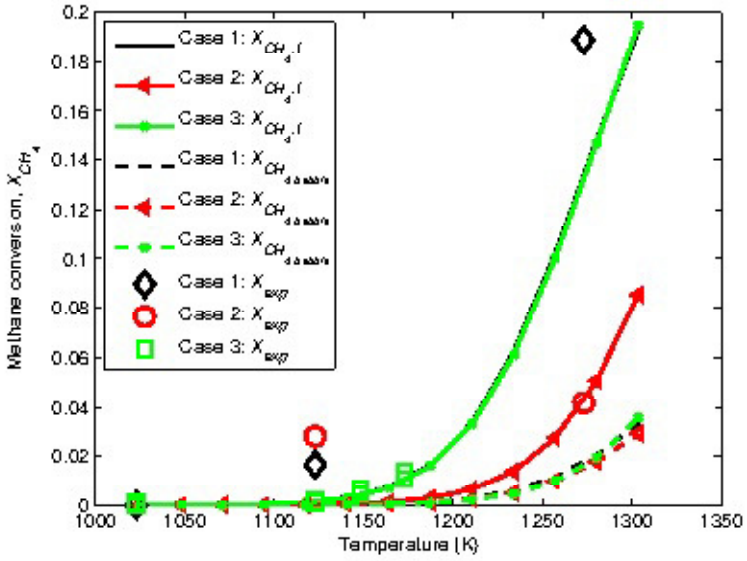

Figure 4.17 – Comparison of numerical model to experimental results for the molten metal CH_4 cracking reactor. $\beta = 0.77$.

Serban et al. [2] reported results from several molten metal experiments. The parameters were tabulated and entered into the model to estimate the magnitude of CH_4 conversion in the bath. A list of the experimental conditions and results for these tests are given in Table 4.6. Serban et al. [2] performed the experiments with a bath height of 0.102 m.

The results are shown in Figure 4.18. The model predicted that zero CH_4 conversion would occur in the molten bath. This is not in agreement with what Serban et al. [2] found experimentally. Serban et al. performed blank reactor and molten metal reactor tests and compared them. It was shown that having molten metal increased CH_4 conversion [2]. However, it was shown in Chapter 2 that the experimental results from the work in this thesis were not similar to the results by Serban et al. Having molten metal in the reactor dramatically reduced CH_4 conversion in the experimental work in this thesis, to values of near zero conversion. It is possible that the molten metal in Serban et al.'s study had some impurities that catalyzed the reaction, or the bubbles were attracted to the SS reactor walls if molten metal was present. Serban et al. [2] did find some iron carbide in X-ray diffraction analysis of carbon samples. Otherwise the reason of the discrepancies between this work and Serban et al.'s is unknown, but both the model and experimental work of this thesis are consistent with each other. Therefore it is recommended that future studies be performed to

Table 4.6 – List of experimental runs by Serban et al. [2] that are compared to the numerical molten metal CH_4 cracking model.

No.	T_0 **(K)**	$\dot{V}_{CH_4}$ **(ccm)**	**Injector type**	$X_{CH_4,Sn}$
1	1023	9	1/4 inch tube	0.02
2	1023	5	1/4 inch tube	0.04
3	1023	15	1/16 inch tube	0.09
4	1023	9	1/16 inch tube	0.14
5	1023	25	10 μm Mott sparger	0.07
6	1023	15	10 μm Mott sparger	0.16
7	1023	9	10 μm Mott sparger	0.22
8	1023	25	0.5 μm Mott sparger	0.14
9	1023	15	0.5 μm Mott sparger	0.20
10	1023	9	0.5 μm Mott sparger	0.25
11	823	15	0.5 μm Mott sparger	0.05
12	873	15	0.5 μm Mott sparger	0.17
13	923	15	0.5 μm Mott sparger	0.30
14	973	15	0.5 μm Mott sparger	0.46
15	973	15	0.5 μm Mott sparger	0.42
16	1023	15	0.5 μm Mott sparger	0.51
17	1023	15	0.5 μm Mott sparger	0.54
18	1073	15	0.5 μm Mott sparger	0.70

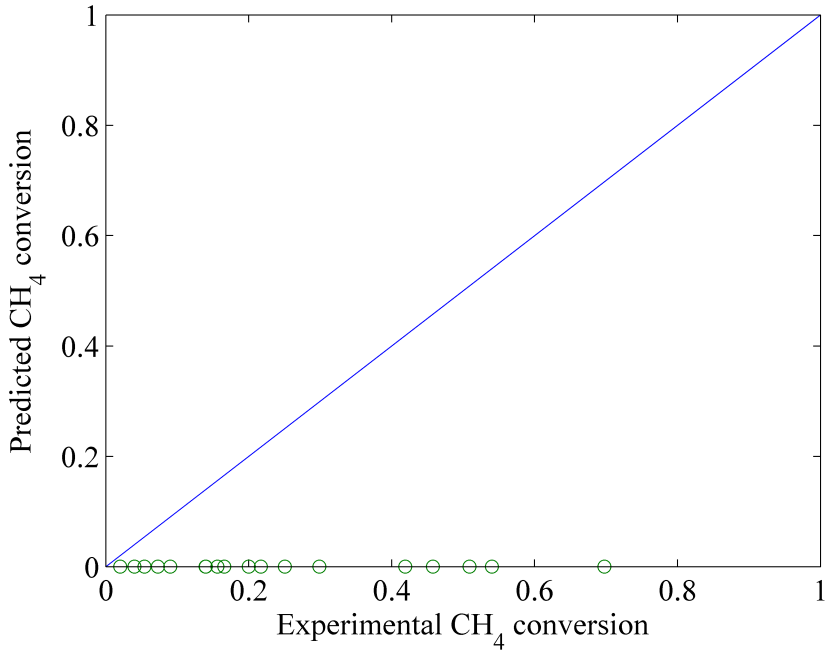

Figure 4.18 – Comparison of numerical molten metal reactor model to results reported by Serban et al. [2].

see if either Serban et al.'s work or the work in this thesis can be replicated.

4.3.4 Sensitivity analysis

The impacts of bubble diameter, bath height, inner reactor diameter, and activation energy were studied by varying the respective parameters. Each sensitivity analysis was also performed for operating temperatures ranging from 1030 K to 1500 K. The operating parameters are given in Table 4.2, unless otherwise stated. The total volumetric flow rate was set to 17 ccm, with a 50% split between N_2 and CH_4.

4.3.4.1 Bubble diameter

The molten metal CH_4 cracking reactor model was used to estimate conversion rates. The results are shown in Figure 4.19. Bubble diameter had a significant effect on CH_4 conversion. A larger portion of conversion occurred in the bubble as the bubbles grew smaller. Bubbles at 1030 K and 1148 K showed zero conversion. Higher temperatures of 1400 K and 1500 K at 17 ccm reached 100% conversion by approximately $D_{bubble} = 5 \times 10^{-5}$ m and 2.2×10^{-4} m, respectively. At 200 ccm, the 1400 K and 1500 K curves reach 100% conversion by approximately $D_{bubble} = 8 \times 10^{-5}$ m and 2.2×10^{-4} m. Thus the higher flow rate had better conversion than the lower flow rate. 100% conversion

was obtained at 200 ccm at larger bubble diameters than the 17 ccm results. It was noticed in Figures 4.12 and 4.13 that the residence times for the higher flow rate were slightly larger than the residence times for the lower flow rates at the smaller bubble diameters. This is probably due to the effect of the void fraction increasing due to more bubbles being produced at a higher flow rate. The swarm effect of the bubbles increased the drag coefficient and gave higher residence times. If the bubble diameters can be produced small enough ($\leq$ 400 μm) without significant bubble coalescence, then having a higher flow rate may be beneficial to conversion.

By comparing Figures 4.19(a) and 4.19(b), it is clear that changing $\dot{V}$ had an effect on the final CH_4 conversion. There was no difference in conversion that occurred in the molten metal, however. The impact was noticed in the resulting conversion in the blank space. This is because the residence time in the blank space increased with the decreasing volume flow rate, but the increase in flow rate did not significantly affect the bubble residence time in the bath, with the exception of the very small bubble sizes. Therefore if the bubbles cannot be produced smaller than approximatey 400 μm, than lower flow rates will produce higher CH_4 conversion.

4.3.4.2 Bath height

The molten metal bath height was also varied to determine the optimal bath height. The bath height was varied between 0.05 m to 1 m. The temperature for the varying bed heights is unknown, and as such the blank space above the reactor was neglected. The results are shown in Figure 4.20. As can be seen, bath height had a large impact on systems where the bubbles are smaller. A 1 m bath height is predicted to give 85% conversion at an operating temperature of 1265 K and $D_{bubble} = 5 \times 10^{-5}$ m. An intermediate bubble size of 1.6×10^{-3} would obtain approximately 48% conversion at 1383 K. The 6.35 mm tube injector produced a bubble the size of 8×10^{-3} m, so it is expected that the tube injector would obtain a lower conversion than 48%. The quartz sparger, on the other hand, produced a bubble on the order of 7×10^{-4}, therefore it is expected that the reactor would obtain a higher conversion. The largest bubble diameter showed a negligible effect on varying the bath height, increasing conversion in the first 0.05 m to 0.3 m and then leveling off. A total change of approximately 0.05% conversion was predicted. From these findings it is recommended that higher bath heights be used for smaller bubbles. Depending on bubble size, increasing the bath height will have diminishing returns.

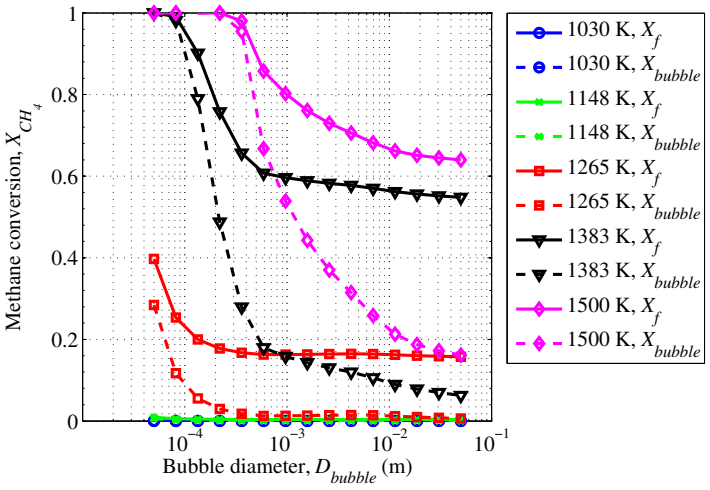

(a)

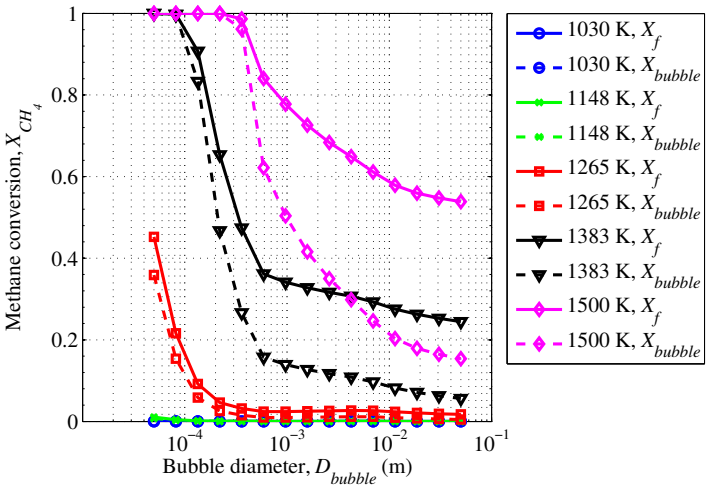

(b)

Figure 4.19 – Effect of bubble diameter on CH_4 conversion for (a) $\dot{V} = 17$ ccm and (b) $\dot{V} = 200$ ccm

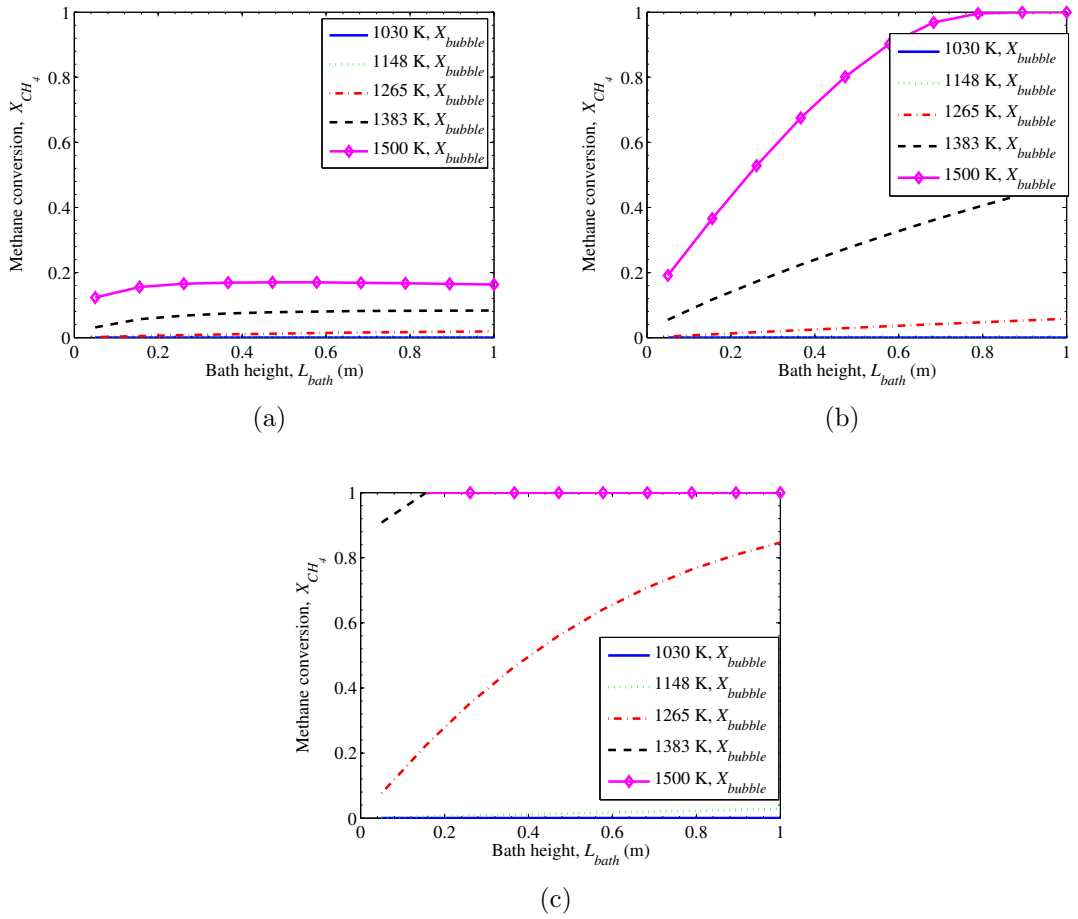

Figure 4.20 – Effect of bath height on CH_4 conversion for bubble diameters of (a) $5 \times 10^{-}2$ m, (b) 1.6×10^{-3} m, (c) and 5×10^{-5} m.

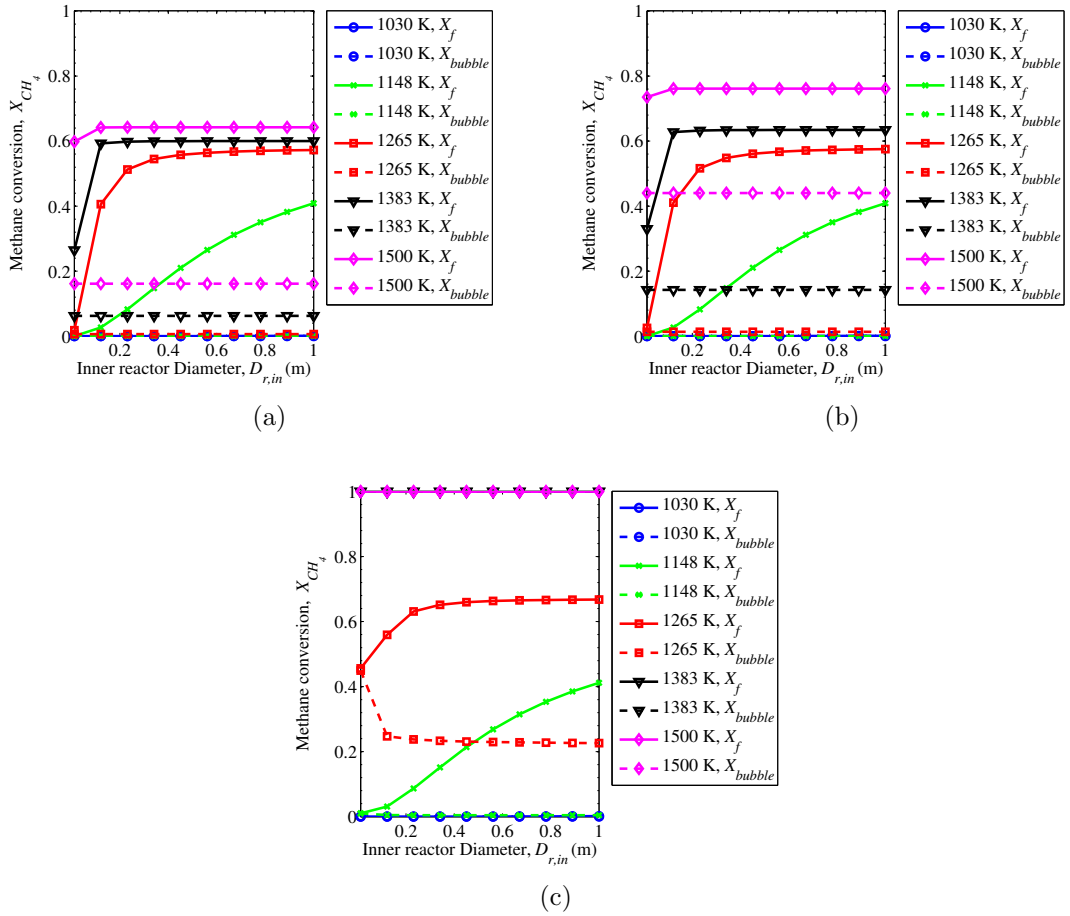

Figure 4.21 – Effect of the inner diameter of the reactor vessel on CH_4 conversion for bubble diameters of (a) $5 \times 10^{-}2$ m, (b) 1.6×10^{-3} m, (c) and 5×10^{-5} m.

4.3.4.3 Reactor vessel inner diameter

The inner diameter of the reactor vessel was varied between 0.012 m to 0.3 m. The results are shown in Figure 4.21. As can be seen, the reactor vessel inner diameter has some effect on $X_{CH_4,f}$. However, only the 1265 K and $D_{bubble} = 5 \times 10^{-5}$ m showed any effect for $X_{CH_4,bubble}$. In this case the conversion dropped from 0.45 to approximately 0.23. Otherwise the majority of the effect was noticed in the blank space conversion. This is because the blank volume of the reactor increases with residence time and provides a longer residence time in the heated blank volume above the molten metal. The maximum effect of reactor radius levels off at different values depending on temperature. The most significant gains in conversion are obtained between $D_{r,in} =$ 0.012 m to 0.34 m at 1265 K for $D_{bubble} = 2 \times 10^{-5}$ m and $D_{bubble} = 1.6 \times 10^{-3}$ m.

4.3.4.4 Activation energy

The sensitivity of the activation energy was studied to simulate the effects of including a catalyst into the system. A catalyst is expected to reduce the activation energy. Therefore E_a was varied between 210.3 kJ/mol and 462.7 kJ/mol, or $0.5 \times E_{a,CPMR}$ to $1.1 \times E_{a,CPMR}$. $E_{a,CPMR}$ is the best fit value obtained by the CPMR model in Chapter 3. The results are shown in Figure 4.22. $X_{CH_4,bubble}$ and $X_{CH_4,f}$ both increased significantly with decreasing E_a. The slope of $X_{CH_4,f}$ with respect to E_a grew more steep as bubble size decreased. The slope of $X_{CH_4,bubble}$ with respect to E_a grew even more dramatically steeper with decreasing bubble size. At $T_0 = 1030$ K, total conversion was reached at approximately $E_a = 320$ kJ/mol for $D_{bubble} = 5 \times 10^{-5}$, and $E_a = 218$ kJ/mol for $D_{bubble} = 1.6 \times 10^{-3}$. A maximum of 0.72 conversion was predicted for $E_a = 210.3$ kJ/mol and $D_{bubble} = 5 \times 10^{-2}$. If E_a is reduced further, 100% conversion would be obtained at 114 kJ/mol.

Nearly all CH_4 conversion occurred in the bubble for bubble sizes of $D_{bubble} = 5 \times 10^{-5}$ m. The portion of CH_4 conversion in the bubble compared to overall conversion in the reactor decreased as bubble size increased. In summary, smaller bubbles are recommended to reduce the required amount of catalyst.

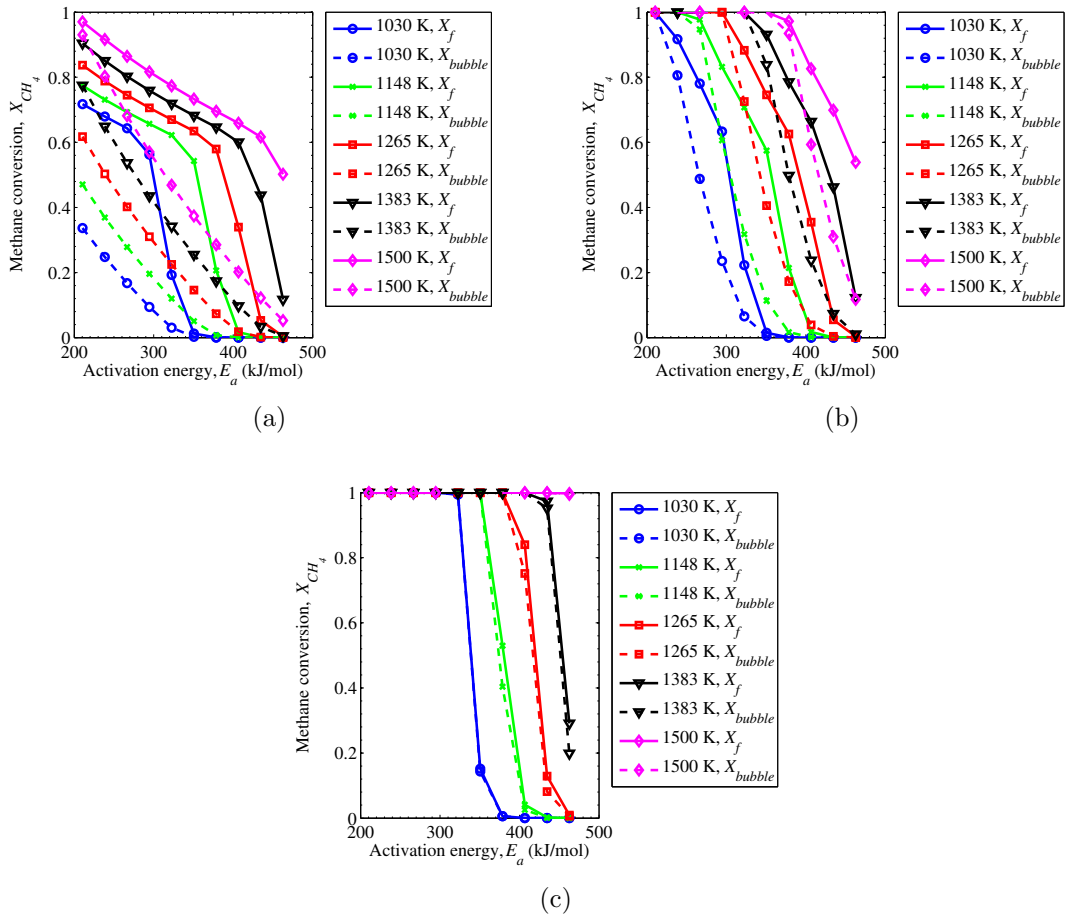

Figure 4.22 – Effect of the activation energy on CH_4 conversion for bubble diameters of (a) $5 \times 10^{-}2$ m, (b) 1.6×10^{-3} m, (c) and 5×10^{-5} m.

Chapter 5

Conclusions and future work

5.1 Conclusions

The main goal of this study was to determine the feasibility of molten metal CH_4 cracking using experimental and numerical means. Serban et al. [2] studied molten metal CH_4 cracking and reported that bubbling CH_4 through molten metal improved conversion compared to a reactor that does not contain any molten metal, or a blank reactor. Experiments are expensive, and so the numerical models were created to further the understanding of key fundamental parameters that control the effectiveness of the molten metal reactor. The activation energy and pre-exponential factor for the reaction rate of CH_4 dissociation vary widely in literature. Therefore in this study it was necessary to determine the kinetic parameters for thermal CH_4 dissociation by performing a series of blank reactor experiments that were void of the molten bath. The numerical models were used to fit the kinetic parameters using the experimental results. A series of molten metal experiments were also performed to determine the effectiveness of molten metal CH_4 cracking. Comparisons were made between the numerical models and experimental work, as well as a study made by Serban et al. [2] on molten metal CH_4 cracking.

The reactor assembly consisted of an Al_2O_3 tubular reactor vessel that was closed on one end and capped on the other with a 304 SS cap. The cap was machined and fitted to allow an injector and thermocouple to extend into the reactor and remain parallel to the reactor vessel walls. The injector was inserted until the tip was approximately 1.3 cm away from the closed end of the reactor vessel. The reactor assembly was orientated vertically in a cylindrical three-zone Thermcraft furnace with the closed end of the reactor assembly in the isothermal heated zone of the furnace and the capped end extending out of the furnace. The capped end was cooled with a

fan, thus causing the large temperature differential inside the reactor. The product gas exited the reactor assembly through the cap and was analyzed in a micro gas chromatograph. The total flow rate in the blank reactor varied between 30 to 200 ccm. The operating temperature varied between 1023 K and 1373 K. A 6.35 mm Al_2O_3 tube injector was used for the blank reactor experiments.

The molten metal experiments were designed to be as similar to the apparatus used by Serban et al. [2] as possible. Higher temperatures were desired though, so Al_2O_3 reactor wall material was chosen instead of 304 SS, which was used by Serban et al.

The same reactor vessel that was used in the thesis blank reactor experiments was used for the molten metal experiments with the addition of the molten bath. Sn of 99.97% purity was selected for the bath material in the molten metal reactor experiments. 20.3 cm bath heights were used. The reactor was positioned so that the heated blank space above the molten metal would be minimized. The molten metal experiments were performed with total flow rates of 17 ccm to 140 ccm, and temperatures of 1023 K to 1273 K. Two different injectors were used. The first was a 6.35 mm Al_2O_3 tube injector, and the second a quartz tube with a porous sparger at the tip. The sparger had a porosity of 4 to 10 μm.

In the blank reactor experiments, temperature was shown to have a large impact on CH_4 conversion. Higher temperatures produced higher conversions. Flow rate had a small impact on CH_4 conversion, with lower conversions at higher flow rates.

The molten media experiments showed zero conversion for all experiments performed at $\dot{V} \geq 30$ ccm, or the flow rates used in the blank reactor experiments. Therefore the flow rates were reduced to 17 ccm. At 17 ccm and 1273 K the 6.35 mm tube injector produced a maximum of 18.9% conversion. Otherwise all conversion values remained below 4%. The quartz sparger was tested up to 1173 K only due to temperature restraints.

Three different models were created to simulate the conditions in a blank reactor. These were the one-dimensional plug flow reactor (PFR), the zero-dimensional perfectly mixed reactor (PMR) and the zero-dimensional perfectly mixed reactor combined with a bypass (CPMR). It was shown that high temperature CH_4 cracking reactors exhibit large temperature variations. Significant buoyant forces cause tur-

bulent mixing if the reactor is heated at the lower section. It was verified that the reactor studied in this thesis was subject to large buoyancy mixing effects because the reactor was vertically orientated and the heated section was at the bottom section of the tube, with a temperature differential of at least 650 K. The CPMR model added a third fitting parameter, β, that describes the amount of reactant gas flow that by-passes the reacting zone to convective flows.

The experimental data from the blank reactor runs were used to fit the kinetic parameters to the PFR, PMR and CPMR models. It was found that the fitted parameters from the PFR and PMR predicted reaction rates much lower than those calculated from literature. The CPMR model kinetic parameters produced reaction rates that were in the expected literature range. The PFR and PMR models had very high residual errors of 0.595 and 0.422, respectively, because they over-predicted the effect of varying inlet gas flow rate. The CPMR model more closely modeled the experimental data points between 993 K and 1323 K with a residual of 0.125. The kinetic parameters from the CPMR model were estimated to be $k_0 = 5.43 \times 10^{15}$ 1/s and $E_a = 420.7$ kJ/mol, which fall into the literature range. β was determined to be 0.426, which suggests that a large portion of the inlet flow leaves the reactor unreacted. The effect of flow rate on β was studied. It was determined that increasing flow rates caused decreasing β.

The CPMR model was validated by simulating the reactor and experimental results reported by Rodat et al. [1]. The average error was 8.3% with a standard deviation of 6.8%. The reactor studied by Rodat et al. [1] exhibited higher volumetric flow rates and smaller reactor cross-sectional area. This coupled with the finding that higher flow rates lead to smaller $\beta = 0.089$. This value was found using the CPMR model with the CPMR kinetic parameters but fitting β to the experimental results of Rodat et al.

The PFR was also compared against the reactor by Rodat et al. [1]. The kinetics determined for the PFR in this thesis predict zero conversion, while using the CPMR kinetics the conversion is nearly 100% for all data points. However, Rodat et al. [37] studied the same reactor and used a PFR to obtain kinetic parameters. If these are used, the results are much closer with an average error of 10.7% and a standard deviation of 8.7%. The simulation in this thesis was done neglecting the conversion effects that occurred in the cooling zone, but Rodat et al. [1] showed that nearly all conversion occurred in the isothermal zone of the reactor.

The CPMR and PFR are both appropriate to analyze experimental reactors in literature. The PFR is more appropriate for reactors where high flow reactors where forced convection would outweigh buoyancy effects. The CPMR model is designed for low flow situations where buoyancy effects are large.

A sensitivity analysis was done on k_0, E_a and β for the PFR, PMR and CPMR. E_a had a large effect. Decreasing E_a severely increased CH_4 conversion. Increasing k_0 increased CH_4 conversion. Decreasing β increased CH_4 conversion in the CPMR reactor because less of the inlet volume flow rate exited without reacting. Thus it is recommended that future blank reactors are designed to minimalize β. This can be done by increasing flow rates, reducing the temperature gradients in the reactor or perhaps using baffles to restrict natural convective flows.

A molten metal reactor model was also developed. The molten metal CH_4 cracking model incorporated one-dimensional spherical partial differential equations for heat transfer and chemical reactions assuming the bubbles were spherical and maintained the same size. Bubble terminal velocity was estimated using a force law balance of buoyancy, drag and weight of the bubble. Bubble residence time in the molten bath was approximated using the height of the bath and buoyancy. The CPMR model was used to predict conversion in the blank heated space above the molten metal. The kinetic parameters from the CPMR blank reactor best fit were used.

The formulation by Tsuge et al. [9] for bubble size showed that increasing flow rate would increase bubble size, and reduce bubble residence time. Tate's law suggested that there was no impact on flow rate, but Tate's law was derived for low-flow rate scenarios. Increasing bath temperature was shown to increase bubble residence time using Tate's Law. The same was observed using the formulation by Tsuge et al. [9], but after a certain flow rate the relationship switched and increasing flow rate decreased residence time. A potential reason for this is that the bubble sizes are very small at low flow rates, as well as bubble velocity, and so bath density takes a larger role in the velocity calculation.

The molten metal reactor model predicted bubble sizes for various injector types. The 6.35 m tube injector and quartz sparger were predicted to form bubbles on the order of 8×10^{-3} and 7×10^{-4} m, respectively. The bubbles from the 6.35 mm tube injector were estimated to have residence times of 0.85 s to 1.12 s, and for the quartz

injector 0.785 to 0.805 s. Thus the smaller bubble did not increase bubble residence time.

The effect of bubble size and temperature on heat transfer and chemical reactions inside the bubble were studied using the partial differential equation bubble model. Bubble diameters of 4×10^{-2} and 1×10^{-4} and temperatures of 1023 K and 1373 K were analyzed. It was found that heat transfer and chemical reactions were essentially uniform throughout the bubbles.

The effect of bubble diameter on the bubble rise parameters such as bubble velocity, drag, Re, residence time, and void fraction was also studied for temperatures ranging from 1030 K and 1500 K, and total flow rates of 17 ccm and 200 ccm. Bubbles smaller than approximately 1×10^{-4} m showed a very significant increase in residence time with decreasing bubble diameter. This is because the drag force becomes very significant at bubble diameters smaller than 1×10^{-4} m. The void fraction increased for bubble sizes smaller than 5×10^{-4} m. In this range the drag coefficient also increased with increasing void fraction. The higher flow rates gave higher void fractions at smaller bubble diameters, thus effectively increasing the residence time. Temperature showed an effect at bubble sizes smaller than 5×10^{-4} m for both flow rates, with lower temperatures providing higher residence times.

The molten metal reactor model was compared against experimental results. A 3% error was found for the one datapoint that was above 4.2% conversion. The model predicted very similar results between the quartz sparger and 6.35 mm injector. This is most likely because the quartz injector and 6.35 mm tube injector produced bubble with diameters that were in the range where no significant changes in bubble residence time were noted. The majority of the conversion occurred in the heated blank space above the molten metal. This is as expected because the residence times of the bath and blank space are on the order of 1 s and 195 s. β was then increased to 0.77 to compensate for the much smaller heated space in the entire blank volume of the molten metal reactor, compared to the 0.426 value for the blank reactor. The residence time for the heated blank space above the bath then reduced from 195 s to 89 s. The majority of the CH_4 conversion still occurred in the heated blank space above the bath.

The results by Serban et al. [2] were also compared against the molten metal reactor model. The model predicted essentially zero CH_4 conversion in the CH_4 bubbles,

which is contrary to what Serban et al. observed experimentally. Similar discrepancies were found in the experimental section of this thesis with the results reported by Serban et al. [2]. It was shown both experimentally and theoretically in this thesis that near zero conversion was achieved at low operating temperatures of 1023 K. The majority of the results reported by Serban et al. [2] were for experiments performed at 1023 K, with the maximum temperatures being at 1073 K. Thus it may be that the Serban et al. reactor had some catalytic effect to the reaction to reduce the required reaction temperature.

A sensitivity analysis for bubble diameter, bath height, reactor vessel inner diameter and the activation energy on CH_4 conversion was also performed. Bubble diameters were varied from 5×10^{-2} m to 5×10^{-5} m. It was found that bubble diameter had a large effect on CH_4 conversion. Bubbles smaller than 4×10^{-4} m are recommended for higher flow rates. Otherwise lower flow rates for larger bubble sizes increases CH_4 conversion.

Bath height, reactor vessel inner diameter and activation energy were varied to study their effect on CH_4. Each parameter was studied at bubble diameters of 5×10^{-2} m, 1.6×10^{-3} m, and 5×10^{-5} m. The volumetric flow rate was set to 17 ccm. Bath height had an impact on CH_4 conversion. CH_4 conversion increased with increasing bath height.

The impact of increasing bath height became more significant as bubble diameter decreased. The larger reactor vessel inner diameters predicted higher CH_4 conversion. The most significant increases was noticed between $D_{r,in} = 0.012$ m to 0.34 m at 1265 K for $D_{bubble} = 2 \times 10^{-5}$ m and $D_{bubble} = 1.6 \times 10^{-3}$. The majority of the increase of CH_4 conversion occurred in the heated blank space above the reactor, where the residence time was increased with diameter increase.

The impact of decreasing the activation energy was investigated. It was found that lower activation energies improved conversion throughout the reactor for all bubble sizes. The impact became more significant as bubble size decreased, however. As bubble size decreased the conversion ratio between the heated blank space above the bath and the bubbles inside the bath decreased, because more CH_4 conversion occurred inside the bubbles. Smaller bubble sizes reached 100% conversion at higher activation energies. Therefore it was recommended that smaller bubble sizes be used to reduce the required amount of catalyst, should catalysts be desired.

In summary, blank and molten metal CH_4 reactor models that included buoyancy effects were created. Experiments were performed to obtain mathematical model parameters. Kinetic parameters that fell within the range of literature were found using a best-fit with experimental data of the blank reactor. The molten metal reactor was modeled and a deeper understanding of the physical phenomena that was occurring in the molten metal reactor was obtained. Significant differences exist between the results obtained in this thesis and what was reported by Serban et al. Therefore it is recommended that future studies be performed by a third party to verify which study is valid.

The molten metal reactor that was tested in this thesis showed that the majority of CH_4 conversion occured in the blank space above with very low conversions obtained in the bath, and as such was not considered feasible. This was because the injectors studied in this thesis provided bubble sizes that were estimated to have large and thereby low drag coefficients. As such, the bubble terminal velocities were very high and had residence times on the order of 1 s in comparison to approximately 89 s in the heated blank space above. Future studies are recommended with different reactor designs because injectors that produce bubbles with diameters on the order of 1×10^{-4} m and smaller have been shown by the MMR model to improve conversion by increasing drag, giving larger residence times. Similarily, residence time in the bath could also be improved by installing baffles or increasing bath height.

5.2 Future work

For the blank reactor experiments, it is recommended that a method be devised to reduce the large temperature differential in the reactor space and reduce buoyancy effects. More replicas should also be performed to determine repeatability. The reactor could be orientated horizontally to reduce the effects of buoyancy. Baffles could also be installed to compartmentalize the reactor and break up the natural convective flows caused by buoyancy effects. Significant amounts of plugging in the downstream filters also occurred in the apparatus and caused a buildup of pressure in the system. A better filtering system should be devised, or perhaps a filtering system from other authors who have tested CH_4 cracking could be adopted.

For the molten metal reactor experiments, it is recommended that further experimentation be performed. This includes more replicas, higher temperatures, and

perhaps using catalysts. The current experimental apparatus produced nearly zero CH_4 conversion at the temperatures studied. The catalysts would reduce the reacting temperature, but would require some sort of regeneration. 304 SS balls could be inserted in the molten metal to determine whether the 304 SS reactor walls were the cause of the high conversion amounts reported by Serban et al. [2]. It is also recommended that some changes be made to the apparatus. If possible an attempt should be made to make the reaction temperature more uniform in the reactor vessel. Perhaps the inlet could be relocated to the bottom of the reactor using a porous media. The porous media should be selected such that it inhibits any molten media to seep through, but still allow the gas bubbles to enter the reactor. Different porosities could be tested to vary the bubble size and distribution in the reactor. Also, injectors pointing upwards produce smaller bubbles than injectors pointing downwards [70]. Given that smaller bubbles have larger residence times, injectors pointing upwards are recommended. More studies have also been performed on upwards pointing injectors than downwards pointing injectors [70].

For the blank reactor models, further experiments could be performed to determine the residence time distribution. This is done using a step tracer experiment [62]. The test consists of injecting a tracer gas that is easily detectable and measuring the response over time. A mass spectrometer would be needed to measure the transient response. Then the tracer response could be compared against known profiles and perhaps a more suitable combination of ideal reactors could be selected [62]. This may give a model that would more accurately predict CH_4 conversion above 1323 K for the reactor studied in this thesis. Another suggestion would be to perform more blank reactor experiments at 1373 K and higher. β and the kinetic parameters k_0 and E_a are highly sensitive to temperature. Only one experiment was performed at 1373 K in the work of this thesis, and so the fitting was limited to the lower temperature range.

For the molten metal reactor model, bubble formation in molten metals should also be studied. The formulations in this thesis were not devised for bubbles in molten Sn, and as such only provided estimations for order of magnitude. Bubble drag coefficients for bubble swarms in molten metals should also be investigated for Reynolds numbers above 100. In this study the effects of CH_4 conversion in the injector were neglected. The residence times were much smaller in the molten metal, and so the effects of CH_4 conversion in the injector may need to be included.

The molten metal reactor model also could be edited to simulate different bath properties to determine if different inert molten metals would be more appropriate than Sn. If the new bath material is catalytic, then new kinetic parameters would have to be determined, however the bubble flow approximation would still be valid. The molten metal model also neglected the effect of H_2 production on bubble pressure or size, as well as static pressure at the bubble location at its depth in the molten metal. It would be beneficial to take these parameters into effect in determining bubble rise parameters.

References

[1] Rodat S, Abanades S, Coulie J, and Flamant G. Kinetic modelling of methane decomposition in a tubular solar reactor. *Chemical Engineering Journal*, 146(1): 120–127, January 2009.

[2] Serban M, Lewis M. A, Marshall C. L, and Doctor R. D. Hydrogen Production by Direct Contact Pyrolysis of Natural Gas. *Energy & Fuels*, 17(3):705–713, May 2003.

[3] Gueret C, Daroux M, and Billaud F. Methane pyrolysis : thermodynamics. *Chemical Engineering Science*, 52(5):815–827, 1997.

[4] Ozalp N and Shilapuram V. Step-by-step methodology of developing a solar reactor for emission-free generation of hydrogen. *International Journal of Hydrogen Energy*, 35(10):4484–4495, May 2010.

[5] Holmen A, Olsvik O, and Rokstad O. Pyrolysis of natural gas : chemistry and process concepts. *Fuel Processing Technology*, 42:249–267, 1995.

[6] Rodrigue D. A general correlation for the rise velocity of single gas bubbles. *The Canadian Journal of Chemical Engineering*, 82(2):382–386, May 2004.

[7] Kishore N, Chhabra R, and Eswaran V. Bubble swarms in power-law liquids at moderate Reynolds numbers: drag and mass transfer. *Chemical Engineering Research and Design*, 86(1):39–53, January 2008.

[8] Park Y, Lamont Tyler A, and Nevers de N. The chamber orifice interaction in the formation of bubbles. *Chemical Engineering Science*, 32(8):907–916, January 1977.

[9] Tsuge H, Tezuka Y, and Mitsudani M. Bubble formation mechanism from downward nozzle: effect of nozzle shape and operating parameters. *Chemical Engineering Science*, 61(10):3290–3298, May 2006.

[10] Moriarty P and Honnery D. Hydrogens role in an uncertain energy future. *International Journal of Hydrogen Energy*, 34:31–39, 2009.

[11] Ozalp N, Ibrik K, and Al-Meer M. Kinetics and heat transfer analysis of carbon catalyzed solar cracking process. *Energy*, 55:74–81, June 2013.

[12] Steinberg M. Fossil fuel decarbonization technology for mitigating global warming. *International Journal of Hydrogen Energy*, 24(8):771–777, August 1999.

[13] Paxman D, Trottier S, Nikoo M, Secanell M, and Ordorica-Garcia G. Initial Experimental and Theoretical Investigation of Solar Molten Media Methane Cracking for Hydrogen Production. *Energy Procedia*, 49:2027–2036, 2014.

[14] Abánades a, Ruiz E, Ferruelo E, Hernández F, Cabanillas A, Martínez-Val J, Rubio J, López C, Gavela R, Barrera G, Rubbia C, Salmieri D, Rodilla E, and Gutiérrez D. Experimental analysis of direct thermal methane cracking. *International Journal of Hydrogen Energy*, 36(20):12877–12886, October 2011.

[15] Wyss J, Martinek J, Kerins M, Dahl J. K, Weimer A. W, Lewandowski A, and Bingham C. Rapid solar-thermal decarbonization of methane in a fluid-wall aerosol flow reactor: fundamentals and application. *International Journal of Chemical Reactor Engineering*, 5(Article A69), 2007.

[16] Communication with Stephanie Trottier at Alberta Innovates - Technology Futures. Edmonton, AB, 2013.

[17] Cengel Y. A and Boles M. A. *Thermodynamics: an engineering approach*. McGraw-Hill, New York, NY, 7th edition, 2011. ISBN 978-0-07-131111-3.

[18] Olsvik O, Rokstad O. A, and Holmen A. Pyrolysis of methane in the presence of hydrogen. *Chemical Engineering & Technology*, 18(5):349–358, October 1995.

[19] Patrianakos G, Kostoglou M, and Konstandopoulos A. One-dimensional model of solar thermal reactors for the co-production of hydrogen and carbon black from methane decomposition. *International Journal of Hydrogen Energy*, 36(1): 189–202, January 2011.

[20] Billaud F, Gueret C, and Weill J. Thermal decomposition of pure methane at 1263 K: experiments and mechanistic modelling. *Thermochimica Acta*, 211 (0040):303–322, December 1992.

[21] Khan M. S and Crynes B. L. Survey of recent methane pyrolysis literature. *Industrial & Engineering Chemistry*, 62(10):54–59, October 1970.

[22] Eisenberg B and Bliss H. Recent advances in kinetics. *Chemical Engineering Progress Symposium Series*, 63(72):3–17, 1967.

[23] Holmen A, Rokstad O, and Solbakken A. High-temperature pyrolysis of hydrocarbons. I. Methane to acetylene. *Industrial & Engineering Chemistry, Process Design and Development*, 15(3):439–444, 1976.

[24] Billaud F, Baronnet B, Freund E, Busson C, and Weill J. Thermal decomposition of methane: bibliographic study and proposal of a mechanism. *Review of the French Petroleum Institute*, 44(6):813–823, 1989.

[25] Chen C, Back M, and Back R. The thermal decomposition of methane. I. Kinetics of the primary decomposition to $C_2H_6 + H_2$; rate constant for the homogeneous unimolecular dissociation of methane and its pressure dependence. *Canadian Journal of Chemistry*, 53(23):3580–90, 1975.

[26] Younessi-Sinaki M, Matida E. A, and Hamdullahpur F. Kinetic model of homogeneous thermal decomposition of methane and ethane. *International Journal of Hydrogen Energy*, 34(9):3710–3716, May 2009.

[27] Abbas H. F and Daud W. M. A. W. Hydrogen production by methane decomposition: a review. *International Journal of Hydrogen Energy*, 35(3):1160–1190, February 2010.

[28] Amin A. M, Croiset E, and Epling W. Review of methane catalytic cracking for hydrogen production. *International Journal of Hydrogen Energy*, 36(4):2904–2935, February 2011.

[29] Steinberg M. Production of hydrogen and methanol from natural gas with reduced CO_2 emission. *International Journal of Hydrogen Energy*, 23(6):419–425, 1998.

[30] Muradov N, Smith F, and T-Raissi A. Catalytic activity of carbons for methane decomposition reaction. *Catalysis Today*, 102-103:225–233, May 2005.

[31] Abanades S, Tescari S, Rodat S, and Flamant G. Natural gas pyrolysis in double-walled reactor tubes using thermal plasma or concentrated solar radiation as external heating source. *Journal of Natural Gas Chemistry*, 18(1):1–8, March 2009.

[32] Rodat S, Flamant G, and Abanades S. Experimental evaluation of indirect heating tubular reactors for solar methane pyrolysis reactors for solar methane pyrolysis. *International Journal of Chemical Reactor Engineering*, 8, 2010.

[33] Hirsch D and Steinfeld A. Solar hydrogen production by thermal decomposition of natural gas using a vortex-flow reactor. *International Journal of Hydrogen Energy*, 29:47–55, January 2004.

[34] Trommer D, Hirsch D, and Steinfeld A. Kinetic investigation of the thermal decomposition of CH_4 by direct irradiation of a vortex-flow laden with carbon particles. *International Journal of Hydrogen Energy*, 29:627–633, May 2004.

[35] Abanades S and Flamant G. Solar hydrogen production from the thermal splitting of methane in a high temperature solar chemical reactor. *Solar Energy*, 80 (10):1321–1332, October 2006.

[36] Abanades S and Flamant G. Experimental study and modeling of a high-temperature solar chemical reactor for hydrogen production from methane cracking. *International Journal of Hydrogen Energy*, 32(10-11):1508–1515, July 2007.

[37] Rodat S, Abanades S, Sans J.-L, and Flamant G. Hydrogen production from solar thermal dissociation of natural gas: development of a 10kW solar chemical reactor prototype. *Solar Energy*, 83(9):1599–1610, September 2009.

[38] Maag G, Rodat S, Flamant G, and Steinfeld A. Heat transfer model and scale-up of an entrained-flow solar reactor for the thermal decomposition of methane. *International Journal of Hydrogen Energy*, 35(24):13232–13241, December 2010.

[39] Dahl J. K, Barocas V. H, Clough D. E, and Weimer A. W. Intrinsic kinetics for rapid decomposition of methane in an aerosol flow reactor. *International Journal of Hydrogen Energy*, 27:377–386, 2002.

[40] Matovich E. High temperature chemical reaction processes utilizing fluid-wall reactors. United States Patent 1978/4095974., 1978.

[41] Dahl J. K, Weimer A. W, Z' Graggen A, and Steinfeld A. Two-dimensional axi-symmetric model of a solar-thermal fluid-wall aerosol flow reactor. *Journal of Solar Energy Engineering*, 127:76–85, 2005.

[42] Homayonifar P, Saboohi Y, and Firoozabadi B. Numerical simulation of nano-carbon deposition in the thermal decomposition of methane. *International Journal of Hydrogen Energy*, 33(23):7027–7038, December 2008.

[43] Olsvik O and Billaud F. Modelling of the decomposition of methane at 1273 K in a plug flow reactor at low conversion. *Journal of Analytical and Applied Pyrolysis*, 25:395–405, 1993.

[44] Ozalp N and Jayakrishna D. Numerical study on the thermal interaction of gas-particle transport for a vortex flow solar reactor. In *ASME 4th International Conference on Energy Sustainability*, pages 1–9, Pheonix, Arizona, USA, 2010.

[45] Ozalp N and Kanjirakat A. A CFD study on the effect of carbon particle seeding for the improvement of solar reactor performance. In *ASME 4th International Conference on Energy Sustainability*, pages 1–10, Pheonix, Arizona, USA, 2010.

[46] Krishna D. J and Ozalp N. Numerical investigation of particle deposition inside aero-shielded solar cyclone reactor: a promising solution for reactor clogging. *International Journal of Heat and Fluid Flow*, 40:198–209, 2013.

[47] Marshall C. L, Lewis M. A, Leibowitz L, and Lewis D. The pyrolysis of methane over liquid metal to form hydrogen and carbon. In *First Information Exchange Meeting on Nuclear Production of Hydrogen, Oct 2-3, 2000*, Paris, France.

[48] Lewis M. A, Serban M, Marshall C. L, and Lewis D. Direct contact pyrolysis of methane using nuclear reactor heat. In *American Nuclear Society 2001 Winter Meeting*, Nevada, USA.

[49] Landgraf M. Hydrogen from methane without CO_2 emissions. URL `http://www.kit.edu/kit/english/pi_2013_12783.php`. Date accessed: May, 2014.

[50] Hirsch D and Steinfeld A. Radiative transfer in a solar chemical reactor for the co-production of hydrogen and carbon by thermal decomposition of methane. *Chemical Engineering Science*, 59(24):5771–5778, December 2004.

[51] Costandy J, El Ghazal N, Mohamed M. T, Menon A, Shilapuram V, and Ozalp N. Effect of reactor geometry on the temperature distribution of hydrogen producing solar reactors. *International Journal of Hydrogen Energy*, 37(21):16581–16590, November 2012.

[52] Linden P. F. The fluid mechanics of natural ventilation. *Annual Review of Fluid Mechanics*, 31(1):201–238, January 1999.

[53] Drazin P. G and Reid W. H. *Hydrodynamic stability*. Cambridge University Press, Cambridge, NY, 1982. ISBN 0-521-28980-7.

[54] Kundu P. K and Cohen I. M. *Fluid Mechanics*. McGraw-Hill, New York, NY, 4th edition, 2008. ISBN 978-0-12-373735-9.

[55] Cengel Y. *Heat and mass transfer: a practical approach*. McGraw-Hill, New York, NY, 3rd edition, 2007. ISBN 978-0-07-312930-3.

[56] McDanel Advanced Ceramic Technologies, 2012. URL `http://mcdanelceramics.thomasnet.com/category/tube-seals`. Date accessed: January, 2014.

[57] Technical Glass Products, 2010. URL `http://www.technicalglass.com/technical_properties.html`. Date accessed: January, 2014.

[58] Petrucci R. H, Harwood W. S, Herring F. G, and Madura J. D. *General Chemistry: Principles and Modern Applications*. Pearson Prentice Hall, Upper Saddle River, NJ, 9th edition, 2007. ISBN 0-13-149330-2.

[59] Jiji L. M. *Heat convection*. Springer-Verlag Berlin Heidelberg, New York, 2006. ISBN 3540-30692-7.

[60] McDanel Advanced Ceramic Technologies . 99.8 percent Alumina data sheet, 2009. URL `http://www.mcdanelceramics.com/alumina.html`. Date accessed: April, 2014.

[61] Environment Canada . National Climate Data and Information Archive, 2013. URL `http://climate.weather.gc.ca/`. Date accessed: January 2014.

[62] Fogler H. S. *Elements of chemical reaction engineering*. Prentice-Hall, Inc., New Jersey, 2nd edition, 1992. ISBN 0-13-263534-8.

[63] Incropera F. P, Dewitt D. P, Bergman T. L, and Lavine A. S. *Fundamentals of heat and mass transfer*. John Wiley & Sons, Inc., Hoboken, NJ, 6th edition, 2007. ISBN 978-0-471-45728-2.

[64] Bird R. B, Stewart W. E, and Lightfoot E. N. *Transport Phenomena*. Wiley India (P.) Ltd., New York, 2nd edition, 2005. ISBN 978-81-265-0808-2.

[65] Haberman R. *Applied parital differential equations with Fourier Series and boundary value problems*. Pearson Prentice Hall, Upper Saddle River, NJ, 4th edition, 2004. ISBN 0-13-065243-1.

[66] The MathWorks Inc . MATLAB product help, 2012. URL `mathworks.com`. Date accessed: June, 2014.

[67] Vanderplaats, Garret N. *Numerical optimization techniques for engineering design*. Vanderplaats Research & Development, Inc., Colorado Springs, CO, 3rd edition, 2001. ISBN 0-944956-01-7.

[68] Kevorkian V, Heath C. E, and Boudart M. The decomposition of methane in shock waves. *The Journal of Physical Chemistry*, 64(8):964–968, August 1960.

[69] Israelachvili J. N. *Intermolecular and surface forces*. Elsevier Inc., San Diego, CA, 3rd edition, 2011. ISBN 978-0-12-391927-4.

[70] Kulkarni A. a and Joshi J. B. Bubble formation and bubble rise velocity in gasliquid systems: a review. *Industrial & Engineering Chemistry Research*, 44 (16):5873–5931, August 2005.

[71] Jamialahmadi M, Zehtaban M. R, Müller-Steinhagen H, Sarrafi A, and Smith J. M. Study of bubble formation under constant flow conditions. *Chemical Engineering Research and Design*, 79(5):523–532, 2001.

[72] Tsuge H, R\"{u}din P, and Kammel R. Bubble formation from a vertically downward facing nozzle in liquids and molten metals. *Journal of Chemical Engineering of Japan*, 19(4):326–330, 1986.

[73] Tsuge H, Mitsudani M, and Tezuka Y. The Effect of Nozzle Shape on Bubble Formation from a Downward Nozzle. *Chemical Engineering & Technology*, 29 (9):1097–1101, September 2006.

[74] Tate T. On the magnitude of a drop of liquid formed under different circumstances. *The London, Edinburgh, and Dublin Philosophical Magazine and Journal of Science*, XXVII:176–180, 1864.

[75] Blanchard D and Syzek L. Production of air bubbles of a specified size. *Chemical Engineering Science*, 32:1109–1112.

[76] Trottier S. Design of an experimental apparatus for molten media CH_4 cracking - Task Two Report. Technical report, Alberta Innovates - Technology Futures, 2012.

[77] Delnoij E, Lammers F, Kuipers J, and Swaaij van W. Dynamic simulation of dispersed gas-liquid two-phase flow using a discrete bubble model. *Chemical Engineering Science*, 52(9):1429–1458, May 1997.

[78] Ford B and Loth E. Forces on ellipsoidal bubbles in a turbulent shear layer. *Physics of Fluids*, 10(1):178–187, 1998.

[79] Kendoush A. A. Hydrodynamic model for bubbles in a swarm. *Chemical Engineering Science*, 56(1):235–238, January 2001.

[80] Cengel Y. A and Cimbala J. M. *Fluid mechanics fundamentals and applications*. McGraw-Hill, New York, NY, 2nd edition, 2010. ISBN 978-0-07-352926-4.

[81] Cussler E. *Diffusion: Mass transfer in fluid systems*. Foundation Books, New Delhi, 2nd edition, 1998. ISBN 81-7596-037-X (pb).

[82] Keene B. J. Review of data for the surface tension of pure metals. *International Materials Reviews*, 38(4):157–192, January 1993.

[83] Yaws C. L. *Yaws' handbook of properties of the chemical elements*. Knovel, December 2011.

[84] Handbook Committee . *ASM Handbook. Vol. 2*. ASM International, USA, 1990. ISBN 0-87170-378-5.

Appendix A

Material properties

A.1 Gas mixture properties

Tabulated data from Cengel [55] was used to obtain polynomial relationships for CH_4, H_2 and N_2. The equations for gas mixtures are given in this section.

Molar mass of mixture

The molar mass of a gas mixture is calculated by

$$M_{mix} = \sum_j M_j x_j \tag{A.1}$$

where M_j and x_j are the molar mass and molar fraction of species j, respectively.

Dynamic viscosity

The dynamic viscosity of a gas mixture is calculated by [64]

$$k_{mix} = \sum_\lambda \frac{x_\lambda \mu_\lambda}{\sum_\varphi x_\varphi \Phi_{\lambda\varphi}} \tag{A.2}$$

where $\Phi_{\lambda\varphi}$ is given by [64]

$$\Phi_{\lambda\varphi} = \frac{1}{\sqrt{8}} \left(1 + \frac{M_\lambda}{M_\varphi}\right)^{-1/2} \left[1 + \left(\frac{\mu_\lambda}{\mu_\varphi}\right)^{1/2} \left(\frac{M_\varphi}{M_\lambda}\right)^{1/4}\right]^2 \tag{A.3}$$

Thermal conductivity

The thermal conductivity of a gas mixture is calculated by [64]

$$k_{mix} = \sum_\lambda \frac{x_\lambda k_\lambda}{\sum_\varphi x_\varphi \Phi_{\lambda\varphi}} \tag{A.4}$$

where $\Phi_{\lambda\varphi}$ was given by Equation (A.3)

Specific heat capacity

The specific heat capacity at constant pressure for a gas mixture is given by

$$C_{p,mix} = \sum_j C_{p,j} x_j \tag{A.5}$$

where $C_{p,j}$ is the specific heat capacity at constant pressure of species j.

The specific heat capacity of a gas at constant volume for an ideal gas is given by [17]

$$C_{v,mix} = C_{p,mix} - R \tag{A.6}$$

where R is the universal gas constant.

Density

The density of a gas mixture is given by

$$\rho_{mix} = \sum_j \rho_j x_j \tag{A.7}$$

where ρ_j is the density of gas species j.

Gas diffusion

The gas diffusion coefficient for a binary gas was determined using the method and data presented in Chapter 5 of the book by Cussler [81].

A.2 Tin properties

The properties for Sn are discussed in this section.

Surface tension

The surface tension of Sn was taken from Keene [82], who compiled a general equation using data from literature.

$$\sigma = 0.001 \times (561.6 - 0.103 \times (T - 505.15)) \tag{A.8}$$

where T is the temperature in units of [K]. σ is calculated in units of [N/m].

Other properties

Polynomial relationships for thermal conductivity k_{Sn} [83], specific heat capacity $C_{p,Sn}$ [83], density ρ_{Sn} [84] were determined using data from their respective sources. Data for the dynamic viscosity of Sn, μ_{Sn}, was available only from 505 K to 1073 K

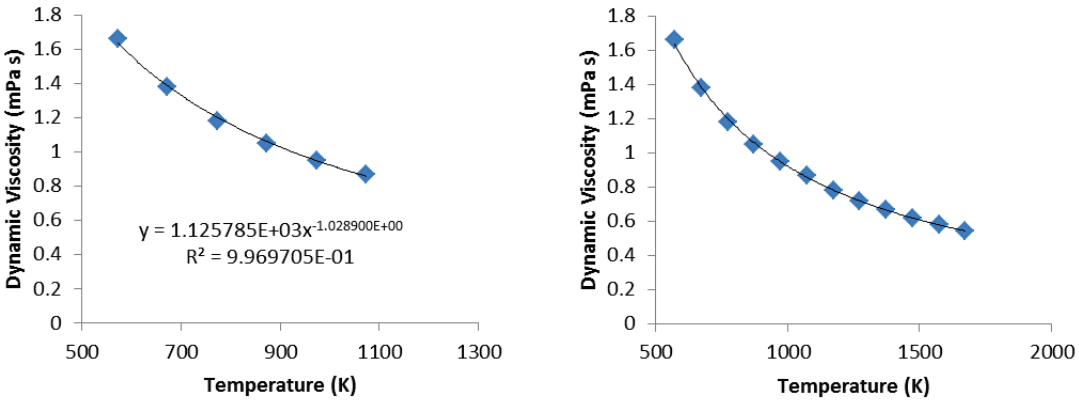

Figure A.1 – Dynamic viscosity curves for Sn with (a) fitting data, and (b) extrapolating to higher temperatures

[83, 84]. Therefore a relationship was determined using data from the 573 K to 1073 K range [84]. A power-law best fit was assumed. The relationship was then used to extrapolate up to 1673 K. The fitting curve and extrapolation result is shown in Figure A.1.